Advances in Printing and Media Technology

Vol. XLIV(IV)

Edited by Patrick Gane
Associate editor: Cathy Ridgway

Darmstadt
MMXVII

Advances in Printing and Media Technology

Proceedings of the 44th International Research Conference of iarigai
Fribourg , Switzerland, September 2017

Published by the International Association of
Research Organizations for the Information,
Media and Graphic Arts Industries
Darmstadt, Germany, 2017

Edited by Patrick Gane, Aalto, Finland
Associate editor: Cathy Ridgway, Oftringen, Switzerland

Online edition
ISBN 978-3-9870704-7-1
ISSN 2409-4021

Contents

5A – Printing inks

5B – Print quality

6A – Printing functionality 2

6B – Substrates for printing

7 – Plenary session – Introduction & panel discussion on digital direct manufacturing

Moderator: *Fritz Bircher*

Digital Direct Technologies
Steve Knight

Polytype SA
Jean-Marc Moriggia

3D iam
Reto von Arx

Introduction to the proceeding of the iarigai conference 2017

The iarigai International Research Conference is the major scientific and technical event of the print and media field. This year's Conference on "Advances in Printing and Media Technology" takes place in Fribourg, Switzerland from 10th to 13th September 2017, hosted by the iPrint Institute of the University of Applied Sciences of Western Switzerland. Under the general topic of expanding "from printing to manufacturing", the focus of this 44th iarigai conference is on functional printing, media developments, and print science with new research findings and topical observations - information that will benefit both industry and the research community.

We are convinced that the proceedings of the Fribourg conference will contribute to the international exchange of knowledge between researchers from various fields as well as between research and industry. Thus, let us all work together for the further development of the print and media industries.

With our best regards,

Prof. Fritz Bircher,
Conference Chair

A Model of Inkjet Printing on porous Substrates incorporating Droplet Impact

Li Yang[1], *Jianghao Liu*[2] *and Xianfu Wei*[2]

[1] Research Institute of Sweden, RISE Bioeconomy/Papermaking and Packaging, Drottning Kristinas väg 61, 11428 Stockholm, Sweden

[2] Beijing Institute of Graphic Communication, School of Printing and Packaging, 102600, People's Republic of China

E-mail: li.yang@ri.com

Abstract

A model of inkjet printing has been developed, with which ink absorption driven by the force of ink droplet as well as capillary pressure can be simulated and studied. Thanks to the analytical solution, a comprehensive view of the relationships between the characteristics of the ink (volume, striking speed, viscosity and surface tension), substrate properties (pore size and surface energy etc.), and interactions between the ink and the substrate (striking pressure, contact angle, depth of ink penetration etc.) can be obtained.

Keywords: printing dynamics, inkjet printing, paper and ink interaction

1. Introduction

Inkjet printing is a rapidly growing business area as it offers a number of advantages compared to conventional printing technologies, for instance no restriction to surface roughness. Inkjet has widely been used in home and office applications and is gaining strong positions in packaging and functional printing lications. There have been a large number of research reports on inkjet printing of both theoretical and experimental nature. Nevertheless, up to date the inkjet printing processes have often been oversimplified. The focus has mainly been given to the post ink-striking processes, e.g. wetting and absorption (Kettle, et al., 2010), while the ink-striking process has largely been overlooked. Hence, the knowledge of inkjet printing is incomplete.

The behaviour of droplets impacting against porous media finds its importance in a myriad of applications and process (Alam, et al., 2007). Yet the existing knowledge has been limited, amid to complexity and highly dynamic nature in combination with short duration time of the impacting process (Josserand and Thoroddsen, 2016). Girard, et al. (2006) modelled impacting droplets as having an initial state with bulging rims and a central depression. Starov, et al. (2002) and Alleborn and Raszillier (2004) modelled droplet spreading and absorption into topographically flat porous layers. Alam, et al. (2007) modelled impact spreading and absorption of Newtonian droplets on topographically irregular porous materials.

In this work, we present a model of inkjet printing dynamics, which is analytically solvable. This enables one to obtain a comprehensive view of the relationships between the characteristics of the ink droplet (volume, striking speed, viscosity and surface tension), substrate properties (pore size and surface energy etc), and interactions between the ink and the substrate (striking pressure, contact angle, depth of ink penetration etc). This work relates closely to our previous work on the dynamics of conventional printing processes (Yang, 2013).

2. The model of dynamics of inkjet printing

Assuming the striking force of the ink droplet at time t is $F(t)$. As the ink droplet is spherical, the detailed process can be viewed as that the ink droplet strikes the substrate surface in a slice by slice manner, see Figure 1. According to the Impulse Theorem, the impulse and the change in momentum fulfil the following relationship, provided the slice has zero speed in the vertical direction after striking,

$$F(t)dt = \pi\rho(2rz - z^2)vdz \quad [1]$$

where ρ is the mass density of the ink, r the radius of the ink droplet, z the height of the slice counted when the bottom side of the sphere kisses the substrate surface, and dz the thickness of the slice. Let the volume of the ink droplet be Vol. The radius of the ink droplet equals,

$$r = \left(\frac{3Vol}{4\pi}\right)^{1/3} \quad [2]$$

Using the relationship $z = v$, from Eq. 1 we receive

$$F(t) = \rho\pi\left[2rvt - (vt)^2\right]v^2 \quad [3]$$

Provided that the surface porosity is φ the mean pressure resulting from the striking force equals,

$$P(t) = \frac{F(t)}{(1-\phi)\pi r^2} = \rho v^2 \frac{2rvt - (vt)^2}{(1-\phi)r^2} \quad [4]$$

This expression describes the detailed time dependence of the striking pressure. In all of the preceding equations, the time is within the duration of ink droplet's striking, i.e. $0 \le t \le \frac{2r}{v}$.

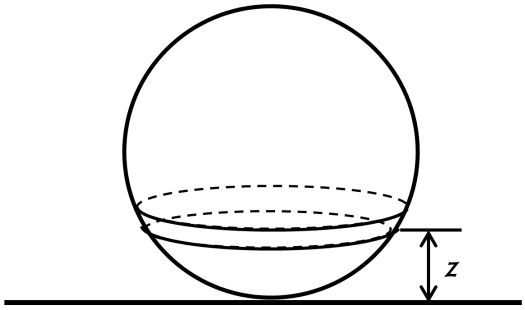

Figure 1: Illustration of the ink droplet that strikes the substrate surface

Due to the fact that the ink droplet is small, the duration of the striking is extremely short, in micro seconds. Hence, it is practically convenient to write the striking force in form of delta function, i.e.

$$F(t) = C_0\delta(t) \quad [5]$$

where the quantity C_0 is a constant. According to the Impulse Theorem, we can easily see that

$$C_0 = mv \quad [6]$$

where $m = \rho Vol$ is the mass of the ink droplet. Put this expression into the Lucas-Washburn equation (Washburn, 1921), one obtains

$$8\pi\eta L\frac{dL}{dt} = \frac{R^2}{(1-\phi)r^2}mv\delta(t) + 2\pi R\gamma\cos\theta \quad [7]$$

where L stands for the length of ink penetration as the ink penetration does not necessary only going downwards into the substrate. In Eq. 7, the term on the left hand side stands for the viscos drag, while the

first term on the right hand side comes from the (ink droplet) striking force and the second term from the capillary force. The general expression for the length of the ink penetration at time t is,

$$L = \sqrt{\frac{R\gamma\cos\theta}{2\eta}t + L_0^2} = \sqrt{\frac{R\gamma\cos\theta}{2\eta}t + \frac{mvR^2}{4\pi(1-\phi)\eta r^2}} \quad [8]$$

In Eq. 8 L_0 is the initial length of ink penetration resulted from the striking of the ink droplet,

$$L_0 = \frac{R}{r}\sqrt{\frac{mv}{4\pi(1-\phi)\eta}} \quad [9]$$

3. Results and discussion

Equations 4, 8 and 9 are the major results of the model. They give one a comprehensive view of the relationships between the characteristics of the ink droplet, substrate properties, and interactions between the ink and the substrate. Simulations based on these equations shed a light on the basics of inkjet printing, which are otherwise difficult to be obtained by experimental means. The surface porosity of the substrate has been assumed to φ = 30 % in all of the simulations.

3.1 Striking pressure of ink droplet

Figure 2 depicts the pressure profiles resulted from ink-striking by ink droplets of different volumes and jetting speeds. The time duration of the striking process is in the order of microsecond. One can also see that the peaks of the striking pressure depend solely on the jetting velocities while the duration time of the striking processes depend only on the droplets volumes.

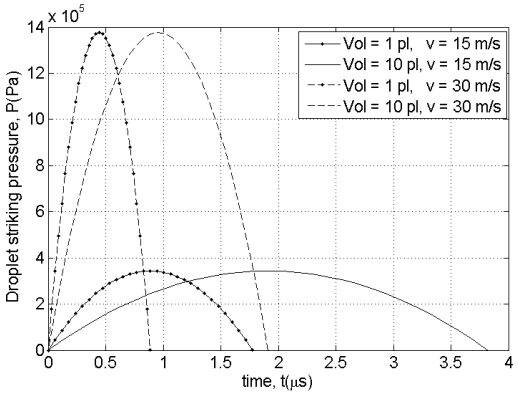

Figure 2: The pressure profiles of striking by ink droplets of different volume and speed, calculated by Eq. 4

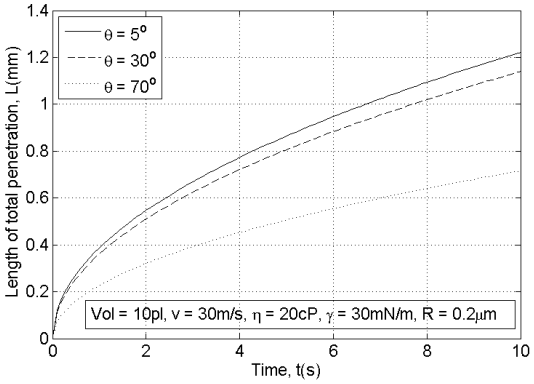

Figure 3: The length of ink-penetration corresponding to different contact angles, 5, 35 and 70 degrees, calculated by Eq. 8; the other parameters remain the same (given in the figure) in all of the calculation

3.2 Depth of ink-penetration

Figure 3 shows the time evolution of the ink penetration length corresponding to inks of different contact angles with the substrate surface. As seen the penetration length (depth) depends heavily on the contact angle, which is expected from Eq. 8. The initial penetration depth (L_0) in relation with the striking speed, calculated using Eq. 9, is shown in Figure 4. For a coated surface of small pores (R = 0.2 μm), the initial penetration depth is 0.26 μm when the striking speed is 30 m/s, while for a larger pore (R = 1 μm) the corresponding depth becomes 1.30 μm.

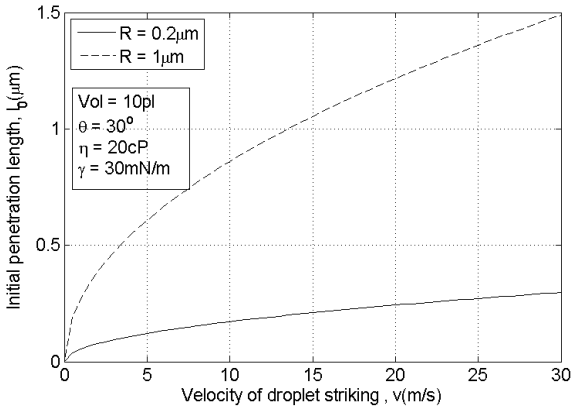

Figure 4: The initial lengths of ink-penetration corresponding to different pore radii of substrates, calculated by Eq. 9; the other parameters remain the same (given in the Figure) in the calculations

4. Conclusion

An extended model of inkjet printing has been developed, with inclusion of impact of ink droplet. Through the analytical solution, a comprehensive view of the relationships between the characteristics of the ink, substrate properties, and interactions between the ink and the substrate can be obtained.

Acknowledgements

This work has partly been financed by NSFC through project: Printing dynamics for high-definition printed electronics (61474144).

References

Alam, P, Toivakka, M, Backfolk, K., and Sirviö, P., 2007. Impact spreading and absorption of Newtonian droplets on topographically irregular porous materials. *Chemical Engineering Science*, 62(12), pp. 3142–3158.

Alleborn, N. and Raszillier, H., 2004. Spreading and absorption of droplets on layered porous substrates. *Journal of Colloid and Interface Science*, 280(2), pp. 449–464.

Girard, F., Attané, P., and Morin, V., 2006. A new analytical model for impact and spreading of a one drop application to inkjet printing. In: *TAPPI Ninth Coating Fundamentals Symposium*, Turku, Finland. TAPPI Press.

Josserand, C. and Thoroddsen, S.T., 2016. Drop Impact on a Solid Surface. *Annual Review of Fluid Mechanics*, 48, 365–391.

Kettle, J., Lamminmäki, T., and Gane, P., 2010. A review of modified surfaces for high speed inkjet coating. *Surface and Coating Technology*, 204(12–13), pp. 2103–2109.

Starov, V.M., Kostvintsev, S.R., Sobolev, V.D., Verlarde, V.D., and Zhdanov, S.A., 2002. Spreading of liquid drops over dry porous layers: complete wetting case. *Journal of Colloid and Interface Science*, 252, pp. 397–408.

Washburn, E.W., 1921. The dynamics of capillary flow. *Physical Review*, 17(3), pp. 271–283.

Yang, L, 2013. A physical model for liquid movement into a porous substrate under the action of a pressure pulse. *Nordic Pulp and Paper Research Journal*, 28(1), pp. 95–100.

Ink Jet Matching of Gravure Printed Wood Grain

Vinay Anil Turke[1], *Paul D. Fleming, Veronika Husovska*[2] *and Alexandra Pekarovicova*[3]

[1] ProEdge Inc., 23326 Shelby Road, Shelby, IN 46377
[2] Pressburg, LLC, Kalamazoo, MI 49009
[3] Center for Ink and Printability, Western Michigan University, 4601 Campus Drive, A-217 Parkview, Kalamazoo, MI 49008

E-mail: vturke@proedgefilms.com; dan.fleming@wmich.edu; v.husovska@pressburgllc.com; a.pekarovicova@wmich.edu

Abstract

Rotogravure cannot be used for prototyping, because of high manufacturing cost of gravure cylinders. Such challenges can be successfully tackled by use of relatively cheap and flexible printing processes, such as inkjet. Even though inkjet printing is a cost-effective way for prototyping, it has its own limitations, especially in the case of wood-grain printing. Wood-grain patterns need to be printed with a release coating and adhesive. Inkjet printers are incapable of printing neither release coating nor adhesive, because they require certain amount of coat weight, not possible to deliver with inkjet printing. Inaccurate color reproduction, metamerism and incompatibility with release coat are the commonly seen problems during ink jet prototyping. The main aim of this study was to resolve problems such as metamerism and close color match of ink jet and gravure printed wood grain. A design of experiments (DOE) was carried out by using different factors such as gray component replacement (GCR) settings, release coat weight and use of tie coat to analyze their effect on metamerism. Results showed that pre-press GCR settings were the most influential among all evaluated factors.

Keywords: rotogravure, inkjet, metamerism, color match

1. Introduction and background

Currently, most of the décor or wood-grain printing is mainly done by the gravure printing process, due to its effectiveness in achieving consistent results in long production jobs. But as market requirements are changing, customers are looking for more diverse wood-grain designs, specifically in small quantities and variable color palettes. Gravure printing is cost effective only if it is used for relatively long runs because of high cost for cylinder engraving. Hence, many printers are exploring other printing processes for wood-grain prototyping and production of small quantity jobs. Every conventional impact printing process requires an image carrier that increases cost. Therefore, the inkjet printing process is one the most feasible options to print wood-grain patterns in a most cost-effective way with flexibility of short quantity jobs (Wu, 2008). However, inkjet printing has its own disadvantages, too. An inkjet printer uses process inks (Wu, 2008), whereas gravure uses spot color inks to print wood-grain patterns. Thus, color matching is one of the main concerns during ink jet prototyping. Most likely, pigments used in inkjet inks are different from those used in gravure inks, which often leads to metamerism. Color matching issues can be resolved by implementation of color management systems into the process workflow. Metamerism can be minimized by using the same or somewhat similar types of pigments for both printing processes. It helps to get a closer spectral match between samples, but it is an expensive option. The greater is the difference between spectral power reflectance of two metameric samples, a greater color shift occurs when illuminants or observers are changed. Though it is impossible to eliminate metamerism, it can be reduced to certain acceptable levels (Shendye, 2010).

The degree of metamerism can be quantified by calculating the metamerism index (Shendye, 2010). Metamerism indices can be of two types, general and special. General indices are spectral indices based on spectral differences between the members of the metameric pair and are independent of illuminant. Bridgeman`s Index (BMAN) (Bridgeman,1969) was used for calculation of an index, but it does not consider the variation of eye sensitivity throughout the visible spectrum of light. Hence the Nimeroff and Yurow`s index was introduced (Nimeroff, 1965; Choudhary,1996). Even though the new index is modified, if the spectral difference is averaged throughout the spectrum, it decreases the difference in spectral values and may be lessened as two ends of spectra are approached. Therefore, it is important to calculate the difference, which is mainly dependent on illuminant and observer. Hence, it is more mathematically accurate to use a special metamerism index than a general one. Special indices are based on XYZ tristimulus values. Especially for illuminants, there are two commonly used special metamerism indices: CIELAB special metamerism index, in which metamerism index is calculated assuming the ΔE^*_{ab}difference between the pair under the reference illuminant is equal to zero. DIN 6172 metamerism index, in which metamerism index is calculated assuming the ΔE^*_{ab} difference between the pair under reference illuminant is not equal to zero. Special metamerism indices should not be used if ΔE^*_{ab} difference between two samples under reference illuminant is more than 5 (Berns, 2008). CIELAB special metamerism index can be calculated based on following formula:

$$MI = \sqrt{(\Delta L_{n_1} - \Delta L_{n_2})^2 + (\Delta a_{n_1} - \Delta a_{n_2})^2 + (\Delta b_{n_1} - \Delta b_{n_2})^2} \qquad [1]$$

Where n_1 is the 1st illuminant and n_2 is the 2nd illuminant and Δ=Value of sample – Value of standard (Metamerism Index, 2008). Equation 1 is algebraically equal to both the CIE and DIN indices, but the interpretation is different. Under the CIE index, the colors perfectly match under an illuminant and small MI means they match well under a second illuminant. For the DIN index, the colors are assumed to match well under an illuminant and small *MI* means they match almost as well under a second illuminant. In either case, if the *MI* value is high, then there is a significant color difference between the sample pair under different illuminants.

UCR (Under Color Removal) and GCR (Gray Component Replacement) basically deal with color separations of four process colors (UCR&GCR, 1996). When all secondary colors (Cyan, Magenta and Yellow) are overprinted, they should create black, but in reality, they give brownish or muddy black appearance. Overprint black percentage can be replaced with black ink by UCR or GCR. The main difference between UCR and GCR is that UCR is process of removal of cyan, magenta and yellow, wherever black is present, whereas GCR is process of replacing the gray component with black ink throughout entire image (UCR&GCR, 1996). GCR is preferred over UCR because UCR deals with removal of CMY inks in dark and near neutral areas. Contrary to that, GCR is capable of replacing gray component from all colors in separation including highlights. Use of GCR has multiple advantages, such as fewer trapping problems, less dot gain fluctuation and fewer registration problems of use of only one ink instead of three. Use of GCR reduces consumption of ink substantially, reducing cost of an ink by 50 % (Nimeroff, 1965). Also, GCR improves color gamut, as black level increases, color gamut volume also increases to some extent (Zou, 2012; Spiridonov, 2013). The color gamut volume is a volume in CIELAB space that represents the number of colors that the device (here ink jet printer) can produce with a tolerance of the $\sqrt{3}$ (Chovancova-Lovell, 2009). The main aim of this study was to resolve problems such as metamerism and close color match between rotogravure and ink jet print. To accomplish this goal, sample patches were printed on a Roland VS 540i inkjet printer and color matched to reference gravure printed patches with ΔE^*_{ab} less than 5. Custom created ICC profiles were compared with the default printer profiles. Manual GCR adjustment was done to assess its role in color matching. A Design of Experiments (DOE) was carried out by using different factors such as GCR settings, release coat weight and use of tie coat to analyze their effects on metamerism.

2. Materials and methods

Four gravure printed shades of wood grain were selected as reference patches. These four shades were printed as solid patches for ease of the measurement. CIELAB values of gravure reference patches were measured using an X-Rite Ci6x spectrophotometer. Four sample patches were constructed in Adobe Illustrator by assigning previously measured CIELAB values of the reference patches. Patches were labeled as Galaxy Oak, Smooth Grey, Hunter 655 and Rustic Maple, respectively (Figure 1).

Figure 1: Sample Patches, with CIELAB values

A customized ICC profile was created using X-Rite 'i1Profiler'. For customized ICC profile creation, the 800-patch chart was created from i1Profiler software. Sample Patches (Figure 1) were printed on the Roland VS 540i inkjet printer by applying the standard printer profile and customized ICC profile. Patches were once again printed by applying the customized ICC profile, but with additional manual GCR adjustment. In manual GCR adjustment, a % of CMY ink was replaced by the same % of K ink. ΔE^*_{ab} and metamerism indices for the four patches were calculated and spectral graphs were compared to determine the initial significance of custom created ICC profile over default printer profile as well as effectiveness of manual GCR adjustment and its effect on metamerism index.

Table 1: Trials for Design of Experiments

Trials	Factor 1: Release Coat Weight (g/m^2)	Factor 2: Use of Tie Coat	Factor 3: GCR levels
1	7	Yes	Minimum
2	10.5	No	Medium+
3	7	Yes	Maximum
4	10.5	No	Minimum
5	7	Yes	Medium+
6	10.5	No	Maximum
7	7	No	Minimum
8	10.5	Yes	Medium+
9	7	No	Maximum
10	10.5	Yes	Minimum
11	7	No	Medium+
12	10.5	Yes	Maximum

To analyze the influence of various factors on metamerism, a design of experiments (DOE) was conducted by using three factors, GCR level settings, release coat weight, and use of tie coat. (Tie coat is an acrylic

based clear used to promote adhesion between printed ink and adhesive.) Table 1 shows number of trials and factors for a DOE experiment. Trials 3, 6, 9 and 12 were conducted again with additional manual GCR adjustment in Adobe Illustrator to check its effect on metamerism index. Spectral graphs were compared. Metamerism indices and ΔE^*_{ab} were calculated. Printed wood grain products were transferred onto the base wood by means of heat and pressure. Thus, all layers of the product needed to be printed in reverse order. All the layers of the wood grain in their respective order are shown in the Figure 2.

Figure 2: Schematic of Wood Grain Layers Printing

2.1 Release coat weight

After application of wood grain to the wood, release coat becomes the top layer of the wood grain that gives chemical and abrasive resistance to the wood grain product. In the absence of tie coat, the release coat is the 1st layer that comes in contact with the inkjet ink. Release coat weight determines the degree of chemical and abrasive resistance as well as gloss/matt finish of the product. Initially, substrates with 3 g/m^2 of release coat were used to create the customized ICC profile. Substrates were unable to take more than 100 % total ink limit value during media calibration for the Roland VS540i inkjet printer. Cracks were observed after drying. The recommended minimum total ink limit as per printer manufacturer is 140 % to achieve acceptable print quality. To increase total ink limit value, substrates with higher release coat were used. 7 g/m^2 and 10.5 g/m^2 substrates showed higher total ink limit than 140 %. Higher release coat substrates showed some cracking but it was not as visible to naked eyes. 7 g/m^2 and 10 g/m^2 were able to accept 180 % and 200 % of total ink limit, respectively.

2.2 Use of tie coat

The vehicles in the inkjet ink make polymers in release coat less elastic with the increased stress due to shrinking, causing cracks in a print area after drying. In wood grain printing, tie coat is usually used to promote adhesion between printed ink and adhesive, but it can also be used as an alternative to the original release coat. Tie coat contains low molecular weight polymers; hence it creates relatively softer and more flexible layer of coating than release coat, which avoids cracking after drying. The use of tie coat leads to reduced rub resistance. Hence, tie coat is coated over release coat to maintain original rub resistance of the substrate as well as to avoid cracking. When substrates with tie coat over release coat were calibrated for Roland VS540i inkjet printer, they showed no ink cracking. However, tie coat did not significantly improve total ink limit capability of substrate. 7 g/m^2 and 10 g/m^2 substrates with tie coat both were able to accept 160 % of total ink limit.

2.3 GCR settings

Unlike older version of X-Rite profile making software “Profile Maker 5.0”, the new software i1Profiler does not specify percent of gray component replacement. Instead, it provides eight different steps under the name “Black Generation Curve”. Eight GCR settings options are minimum, light, light+, medium, medium+, heavy, heavy+ and maximum. To analyze effect of the GCR, three settings of GCR (minimum, medium+ and

maximum) were used in the design of experiments. The fundamental approach behind the use of different coat weight and tie coat was to increase color gamut volume by improving total ink limit and to analyze the effect of increased color gamut volume on metamerism index. Use of the factor 3, GCR settings were used to understand its effect on metamerism index.

3. Results and discussion

The ΔE^*_{ab} comparison of inkjet and gravure reference patches showed less than 5 color difference for all four patches (Galaxy Oak, Smooth Grey, Hunter 655, and Rustic Maple). Galaxy Oak color match with default printer profile, custom ICC profile, and manually adjusted GCR is illustrated in Figure 3.

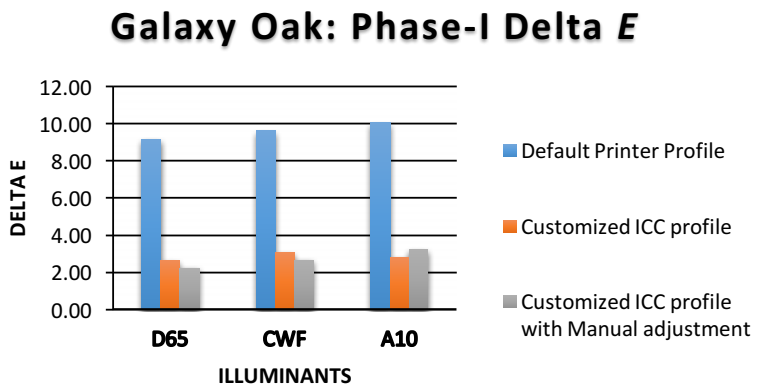

Figure 3: Delta E between gravure and inkjet printed patch using three different illuminants

The customized ICC profile further decreased color difference for all illuminants (Figure 3). On the other hand, manual GCR adjustment in addition to customized ICC profile increased color difference for all patches (not shown), except Galaxy Oak D65 and CWF light source (Figure 3). Metamerism Index comparison of all four sample patches showed that customized ICC profile significantly improved the metamerism index for all illuminants, and unlike ΔE^*_{ab} difference, metamerism index was decreased further by use of manual GCR adjustment in the custom ICC profile, except for Galaxy Oak CWF & A10 (Figure 4).

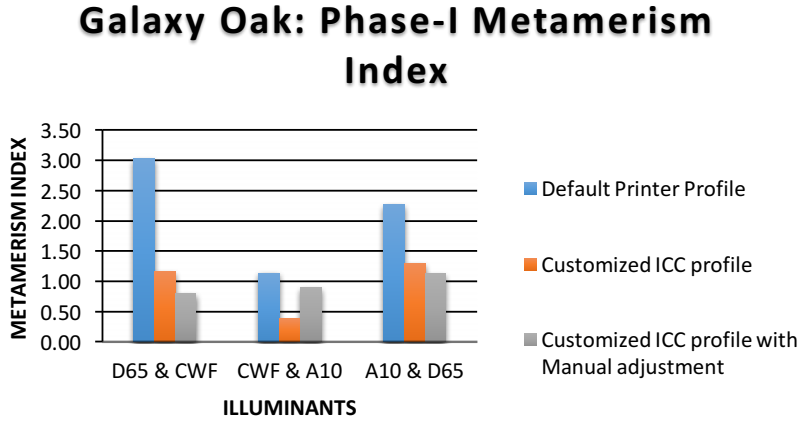

Figure 4: Galaxy Oak Metamerism Index Dependency on type of ICC profile used

Spectral reflectance curves of gravure printed reference patches and inkjet printed patches with default printer profile, manual GCR adjustment and customized ICC profile were plotted for comparison. Spectral reflectance plots of all patches showed that custom created ICC profiles brought spectral reflectance curve closer to the reference spectral curve, mainly because of improvement in ΔE^*_{ab} (especially improvement in

lightness). Manual GCR setting, in addition to custom ICC profiles improved spectral plot to some extent. Spectral reflectance curves for Galaxy Oak are illustrated in the Figure 5.

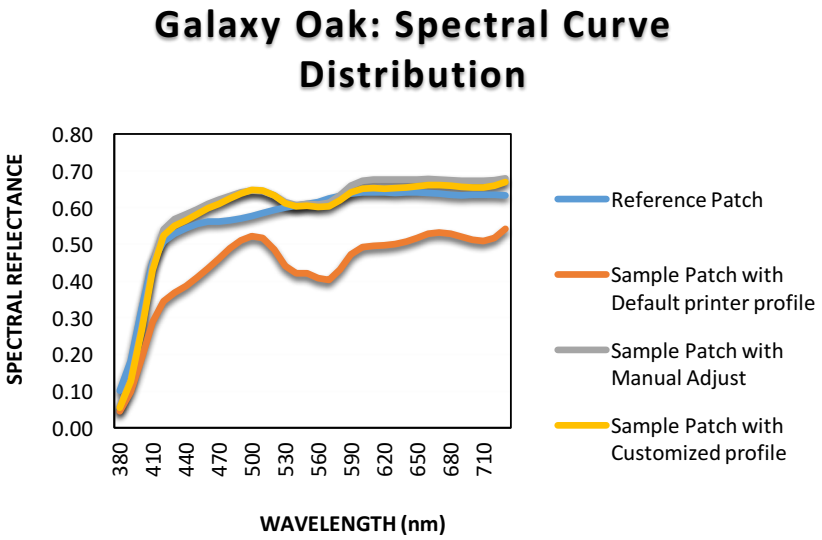

Figure 5: Galaxy Oak Spectral Reflectance Curves

To further explore the effect of three different factors (release and tie coat weight, and GCR settings) on the metamerism index, a design of experiments was conducted (Table 1). Manual GCR adjustment were done to the trials with maximum GCR setting and compared with other DOE trials. For ease of analysis, 12 trials were divided into 4 substrate types based on release coat weight and use of tie coat. Then, each substrate was analyzed for 3 different GCR settings. Four different color patches were printed to understand which CIELAB values improvement in metamerism index was significant.

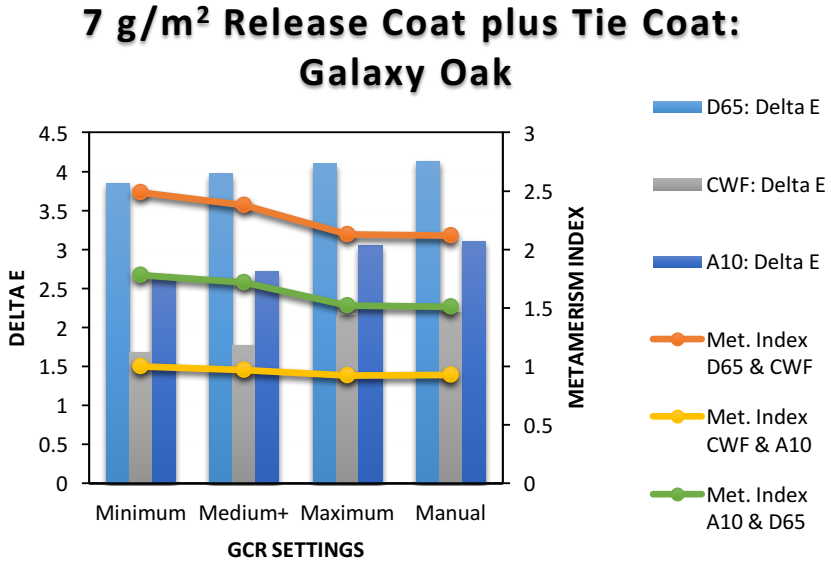

Figure 6: Galaxy Oak 7 g/m² Release Coat plus Tie Coat – ΔE^*_{ab} & Metamerism Index

To analyze the effect of GCR settings on ΔE^*_{ab} and Metamerism Index simultaneously, GCR settings were plotted on the *x*-axis, whereas both ΔE^*_{ab} and Metamerism index were plotted on the *y*-axis (Figure 6). For all types of substrates, color patches, and all illuminants (D65, CWF and A10), the minimum GCR setting showed the highest metameric index, whereas the maximum GCR setting showed the smallest metameric index. The ΔE^*_{ab} and GCR settings did not show any significant correlation between each other except for the Smooth Gray patch. For Smooth Grey patch, ΔE^*_{ab} decreased significantly with increase in GCR settings,

contrary to that for rest of the patches ΔE^*_{ab} fluctuated by 1–2 ΔE^*_{ab} range. Among all patches, Smooth Grey patch showed the highest improvement in metamerism index, Hunter 655 showed least improvement whereas Galaxy Oak and Rustic Maple showed slightly more improvement than Hunter 655 (data not shown). For all trials, manual GCR adjustment neither improved metamerism index nor ΔE^*_{ab} to a significant extent.

As manual GCR adjustment did not show any significant improvement in metamerism index, it was not included in Spectral Distribution Curve comparison. Spectral reflectance of gravure printed reference patches and inkjet printed sample patches with Minimum, Medium+ and Maximum GCR setting were plotted. Spectral graphs of all color patches crossed reference patches spectral reflectance curve patch thrice and are thus are considered to be metameric. Even though color patches were metameric, spectral reflectance curves of maximum GCR setting were closest to the spectral curve of reference patch, followed by medium GCR setting and minimum GCR setting spectral curves respectively. Among all patches, the Smooth Grey patch showed highest improvement in spectral curve (Figure 7), and Hunter 655 showed the least improvement, whereas Galaxy Oak and Rustic Maple showed slightly more improvement than Hunter 655 (data not shown).

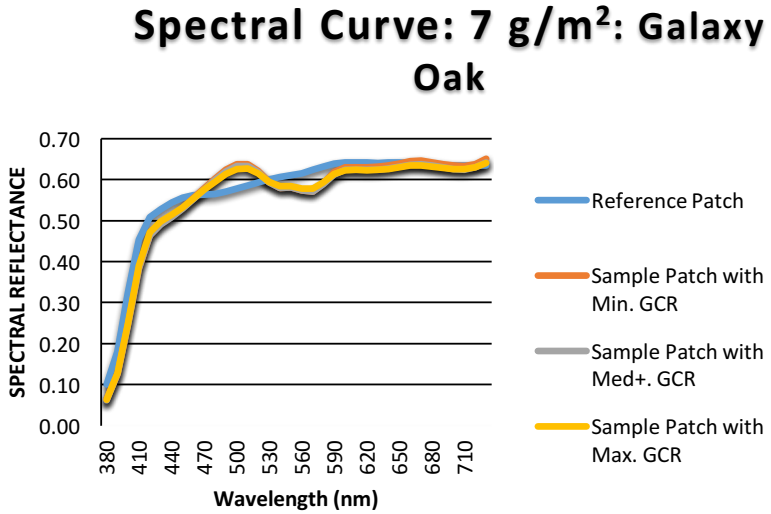

Figure 7: Spectral Curve 7 g/m² Release Coat with different GCR settings – Galaxy Oak

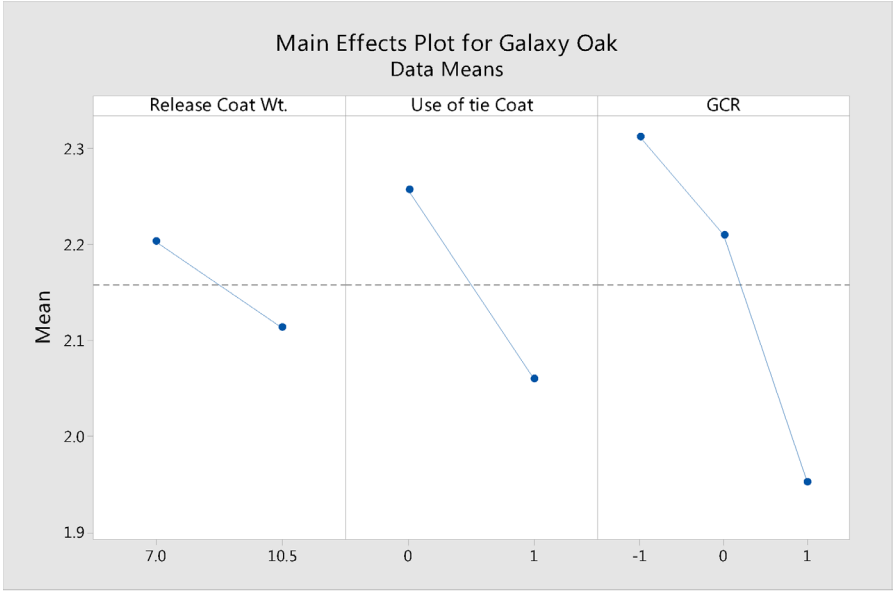

Figure 8: Metamerism Index ANOVA-Main Effect Plot- Galaxy Oak

Analysis of Variance was conducted for metamerism index obtained from 12 DOE trials for all patches. P-values showed that for all patches except Hunter 655, GCR settings significantly influenced metamerism index followed by tie coat (data not shown). For Hunter 655 patch, use of tie coat was the most significant factor. However, release coat weight had an insignificant effect on the metamerism index response (data not shown). This indicates that after a certain release coat weight, there is no value in increasing the release coat weight. Based on the results, this value is about 7 g/m^2. Metamerism index ANOVA results for Galaxy Oak are illustrated in Figure 8.

4. Conclusions

Custom created ICC profiles decreased the metamerism index and ΔE^*_{ab} difference significantly, when compared with the generic RIP printer profile. Analysis of spectral reflectance curves justified the significance of custom created ICC profiles over generic RIP printer profile. Manual GCR adjustment in addition to custom created ICC profiles decreased metamerism index further, but at the same time increased ΔE^*_{ab} difference to some extent. Design of experiments consisting of 12 trials was conducted using different multi-level factors. Results showed that increased GCR settings had considerable impact on metamerism index, and it varied per color shade. Darker patches showed the highest reduction in metamerism index, contrary to that, the response to GCR settings by lighter patches was none or insignificant. Analysis of spectral reflectance showed similar results for dark and light patches of colors. GCR settings neither improved nor deteriorated color difference, and ΔE^*_{ab} differences fluctuated up and down in range of 1–2 ΔE^*_{ab} units.

Acknowledgement

We would like to thank ProEdge Inc. and Gravure Education Foundation for partial support for this work.

References

Berns, R. S., 2008. The proper use of indices of metamerism. *Color Research and Applications,* 33(6), p. 509.

Bridgeman, T. and Hudson, N.E., 1969. Calculation of degree of metamerism between two colours. In: M. Richter, ed., 1970. *Proceedings of the 1st AIC Congress: Color 69*. Stockholm, 9–13 June 1996. Göttingen: Muster-Schmidt, p. 745.

Choudhary, A., Roy, K., and. Chattergee S.M.,1996. Evaluation of the performance of metameric indices. *Color Research and Applications*, 21(1), pp. 26–34.

Chovancova-Lovell, V. and Fleming, P.D., 2009. Color Gamut – New tool in the pressroom?, *TAPPI Journal*, 8(2), pp. 4–11.

Nimeroff I., and Yurow J. A., 1965. Degree of metamerism. *J. Opt. Soc. Am*., 55, pp. 185–190.

Shendye, A., Fleming III, P.D. and Pekarovicova, A., 2010. Metamerism, color inconstancy and chromatic adaptation for spot color printing. In: *Proceedings of TAGA*, San Diego, March 2010, p. 4.

Spiridonov, I., and Shopova, M., 2013. Determination of the effect of Gray Component Replacement level on colorimetric characteristics of color proof. *Journal of Chemical Technology and Metallurgy*, 48(3), pp. 247–53.

UCR & GCR, 1996. UCR and GCR: What are they?, 1996. 15 US Inks. [online] Available at: <http://www.sunchemical.com/?wpdmact=process&did=NzEuaG90bGluaw==&usg=AFQjCNHmemR8o2WAgE-fDjzkngPBi0xFKQ&sig2=K2_TEcg2g_57lHo6grtYqw > [Accessed June 2017].

Wu, Y.-J., Suchy, M., Fleming III, P.D., and Pekarovicova, A., 2006. Quality analysis of spot color reproduction with inkjet printers. *22nd International Conference on Digital Printing Technologies: Digital Fabrication 2006, NIP22*. Denver, Colorado, 17-22 September 2006. IS&T.

Waveform Optimization for Piezo Drop on Demand Inkjet Print Heads by Meniscus Motion Analysis

Johannes Renner and Fritz Bircher

University of Applied Sciences Western Switzerland, Ecole d'Ingénieurs et d'Architectes de Fribourg, iPrint Institute, Route de l'Ancienne Papeterie 180, CH-1723 Marly, Switzerland

E-mail: johannes.renner@hefr.ch

Abstract

Waveform optimization is a key to success for piezo drop on demand printing systems. The industry established method for waveform analysis and optimization is a drop watching analysis. With a drop watching system, usually a large number of droplets has to be jetted for each configuration of the printing system. As inkjet is increasingly being used in functional printing, an increasing number of fluids with a certain toxicity, limited stability or very high material cost are jetted. For such applications, there is a need to reduce the amount of wasted fluid. The aim of this publication is to explore the potential of estimating jetting properties and optimizing waveforms by meniscus motion analysis with a standard drop watching setup. By analyzing the meniscus motion at different pulse amplitudes below the drop emission threshold, the voltage necessary to reach a certain drop speed could be estimated. An estimation of the frequency - velocity variation can be obtained by analysis of the meniscus motion in the range of actual jetting frequencies.

Keywords: waveform optimization, meniscus motion, inkjet analysis, drop watching

1. Introduction and background

In piezo drop on demand (DoD) inkjet print heads, fluid droplets are generated due to pressure waves introduced by the motion of piezoelectric actuators. As the propagation time (speed of sound of the jetted fluid in relation to the channel length) of the pressure waves in an inkjet channel is significantly larger than the time needed for the piezoelectric actuator to reach its full amplitude, acoustic interference effects dominate the jetting process. A piezo inkjet channel can be seen as an acoustic resonator where pressure waves are reflected with the same polarity on closed ends or with inverse polarity at open ends (Bogy and Talke, 1984). Each movement of the piezoelectric actuator creates a new pressure wave, which is resonating in the inkjet channel (with a certain attenuation per cycle) and can constructively (pressure amplification) or destructively (pressure attenuation) interfere with previously created pressure waves. In fact, drive waveforms for piezo drop on demand print heads are often designed with acoustic superposition for the generation of drops and attenuating elements to reduce interference with the generation of next drops. The industry-established method to design drive waveforms for piezo DoD print heads, is analysis of drops in flight with drop watching systems. Thereby drop properties like drop volumes, velocities, trajectory angles or the presence of satellite droplets are measured for different waveform settings and jetting frequencies. The goal of waveform optimizations for piezo DoD print heads is mainly the calibration of certain mean drop speeds and drop volumes while achieving a minimum of velocity variation and satellite droplets throughout all jetting frequencies. While the analysis of piezo DoD waveforms with drop watching systems is very fast and convenient in contrast to alternatives like the evaluation of printed test patches, there are some disadvantages. With conventional drop watching analysis systems a rather large quantity of drops or liquid volume has to be jetted to evaluate the quality of a waveform. This can be an issue if the jetted

fluids are toxic or only available in little quantities. When jetting at higher frequencies with poor waveform settings, frequent print head maintenance may be required due to strong nozzle plate wetting which again requires larger fluid quantities and additional operator time. If, without a tuned waveform, the fluid's viscosity is too high for the generation of drops, optimization with drop watching techniques is inefficient. To reduce the required amount of fluid and the time needed for waveform optimization as well as to optimize waveform parameters, without the need to analyze drops, various methods can be used. Suitable waveform timing can be approximated if the speed of sound of the jetted fluid is known (Antohe and Wallace, 2002), waveform parameters can be optimized using the piezoelectric actuators in self - sensing operation (Kwon and Kim, 2007), or by measuring the motion of the liquid in the nozzle (also known as meniscus motion) after applying a pressure pulse (Kwon, 2009).

As self - sensing measurements can only be used with a limited number of print head models and are difficult to relate to actual jetting behavior, they appear to have limited industrial importance. On the other hand, waveform optimization by meniscus motion analysis can be realized with the same equipment as for inkjet drop watching systems, which is already the industrial standard. As the meniscus for DoD nozzles can take negative (inside the print head) and positive angles (protruding the nozzle plate), for continuous meniscus observation rather complex evaluation with ray tracing (Hsiao, et al., 2011) or analysis with laser Doppler velocimetry (van der Meulen, 2014) is required. For waveform optimization by analyzing the pulse response of the meniscus it is sufficient to measure positive amplitudes of the meniscus (Kwon, 2009). Previous research on waveform analysis without generating drops focused however on the optimization of waveform parameters by evaluating a pulse response of either the piezoelectric actuator or the meniscus motion. No research could however be found on the estimation of jetting properties such as drop velocity or frequency dependent speed variations without generating drops.

The aim of this publication is to explore the potential of estimating jetting properties by meniscus motion analysis and a standard drop watching set up without generating droplets. Thereby the number of jetted drops required for waveform optimization can be reduced. By analyzing the meniscus motion at different pulse amplitudes below the drop emission threshold, the voltage necessary to reach a certain drop speed could be estimated. An estimation of the frequency - velocity variation can be obtained by analysis of the meniscus motion in the range of actual jetting frequencies.

2. Materials and methods

2.1 Test setup

First tests are done with the test setup depicted in Figure 1. The print drive electronics is triggered together with a delayed LED Flash and a camera by an external synchronization device. The synchronization device is a development of the iPrint Institute for Printing and is based on a Spartan 6 FPGA with an effective time resolution of 10 ns. A print drive electronics from Global Inkjet Systems (PMB-C2 with HPB-FD-W4D4 and HIB-FD-AMP-4) is used to control the print head (Dimatix PQ256/85). The camera (TheImagingSource DMK23 GP031) has a grayscale area scan CCD with 12 bit of color depth and a resolution of 2592 pixels × 1944 pixels. The optics is realized by a custom Thorlabs SM2 lens tube assembly. Two achromatic pairs (Thorlabs AC-508-075 on the front and AC508-150 on the rear) are mounted in the lens tube with a separation of 30 mm. With an optical distance of approximately 66.3 mm between the observed nozzle row and the optical center of the front lens, an effective resolution of 769 nm per pixel is achieved, which does correspond to a field of view of approximately 2 mm × 1.5 mm on the CCD of the camera. The LED Flash consists out of a 40 W LED Emitter from LEDEngin (LZC-83MC00), a flash LED driver which was developed at the iPrint Institute for Printing and a condensing lens (Thorlabs AC-508-100).

To increase the visibility of the meniscus, the LED flash and the camera are tilted by approximately 1° in relation to the plane of the nozzle plate.

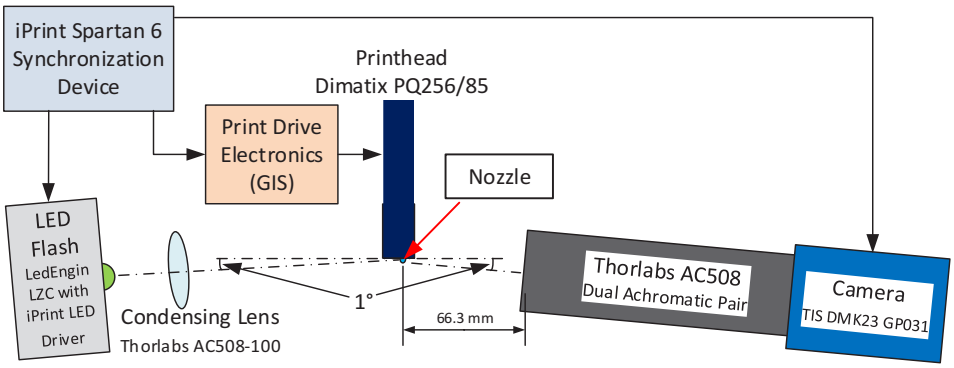

Figure 1: Schematic illustration of the test setup

2.2 Image analysis

For initial tests, the movement of the meniscus is evaluated by computing the sum of color values in the area around the nozzle center. Figure 2 shows an image of a captured positive meniscus at one nozzle. The actual shape of the meniscus is only half of the black object visible in Figure 2. The upper half is a reflection of the meniscus mirrored by the nozzle plate of the print head. As depicted by the dashed red lines in Figure 2, the total sum of color values is calculated within a width of 8 pixels including the part reflected by the nozzle plate. After evaluation of one measurement sequence, the computed color sums are normalized by subtracting the minimum value of all values in the sequence. As the curvature of the meniscus around its center line is relatively small, it is assumed that the sum of color values are with good approximation linearly related to the peak positon of the meniscus. To calculate the peak meniscus position, the sum of color values are calibrated by a reference measurement with edge detection. On a number of manual reference measurements, the actual measured position deviates up to 2 µm from the position calculated by the sum of color values. As mainly relative information are required to perform waveform analysis by measuring meniscus motion, the accuracy is considered to be acceptable. By making use of the mirrored reflection of the nozzle plate, this method does not require a reference to the nozzle plate location, which simplifies evaluation and is not affected by vibrations or transient position shifts.

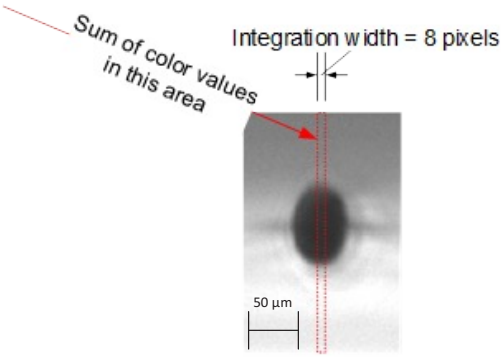

Figure 2: Illustration of the integration area for initial evaluation of the meniscus movement

3. Results and discussion

The meniscus motion is captured with different hold times from 4.0 µs to 9.0 µs in steps of 0.5 µs. A single pulse waveform with a rise and fall time of 2.0 µs is used. A non-volatile UV flush and storage solution from HAPA is chosen as fluid for the test. The acoustic optimum timing is measured to be 10.63 µs by means of

drop watching with an amplitude of 55 V. With a rise time of 2 µs, this corresponds to a hold time of 8.63 µs (see Figure 6 left). A negative meniscus pressure of3 mbar and a fluid temperature of 30 °C are set. With the test liquid and a hold time of 8.6 µs, the drop emission threshold is reached at an amplitude of approximately 40 V. The amplitude for the test is chosen with 20 V due to increasing nozzle plate wetting at higher amplitudes. For each hold time, the state of the meniscus is captured in steps of 1 µs starting with 30 µs after triggering the print drive electronics. Figure 3 shows an arrangement of all captured images of the henceforth evaluated measurement.

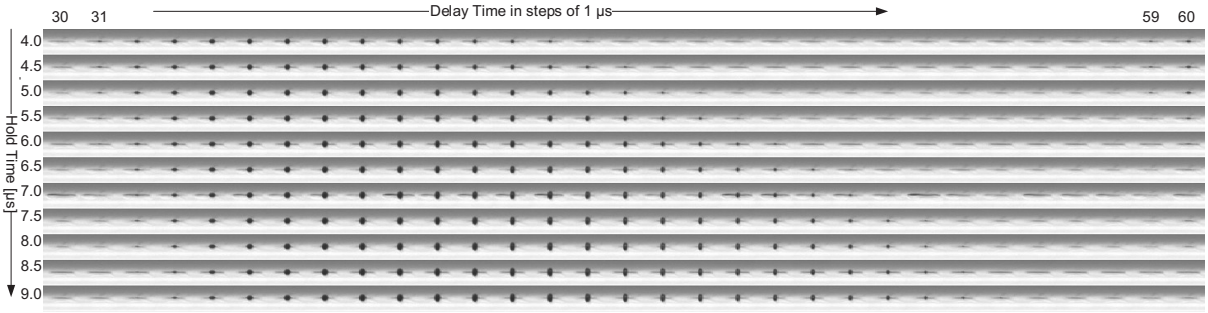

Figure 3: Meniscus motion images with different hold and flash delay times

Figure 4 shows a plot with the data of Figure 3 evaluated according to the method described in Section 2.2. The meniscus center positions are plotted for each hold time (HT) against the delay time. The maximum meniscus position in relation to the nozzle plate is reached at the maximum hold time and is approximately 45 µm. It may be noticed that with increasing hold time, the response of the meniscus motion is delayed with an apparently constant additional delay of 0.33 µs per microsecond hold time. This is due to the fact that the pressure wave is reaching a certain positive pressure level at the nozzle earlier with shorter pulse durations, as the falling edge of the waveform does generate a positive pressure directly (without being reflected by the open end in the inkjet channel). At a flash delay time of approximately 57 µs the start of a second external meniscus oscillation can be observed.

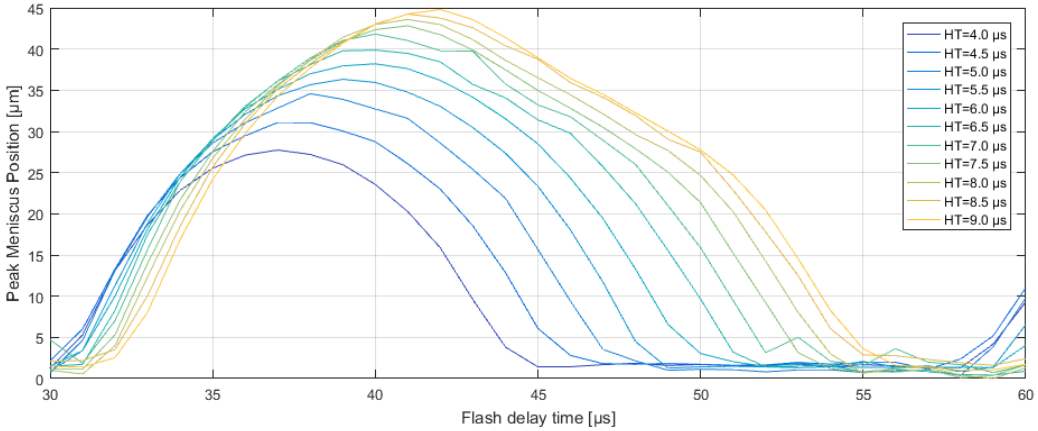

Figure 4: Propagation of the meniscus center for different hold times

By discrete differentiation of the meniscus motion curves in Figure 4 the speed of the meniscus center can be approximated. Figure 5 shows the approximated velocities of the meniscus center at different hold times. As the center of the meniscus is accelerated from its initial negative resting position, it already has gained its full velocity in the moment it leaves the nozzle plate. The lower initial velocities as well as the delayed transitions from −6 m/s to zero velocity in the plot are incorrect. These errors are caused by insufficient accuracy of the measurement with meniscus positions that are smaller than 3 µm and discretization errors, as the point in time where the meniscus center leaves the nozzle was not captured. The initial speed of the meniscus center is for all hold times approximately 8 m/s and decreases to a minimum of −6 m/s when entering the nozzle plane again.

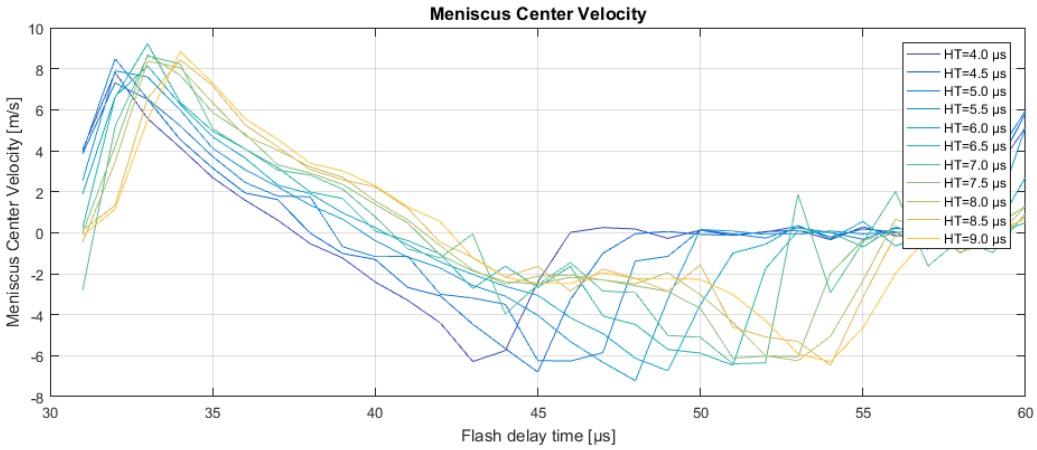

Figure 5: Meniscus center velocity for different hold times

Plotting the hold time in relation to maximum meniscus center positions (the highest points for each hold time in Figure 4) in the same chart as the drop speeds at 55 V amplitude, results in the graph in Figure 6 left. Looking at the similar shape of the two curves suggests that drop speeds at a higher voltage amplitude can be related to maximum meniscus positions at a low amplitude. In Figure 6 right, the drop velocities at 55 V amplitude are plotted against the maximum meniscus positions at 20 V. Calculating a polynomial fit of first order leads to a value of 0.22 m/s additional drop speed per micrometer of peak meniscus amplitude. It is however assumed that increasing the hold time further will not lead to a direct relationship between peak meniscus position and drop velocities.

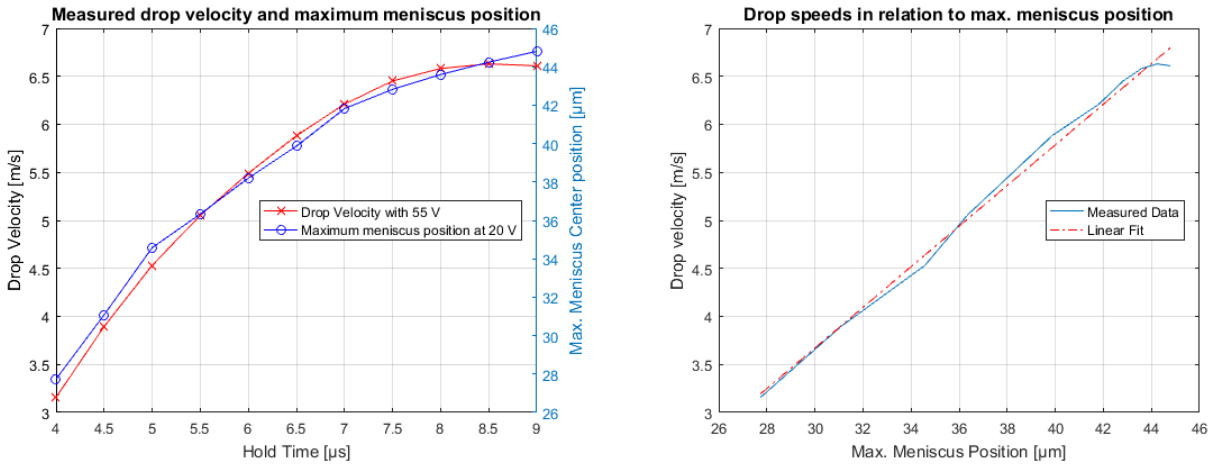

Figure 6: Drop velocities at 55 V amplitude and maximum meniscus positions at 20 V amplitude

To predict drop velocities with arbitrary waveforms without a drop watching reference measurement, a second meniscus motion measurement with a different amplitude below the drop emission threshold is suggested. Out of the relationship between the two different responses with identical timing, it is assumed that the amplitude, required for a certain drop velocity can be estimated. As drop speeds are strongly affected by the fluid's viscous behavior and surface tension at the shear rate of the droplet generation, a prediction of drop speeds by meniscus motion analysis without a reference measurement may only be accurate for homogeneous Newtonian fluids with sinusoidal ligament break-up.

While it is assumed that meniscus motion analysis is a suitable tool to significantly reduce the required volume, maintenance cycles and time for waveform optimization by narrowing down suitable parameters with acoustic optimization and relationships between pulse amplitudes of waveforms, it is not assumed that it could replace drop watching. Without the generation of drops at the actual drop frequency and velocity to be analyzed, fluid dynamic effects of the droplet generation and in the print system cannot be

predicted. To measure ligament break-up, the drop formation distance, the presence of satellite droplets, reduce nozzle plate wetting, detect air entrapment during meniscus restitution, or degassing in the nozzle channels at higher waveform amplitudes, meniscus motion analysis cannot be used. Further if a fluid is changing its acoustic properties at the nozzles when not being jetted for some time, e. g. due to concentration of particles or evaporation of a solvent at the nozzles, meniscus motion analysis may be unsuitable for optimization of acoustic timing. For such fluids with a short open nozzle time the accuracy of a meniscus motion analysis can be increased by using print heads with fluid circulation at the nozzles or by analyzing within an atmosphere controlled environment that prevents evaporation at the nozzles.

4. Conclusions

The measured meniscus pulse responses shown in this publication, support that drop speeds at a higher voltage can be related to the meniscus motion of the same waveform at a voltage that does not generate drops. It is assumed that this relationship is valid for complex waveforms as far as the amplitude of a waveform is proportionally reduced while maintaining the timing. Therefore, drop speed variations in jetting frequency sweeps or due to acoustic crosstalk, can be estimated and waveforms acoustically be optimized without generating drops, which in turn could significantly reduce the number of jetted drops for waveform optimizations.

Waveform optimization by meniscus motion analysis cannot be used to predict fluid dynamic effects in the generation of drops or the behavior of the print system when actually jetting at a certain frequency, it can only complement drop watching. In addition, the method may not be suitable for the analysis of fluids which transiently change their acoustic properties at the nozzles when not being jetted.

As meniscus motion analysis can be performed with the same equipment used for drop watching its integration in existing drop watching systems is expected to be simple. To achieve good contrast ratio of the meniscus shadow, only camera and LED assemblies were slightly tilted on the test system. By computing the sum of color values of the meniscus shadow including its reflection from the nozzle plate, simple and efficient evaluation of the peak meniscus position can be realized.

Acknowledgments

The author would like to thank Dr. Steve Hoath for giving a few inputs contributing to this publication.

References

Antohe, B.V. and Wallace, D.B., 2002. Acoustic phenomena in a demand-mode piezoelectric ink-jet printer. *Journal of Imaging Science and Technology*, 46(5), pp. 409–414.

Bogy, D.B. and Talke, F.E., 1984. Experimental and theoretical study of wave propagation phenomena in drop-on-demand ink jet devices. *IBM Journal of Research and Develop*ment, 28(3), pp. 314–321.

Hsiao, W.K., Hoath, S.D., Martin, G.D. and Hutchings, I.M., 2011. Jetting, in-nozzle meniscus motion and nozzle-plate flooding in an industrial Drop-on-Demand print head. In: *Proceedings of the 27th International Conference on Digital Printing Technologies: Digital Fabrication 2011*, NIP27. Minneapolis, MN, USA, 2–6 October 2011. IS&T, pp. 66–69.

Kwon, K.-S., 2009. Waveform design methods for piezo inkjet dispensers based on measured meniscus motion. *Journal of Microelectromechanical Systems*, 18(5), pp. 1118–1125.

Kwon, K.-S. and Kim, W., 2007. A waveform design method for high speed piezo inkjet printing based on self-sensing measurement. *Sensors and Actuators A: Physical*, 140(1), pp. 75–83.

van der Meulen, M.-J.P., 2014. *Meniscus motion and drop formation in inkjet printing*. Doctoral Thesis. University of Twente.

Calculation of Mesh Depression due to Squeegee Forces during Screen-Printing Process

Gunter Hübner

Institut für Innovative Anwendungen der Drucktechnologien (IAD), Hochschule der Medien, Nobelstr. 10, 70569 Stuttgart, Germany

Email: huebner@hdm-stuttgart.de

Abstract

In screen printing sometimes at the edges of an ink deposit that is wider than a few millimetres a phenomena occurs which can be described as an elevated edge or better as out-bulged shoulders. This can be a print quality issue if subsequent overprints need to be carried out. The effect of the out-bulged shoulders typically occurs if the stencil built-up is not well adapted to the targeted type of print pattern (e.g. fine lines vs large solid tones areas). It is described in screen printing text books and some scientific articles but not yet tackled theoretically. A simple model (a quasi-infinite line) is used combining the elongation of the mesh caused by the mesh tension and the additional stress applied by the squeegee with the depression of the mesh towards the substrate between the edges of the stencil opening. The developed relationship ends up in an equation that will be solved numerically by means of a look-up-table (LUT) approach. Graphs are derived that show the dependencies on print line width, stencil built-up, stresses applied and materials used.

Keywords: screen-printing; squeegee pressure; mesh elongation, out-bulged shoulders

1. Introduction

During recent years, screen-printing is experiencing a kind of renaissance. It is increasingly regarded as a reliable, high-level quality prolific process. The focus is on medium to high volume functional and industrial printing. In industrial printing the accuracy of the geometrical properties of the prints such as edge definition and surface smoothness are much more important rather than colour matching as in graphic applications. One issue that will be investigated theoretically in this paper, is the effect of the out-bulged shoulders that can occur if the stencil built-up is not well adapted to the targeted type of print (e.g. fine lines vs large solid tones areas) see handbooks like SEFAR (2008), online guidebooks (Hobby, 1997) or scientific articles (Riemer, 1989). The stencil built-up, which is commonly called EOM (Emulsion Over Mesh), can be one of the reasons of the out-bulged shoulder especially if the EOM is too high. Even though the stencil can be prepared in very many ways, the typical way is coating a photosensitive emulsion onto the mesh.

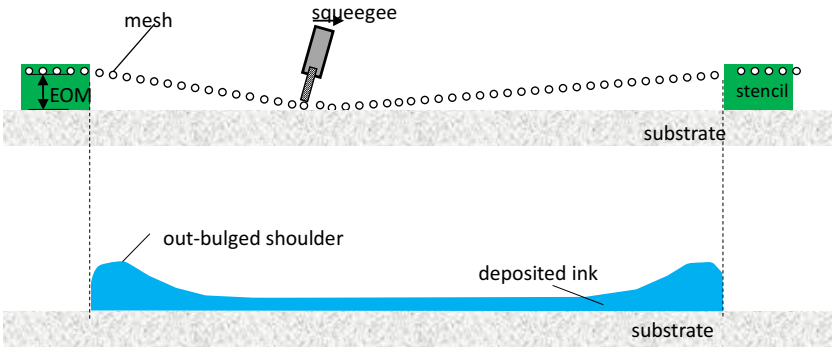

Figure 1: Out-bulged shoulders can occur at the edges of a printing area due to a very high EOM

Figure 1 shows the situation (not drawn to scale) when the squeegee presses down the printing form onto the substrate. The EOM is quite high and in the vicinity of the stencil-edge, the squeegee is not able to press down the mesh close to the substrate. Thus, a higher amount of ink is deposited there in comparison to the centre of the printed area where the threads of the mesh touch the substrate. One of the targeted questions is how the width of the printed line affects the out-bulging effect. Experienced printers estimate the width at about 2 mm, which is confirmed by Riemer in his dissertation (Riemer, 1988). Important to mention is that the snap-off distance does not play a role in this investigation as it is assumed that the squeegee pressure is high enough to press both of the stencil edges tightly down to the substrate.

2. Research methods

During the printing process the squeegee moves from left to right applying a certain vertical force. The physical and geometrical properties will be idealized and it is assumed to print a line with an infinite length (in squeegee-width direction).

Introducing geometrical properties according to Figure 2 the aim of the study is to find the following dependencies:

$\alpha = f(F, x, L$ and mesh properties) and
$t = f(F, x, L$ and mesh properties)

Whereas F is the force exerted by the squeegee pressure, x the squeegee position, α and β the angles at the stencil edges and L the width of the printed feature. The depression of the mesh is called t.

The relevant mesh properties are the
- Young's modulus E in Pa and the
- specific cross section A_q in mm^2/cm

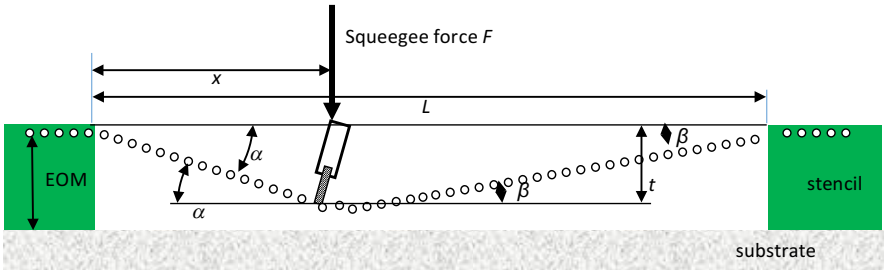

Figure 2: geometrical dimensions of the problem

The set-up can be regarded as a two dimensional problem in an x-z-plane. In y-direction the printed feature is assumed to be infinite. The squeegee force F causes forces in the mesh on the left hand side F_A and F_B on the right hand side. Thus, according to Figure 3 and Figure 4, an equilibrium of forces can be found.

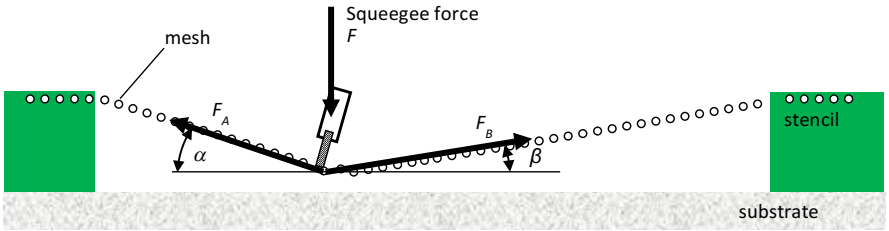

Figure 3: Acting forces

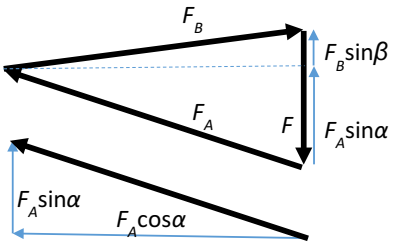

Figure 4: equilibrium of forces

If the EOM (Emulsion over mesh) is high enough, the mesh does not touch the substrate. Then the equilibrium of forces in vertical direction yield:

$$F = F_A \sin\alpha + F_B \sin\beta \qquad [1]$$

In addition, with neglected horizontal forces that may be caused by friction (in this first approximation, it is assumed that the presence of ink lubricates the contact point):

$$F_A \cos\alpha = F_B \cos\beta \qquad [2]$$

Thus, by combining Equations 1 and 2

$$F_A = \frac{F}{(\sin\alpha + \cos\alpha \tan\beta)} \qquad [3]$$

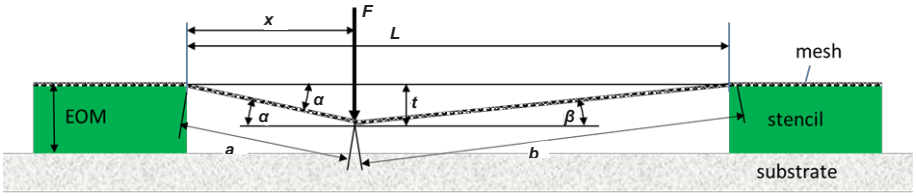

Figure 5: Elongation of the mesh

Due to the forces in the mesh caused by the squeegee pressure according to Figure 5 an elongation of the mesh occurs: $a + b > L$. In dimensionless representation the total elongation ε_{tot} is

$$\varepsilon_{tot} = \frac{a + b - L}{L} \qquad [4]$$

Since the forces left and right hand side of the squeegee position are different, the total elongation comprises of two parts:

$$\varepsilon_1 = \frac{a-x}{x} \text{ and } \varepsilon_2 = \frac{b-(L-x)}{L-x} \quad \text{thus } \varepsilon_{tot} = \frac{\varepsilon_1 x + \varepsilon_2 (L-x)}{L} \qquad [5]$$

Some geometric considerations help to find relations between α and β and between a, b and x. Depending on the position x of the squeegee, the depression of the mesh t is

$$t = x\tan\alpha = (L - x)\tan\beta \quad \text{or} \quad \frac{\tan\alpha}{\tan\beta} = \frac{L-x}{x}$$

The elongated lengths of the mesh are $a = \frac{x}{\cos\alpha}$ and $b = \frac{L-x}{\cos\beta}$

Introducing the relative position $\xi = \frac{x}{L}$ in dimensionless representation with $0 < \xi < 1$ then

$$\frac{\tan\alpha}{\tan\beta} = \frac{1-\xi}{\xi} \quad \text{or} \quad \tan\beta = \frac{\xi}{1-\xi}\tan\alpha \qquad [6]$$

And finally:

$$\varepsilon_1 = \frac{1}{\cos\alpha} - 1 \text{ and } \varepsilon_2 = \frac{1}{\cos\beta} - 1 \qquad [7]$$

As long as we are in elastic behavior, there is the well-known relation between the stress (tension) and the elongation:

$$\sigma = E \cdot \varepsilon \qquad [8]$$

Thus, left from squeegee position: $\frac{\sigma_1}{E} = \varepsilon_1$ and right from squeegee: $\frac{\sigma_2}{E} = \varepsilon_2$

The total stress applied to the mesh during the printing process comprises of the mesh tension applied by the stretching plus the stress caused by the squeegee pressure. Normally the mechanical stress is measured in force per area (e.g. N/mm^2). For screen-printing meshes, however, it is preferred to specify the mesh tension and the squeegee pressure in force per unit length, i.e. N/cm. Let us call the squeegee pressure F_q in N/cm and the mesh tension F_t in N/cm respectively. The area of a cross section of a mesh is easily defined by the specific cross section A_q in mm^2/cm. The elongations caused by the mesh tension and the squeegee pressure ε_q add to the total elongation:

$$\frac{\sigma}{E} = \varepsilon_{\text{tot}} = \varepsilon_t + \varepsilon_q = \frac{F_t}{EA_q} + \frac{F_q}{A_q E} \qquad [9]$$

The total elongation is caused by the sum of forces according to equation (3). Differentiating between left from squeegee (index A or 1) and right from squeegee (index B or 2)

$$\frac{F_{Aq}}{EA_q} = \varepsilon_1 + \varepsilon_t \quad \text{and} \quad \frac{F_{Bq}}{EA_q} = \varepsilon_2 + \varepsilon_t \qquad [10]$$

Now Equations 7 and 10 can be combined, yielding (for left hand side):

$$\frac{F_{Aq}}{EA_q} = \frac{1}{\cos\alpha} - 1 + \frac{F_t}{EA_q} \qquad [11]$$

Whereas F_t (representing the mesh tension) is a constant, F_{Aq} depends on the applied squeegee pressure F_q and on the squeegee position (respectively the angle α) according to Equation 3

$$F_{Aq} = \frac{F}{(\sin\alpha + \cos\alpha \cdot \tan\beta)}.$$

Inserting Equation 3 (left from squeegee) yield

$$\frac{\frac{F}{(\sin\alpha+\cos\alpha\cdot\tan\beta)}}{A_q E} = \frac{1}{\cos\alpha} - 1 + \frac{F_t}{EA_q} \qquad [12]$$

The final step is replacing β by a function of It was $\tan\beta = \frac{\xi}{1-\xi}\tan\alpha$, which implies $\sin\alpha + \cos\alpha \cdot \tan\beta = \frac{\sin\alpha}{1-\xi}$ and thus (after some rearranging and introducing abbreviations for the constants $K = \frac{F_q}{A_q E}$ and $\varepsilon_t = \frac{F_t}{A_q E}$):

$$\frac{F_q}{A_q E} = K = \frac{\tan\alpha - (\varepsilon_t - 1)\sin\alpha}{1-\xi} \qquad [13]$$

There might be some mathematical, trigonometric tricks, but it seems that – to the knowledge of the author – the right hand side of the Equation 13 cannot be solved for α. The left hand side, however, contains all well-known parameters that remain constant:

F_q = squeegee pressure in N/cm, ranging somewhere from 0.5 to 10 N/cm
E = Young's modulus (e.g. E_{PET} = 4500 N/mm² = 4.5 GPa and $E_{stainless}$ = 180 GPa)
A_q = the specific cross section
(= mesh count times single thread cross section; e.g. for a 380-14 mesh A_q = 0,058 mm²/cm, for a 48-70 mesh A_q = 0,185 mm²/cm)

The following Table 1 shows some values for A_q (the nomenclature is *n*-*d*, where *n* is the fineness in threads per cm and *d* is the thread diameter in µm. Figures are calculated from specifications found for PET-meshes from vendor SEFAR):

Table 1: Overview of values A_q for some meshes

Mesh	A_q in mm²/cm
48-70	0.185
110-34	0.099
110-40	0.138
120-31	0.091
120-34	0.109
120-40	0.151
150-27	0.086
150-34	0.136

For stainless steel, A_q could be below the PET values. A mesh with 159–18 for instance has A_q = 0.04 mm²/cm. Therefore, the values of the dimensionless constant K may vary extremely, i.e. from $4 \cdot 10^{-8}$ to 0.15.

On the right hand side of Equation 13, the constant ε_t, the elongation caused by stretching of the mesh, also contains known values E, A_q and F_t.

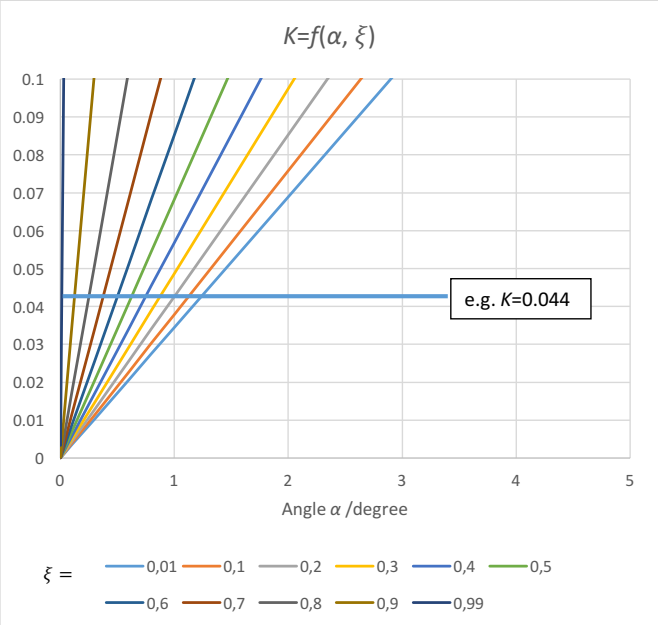

Figure 6: Look-up approach for solving the Equation 13

To solve the problem a simple LUT (look-up table) approach is used. According to Figure 6, the right hand side of Equation 13 is plotted by using known and fixed values of ε_t and varying α while ξ as a parameter ranges from 0 to 1 in 10 steps.

Then, if $K = \frac{F_q}{A_q E}$ is given, the value can be searched on the *y*-axis and on the *x*-axis the angle α can be looked up in the set of curves in the plot. In the example the value for $K = 0.044$ is a realistic medium value.

3. Summary of results

According to Figure 2, the squeegee pressure causes a depression t of the mesh because it is not supported between the edges of the stencil. The depression is given by $t = x\tan\alpha = \xi L\tan\alpha$. In Figure 7, a typical resulting curve is shown, where the depression t is plotted in negative direction to make the plot more descriptive. The angle α is found by interpolating in the look-up table that lies behind the plot according to Figure 6. The angle has very low values, less than 1 degree, and thus the curve looks as it decreases linearly with the relative squeegee position .

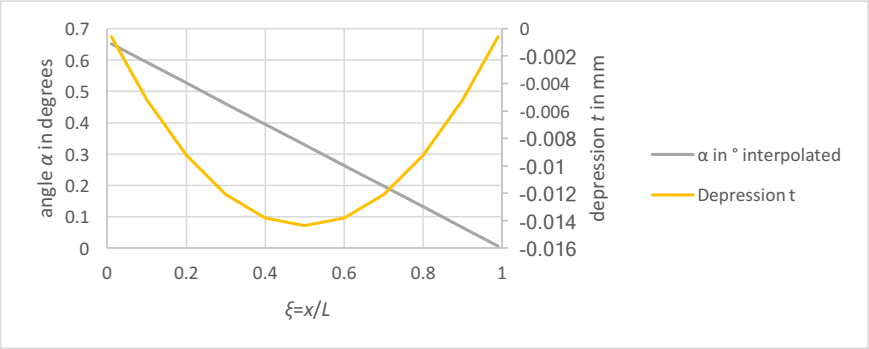

Figure 7: Depression t and angle α as function of the relative squeegee position ξ
Settings: L = 5 mm; F_t = 20 N/cm; F = 10 N/cm; A_q = 0.1 mm²/cm; E = 4500 N/mm² (PET); (yielding K = 0.04444)

As can be seen in Figure 7 the depression is symmetric and reaches a maximum in the middle position. If the EOM is smaller than the maximum depression at about 14 µm, in this case the mesh will touch the substrate. The curve describes the tip of the squeegee and therefore looks rounded. However, the mesh can be assumed as not bending resistant (especially if it is PET). Thus, it will more look like the snapshot in Figure 2. Figure 8 shows a plot of such subsequent snapshots.

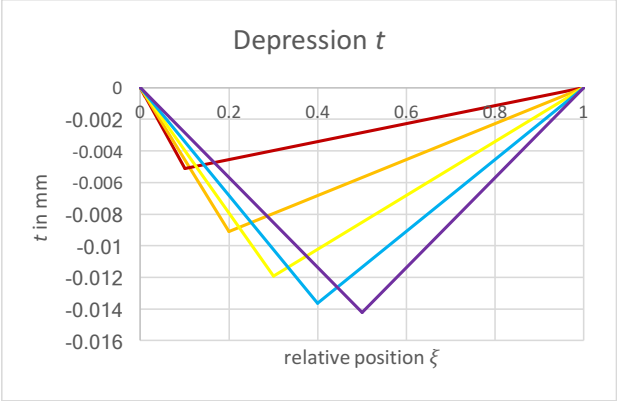

Figure 8: Depression t as a function of the relative squeegee position ξ (snapshots at ξ = 0.1; 0.2; 0.3; 0.4; 0.5); same parameter settings as in Figure 7

One of the major questions is the influence of the printed line width L. This is shown in Figure 9. If a typical value of the EOM is around 10 µm at a little more than L = 2 mm the depression is high enough to touch the substrate.

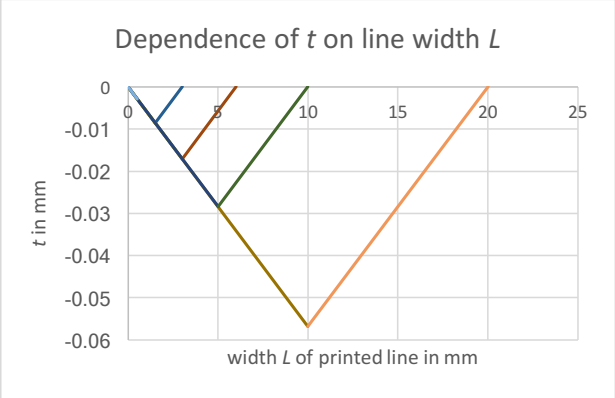

Figure 9: Depression t (at the middle position ξ = 0.5) as a function of the printing width of the line except L using the same parameter settings as in Figure 7

It seems that this finding is in accordance to the observations by experienced printers. In Figure 10 the influence of the mesh tension is shown, which is not very high as it seems. The influence of the mesh material, however, is extraordinary. The different modulus of elasticity E_{Pet} = 4.5 GPa and $E_{stainless}$ = 180 GPa plays an important role in a way that the depression of stainless steel is almost negligible.

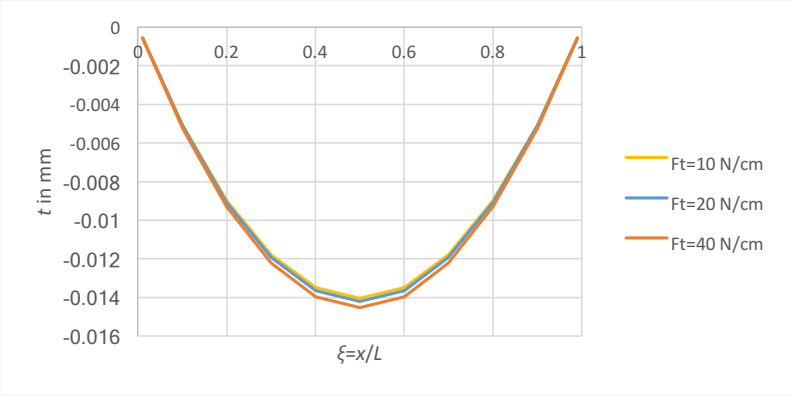

Figure 10: Depression t as a function of the mesh tension F_t other parameters as in Figure 7

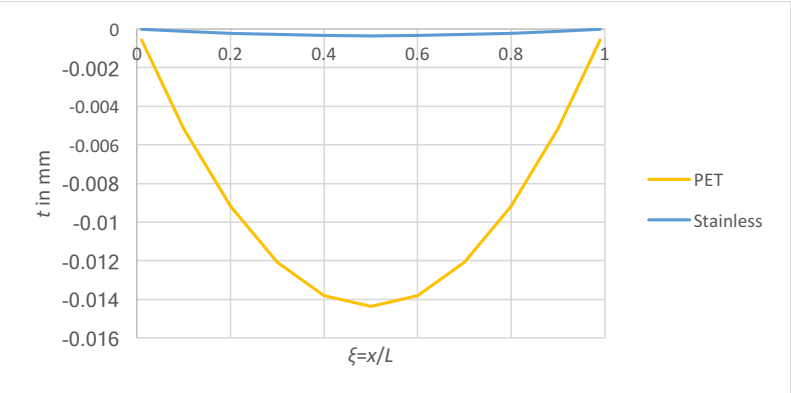

Figure 11: Depression t depending on different mesh material

4. Conclusion

It could be shown that with some simple assumptions the depression that a screen-printing mesh is undergoing during the squeegee movement over an infinite printing line under the impact of the squeegee pressure can be calculated theoretically. To prove the theoretical results an approach is to conduct print trials with different line widths and measure the cross section profiles of the ink deposit with a 3D-microscope. In a practical lab with students we tried to print such lines (0.5 to 5 mm width and 50 mm long). Unfortunately, the print samples did not show a measurable out-bulging at all. It seemed that the thixotropic ink levelled quite well after printing and before drying. These experiments should be repeated with an ink showing no thixotropy at all.

There might be influences by horizontal forces (friction between squeegee and mesh), which are not taken into account, yet. In future, the simple theory can be broadened in this way. However, it can be assumed that in presence of ink, there is a lubrication effect rendering horizontal forces almost negligible. For further broadening considerations, a certain bending stiffness (especially for stainless steel) should be assumed.

In the calculations done here, the approach in *x*-*z*-plane with infinite *y*-length of the printed feature parallel to the squeegee extension represents the worst case with maximum depression of the mesh. Any stencil material before or behind the observed *x*-*z*-plane would support the squeegee and decrease the depression.

List of symbols

α, β = squeegee deflection angles at edges (left and right hand side of squeegee)
t = mesh depression
L = width of the printed feature
E = Young's modulus od elasticity in Pa
A_q = specific cross section of the mesh in mm^2/cm
x = squeegee position ($0<x<L$)
F = vertical squeegee force
F_A, F_B = forces in mesh in N (A = left and B = right hand side of squeegee)
F_q = squeegee pressure in N/cm
F_t = mesh tension in N/cm
F_{Aq}, F_{Bq} = forces in the mesh per unit length in N/cm (left and right hand side of squeegee)
a, b = elongated lengths of the mesh (left and right hand side of squeegee)
ε = relative elongation, ε_1 left and ε_2 right hand side of the squeegee
ε_t = mesh tension in %
ε_q = mesh elongation caused by the squeegee pressure in %
$\xi = \frac{x}{L}$ = squeegee position in dimensionless representation with $0 < \xi < 1$
$K = \frac{F_q}{A_q E}$ = dimensionless constant

References

Hobby, A, 1997. *Printing Thick Film Hybrids*. [online] Available at: <http://www.gwent.org/gem_thick_film.html> [Accesed June 2017].

Riemer, D.E., 1988. *Ein Beitrag zur Untersuchung der physikalisch-technischen Grundlagen des Siebdruckverfahrens*. Doctoral Thesis. Technische Universität Berlin.

Riemer, D.E., 1989. The theoretical fundamentals of the screen printing process. *Hybrid Circuits*, 18, pp. 8–17.

SEFAR, 2008. *Siebdruckhandbuch*. Thal, Switzerland: Sefar.

On the Measurement of the Pick-up Volume of Anilox Rollers by Fluorescence

Felipe Fernandes, Fabio Campanelli and Edgar Dörsam

Institute of Printing Science and Technology, Darmstadt University of Technology, Magdalenenstr.2, 64289 Darmstadt

E-mail: fernandes@idd.tu-darmstadt.de; fabio.campanelli@stud.tu-darmstadt.de; doersam@idd.tu-darmstadt.de

Abstract

In this research an approach is shown how a fluorescent fluid can help to determine the pick-up volume of anilox rollers. The aim is to develop a method, which allows for fast measurements with simple test equipment and is easy to perform. Based on a list of requirements fluids are chosen and characterized. A simple test rig is provided to acquire images of different anilox rollers. In order to obtain information about the pick-up volume, the anilox rollers are wetted using fluorescent fluids, doctor bladed afterwards and illuminated using UV light. A monochrome camera acquires images in a shielded environment to eliminate the influence of ambient and scattered light. The chosen fluid is tested with three different mixing ratios on three different anilox rollers.

Keywords: pick-up volume, anilox roller, fluorescence, image processing

1. Introduction and background

1.1 Aim of the research

In this paper we present a new approach for measuring the pick-up volume of anilox rollers with a focus on usability and required time by usage of fluorescence indicators. In order to give an estimation of viability, suitable fluids and fluorescence indicators are reviewed and compared to a planimetric reference fluid measurement. A test rig for measuring fluorescence brightness of anilox roller surfaces in a static environment is presented. Tests made include measurements of different anilox roller lineatures.

1.2 Introduction to the cell and pick-up volume defined by an anilox roller

Flexographic printing is one of the most important industrial printing processes and for example dominating package printing. Anilox rollers are used for ink acquisition from the reservoir, predosing by using a doctor blade, and for dosing the ink by transfer onto the printing plate. Precise control of the roller parameters is of vital importance for the quality of the print product. One of those parameters is the cell volume of the cells engraved on the anilox roller´s surface. The cell volume is not identical with the pick-up volume of the anilox roller (see Figure 1). Nevertheless, exact knowledge of the cell respectively the pick-up volume is of crucial importance to machine operators in order to ensure reproducibility of the printing conditions. In industrial practice, however, the specifications of the roller parameters are dependent on a measurement standard that is used by the manufacturer. The values given do not necessarily match the cell or pick-up volume as would be desirable for high-quality printed products. Furthermore, cell volume may decrease by wear and stain deposition with time. Therefore an inspection of anilox rollers is desirable not only for freshly produced rollers, but also in certain periodical inspection intervals.

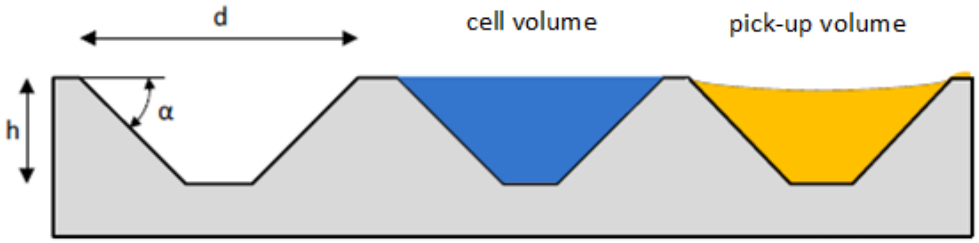

Figure 1: Geometrical and actual pick-up volume for a given gravure of width d and depth h by Maßfelder (2013)

The cell volume is specified by cm^3/cm^2, respectively ml/cm^2 (Meyer and DFTA, 2006) and is a unique function of the gravure of the anilox roller. The cell volume describes the amount of fluid in an ideally filled gravure, i.e. a gravure that is completely filled with ink up to the wall level. In practice, however, the pick-up volume is different by the fact that also the cell walls contribute to ink transfer by a thin liquid film that remains even after blading. Furthermore capillary forces create a curved, not a planar ink meniscus in the cells. This may prohibit a complete filling of the gravure.

1.3 State of the art in measuring of the cell volume

Current methods to determine the cell volume of anilox rollers include different measuring methods which can be distinguished according to the following categories:

1. Measuring the cell volume via direct (optical or tactile) cell geometry
2. Measuring the pick-up volume via reference fluids and measurements

The first approach includes measuring the geometry of the cells via confocal microscopy, interferometry and focus variation (Meyer and DFTA, 2006; Maßfelder, 2013). While these methods are used to determine the rollers quality and wear, and are influenced by less process parameters during the measurement than measuring by the use of test-fluids (Meyer and DFTA, 2006), the results reflect the cell volume which is different from the pick-up volume of the anilox roller due to fluid specific properties like wetting behavior (Maßfelder, 2013). Additionally, the gravure pattern type of the considered roller has to be known (cell raster vs. hachure) for usage of these methods.

Measuring the pick-up volume via test fluids and references includes planimetric measurement methods is the second approach, where a specific amount of test fluid is coated with a doctor blade on the surface and the size of the moistened area is measured and compared to reference measurements (Meyer and DFTA, 2006; Zecher, n.d.). Here the pick-up volume is determined and is highly influenced by the process parameters during the measurement. These methods can be used without knowing the gravure pattern type of the anilox roller and are often more efficient to be used by printing companies (Meyer and DFTA, 2006).

2. Materials and methods

2.1 Fluid selection

In order to select fluids for fluorescence measurements, a list of requirements is compiled. Main requirements for the used fluid are homogenous wettability and coating on ceramic anilox rollers, as well as a sufficiently small volatility of the liquid film in a static test environment and non-toxicity for easy and safe handling. While a lot of different indicators are available on the market, only few of them are practicable for technical use due to the fact that the main application cases for fluorescence indicators are located in the field of medicine or microbiology which demands highest quality and purity at low quantity, resulting in el-

evated expenses for the inspection of extended gravure surfaces (Sabnis, 2008). The fluorescence indicator has to offer an absorption maximum in the near UV-area (200-400 nm) and an emission spectrum in the visible light spectrum (400-700 nm) in order to be detected by an ordinary industrial monochrome camera.

The reviewed indicators are Fluorescein Disodium Salt (Uranine, 2014), Rhodamin 6G (Rhodamin 6G, 2013) and Lumogen F Red 305 (Lumogen, 1997) as well as dissolved Tinopal CBS-X in Tinopal CBS Slurry or Tinopal CBS-CL (Tinopal CBS SP Slurry, 2016; Tinopal CBS-CL, 2015). While Fluorescein Disodium Salt and Lumogen F Red 305 cover the main requirements regarding the fluorescence spectrum, a suitable solvent that offers a stable fluid film and little evaporation was not found during this research. All solvents either show a high evaporation rate or contain toxic components, which both make them unusable in this test environment. Additionally, Lumogen F Red 305 shows no visible fluorescence emission with the tested solvents under UV-Radiation. The absorption spectrum of Rhodamin 6G shows an absorption maximum at approx. 530 nm and does not meet the requirement as well.

Tinopal CBS-X showed the desired characteristics in terms of absorption and emission. In pretests the solvent Tinopal CBS-CL proved to have a good wettability on anilox rollers in combination with water, as well as a highly stable coating and little to none evaporation of the thin fluid film. Figure 2 shows the relative absorption and emission.

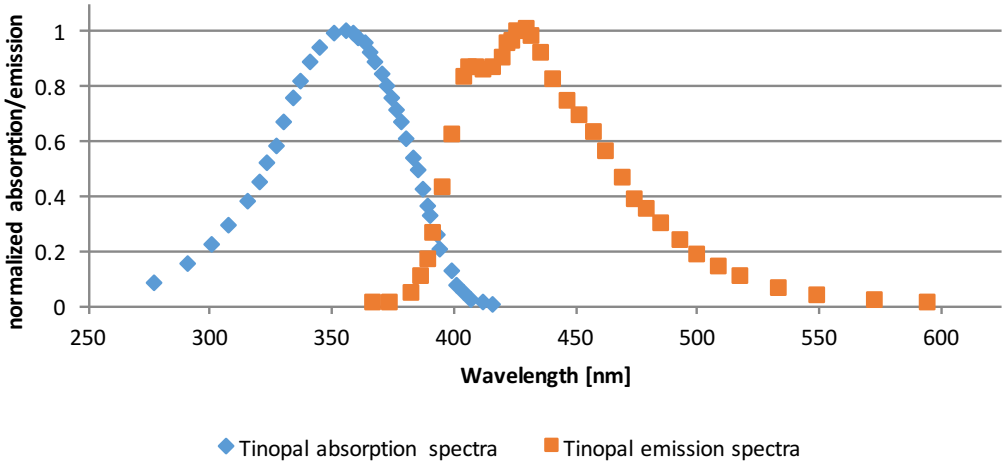

Figure 2: Absorption and emission spectra of Tinopal CBS-X by Tinopal NFW Liquid (2010)

It can be seen that the wavelength range of emission lies within the detectable range of most cameras whereas the absorption maximum is within UV range. For further studies Tinopal CBS-CL is chosen in three different mixing ratios with water (see Table 1). These three mixtures show desirable fluid films as well as wettability behavior and film stability. The used fluids are compared to Volucheck Ink® (Zecher, n.d.), a fluid for planimetric cell volume measurement in industrial applications where a defined amount of fluid is doctored on an anilox roller and re-absorbed with a test strip. Through the wetted area on the strip cell volume is measured indirectly via a used fluid to area ratio. The densities of the fluids as well as their surface tensions are given in Table 1.

Table 1: Densities and surface tensions of the chosen fluids

	Tinopal CBS-CL without water	**Tinopal CBS-CL with 25 % H_2O**	**Tinopal CBS-CL with 50 % H_2O**	**Volucheck Ink**
Density ρ [g/cm^3]	1.24	1.21	1.08	0.77
Surface tension [mN/m]	57.56 ±0.30	60.76 ±0.25	58.32 ±0.32	22.13 ±0.15

All measurements are performed five times using the KRÜSS DSA 100 contact angle measuring device using the pendant drop method. All measured surface tension values differ highly from the test-fluid Volucheck. While typical inks for flexographic printing show surface tensions between 20 and 40 mN/m (Nisato, Lupo and Ganz, 2016), a higher value as seen for Tinopal increases the chance that the cell walls of the anilox rollers are not wetted and therefore just the cells contain ink. While the measured fluid parameters differ significantly from the chosen reference fluid, the wetting behaviour on the used anilox rollers is comparable.

2.2 Experimental setup

The test rig used in this study (see Figure 3) contains the industrial monochrome area scan camera P83M-GigE-AS from PicSight (Leutron Vision, 2010) and UV-LEDs for illumination (LED-Tech, n.d.). For shielding reasons the rig is covered by black molleton (detached in Figure 3). The geometry of the test setup is shown on the left whereas the actual test rig is shown on the right. The camera perspective is in downward direction and the UV illumination is placed at an angle of 45°/-45° to the vertical axis.

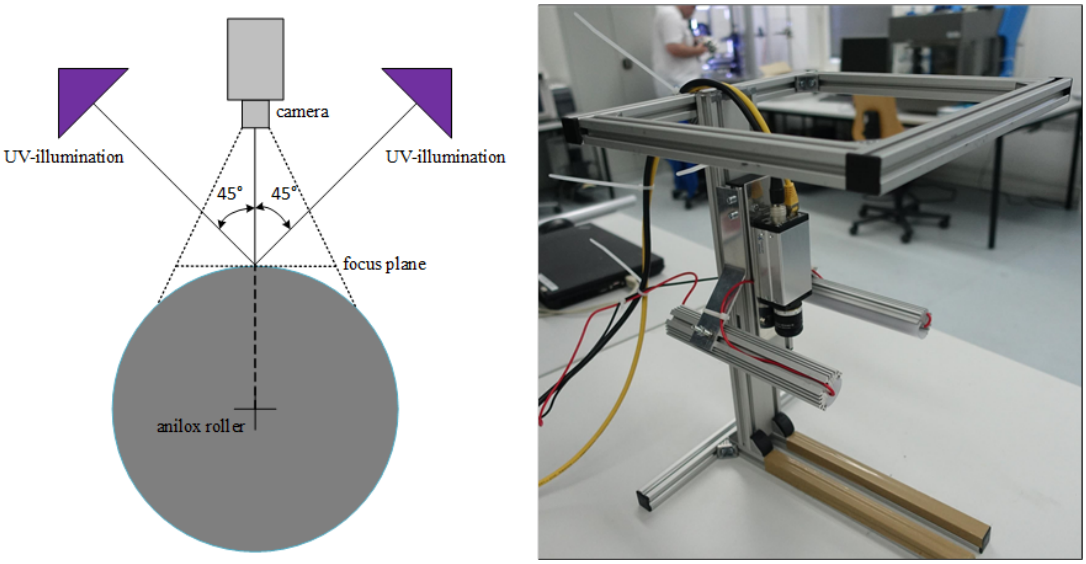

Figure 3: Geometry of the test setup (left) and test rig without shielding by black molleton (right)

The anilox roller is treated with the fluorescent fluid and doctor bladed using a doctor blade carriage (see Figure 4).

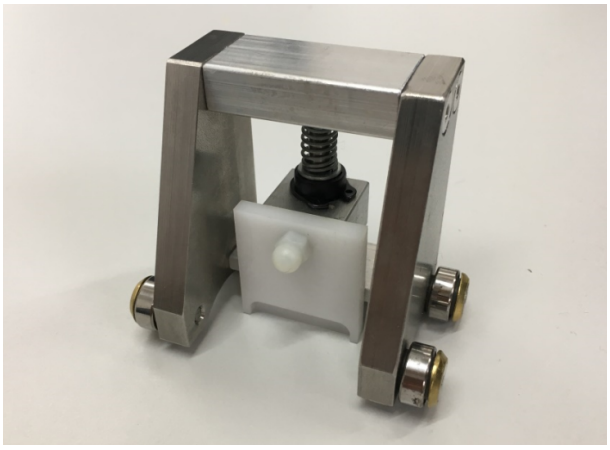

Figure 4: Doctor blade carriage

The anilox roller is subsequently placed underneath the imaging unit consisting of camera and illumination. The camera is focused on the roller surface using a limit stop which has to touch the surface of the anilox roller. Finally an image is acquired. Each test is performed three times. Thus the test rig always provides the same relative positioning between camera, illumination and anilox roller. Because the emission is within the detectable wavelength range of the camera, no additional filters are needed. The Comparison between the Absorption/Emission Spectra of Tinopal CBS-CL and the relative response of the used PICSIGHT Camera shows only a small overlap in wavelengths as shown in Figure 5. Since the used UV-LEDS offer only a small emission in this range of wavelengths no other filters are used.

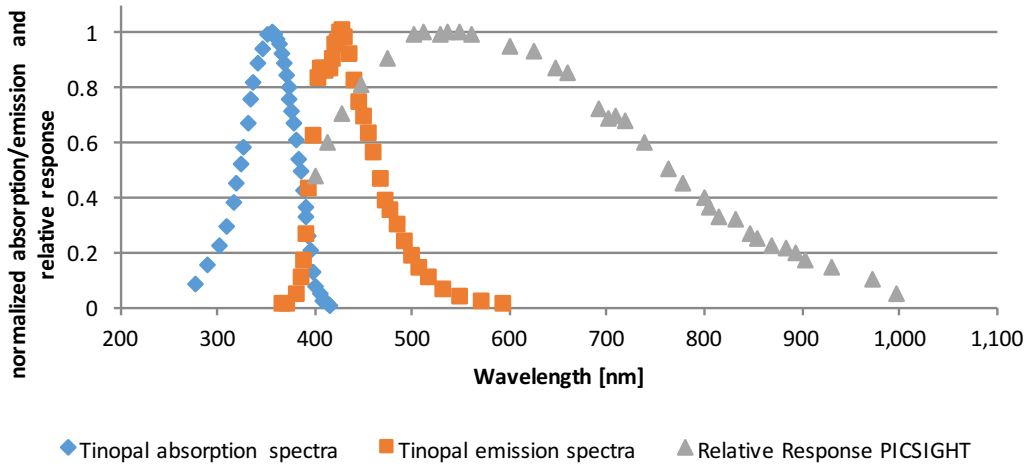

Figure 5: Comparision of the Tinopal CBS-X by Tinopal NFW Liquid (2010) spectra and response spectra of the used camera PICSIGHT P83M-GigE-AS by Leutron Vision (2010)

The later tests show a significant camera response on the used UV-LEDs, whereby measurements without fluids as comparable zero point measurements are taken. The used LEDs offer a peak wavelength emission of 365 nm (LED-Tech, n.d.). The influence on the measured gray values is determined via a zero-point reference measurement of all used anilox rollers without fluid. The results are shown in Figure 11.

3. Results and discussion

The obtained images exhibit gray values between 0 and 255, as they are acquired with 8bit of data resolution. In image processing, the gray values are normalized by setting the brightest pixel of the image to one. The obtained gray values are subtracted from the images taken from the wetted surfaces for each individual pixel of the image. This step is needed since the chosen UV-LEDS show an emission above the limit of 400 nm and therefore are visible for the camera. The results all refer to a field of 1 cm^2. The square cropped from the original picture is placed in the middle of the anilox roller. Figure 6 shows an example of an acquired image and the cropped image.

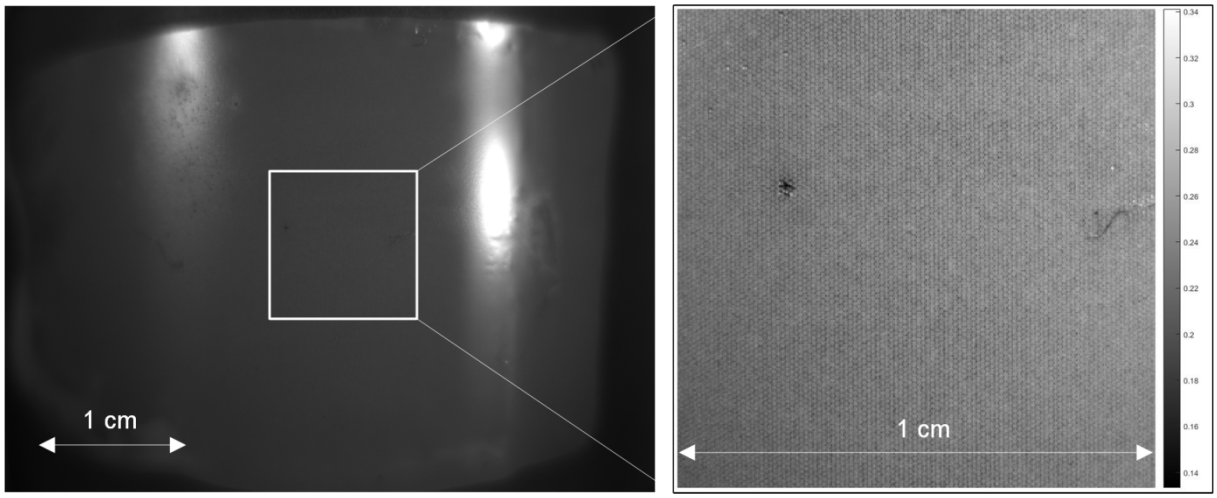

Figure 6: Original camera image (left) and cropped and normalized image (right); by cropping the image the visible reflections of the UV illumination on the anilox roller do not influence the measurements

Different anilox rollers are investigated with three fluid mixtures. Investigated lineatures are 90 L/cm, 180 L/cm and 300 L/cm of ceramic anilox rollers. In order to determine the influence of evaporation within the time between wetting the anilox roller and image acquisition, a series of measurements is conducted.

1. The loss of mass from a thin liquid film is determined that occurs within 30 seconds at room temperature (see Table 2).
2. The alteration on brightness in terms of gray values on a 300 L/cm anilox roller surface is determined every 5 seconds over a period of 25 seconds (see Figure 6).

Table 2: Percentage loss of mass after 30 s

	Tinopal CBS-C without H_2O	**Tinopal CBS-CL with 25 % H_2O**	**Tinopal CBS-CL with 50 % H_2O**
Average loss of mass over 30 seconds [%]	0.16	0.83	0.92

The results show a low loss of mass (< 1 %) for all fluid configurations over the tested time. This correlates with the specification, that Tinopal CBS-CL is non-volatile (Tinopal CBS-CL, 2015).

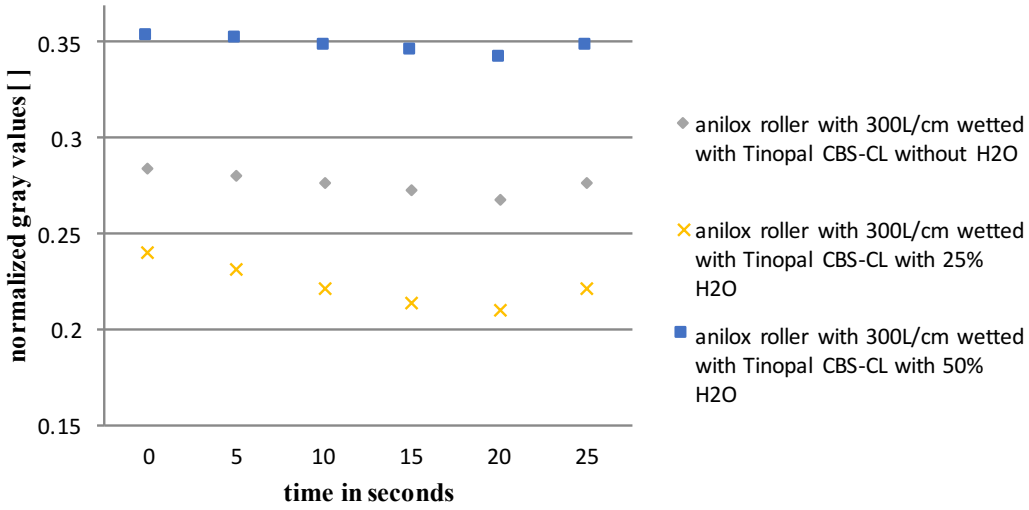

Figure 7: Variation of measured gray values of all fluids on a anilox roller with a lineature of 300 L/cm over 25 seconds

The 300 L/cm lineature is chosen because in preliminary tests it showed the qualitative highest decrease in brightness between the three chosen mixing ratios. Surprisingly, intensity of radiation increases between 20 and 25 seconds. A possible explanation is the complete drying of the fluid film in this period of time and therefore the indicator particle deposit directly on the anilox roller surface without any fluid surface that fractures and reflects UV-Radiation. The studied fluids exhibit a big variety of apparent fluid surface qualities on the chosen anilox rollers. This is observed for all of the fluids, especially at a lineature of 300 L/cm. Figure 8 and Figure 9 show different lineature/fluid combinations that differ in fluid film quality.

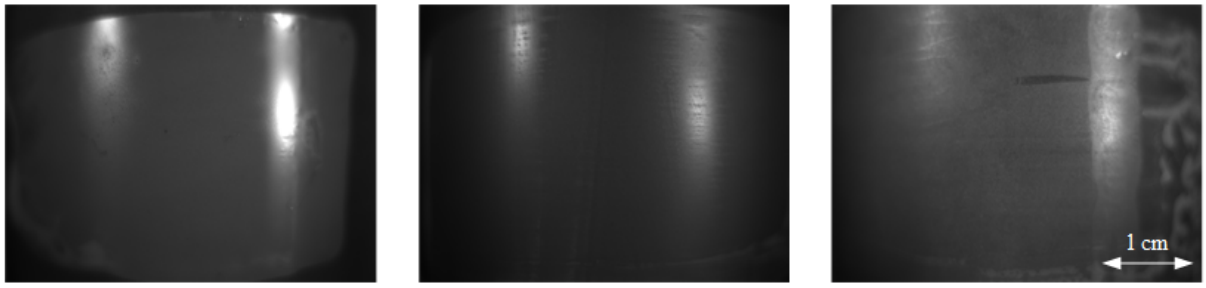

Figure 8: Anilox rollers with 90 L/cm (left), 180 L/cm (middle) and 300 L/cm (right) wetted with Tinopal CBS-CL; pictures taken within 10 seconds after wetting

Figure 9: Anilox rollers with 180 L/cm wetted with Tinopal CBS-CL pure (left), in a mixture with 25 % water (middle) and 50 % water (right); pictures taken within 10 seconds after wetting

It can be seen in Figure 8, that lineatures of 90 L/cm and 180 L/cm provide a uniform fluid film whereas the anilox roller with 300 L/cm shows some dry spots. While Tinopal CBS-CL without water content shows good coating qualities on all used anilox rollers, the 25 % H_2O solution shows an good coating on the 90 L/cm and 180 L/cm anilox rollers after doctor blading. Measurements taken on the 300 L/cm anilox roller show big differences in coating quality as well as in brightness of the acquired images. Furthermore Figure 9 provides the finding, that only Tinopal CBS-CL without water delivers demanded quality of the fluid film on a larger area. In a mixture with 25 % water the film already starts to break and is not always usable. By usage of a mixture with 50 % water the results downgrade further. None of the used mixtures can form a high-quality fluid surface on the 300 L/cm anilox roller. Nevertheless, the required area of 1 cm^2 remains usable. Figure 10 shows a histogram of relative brightness values of Tinopal CBS-CL without water content.

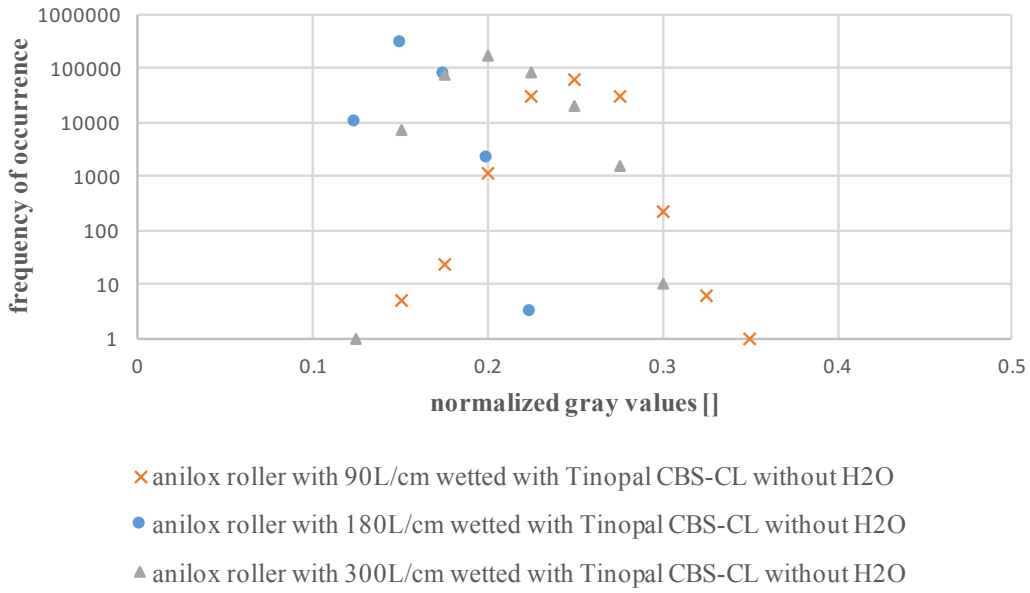

Figure 10: Histogram of Tinopal CBS-CL without H_2O on different anilox roller lineatures

Figure 10 shows significant differences in gray value peak occurrences. Therefore, the used anilox roller lineatures are distinguishable with the used procedure. The spreading of the histograms is comparable. However, increasing lineature and therefore decreasing cell volume neither correlates with descending peaks nor with descending mean gray values. Figure 11 gives an overview over all tested mixtures with every anilox roller. Additionally, the normalized gray values of the zero-point measurements without fluid are shown.

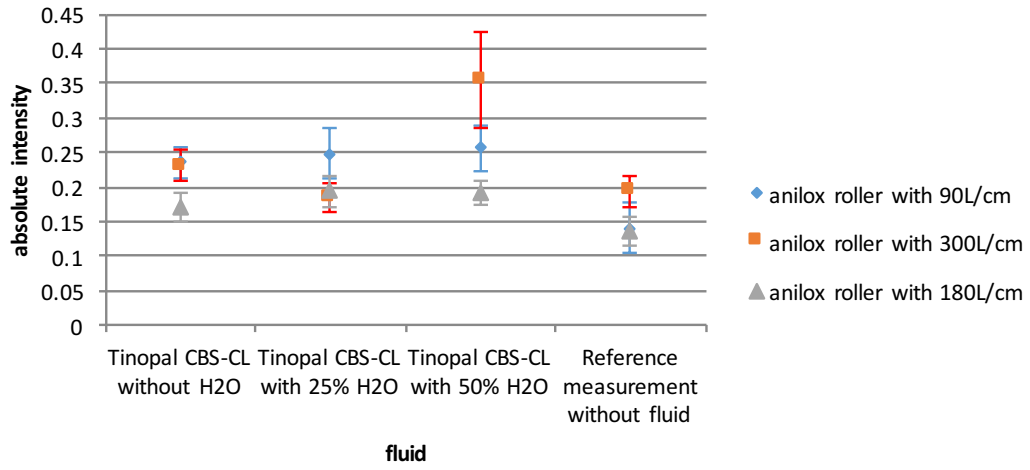

Figure 11: Absolute intensity comparision of 90 L/cm and 180 L/cm with all fluids (95 % confidence interval)

For Tinopal CBS-CL without water the anilox roller with 180 L/cm is distinguishable from the other two anilox rollers whereas results for 90 L/cm and 300 L/cm look similar. Measurements using Tinopal CBS-CL with 25 % water show distinguishability between the anilox roller with 90 L/cm and the other two anilox rollers. Only Tinopal CBS-CL with 50 % water shows distinguishability between all three anilox rollers. The 90 L/cm and 180 L/cm anilox rollers are distinguishable with all fluid configurations.

In order to compare the anilox rollers with a conventional method, the used anilox rollers cell volume is measured via a confocal microscope Sensofar Plu NeoX and the results are compared to the measured gray values. The results are shown in Table 3. Figure 12 shows the different measured topography of the 300 L/cm (left) and 180 L/cm (right) anilox roller.

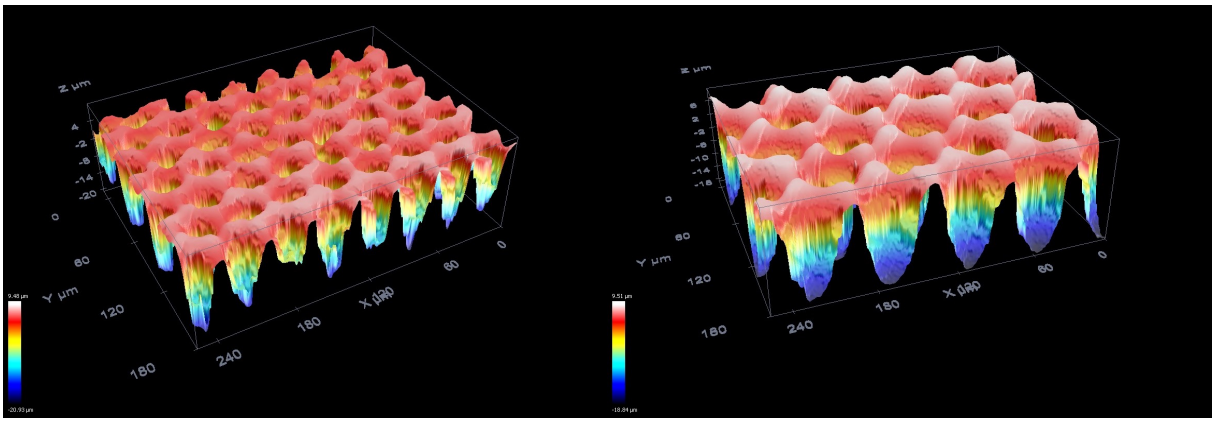

Figure 12: Topography measurements of the 300 L/cm and 180 L/cm anilox roller

The 300 L/cm anilox roller shows significant wear, resulting in an inhomogeneous pattern of the cells and differences in cell depth, while the 180 L/cm shows minimal wear. This effect is also seen in the measured cell volume compared to the manufacturer specification as shown in Table 3.

Table 3: Comparision of manufacturers specification and measured cell volume; comparision with mean gray value

anilox Roller	manufacturer specification [ml/m²]	measured Volume [ml/m²]	mean gray value (normalized)	normalized gray value per measured volume ratio
90 L/cm	16	14.14	0.25	57.18
180 L/cm	8	9.56	0.19	51.39
300 L/cm	4.5	6.37	0.26	24.79

While differences from the manufactures specification to the measured cell volume of the 90 L/cm (11.6 %) and 180 L/cm (19.5 %) are comparable, the 300 L/cm shows a big difference of 41.5 %. A comparision of the measured mean gray value and measured cell volume ratios also shows a big variation of results for the 300 L/cm. Possible explanations are the wear of the used anilox roller as well as the poor wetting behaviour of all used fluids.

The comparision of gray value measurements with fluids to the zero point measurements shows a similar value of the 90 L/cm and 180 L/cm anilox roller with an significant amount of measured intensity from LED emission. The zero point measurements create an offset to the measured gray values. While the gray value offsets for the 90 L/cm and 180 L/cm show detectable differences in emission and recognisability between these anilox rollers from the gray values alone, the zero-point reference measurement of the 300 L/cm anilox roller shows a nearly identical value compared to the gray value of the measurements with Tinopal CBS-CL with 25 % H2O. A possible explanation could be the differences in wetting behaviour as shown in Figure 11 or differences in cell volume as stated in Table 3. All measurements and comparisons indicate that a single mixture with a fixed water rate is not suitable for a variety of cell volumes and that wear has a major impact on the results in general.

4. Conclusions

Different fluids were reviewed and different anilox roller lineatures in a test rig investigated in order to give an estimation of the practicability of measurements of anilox rollers pick-up volume via fluorescence. The research shows that the chosen fluid/indicator characteristics have serious impact on the measurement possibilities and it is not possible to find one fluid to cover all chosen lineatures for the same qual-

ity of measurement. In general, Tinopal CBS-CL enables differentiation between the different lineatures. Further investigations have to be performed in order to estimate if for example a higher magnification of the acquired images improves the method and therefore allows drawing a conclusion about the pick-up volume of anilox rollers. While the results for the 90 L/cm and 180 L/cm anilox rollers show recognizable differences in gray value measurements and similar differences of the manufacturer specification, the results for the 300 L/cm anilox roller are difficult to interpret. More tests with unused anilox rollers and identical cell geometry are necessary to refine this method and find correlations. The aim of further research is to close the loop between gray values to specific cell volumes. Additionally, further investigations of the exact wetting behavior alongside with the fluorescence particle distribution of single cells as well as fluid surface and cell wall reflection behavior are needed to achieve exact measurements of cell volume.

Acknowledgments

The authors gratefully acknowledge the support of the ZECHER GmbH.

References

LED-Tech, n.d. *SSC VIOSYS UV 365nm CUN66B1B auf Star Platine*. [online] LED-Tech Optoelectronics. Available at: <https://www.led-tech.de/; https://www.led-tech.de/de/High-Power-LEDs-Seoul/SSC-VIOSYS/SSC-VIOSYS-UV-CUN66B1B-auf-Star-Platine--LT-2574_121_240.html> [Accessed 30 August 2016].

Leutron Vision, 2010. *PicSight P83M-Gig-As: GigE Vision camera*. [online] Leutron Vision. Available at: <http://www.leutron.com/english/product/picsight/gige/P83M-GigE.pdf> [Accessed 15 February 2017].

Lumogen, 1997. Lumogen F: Collector dyes. [online] BASF. Available at: <http://www2.basf.us/additives/pdfs/p3201e.pdf> [Accessed 28 February 2017].

Maßfelder, D., 2013. *Untersuchung der Verfahren zur Messung des Schöpfvolumens von Keramikbeschichteten Rasterwalzen*. Darmstadt: TU Darmstadt.

Meyer, K.-H. and DFTA, Deutschsprachige Flexodruck-Fachgruppe e.V., 2006. *Technik des Flexodrucks*. St. Gallen: Rek und Thomas.

Nisato, G., Lupo, D. and Ganz, S., eds., 2016. *Organic and Printed Electronics: Fundamentals and Applications*. Singapore: Pan Stanford Publishing Pte. Ltd.

Rhodamin 6G, 2013. *Material Safety Data Sheet: Rhoramine 6G MSDS*. [online] ScienceLab. Available at: <https://www.sciencelab.com/msds.php?msdsId=9927579> [Accessed 28 February 2017].

Sabnis, R.W., 2008. *Handbook of Acid-Base Indicators*. Boca Raton: CRC Press.

Tinopal CBS SP Slurry, 2016. *Safety Data sheet: Tinopal CBS SP Slurry 33*. [online] BASF. Available at: <http://worldaccount.basf.com/wa/NAFTA~fr_FR/Catalog/Detergents/doc4/BASF/PRD/30475200/.pdf?urn=urn:documentum:ProductBase_EU:09007af880187087.pdf> [Accessed 28 February 2017].

Tinopal CBS-CL, 2015. *Safety Data sheet: Tinopal CBS-CL*. [online] BASF. Available at: <http://worldaccount.basf.com/wa/NAFTA~fr_FR/Catalog/Detergents/doc4/BASF/PRD/30485516/.pdf?urn=urn:documentum:ProductBase_EU:09007af88019e5a3.pdf> [Accessed 28 February 2017].

Tinopal NFW Liquid, 2010. *Safety Data sheet: Tinopal NFW Liquid*. [online] BASF. Available at: <http://worldaccount.basf.com/wa/NAFTA~en_GB/Catalog/FunctionalPolymers/doc4/BASF/PRD/30425316/.pdf?asset_type=ti/pdf&language=EN&urn=urn:documentum:eCommerce_sol_EU:09007bb280084836.pdf> [Accessed 28 February 2017].

Uranine, 2014. *Safety Data Sheet: Uranine AP*. [online] Merck. Available at: <http://www.merckmillipore.com/INTERSHOP/web/WFS/Merck-INTL-Site/en_US/-/USD/ShowDocument-File?ProductSKU=MDA_CHEM-108462&DocumentType=MSD&Language=EN&Country=EN> [Accessed 28 February 2017].

Zecher, n.d. Volucheck. [online] Zecher GmbH. Available at: <http://www.zecher.com/en/printing-technology/roller-inspection/#volucheck> [Accessed 30 August 2016].

Accelerated Weathering Tests of Parking Vignettes

László Koltai, Csaba Horváth and Eszter Bartha

Óbuda University, Institute of Media Technology and Light Industry Engineering, Doberdó út 6., Budapest, Hungary

E-mail: koltai.laszlo@rkk.uni-obuda.hu; horvath.csaba@rkk.uni-obuda.hu; bartha eszter@rkk.uni-obuda.hu

Abstract

In modern urban life, it has become fairly natural that motor vehicle parking falls under regulations. One frequently applied form of indicating vehicles that carry special permits is the use of vignettes that can be stuck on the windscreen. The largest Hungarian producer of these vignettes used for the regulation of parking has demanded the elaboration of a test method that offers preliminary information in connection with the resistance of the manufactured products to weather conditions. The research order focused on individually numbered vignettes made with flexography on plastic film, and covered the testing of four differently coloured products. In this case, colours carried meanings as to the potentials of use. Our objective was to work out an accelerated weathering test model that simulated use properly, could be appropriately repeated and allowed precise measurements.

Keywords: accelerated weathering tests, flexography, colorimetry, printed vignettes

1. Introduction and background

In modern urban life, it has become fairly natural that motor vehicle parking falls under regulations. One frequently applied form of indicating vehicles that carry special permits is the use of vignettes that can be stuck on the windscreen. These coloured indicators are usually valid for one year. They need to be renewed annually. This is the period of time during which they are required to remain suitable for preserving the correct information. It is also a frequent solution that distinct meanings are associated with the different colours of the vignettes, and therefore their colour fastness can also be an important quality factor.

The largest Hungarian producer of these vignettes used for the regulation of parking has demanded the elaboration of a test method that offers preliminary information in connection with the resistance of the manufactured products to weather conditions.

Such modeling called for a number of special conditions. Vignettes are stuck on car windscreens from the inside. The test needed to take the modifying effects of this special location into account.

2. Methods of research

The research order focused on individually numbered vignettes made with flexography on plastic film, and covered the testing of four differently coloured products. In this case, colours carried meanings as to the potentials of use. The main goal of the test was to find out how the colour fastness of vignettes changes during their term of validity. Our objective was to work out an accelerated weathering test model that simulated use properly, could be appropriately repeated and allowed precise measurements.

2.1 Equipment used for the aging test

To conduct the aging test, SUNTEST XLS+ equipment was used (Figure 1). This equipment is suitable for the performance of indoor, i.e. laboratory weather resistance tests. This accelerated test method is classified to belong to the group of xenon lamp tests.

Figure 1: SUNTEST XLS+ equipment

The sample holder is located in the lower part of the test cabinet, whereas in the upper part there is a 1700 W air-cooled xenon lamp.

For the test, test graphics can be placed into the sample holders horizontally. It has specific significance, because radiation arrives at the sample on car windscreens at an angle of approx. 45°, which needs to be taken into account during the evaluation of the results.

A particular request of the client was that the tests were to be conducted mostly in the UVA radiation range, as the conformity of the products was intended to be reviewed in relation to this weather impact, and for this reason a suitable source of light was used.

The Sun Test parameters used for the measurement were:
- Radiation range: 300–400 nm, using a special auxiliary quartz glass filter for UV
- Irradiation: 45 W/m^2
- 24 hours of irradiation: 1 080 Wh/m^2
- Temperature: 16–50 °C
- Relative humidity: approx. 29 %

This project is continued and extends the earlier investigations from our institute (Borbély, Horváth and Szentgyörgyvölgyi, 2012; 2013).

2.2 Procedure for the measurement of the light fastness of vignettes

Four kinds of samples were tested: red, green, crimson and yellow with four test pieces from each.
The supplied samples were stuck on a 2 mm glass plate (Figure 2) and placed in the sample holder, and then another 2 mm glass plate was placed on them for the duration of illumination, because the thickness of windscreens tends to be larger than 2 mm.

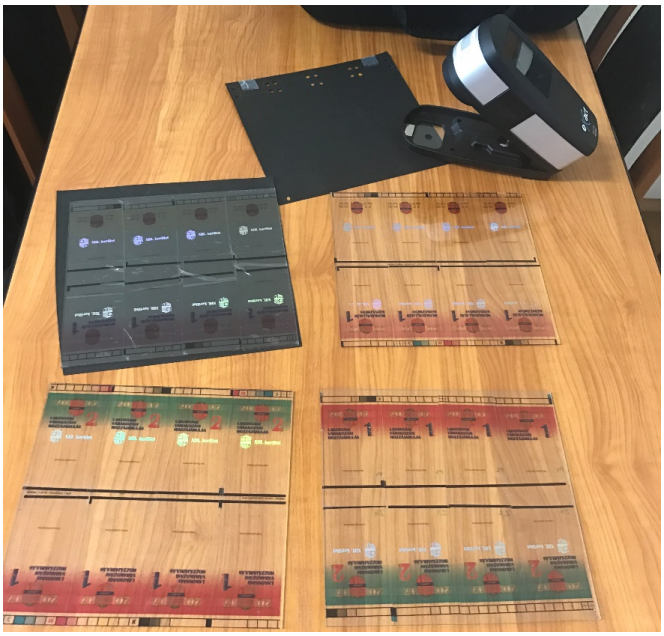

Figure 2: The supplied samples stuck on the glass plate, underplate and gauge

CIELAB values were measured on the samples to calculate the corresponding differences in colour stimulus, and consequently determine the degree of changes. The measurements were carried out on a glass plate, with a black cardboard piece used as the underplate. For the accurate reproducibility of the measurements, a gauge was made. In the gauge, 4 measuring points were defined for every sample, and additionally such registers were applied that allowed the performance of colour measurement during the aging test invariably at the very same points. The extent and possibilities of measurement were restricted by the fact that the tests were carried out on the produced, strictly administered, numbered samples.
The duration of the aging test was restricted by the limited time scales defined by the client. Consequently, the total duration of the aging test was 192 hours. In the first phase of the test, several measurements were made (in 24-hour intervals), because it was presumed that changes were more pronounced in the initial phase. Measuring times are during the entire weathering phase, following 24, 48, 72, 96 and 192 hours. The measurements performed prior to the accelerated weathering test were handled as benchmarks to which the changes were compared. Alterations in the colours of the test samples were measured with an X-rite eXact spectrophotometer (Figure 3), at measuring conditions: D65/2°.

Figure 3: X-rite eXact colorimeter

3. Results and Discussion

During the aging test, the colour values at the designated points of the individual vignettes were measured at 24-hour intervals in the first phase and at the end of the second phase. From these values, colour changes (as per the CIELAB system) and colour differences were calculated against the corresponding values of the prints before the test (International Organization for Standardization, 2007; 2013).

The resulting colour difference values measured on a single vignette (4 testing points) were averaged; the values for the same types of vignettes (4 vignettes) were similarly averaged in order to demonstrate the changes in the colours of the individual types of vignettes in the tables and graphs as a function of time (Figures 4–7).

	Green				
hours	24	48	72	96	192
ΔE^*_{ab} (average)	3.26	5.82	8.56	10.23	11.48

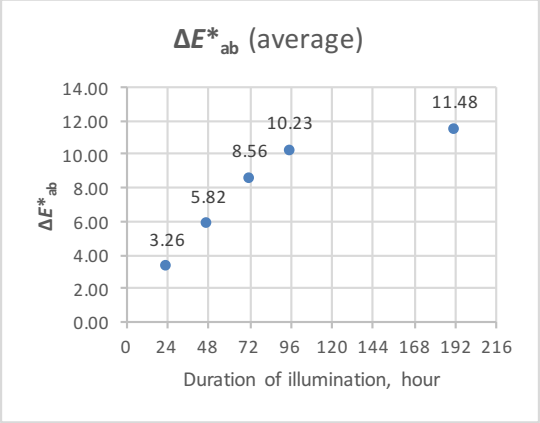

Figure 4: Changes in the colour of the green parking permits as a function of weathering time

	Red				
hours	24	48	72	96	192
ΔE^*_{ab} (average)	1.70	3.05	4.45	6.42	11.13

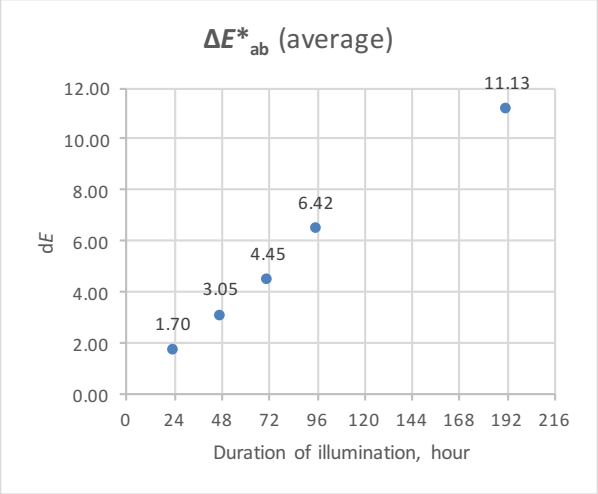

Figure 5: Changes in the colour of the red parking permits as a function of weathering time

	Crimson				
hours	24	48	72	96	192
ΔE^*_{ab} (average)	2.92	2.50	1.72	2.44	2.50

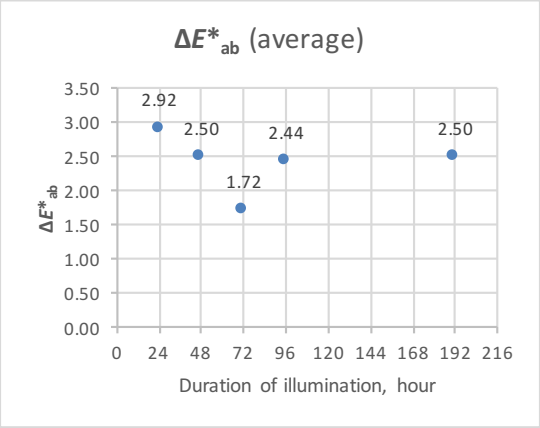

Figure 6: Changes in the colour of the crimson parking permits as a function of weathering time

	Yellow				
hours	24	48	72	96	192
ΔE^*_{ab} (average)	4.60	8.36	10.83	12.46	13.85

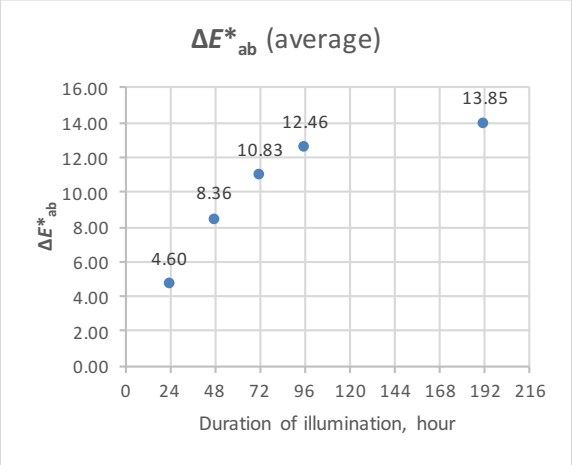

Figure 7: Changes in the colour of the yellow parking permits as a function of weathering time

During the evaluation of the measurement results, the solar radiation data for 2016 was referenced on the basis of Figure 8.

- Annual radiation in total: 1368.6 kWh/m^2
- Average daily radiation: 3750 Wh/m^2
- Ratio of UVA radiation in the total value: 9 %.
- As a result, average daily radiation in the UVA range 337.5 Wh/m^2

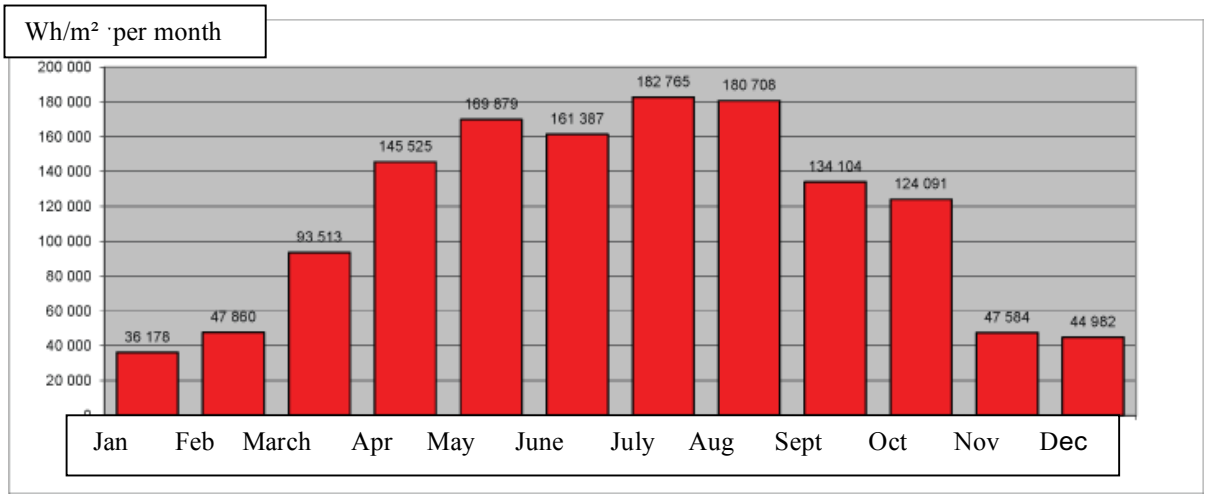

Figure 8: Monthly breakdown of solar radiation

Irradiation value of the source of illumination we use for 24 hours was 1080 Wh/m^2 at the surface area. As a result of the comparison, the 192 hours, that is 8 days we tested in reality correspond to approx. 26 days in the case of the horizontal surface.

4. Conclusions

For the yellow, red and green samples, the measurement results apparently changes almost evenly, and the ΔE^*_{ab} values are around 12. They are clearly perceivable colour differences.

As it is a rising tendency, for these samples it can be expected that as an impact of UVA radiation the colours of the vignettes will alter to an unacceptable extent.

In the case of the crimson sample, the nature of the change is not obvious, but the extent of colour alteration remains acceptable.

Although the result is evident with respect to the non-conformity of the samples, a longer aging test with the addition of the parallel measurement of the impacts of natural sunlight could offer further information in view of the correct selection of vignette materials and colouring agents.

References

Borbély, Á., Horváth, C. and Szentgyörgyvölgyi, R., 2012. Accelerated light aging of digital prints, In: N. Edlund, M. Lovrecek (ed.) Vol. XXXIX of the *Advances in Printing and Media Technology: Proceedings of the 39th International Research Conference of iarigai*. Ljubljana, Slovenia, 09–12 September 2012. Darmstadt: iarigai, pp. 117–122.

Borbély, Á., Horváth, C. and Szentgyörgyvölgyi, R., 2013. Artificial aging of outdoor prints, In: N. Edlund and M. Lovreček, eds. *Advances in Printing and Media Technology: Proceedings of the 40th International Research Conference of iarigai*. Chemnitz, Germany, 08–10 September, 2013. Darmstadt: iarigai, pp. 251–254.

International Organization for Standardization, 2007. *ISO 12647-7:2007 Graphic technology -- Process control for the production of half-tone colour separations, proof and production prints -- Part 7: Proofing processes working directly from digital data*. Geneva: ISO.

International Organization for Standardization, 2013. *ISO 105-B02:2013 Textiles -- Tests for colour fastness -- Part B02: Colour fastness to artificial light: Xenon arc fading lamp test*. Geneva: ISO.

Co-Developing Services utilizing Printed Functionality

Liisa Hakola, Kaisa Vehmas, Thea Sipiläinen-Malm, Reetta Grenman and Anu Seisto

VTT Technical Research Centre of Finland Ltd

E-mail: liisa.hakola@vtt.fi; kaisa.vehmas@vtt.fi; thea.sipilainen-malm@vtt.fi; reetta.grenman@vtt.fi; anu.seisto@vtt.fi

Abstract

2D bar codes have been available for almost 30 years, but during the recent years, their popularity has increased. The use of functional printing methods in code printing enables that novel digital services are created for the consumers and other stakeholders. Functional inks make it possible for parts of the 2D code to disappear, to appear, or to change colour e.g. after certain time or at certain temperature. These changes in codes enable changing the information content achievable through reading the codes. The content behind the codes should offer added value for the users, as consumers are not willing to read the codes just for getting a link to a web page. Novel services utilising functional printed codes, can take into account different types of user and context related data, such as user profile and GPS location of the smartphone. These context-aware features will further improve the value and quality of the services provided. In this study, we tested consumer attitude towards services in which functional 2D codes were used and demonstrated their printing in pilot scale.

Keywords: printed functionality, 2D codes, flexo, IoT, co-development

1. Introduction and background

IoT (Internet of Things) is about connecting objects, things and devices and often adding digital services to them. The usual examples of such connected objects are from our everyday life, including e.g. cars and fridges. Tags available today, e.g. in mass-market products like milk cartons and other food packages or books are usually static, i.e. the information they provide does not change. This is an area where functional inks can add immense value. These kinds of novel solutions combining physical products and digital services can be successful and their entry to market may be fastened when their potential users have been involved in the innovation and development process (Vehmas, et al., 2015).

In this study, the aim was to collect feedback from potential users of novel service concepts created around functional 2D codes to further develop the concepts and to ensure the acceptability of the solutions. In addition, we tested printing methods and circumstances suitable for functional printing based on the requirements from different concepts in pilot scale. Our aim in the pilot scale testing was to ensure that the functional codes are readable (e.g. by optimizing the size of the codes) and find out the suitability of materials used.

1.1 Technical concept

The 2D bar codes have gained popularity during recent years, but the first 2D bar code type, Code 49, was published already in 1988. Nowadays there are over 20 different bar code types used for different purposes in logistics, manufacturing and information transfer. Some examples are in Figure 1. Some 2D bar code types are in public domain, which means they can be used freely, such as the two most popular code types

Data Matrix and QR Code. Some code types are protected and require a user licence, such as DataGlyph. 2D bar codes typically consist of black and white cells (e.g. small squares).

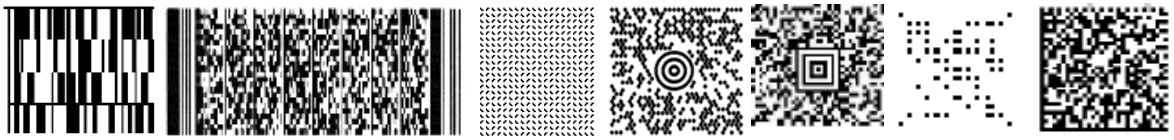

Figure 1: Different 2D bar code types: Code 49, PDF417, DataGlyph, MaxiCode, Aztec Code, Snowflake and Data Matrix

Compared to linear bar codes 2D bar codes provide a large information capacity, even up to several thousands of characters per code. Many 2D bar codes contain a sophisticated error correction algorithm, which means that information is readable even if up to 30 % of the code is destroyed. 2D bar codes can serve as a link to a database similar to linear bar codes, but they can also serve as an independent database. The physical size of the code is scalable without affecting the information capacity. QR code and Data Matrix codes have been used in the trials described in this paper. They enable encoding of even up to several thousand alphanumeric characters.

The concept for using functional inks in enhancing dynamic nature of 2D bar codes is that parts (e.g. some of the cells) of a 2D bar code are printed with a functional ink that reacts to the surrounding environment, e.g. temperature, humidity or light conditions. Changes in the environmental conditions cause the cells printed with a functional ink to disappear, to appear, or to change colour. This changes the physical layout of the 2D bar code thus also changing the information content (e.g. website address). Thereby the environmental conditions have an effect on the scanning process and resulting digital service. The services can also take into account the other user and context related data, such as user profile on the smartphone and GPS location of the smartphone. These context-aware features will further improve the value and quality of the services provided.

1.2 Functional ink technologies

There is a range of colour-changing technologies, out of which the most popular and readily printable are thermochromic (changing colour with temperature) and photochromic (changing colour with sun or ultraviolet light, even camera flash light). Functional ink technologies are available at the moment mainly for analogue printing methods (flexography, screen printing, offset printing). For digital printing mostly, fluorescent inks are available. This is due to the large particle size of the colour-changing pigments, which present challenges in inkjet ink formulation. Functional inks can be used for printing 2D bar codes similar to regular printing inks, and detected by smartphones (Hakola and Linna, 2005).

Thermochromic ink is a type of ink that changes colour with heat. This can make certain images appear (or disappear) as soon as the label or product goes above or below a certain temperature. These temperatures can vary from -10 to +65 °C. Temperature-sensitive inks come in two varieties: reversible and irreversible. With reversible thermochromic ink, the colour will revert when the temperature returns to its original level, whereas the colour remains constant after a change in temperature with irreversible thermochromic ink.

Photochromic materials change their colour when the intensity of incoming light changes. Most photochromics change from colourless to coloured upon exposure to UV light, and then fade back to colourless upon removal from the UV source. The normal wavelength of excitation is around 360 nanometres. Moreover, while sunlight works the best, a fluorescent black light, which emits near-UV light (320–400 nm), will usually work. Different dyes have different kinetics, meaning some will colour and fade quickly, while others will colour and then fade slowly.

In addition to thermochromic and photochromic inks, there are several other functional ink types on the market. Examples of various other ink types on the market are:

- Invisible fluorescent inks and varnishes can only be seen under UV or IR light.
- Phosphorescent ink glows in the dark after it has been exposed to a source of light.
- Hydrochromic ink changes colour if water has been applied.
- Scratch-off ink, has to be scratched or scraped away. The message, which can be printed in various colours, is hidden beneath a top layer that is printed in e.g. silver or gold colour.
- Prismatic effect ink provides a holographic effect.

2. Materials and Methods

2.1 Owela tool for collaboration with users

An online Open Web Laboratory, Owela (http://owela.fi), has been developed at VTT for user-centric studies. Owela supports active user involvement in the innovation process from the early ideas to piloting and actual use (Friedrich, 2013). Owela can be utilized to involve users in all phases of a development process for an innovation.

In this project, Owela was utilized to gather knowledge about use of functional 2D codes among Finnish consumers and to clarify what kind of services would the consumers like to combine with printed functionality. Consumers were also able to evaluate different concepts developed in the project and to co-innovate novel solutions.

The concepts were presented to the consumers as stories to make it easier for them to understand the idea of novel solutions and easily realize the possibilities the solution offers for their daily life. The concept themes were about:

1) Digital product and recycling,
2) Fast moving consumer goods and dynamic pricing, and
3) Authenticity of the products.

In the first story, *Digital product and recycling*, the idea was described by using beer bottles from a local brewery as an example. The consumer in this story had bought a bottle of beer from a local producer and read a unique code from the label on the bottle. The consumer received useful and entertaining information e.g. about the origin of ingredients, the producer, recycling of the package, and information if the temperature of the beer is optimal. By reading the code the consumer was also able to create an interactive connection with the local producer, that makes it possible e.g. to personalize an own drink together with the producer and order the drinks via a digital service.

The second story, *Fast moving consumer goods and dynamic pricing*, describes a situation in a retail store, where the consumer can easily get information if the best before date of the product is close enough to get a discount. This can be done by LED lights that automatically turn on after a certain time period. This can be based on e.g. time-temperature indicators that after a certain period give an electric signal to the LED lights causing the lights to turn on. While being informative towards the consumer, it also makes the work of the retailer more effective. The retailer can also by reading the codes ensure that the products that arrive to the store, are in good condition after transportation and also the origin of the products. In this story, meat products were used as an example, so e.g. ensuring that the temperature has been correct during transportation is very important for all the stakeholders.

In the third story, *Authenticity of the products*, a family was on holiday abroad. There, they were able to ensure the authenticity of the medicine and sunglasses they purchased by reading the 2D codes from the products in certain lighting conditions. Similar authenticity check could also be done with other products purchased from the internet.

After reading the stories, participants discussed about their interest towards the different concepts. Totally, 45 Finnish consumers participated the discussion and gave 341 comments to the discussion during two weeks in January 2017. Fifty-three percent of the participants were female, and 47 % of male. Age distribution varied between 17–79 years, the average age of the participants was 49 years.

All these concepts selected for the Owela discussion can significantly benefit from use of functional inks (Hakola, et al, 2013). Thermochromic ink technologies have potential in many food related solutions (concepts 1 and 2). Also, photochromic inks are relevant when dealing with light-sensitive products. Photochromic inks can also be used in brand protection (concept 3) where the codes can be fully readable only under specific lighting conditions.

2.2 Printing trials

The following functional ink technologies have been evaluated by VTT for their suitability for printing Smart Tags, specifically QR and Data Matrix codes or parts of those:

- Reversible thermochromic ink Chameleon WB flexo ink slurry, colour red, temperature 47 °C from LCR Hallcrest, the ink is red < +47 °C and clear > +47 °C (Ink a).
- Reversible photochromic ink UV flexo red photo from Chromatic Technologies Inc., the ink is red under UV or sunlight, but otherwise clear (Ink b).
- Irreversible oxygen sensitive ink, VTT proprietary formulation (Ink c).

The following printing equipment was used for the printing trials (Figure 2): laboratory scale flexography printer with camera-based alignment: RK Flexiproof.

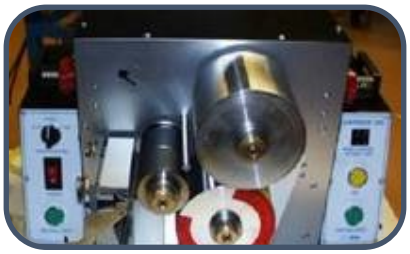

Figure 2: Printing machinery used: flexography printer

The following paper based substrates have been used for the printing trials:

- Colour copier paper 100 g/m^2 (copy paper)
- DIG UV INKJET MC80 FSC PET coated paper (IJ label)
- PE85 TOP WHITE (PE coated paper)
- DuPont Melinex 504 (PET film)

Printed codes were scanned with Samsung Galaxy S7 mobile phone and Upcode code reader software was used.

3. Results and discussion

3.1 Consumers attitudes towards services enabled by functional codes

Based on the consumer study, it was clear that people in Finland are familiar with 2D codes. All the participants had seen them e.g. in the packages, advertisements and tickets. Three out of four had read 2D codes with their smart phones but only 17 % said that they read the codes regularly. Consumers found all of these concepts interesting. Seventy-nine percent of the participants evaluated it to be interesting to read the codes from local producers' products and to create an interactive relationship (story 1). To utilize the codes in fast moving consumer goods, like meat packages, was in the interest of 55 % of the participants (story 2). Finnish consumers did not see so much potential in using the codes in cheap products and they were not concerned about the origin and safety of the products. That was also the case in the authenticity of the products (story 3), but still consumers saw a lot of potential in this case. Authenticity of the products was evaluated interesting by 85 % of the participants.

When consumers asked to choose the most interesting concept for them, 52 % chose the Digital product and recycling (story 1). Reasons for that were e.g. consumers' willingness to support local producers, their interest to discuss interactively with the producer and personalized experiences. Thirty-one percent preferred the Fast moving consumer goods and dynamic pricing (story 2) and 17 % of the participants chose the Authenticity of the products (story 3) to be the most useful one for them.

3.2 Code printing

For the concept definition and evaluation printing of cells of QR codes was evaluated with Ink a. The following printing settings were used: three printed layers, anilox 18 cm^3/m^2. The layout contained an original QR code, logos and other elements printed with regular inks (office copier), and areas to be printed with a thermochromic ink (Figure 3 and Figure 4). Cells were printed on QR codes that were 3 cm × 3 cm. Copy paper was used as a substrate. The layout contained also a circle printed with the thermochromic ink for demonstration purposes.

(a) *(b)* *(c)*

Figure 3: QR code layout for concept definition: (a) original QR code printed with regular ink, (b) cells printed with the thermochromic ink, (c) resulting QR code containing (a) and (b)

Figure 4: Final layout of the printed tags and working principle when attached to a coffee cup: on the left, the coffee cup is empty; on the right, the cup contains hot water resulting in cells and a circle printed with the red thermochromic ink to disappear, when the water is cooled below +47 °C

When attached to an empty coffee cup the scanner software led to a website. When attached to a coffee cup full of hot water (>+47 °C), the cells printed with the thermochromic ink disappeared and the after scanning the code led to a different website.

3.3 Evaluation of suitable code size

Printing of photochromic Ink b was carried out on different substrates (copy paper, IJ label, PE coated paper) with different anilox (18 cm^3/m^2 and 38 cm^3/m^2). Only one ink layer was printed in all cases since it already provided dark enough printing and multiple layers spread too much. The printing layout consisted of Data Matrix codes of different size (cell size 0.25 mm – 1.5 mm with 0.25 mm intervals). After printing, the codes are clear, and when exposed to UV or sunlight they turned red in approximately 10–30 seconds. The red colour started to fade immediately when the light source is removed. Printed samples are presented in Figure 5 and Figure 6. The codes with cell size 0.5 mm or more were of good print quality and cells were reproduced properly, but there was too much ink spreading in codes with cell size 0.25 mm. The same applied to all substrates used.

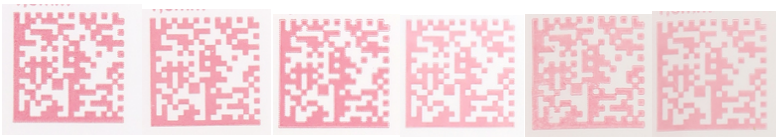

Figure 5: Data Matrix codes with 1 mm cell size printed with a reversible photochromic ink when under UV light; from left: copy paper with 38 cm^3/m^2 anilox, copy paper with 18 cm^3/m^2 anilox, IJ label with 38 cm^3/m^2 anilox, IJ label with 18 cm^3/m^2 anilox, PE coated paper with 38 cm^3/m^2 anilox, and PE coated paper with 18 cm^3/m^2 anilox

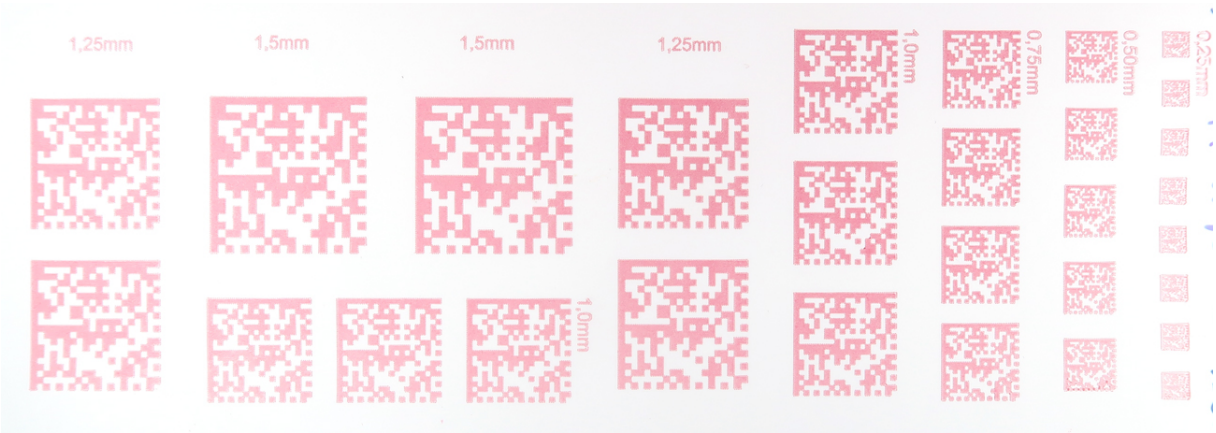

Figure 6: Data Matrix codes with different cell size printed with a reversible photochromic ink when under UV light on copy paper with 38 cm^3/m^2 anilox

With all the substrate and anilox combinations codes with cell size down to 0.50 mm were decoded correctly. With the copy paper substrate, also codes with 0.25 mm cell size were occasionally decoded. Colour change from clear to red occurred in less than 30 seconds under UV light that simulated sunlight.

3.4 Evaluation of oxygen indicator

Flexography printing of oxygen sensitive ink (VTT, proprietary formulation, Ink c) was carried out on plastic film (polyester film DuPont Melinex 504). Anilox 38 cm^3/m^2 was used. The printing layout consisted of Data Matrix codes of different size (cell size 1.00 mm – 1.5 mm with 0.25 mm intervals). Five and ten layers were printed. The codes were of good print quality and cells were reproduced properly. The colour of the print is green. The print colour does not change during storage in air. An example of the codes is presented in Figure 7.

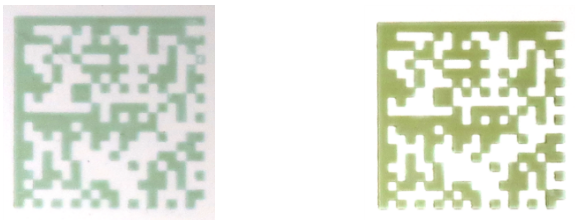

Figure 7: Data Matrix codes 5 (left) and 10 (right) ink layers printed with oxygen sensitive ink on PET plastic film with 38 cm^3/m^2 anilox

The printed codes were placed inside a plastic pouch made of barrier material on a position where it can be seen from the outside. The code was packed in an inert oxygen-free atmosphere (nitrogen) together with an oxygen scavenger. The oxygen scavenger needs some time to remove any remaining oxygen. The packages were stored at room temperature until the next morning. The dye undergoes an automatic chemical reaction during the storage in oxygen-free atmosphere at room temperature resulting in a colour change to yellow. The oxygen sensitive prints are now activated. When the packages were opened the colour changed to green in less than 3 minutes. The colour changes of the reacting ink were documented by taking photographs. The function of the indicator is illustrated in Figure 8.

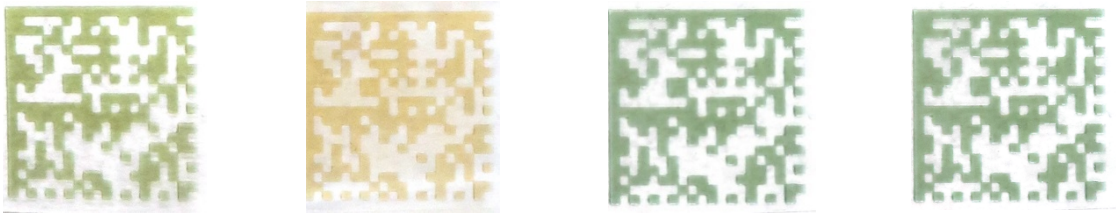

Code just packed in inert atmosphere | *Code the next morning in activated state* | *Code 3 minutes after opening of package* | *Code 50 minutes after opening of package*

Figure 8: Colour changing reaction of Data Matrix code printed using oxygen sensitive ink with cell sizes 1.50 mm, 10 layers

The Data Matrix codes were detected with Samsung Galaxy S7 mobile phone and Upcode code reader software. The codes printed with the green ink, 10 layers, were decodable down to cell size 0.5 mm. The codes printed with 5 layers were more challenging as the colour shade is rather pale.

4. Conclusions

Even if consumers are used to seeing and using 2D codes, they have often been disappointed with the content they can receive by reading the codes. They expect something more - high quality content that offers them additional value. In addition, consumers were also interested in the possibility of interactivity.

In this study, flexography printing was evaluated for its capability to print QR and Data Matrix codes with different functional inks. The concept has been proven to work when a thermochromic ink has been used. Usually, the package designers prefer small code sizes as the space available e.g. in labels is limited. In this study, the smallest cell size printed with a photochromic and with a oxygen sensitive ink was 0.25 mm, and the smallest cell size to be decoded reliably was 0.50 mm (occasionally 0.25 mm). This shows that functional inks have potential in being the initiators of a dynamic and context aware digital service.

From the technical viewpoint, the pilot testing was very successful and it was possible to create functional 2D codes as presented in the Owela stories. However, upscaling the concepts requires for collaboration between partners in the value network and possibly investments into present production systems.

Technology is available to produce novel services for consumers and stakeholders by utilising functional inks and combining them with digital solutions. However, the process of coming up with solutions that will enter the market is iterative, and potential users are involved in different phases. It is important to take into account how the services are communicated so that consumers understand the difference between traditional codes and functional ones, and also to realise the added value.

Acknowledgments

This work was supported by EU; the Tag It Smart project (Grant Agreement No 688061) is part of Horizon 2020 program. In the project, we have altogether 15 partners from Finland, Serbia, United Kingdom, France, Sweden, Romania, Netherlands, Italia, Austria and Spain. We want to thank all the partners for their co-operation during the project.

References

Friedrich, P., 2013. *Web-based co-design: Social media tools to enhance user-centred design and innovation processes*. Doctoral Dissertation, *VTT Science 34*. Aalto University School of Science.

Vehmas, K., Sipiläinen-Malm, T., Seisto, A., Smolander, M. and Majumdar, H., 2015. Co-innovating novel printed-electronic products. In: P. Gane, ed. *Advances in Printing and Media Technology: Proceedings of the 42nd International Research Conference of iarigai*. Helsinki, September 2015.

Hakola, L.; Hartman, J.; Honkapää, K.; Laakso, P.; Penttilä, R.; Pitkänen, M.; Rusko, E.; Sipiläinen-Malm, T. and Vanttaja, I., 2013. New methods for improving food product safety and communication. In: *Proceedings of 29th International conference on Digital Printing Technologies & Digital Fabrication*, NIP29. Seattle, USA, 29 September to 3 October 2013, pp. 498–502.

Hakola, L. and Linna, H., 2005. Detection of printed codes with a camera phone. In: N. Enlund and M. Lovreček, eds. *Advances in Printing and Media Technology: Proceedings of the 32nd International Research Conference of iarigai*. Porvoo, September 2005.

Influence of Drying Temperature on Morphology and Conductivity of Silver Conductive Tracks

Vincent Faure[1,2], *Aurore Denneulin*[1], *Yahya Rharbi*[2], *Albert Magnin*[2] *and Anne Blayo*[1]

[1] Univ. Grenoble Alpes, CNRS, Grenoble INP (Institute of Engineering), LGP2, F-38000 Grenoble, France
[2] Univ. Grenoble Alpes, CNRS, LRP, F-38000 Grenoble, France

E-mail: vincent.faure@lgp2.grenoble-inp.fr; anne.blayo@pagora.grenoble-inp.fr

Abstract

In the context of printed electronics, printing of homogeneous lines with a high conductivity is essential in order to ensure the electrical conduction. Inkjet printing is a direct writing process which offers the possibility to produce fine elements on a large variety of substrates. In inkjet process, lines printed with a silver-nanoparticles ink achieved the highest conductivity. However, the transversal profile of inkjet-line is truly impacted by flows occurring within lines during the ink drying. A flow is responsible for the well-known *coffee ring* effect: particles move from the center to the edge of lines. This effect results in a non-homogeneous profile and affects strongly the electrical conductivity of the printed patterns. In this work, inkjet printing of fine lines was performed by using a commercial silver-nanoparticles ink. A set of measures based on two geometrical indexes was defined to precisely characterize the particles distribution within dried printed lines. The line profile variations were monitored over different substrate temperatures. Correlations between transversal profile of printed lines and conductivity are suggested. An interpretation of profile differences as a function of temperature is proposed through the evolution of ink viscosity with the silver content. To the best of our knowledge, this is the first attempt of analysis conducted with a silver conductive inkjet ink at a picoliter scale.

Keywords: printed electronics, silver nanoparticles, inkjet printing process, lines morphology, conductive tracks

1. Introduction and background

Within the last 15 years, printed electronics appears as an attractive growing sector. The main benefits of printed electronics are: (i) the possibility to implement flexible substrates, (ii) the promise to achieve high productivity level with large area production and (iii) the reduction of production costs. Nowadays, numerous electrical devices can be printed: sensors (Paragua Macuri, 2016; Qin, et al., 2017; Zhang, et al., 2017), organic light emitted diodes (Verma, et al., 2016), photovoltaic cells (Thibert, et al., 2016), batteries (El Baradai, 2014), transistors (Cao, et al., 2016; Homenick, et al., 2016; Kim, et al., 2017; Sowade, et al., 2016) etc. In order to ensure the electrical connection of these different devices, the printing of conductive tracks with low resistances and homogeneous properties is crucial. In inkjet process, lines printed with a silver-nanoparticles ink achieved the highest conductivity: ~ 3.1×10^7 S/m (Kim and Moon, 2005)). Among printing processes, inkjet printing was identified as a promising and relevant technology for printed electronics (Chen, et al., 2015). It is a non-contact and direct writing process, with a large variety of printable substrates and the capacity to reproduce fine elements. Four phases need to be finely controlled in inkjet printing process to allow the production of precise and homogeneous patterns: (i) the droplet ejection, (ii) the droplet impact, (iii) its spreading on the substrate and (iv) the drying phase (Derby, 2010). For each phase, process parameters, ink physico-chemical properties and substrate properties are crucial criteria to consider. Up to now, conductive inkjet inks based on silver nanoparticles are those which provide the highest electrical conductivity, which explains their large implementation. However, like any colloidal suspen-

sions, silver nanoparticle inks are prone to *coffee ring* effect. This effect results from flows occurring within the droplets during the drying phase: particles move from the center to the edge of the droplet resulting in a non-homogeneous profile of drying droplets. This phenomenon is largely reported in literature at a microliter scale (Bhardwaj, et al., 2010; Hendarto and Gianchandani, 2013; Hu and Larson, 2002; Larson, 2014; Sefiane, 2013) but few data are available on the inkjet printing scale (i.e. the picoliter) (Soltman and Subramanian, 2008) and this is particularly true regarding conductive ink materials. This effect is all the more important to explore in the case of conductive patterns as the resulting non-homogeneous repartition of conductive material within the printed pattern may have a strong negative impact on electrical performances. The literature on microliter droplets suggests a temperature substrate conditioning in order to reduce the *coffee ring* effect thanks to Marangoni flow (Hendarto and Gianchandani, 2013; Hu and Larson, 2006; Larson, 2014). A first study was already conducted on the influence of substrate temperature on individual picoliter inkjet printed droplet profile (Faure, et al., 2016). It was shown that c*offee ring* effect increased with increasing temperature, which confirmed the results of Soltman and Subramanian (2008). Those results imply that Marangoni flow does not occur in picoliter droplets, contrary to microliter droplets. In addition, Faure, et al. (2016) showed that lines and droplets profiles do not follow the same tendency with the substrate temperature because of their different geometries (disc shape for droplet and rectangular shape for lines). In the present paper, the evolution of *coffee ring* effect on printed lines with the substrate temperature will be explored through the following strategy:

i. The first part of the study focuses on the morphology analysis of inkjet-printed lines on a polymer film conditioned at different temperatures;
ii. The second part of the study deals with the conductivity of printed line depending on their profiles;
iii. The third part of this study concentrates on the effect of viscosity on the flow within lines and the effect on the morphology.

2. Materials and methods

2.1 Silver nanoparticles inkjet ink and printing process

A commercially available silver-nanoparticles inkjet inks (Tradename: Sicrys™ I30G-1) was purchased from PvNanoCell Ltd. The ink is composed of ethylene glycol as solvent and contains spherical silver nanoparticles as conductive fillers (a mass fraction of 30 %, D50 = 70 nm, D90 = 115 nm, density = 1.81 $g \cdot cm^{-3}$). It consists in a light grey suspension which presents a nearly Newtonian behavior with a viscosity of 26.3 $mPa \cdot s$ and a surface tension of 46.3 $mN \cdot m^{-1}$ at 20 °C. The ink was agitated on a roller apparatus during one hour and then filtered through a 0.45 µm syringe filter before printing.

A laboratory piezoelectric inkjet printing machine (Fujifilm – Dimatix DMP 2831 with 10 pL nominal drop size cartridge) was used for this study. It allows the loading of disposable piezoelectric inkjet print heads including 16 nozzles measuring 21.5 µm each (square shape) and distanced 254 µm from each other. Printing parameters such as drop spacing, nozzle temperature and print height, as well as ejection parameters (voltage and waveform design) were optimized in preliminary adjustments. The resulting print quality is strongly dependent on those printing parameters given in Table 1. In order to achieve comparable line profiles, lines with one drop width were printed with a unique active nozzle, lines with two drops width were printed with two active nozzles and lines with five drops width were printed with five active nozzles. Therefore, the time needed to print a pattern remains equivalent whatever the line width. To print lines, the drop spacing was set at 20 µm (distance between two subsequent droplet centers, see Figure 1). As the average droplet diameter after printing on the substrate was estimated by microscopy observation to be 40 µm, an overlapping of droplets occurs, as illustrated in Figure 1.

A substrate matching the typical requirements of printed electronics, i.e. a substrate presenting a smooth and closed surface with a relatively high dimensional stability over temperature was selected for this study. A polyethylene naphthalate (PEN) film (tradename: TEONEX® – 125 µm) was purchased from Dupont Teijin Film. The selected substrate has a surface energy of 40.2 $mJ \cdot m^{-2}$, an average surface roughness R_a of 4.3 nm and a coefficient of dimensional stability of 0.09 % at 150 °C.

A specific drying protocol was established to allow the monitoring of line profile over drying conditions:

i. First, the substrate was heated thanks to a Peltier plate from 30 °C to 120 °C during 20 minutes;
ii. Droplets were then ejected according to the parameters described in Table 1;
iii. Samples were maintained after printing on the Peltier plate during 20 min. This time scale was determined to be sufficient to allow the suspended particles movement induced by the drying flows. The complete drying of the line was checked thanks to an 'absorption method': a blotting paper was applied onto the printed lines during few seconds to check the drying progress (if ink traces appear on the wipe, the sample was considered as partially dried whereas a clean wipe indicates a sample completely dried);
iv. Printed substrates were put in an oven at 150 °C during 1 hour in order to ensure the silver nanoparticles sintering and to minimize the impact induced by the substrate temperature conditioning (protocol phase (i) and (iii)) on the resulting conductivity.

Table 1: Inkjet printing and drying parameters

Voltage applied	20 V
Inkjet head temperature	35 °C
Substrate (Peltier plate) temperature	30 °C to 120 °C
Gap between two droplets for lines printing	20 µm
Drying protocol	20 minutes on the Peltier plate + 1 hour at 150°C in an oven

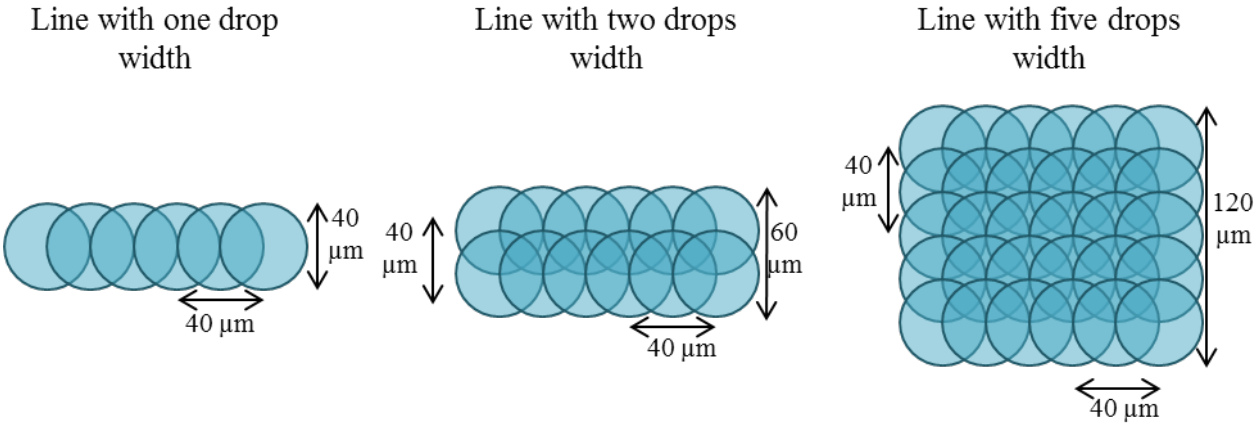

Figure 1: Overlapping of droplets composing a line with one and two drops width

2.2 Morphological characterization of droplets

3D profiles of lines were obtained with a focus variation optical microscope (Alicona InfiniteFocus). 3D data were collected by using a focus variation microscopy technology illuminated with a specular reflection lighting mode. To visualize the morphology of printed patterns, a magnification of 100 × was selected for printed lines.

In order to characterize and compare droplet profiles, two indexes were specifically defined for this study:

$R_{c/e}$ was defined as the amplitude ratio between the droplet center and edge (Figure 2a).

$$R_{c/e} = 100 \cdot \frac{h_c}{h_e} \quad [1]$$

with h_c the height at the center of the drop
h_e the height at the drop edge

For each drying configuration, $R_{c/e}$ was averaged on fifteen profiles (three lines with five different profiles).

$R_{0.5}$ was defined as the radial distance delimitating a distribution of 50 % of material. $R_{0.5}$ corresponds to the position from the droplet center where there is the same quantity of matter before and after this position. For each characterized droplet, the $R_{0.5}$ index was averaged on thirty-six droplet profiles captured every 10°. Each droplet profile was normalized so that the center of the drop became the origin and the droplet radius was equal to 1. A Matlab program was developed to determine the radial position corresponding to the half of the profile area (Figure 2b).

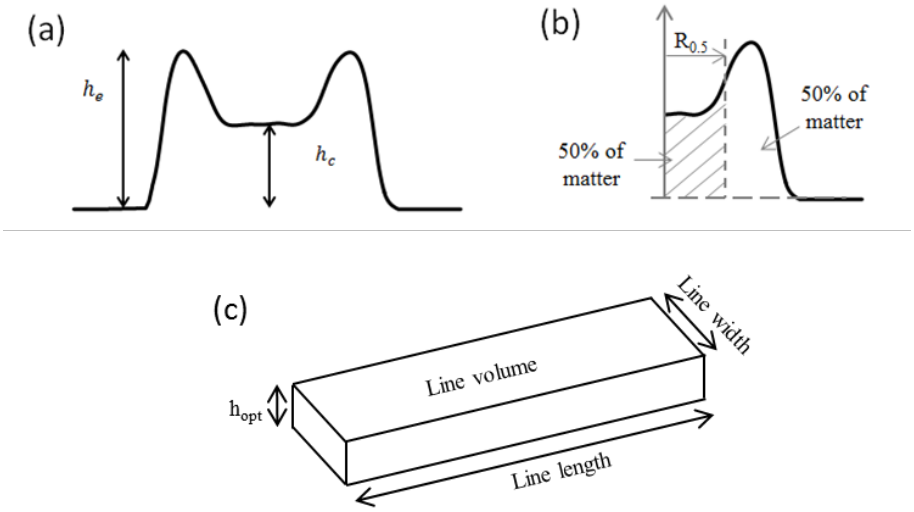

Figure 2: Schematic representation of geometrical indexes: (a) Ratio center/side, (b) $R_{0.5}$, (c) h_{opt}

2.3 Electrical characterization of tracks

The electrical resistance (R) of conductive lines was measured by using a multimeter (Hewlett Packard 34401A) with a 2 mm screw banana plug. Measurements were performed on conductive tracks having a length of 1 cm. The resistance is transformed into conductivity with the following formula:

$$\sigma = \frac{l}{R \cdot S} \quad [2]$$

with σ the conductivity of dried ink
R the resistance measured
S the cross-sectional area of the track and l the length of the track. The cross-sectional area was measured by calculating the dry-weight of printed droplets divided by the line width.

2.4 Rheological characterization of ink

In order to measure the viscosity as a function of silver content, a DHR3 rheometer (TA instrument) was used with cone/plate geometry of 25 mm, 1°. The ink was heated on a heating plate at 30 °C with agitation to evaporate the solvent. A sample of ink was regularly removed to measure the viscosity and another sample was used to measure the silver content by weighting the dry mass. The viscosity was measured at a shear rate of 1 s^{-1}.

3. Results and discussion

3.1 Influence of substrate temperature on line profile

Inkjet printing is constituted of four phases: ejection, impact, spreading and drying. During the last phase, silver nanoparticles contained in the ink move inside the droplet. At the end of drying, most particles are accumulated at the periphery of the deposit. This effect called *coffee ring* was first described on a sessile drop by Deegan, et al. (1997). It is induced by the combination of two phenomena: (i) solvent evaporation is more important at the edge of drops and (ii) the surface contact area between ink and substrate is pinned down as the major part of the drying. A flow takes place to compensate the solvent removal by evaporation at the edge of droplet. The solvent can be totally or partially transferred to the contact line by this flow and which generates a ring shape to the dried droplet. In the case of lines, droplets bond together and change the ring shape of *coffee ring* to a channel shape. The particles flow occurring during the drying depends on evaporation speed which depends on the ink temperature. 2D profiles of silver lines dried at different temperatures are shown Figure 3. Variations in silver particles distribution as a function of printed substrate temperature are observed. With substrate temperature rising from 20 °C to 90 °C, the channel shape induced by the *coffee ring* effect becomes more and more accentuated. For these temperature levels, most particles are located at the droplet edge while a very fine thickness of particles remains in the droplet center area. From 100 °C to 120 °C, the line edge width decreases whereas the center height slightly increases. In contrast, the line profile at 20 °C is homogeneous and does not present the channel-shape.

Similarly to the droplet profile analysis, different indexes were defined to characterize and compare the particle distribution within the different printed lines. As line profiles are channel-shaped, the ratio between heights at the line center and edge $R_{c/e}$ appears relevant for quantify c*offee ring* effect. The evolution of $R_{c/e}$ as a function of substrate temperature is shown in Figure 4a. Theoretically, the closer the index gets to 100 %, the more homogeneous the repartition of nanoparticles within the droplet. As expected, $R_{c/e}$ decreases between 20 °C and 100 °C and rises for temperature ranging from 100 °C to 120 °C. $R_{c/e}$ is much higher at 20 °C (between 40 % and 80 %) than at other temperatures. However, $R_{c/e}$ does not take into account the droplet edge widening. $R_{c/e}$ alone is inadequate to qualify the droplet morphology. $R_{0.5}$, which corresponds to the radial distance delimitating a distribution of 50 % of material, was used to take into account the droplet edge widening. Theoretically, $R_{0.5}$ value approximate 100 % when all the particles are located at the droplet edge and 0 % when all particles are located at the droplet center. The evolution of $R_{0.5}$ with the substrate temperature is given in Figure 4b. $R_{0.5}$ is close to 50 % for lines printed on a substrate at 20 °C. For one drop width line, this value increases to 70 % when the temperature increases until 90 °C. In the case of two drops width line, the same evolution occurs to 100 °C. Above these temperatures, $R_{0.5}$ decreases to 60 % for the both type of lines. This reflects that for this range of temperature, more and more particles stay at the center of the lines.

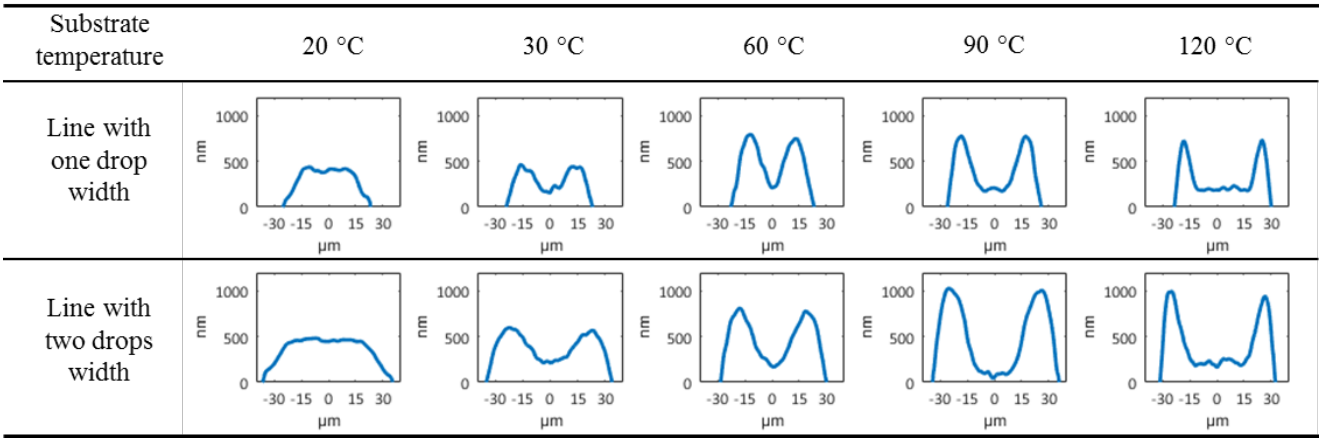

Figure 3: 2D profiles printed lines on PEN at different substrate temperature; 2D profiles are one of the numerous profile constituent droplets in this temperature

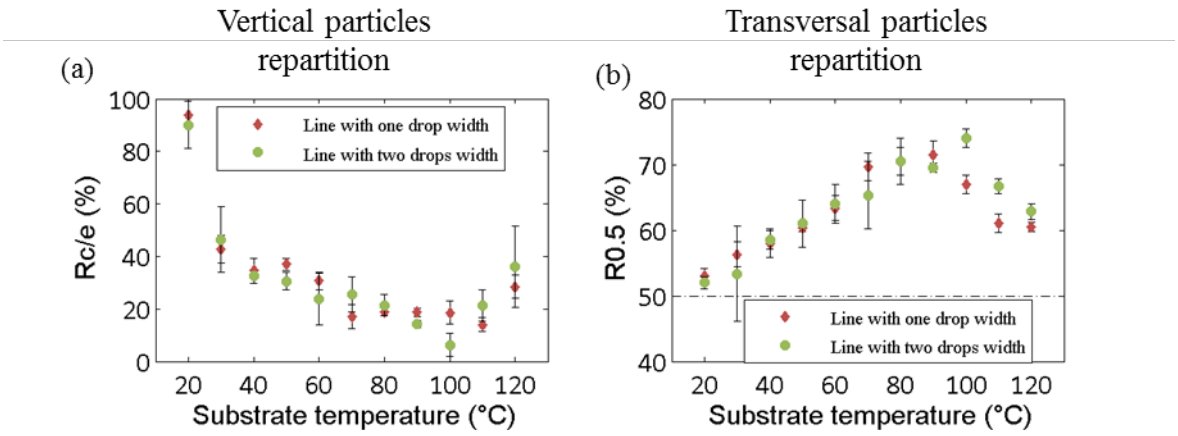

Figure 4: Evolution between (a) $R_{c/e}$, (b) $R_{0.5}$ with temperature substrate

3.2 Influence of the line profile on the conductivity

Line morphology appears to have a strong influence on line conductivity. In this work, the particles distribution evolution is due to a variation of the substrate temperature. As conductivity is directly impacted by the conditions of the sintering step, the substrate temperature conditioning may interfere and impact the resulting conductivity independently to the particles distribution. A protocol minimizing the influence of this perturbation was therefore established. In order to compare the influence of the width of the line, three types of lines were printed: lines with one, two and five drops width which correspond to widths of 40 µm, 60 µm and 120 µm respectively. For each substrate temperature except 20 °C, the line conductivity increases with the width. For the thinnest line (40 µm), the conductivity at 20 °C is higher than for the same line at the other temperatures. In addition, this line is more conductive than 60 µm lines whatever the substrate temperature. Thus, line profiles truly impact the line conductivity because the only important change between 20 °C and other temperatures is the line profile. This allows to achieve the same conductivity with one drop width line than five drops width line with five times less printed ink (Figure 5).

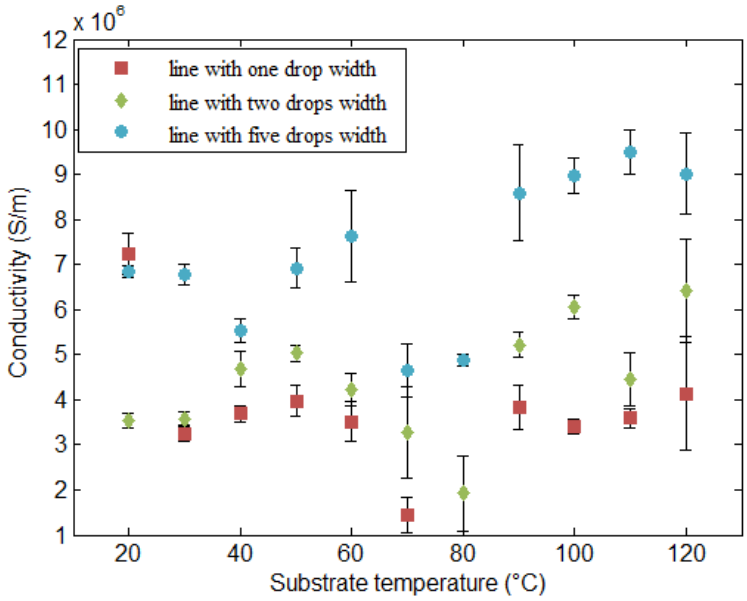

Figure 5: Electrical conductivity of printed lines as a function of substrate temperature

3.3 Rheological properties of the ink influence the profile

The line profile depends on the circulation flow inside the droplet during the evaporation. The intensity of this flow depends on the speed of evaporation and can be restricted by the ink viscosity. The viscosity depends on the temperature and the silver content. The substrate temperature defines the viscosity at the beginning of drying and the evaporation speed whereas silver content characterizes the evolution of the viscosity during drying. In this part, only the viscosity evolution all along the drying will be studied. During the line drying, the silver concentration increases with the solvent evaporation, modifying the ink viscosity. The influence of silver concentration on the viscosity in presented in Figure 6. The viscosity follows a Krieger-Dougherty law:

$$\eta = \eta_s(1 - \phi/\phi_m)^{-[\eta]\phi_m} \qquad [2]$$

with η the ink viscosity (Pa·s)
η_s the solvent viscosity (Pa·s) (= 1.61×10^{-2} Pa·s, for this ink)
Φ the volume concentration (a volume fraction in %)
Φ_m the maximum packing fraction (a volume fraction in %)
$[\eta]$ the intrinsic viscosity (ø)

The best fitting between the experimental result and the law is done for a maximum packing fraction of 61 % and an intrinsic viscosity of 7. Beyond, the suspension has the behavior of a gel with a yield stress.

The viscosity increases with the silver content. The higher the temperature, the faster the evaporation is and the faster the silver content increases. This explains why between 100 °C and 120 °C, line edge widths decrease whereas the center heights slightly increase: particles move quickly at the first time of the drying due to the fast evaporation. A first accentuated edge is formed. However, after the evaporation of a quantity of solvent, the viscosity increases and does not allow particles to move within lines. Future work will be focused on the influence of the viscosity at the beginning of the drying and the quantification of the impact of the evaporation speed on the viscosity.

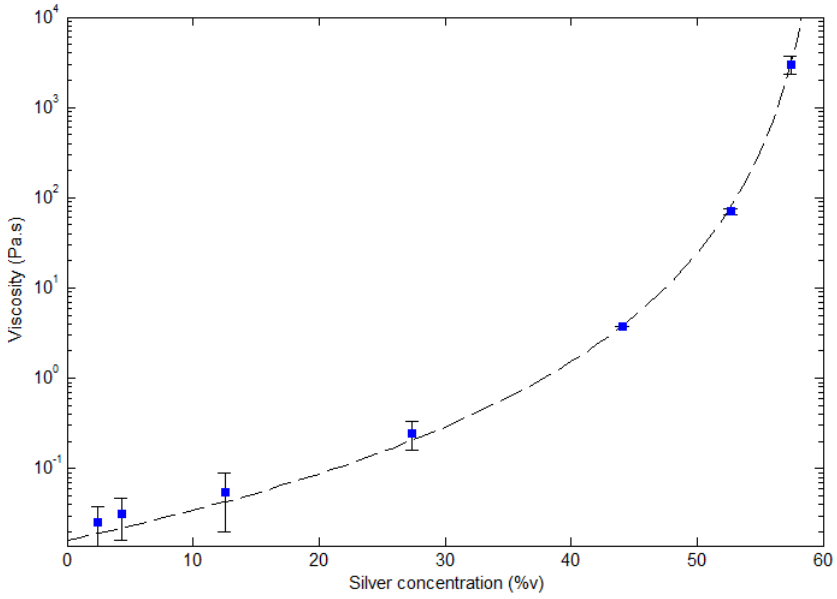

Figure 6: Ink viscosity as a function of silver volume concentration at 30 °C; the blue squares represent the measured viscosity, and the dotted-line represents the fitting with following parameters: intrinsic viscosity = 7, maximum packing fraction = 61 %

4. Conclusion

Inkjet printing process is a relevant technology to print conductive tracks. Inkjet process was used in this work to eject a commercial conductive ink composed of silver nanoparticles in order to print lines on substrate at different temperatures. A combination of two indexes specifically designed for this study was set up in order to quantify and compare the particles distribution within dried lines. Two trends were observed: first, an accentuation of line profile with the increase of temperature, and above 100 °C, a decrease of the line edge width whereas the center height slightly increases. An optimal temperature was found to avoid the *coffee ring* effect. Conductivity measurements were performed on printed lines and showed that the profile homogeneity is a crucial parameter for fine lines. An explanation of the evolution of line profile between 100 °C and 120 °C was given thanks to the quick increase of viscosity with the silver content: particles do not move quickly at the first time of evaporation, but when the viscosity increases particles do not move anymore within lines. Our future works will focus on a more thorough understanding of the flows occurring within the individual droplets and lines during the drying step to find potential solutions to reduce the *coffee ring* effect.

Acknowledgments

LGP2 is part of the LabEx Tec 21 (Investissements d'Avenir – grant agreement n°ANR-11-LABX-0030) and of the Energies du Futur and PolyNat Carnot Institutes. This research was made possible thanks to the facilities of the TecLiCell platform funded by the Région Rhône-Alpes (ERDF: European regional development fund). The Laboratoire Rhéologie et Procédés is part of the Labex Tec 21 (Investissement d'Avenir – grant agreement n° ANR-11-LABX-0033) and of the Polynat Carnot Institut (Investissement d'Avenir – grant agreement n°ANR-11-CARN-030-01)

References

Bhardwaj, R., Fang, X., Somasundaran, P. and Attinger, D., 2010. Self-assembly of colloidal particles from evaporating droplets: role of DLVO interactions and proposition of a phase diagram. *Langmuir,* 26(11), pp. 7833–7842.

Cao, X., Lau, C., Liu, Y., Wu, F., Gui, H., Liu, Q., Ma, Y., Wan, H., Amer, M.R. and Zhou, C., 2016. Fully screen-printed, large-area, and flexible active-matrix electrochromic displays using carbon nanotube thin-film transistors. *ACS Nano,* 10(11), pp. 9816–9822.

Chen, S.-P., Chiu, H.-L., Wang, P.-H. and Liao, Y.-C., 2015. Inkjet printed conductive tracks for printed electronics. *ECS Journal of Solid State Science and Technology*, 4(4), pp. 3026–P3033.

Deegan, R.D., Bakajin, O., Dupont, T.F., Huber, G., Nagel, S.R and Witten, T.A., 1997. Capillary flow as the cause of ring stains from dried liquid drops. *Nature,* 389, pp. 827–829.

Derby, B., 2010. Inkjet Printing of Functional and Structural Materials: Fluid Property Requirements, Feature Stability, and Resolution. *Annual Review of Materials Res*earch, 40, pp. 395–414.

El Baradai, O., 2014. Réalisation d'lectrodes souples pour batteries lithium-ion par procédé d'impression. Other. Université de Grenoble. *NNT : 2014 GRENI036.*

Faure, V., Denneulin, A., Rharbi, Y., Magnin, A. and Blayo, A., 2016. Influence of drying temperature on inkjet printed droplets and lines morphology by using silver nanoparticles based ink: relation with electrical performances. In: P. Gane, ed. *Advances in Printing and Media Technology: Proceedings of the 43rd International Research Conference of iarigai*. Toronto, Canada, August 2016. Darmstadt: iarigai.

Hendarto, E. and Gianchandani, Y.B., 2013. Size sorting of floating spheres based on Marangoni forces in evaporating droplets. *Journal of Micromechanics and Microengineering,* 23(7): 075016.

Homenick, C.M., James, R., Lopinski, G.P., Dunford, J., Sun, J., Park, H., Jung, Y., Cho, G. and Malenfant, P.R., 2016. Fully printed and encapsulated SWCNT-based thin film transistors via a combination of R2R gravure and inkjet printing. *ACS Applied Materials and Interfaces,* 8(41), pp. 27900–27910.

Hu, H. and Larson, R.G., 2002. Evaporation of a sessile droplet on a substrate. *The Journal of Physical Chemistry B,* 106(6), pp. 1334–1344.

Hu, H. and Larson, R.G., 2006. Marangoni effect reverses coffee-ring depositions. *The Journal of Physical Chemistry B,* 110(14), pp. 7090–7094.

Kim, D. and Moon, J., 2005. Highly conductive ink jet printed films of nanosilver particles for printable electronics. *Electrochemical and Solid-State Letters,* 8(11), pp. J30–J33.

Kim, J., Hassinen, T., Lee, W.H. and Ko, S., 2017. Fully solution-processed organic thin-film transistors by consecutive roll-to-roll gravure printing. *Organic Electron*ics, 42, pp. 361–366.

Larson, R.G., 2014. Transport and deposition patterns in drying sessile droplets. *AIChE J*ournal, 60(5), pp. 1538–1571.

Paragua Macuri, C.A., 2016. *Conception de capterus de gaz radiofréquences à base de nanotubes de carbone et imprimés par jet d'encre.* Doctoral Thesis. Université de Limoges.

Qin, H., Cai, Y., Dong, J. and Lee, Y.-S., 2017. Direct printing of capacitive touch sensors on flexible substrates by additive e-jet printing with silver nanoinks. *Journal of Manufacturing Science and Engineering,* 139(3), p. 031011–1.

Sefiane, K., 2013. Patterns from drying drops. *Advanced Colloid Interface Science*, 206, pp. 372-381.

Soltman, D. and Subramanian, V., 2008. Inkjet-printed line morphologies and temperature control of the coffee ring effect. *Langmuir,* 24(5), pp. 2224–2231.

Sowade, E., Mitra, K.Y., Ramon, E., Martinez-Domingo, C., Villani, F., Loffredo, F., Gomes, H.L. and Baumann, R.R., 2016. Up-scaling of the manufacturing of all-inkjet-printed organic thin-film transistors: device performance and manufacturing yield of transistor arrays. *Organic Electronics,* 30, pp. 237–246.

Thibert, S., Jourdan, J., Bechevet, B., Mialon, S., Chaussy, D., Reverdy-Bruas, N. and Beneventi, D., 2016. Study of the high throughput flexographic process for silicon solar cell metallisation. *Progress in Photovoltaics: Research and Application,* 24, pp. 240–252.

Verma, A., Zink, D.M., Fléchon, C., Leganés Carballo, J., Flügge, H., Navarro, J.M., Baumann, T. and Volz, D., 2016. Efficient, inkjet-printed TADF-OLEDs with an ultra-soluble NHetPHOS complex. *Applied Physics A,* 122:191.

Zhang, Y., Anderson, N., Bland, S., Nutt, S., Jursich, G. and Joshi, S., 2017. All-printed strain sensors: building blocks of the aircraft structural health monitoring system. *Sensors and Actuators, A: Physical,* 253, pp. 165–172.

Inkjet-fabricated Coated Reaction Platform for Colorimetric Glucose Detection

Eveliina Jutila[1], *Risto Koivunen*[1], *Roger Bollström*[2] *and Patrick Gane*[1,2]

[1] Aalto University, School of Chemical Engineering, Department of Bioproducts and Biosystems, FI-00076 Aalto, Helsinki, Finland
[2] Omya International AG, Baslerstrasse 42, CH-4665 Oftringen, Switzerland

E-mail: eveliina.jutila@aalto.fi; risto.koivunen@aalto.fi; roger.bollstroem@omya.com; patrick.gane@omya.com

Abstract

Microfluidic paper-based analytical devices (μPADs) provide a simple and low-cost platform for colorimetric glucose assays based on an enzymatic reaction. Most assays utilise filter paper-based reaction platforms, though coated platforms may enable fabrication of even smaller devices and thus lower liquid volumes and increased spatial resolution. In this study, we present a coated microfluidic reaction platform designed for colorimetric detection of glucose, which has been fabricated utilising speciality coated substrates and inkjet printing. The preliminary results show that glucose oxidation takes place on the coated substrates. The glucose assay, nonetheless, can be used to verify the performance of a coated reaction platform, after which the platform could be adapted for detection of other analytes. Evidence is collected to aid future optimisation of the coating formulation, pattern design, reagent application method, preservation of enzyme activity, colorimetric detection improvement to overcome high light scattering, which reduces colour intensity, and defining the detectable glucose range.

Keywords: microfluidics, paper-based device, coated reaction platform, colorimetric detection

1. Introduction and background

Microfluidic paper-based analytical devices (μPADs) represent one of the most promising future applications in functional printing and contribute to a fast-growing new field of biosensors in analytical chemistry. Print-patterned paper consisting of millimetre-sized hydrophobically walled channels offers a small, simple, low-cost, portable and self-standing platform for bioassays (Martinez, et al., 2007). Paper, as a material also offers many other advantages for microfluidics offering high surface-to-volume ratio enabling a greater capacity for bound analytes (for reaction and detection), and the ability to keep reagents active within the fluidised fibre network. Furthermore, the white background is particularly suitable for colorimetric detection (Cate, et al., 2015; Martinez, 2010). The majority of the researchers utilise uncoated cellulose-based filter papers (Yang, et al., 2017), though some researchers have also tested coated paper (Määttänen, et al., 2011; Zhong, Wang, and Huang, 2012). Coated substrates may offer cost savings and extended application for rare analytes compared to filter paper due to decreased reagent and sample volumes and smaller device designs enabled by thin coating layers providing increased spatial resolution. A disadvantage to be overcome can be that the micropores, needed for liquid wicking, in turn lead to high light scattering of the coating, thus creating background "white noise", which reduces the intensity of the colour detection signal thus making colorimetric detection more challenging, so requiring suitable light filter design.

Glucose assays are one of the most common applications of biosensors, because of their relevance to the diagnosis and care of diabetes (Yun, et al., 2011), which is a worldwide pandemic and one of the leading causes of death (WHO, 2016). Laboratory analysis is the most accurate method for monitoring glucose levels, but point-of-care (POC) devices provide a more convenient and low-cost solution for diabetics. There

is a need for a more rapid, reliable, accurate, compact and simple tool for glucose sensing, especially for the developing world (Yoo and Lee, 2010). Glucose assays are based on the oxidation of glucose to gluconic acid and hydrogen peroxide (H_2O_2), catalysed by glucose oxidase (GOx), and the subsequent reduction of hydrogen peroxide to water by horseradish peroxide (HRP) and oxidation of iodide to iodine. As a result, the initially colourless test sample changes to brown depending on glucose content. (Martinez, et al., 2008; Peele Jr, Gadsden and Crews, 1977).

The hydrophobic barrier regions of the first paper-based glucose assay were fabricated using photolithography together with SU-8 photoresist (Martinez, et al., 2007). However, since photolithography is expensive and time consuming (Martinez, et al., 2008; Cai, et al., 2014), other patterning techniques have been used to pattern glucose assays, including flexography (Olkkonen, Lehtinen and Erho, 2010; Määttänen, et al., 2011), wax printing (Sechi, et al., 2013; Jeong, et al., 2015) and chemical patterning (Cai, et al., 2014). Screen printing (Sameenoi, et al., 2014), plasma treatment (Li, et al., 2008; 2010) and inkjet printing (Li, et al., 2010) have also been used for fabrication of paper-based microfluidic devices. Inkjet printing allows a simple fabrication of a complete sensor in one printing process, utilising only two steps, i.e. printing of channel patterns and biomolecules, and the printed pattern can be easily varied electronically (Li, et al., 2010). Inkjet also enables low-cost mass production of microfluidic devices (Jenkins, et al., 2015).

In previous research, the reagents have been applied by spotting (Cai, et al., 2014; Martinez, et al., 2007; 2008; Olkkonen, Lehtinen and Erho, 2010), screen printing (Määttänen, et al., 2011) and inkjet printing (Di Risio and Yan, 2007; Hakola and Lehtinen, 2014; Wang, Cook and Derby, 2008; 2009; Wang, et al., 2012; Yun, et al., 2011). Inkjet printing provides the most precise method to apply small volumes of reagents to the assays in the picolitre range, compared to the larger microlitre or nanolitre volume range achieved by spotting or screen printing (Wang, Cook and Derby,2008; 2009). Furthermore, the high viscosity paste ink used in screen printing sets a limitation in resolution (Yun, et al., 2011). Inkjet printing provides a non-contact deposition method with lower ink consumption, higher resolution and smaller dot sizes making it more suitable for mass production of biosensors than screen printing (Wang, et al., 2012).

Several researchers including Wang, Cook and Derby (2008; 2009) and Yun, et al. (2011) have successfully demonstrated that inkjet technology is suitable for printing low-cost glucose sensors, though increased actuation volumes may decrease the activity of GOx by approximately 30 % (Cook, Wang and Derby, 2010). The damage is probably caused by the rapid compression the solution faces during printing, and the problem can be overcome with the addition of trehalose, a naturally occurring alpha-linked disaccharide constructed from an α,α-1,1-glucoside bond between two α-glucose units (Nishioka, Markey and Holloway, 2004). In addition to trehalose (Martinez, et al., 2008), polyvinyl alcohol (PVOH) has also been used to increase the long-term stability of GOx (Olkkonen, Lehtinen and Erho, 2010) in paper-based assays. Viscosity modifiers typically used in commercial inks have been found to decrease the activity of HRP, though alternative modifiers such as carboxymethyl cellulose (CMC) can be used to increase the ink viscosity without impairing the HRP activity (Di Risio and Yan, 2007).

In this paper, we introduce a speciality porous pigment-based coating used to form an inkjet printed microfluidic reaction platform designed for colorimetric detection of glucose by enzymatic reaction. The results are analysed and evaluated to provide a forward path for further optimisation.

2. Materials and methods

The materials used in the coating formulation, the hydrophobic ink and the glucose assay reagents, the pattern designing process and the preliminary protocol for glucose tests are described in the following sections.

2.1 Coating materials and formulations

The chosen coating pigment is a highly porous form of pharmaceutical grade functionalised calcium carbonate (FCC) provided by Omya International AG, Oftringen, Switzerland, in which the functionalisation consists of a shell-core structure of hydroxyapatite and calcium carbonate, respectively. A commercially available micro-fibrillated cellulose (MFC A), Arbocel MF-40-7 (J. Rettenmaier and Söhne GmbH + Co KG, Rosenberg, Germany) was used as a binder. A coating consisting of 100 pph (by weight) FCC and 5 pph of MFC A, having a solids content of 16.4 %, coat weight of 37.1 g·m^{-2} and thickness of 102 µm, was used in the preliminary tests. The FCC based coating provides a discretely separable bimodal pore size distribution, containing the pore space between the FCC particles, which controls the permeability, and the finer pore space inside the FCC particle pores, which provide the necessary high capillarity. This differs from the standard monomodal size distribution of dispersed non-porous particles as found in typical paper coatings. Full descriptions of the coating structure can be found in publication by Jutila, et al. (2016).

Sheets of impermeable SuperYUPO® (Yupo Corporation), known formerly as Synteape®, a pigment filled polypropylene film of 80 µm thickness and 62 g·m^{-2} basis weight, were used as a base substrate for the coatings. Coating colours were applied with a K202 Control Coater (RK PrintCoat Instruments Ltd.) employing a spiral wire-wound rod, applying a 150 µm thick wet layer at a coating speed of 6 m·min^{-1}. The coatings were allowed to dry freely in the laboratory atmosphere. Two commercially available filter papers, VWR grade 415 filter paper (VWR, Vienna Austria) and Whatman 4 filter paper (GE Healthcare), were used as reference materials.

2.2 Functional inks and printing

A functional hydrophobising ink was prepared using the sizing agent alkyl ketene dimer (AKD), Basoplast 88 (BASF, Ludwigshafen, Germany), dissolved in p-xylene solvent (VWR, Vienna, Austria, product code 28984.292). The AKD ink was coloured with Blue 807 dye (Kremer Pigmente GmbH, and Co. KG, Aichstetten, Germany, product number 94030) to enable clear visibility of the ink-applied areas. The inks were printed with a DMP-2831 research inkjet printer (Fujifilm Dimatix, Santa Clara, USA) employing DMC-11610 ink cartridges with ten picolitre nominal drop volume. The ink preparation process and printing details are described further in publications by Koivunen, Jutila and Gane (2015) and Koivunen, et al. (2015; 2016).

2.3 Glucose assay reagents

The glucose oxidase/peroxide (GOx/HRP) reagent consisting of 500 units of GOx (*Aspergillus niger*), 100 purpurogallin units of HRP, where 1 purpurogallin unit will form 1 mg of purpurogallin from pyrogallol following the reaction

$$2\text{Purpurogallol} + 3\text{H}_2\text{O}_2 \xrightarrow{\text{peroxidase}} \text{Purpurogallin} + 5\text{H}_2\text{O} + \text{CO}_2 \qquad [1]$$

and buffer salts containing sodium and potassium ions (product no. G3660), D-(+)-glucose (product no. G5767) and trehalose (product no. PHR1344) were purchased from Sigma-Aldrich. Potassium iodide (product code 26843.361) was purchased from VWR. The reagents and the glucose were diluted with distilled water.

2.4 Pattern design

Figure 1 shows the designs used in the preliminary glucose tests. The patterns were printed onto the coated substrate such that the aqueous test liquid is contained within the pattern by the surrounding hydro-

phobic printed barrier region. The assay consists of two reaction areas where the reagents are applied and a sample application area where the glucose solution is applied. The glucose solution wicks along the 3 mm wide channel to the reaction areas, where the colour change occurs as the reaction takes place. These preliminary designs enable spotting of reagents with a pipette.

The reagents can, in principle, also be printed by inkjet or spotted using a calibrated micro or nanolitre dispenser, and designs with narrower and shorter channels can be fabricated to optimise volumes needed. These initial designs, however, enable replicate testing, and could be extended to a radial "flower-like" pattern, such as that exemplified by Olkkonen, Lehtinen and Erho (2010), to test multiple replicas simultaneously.

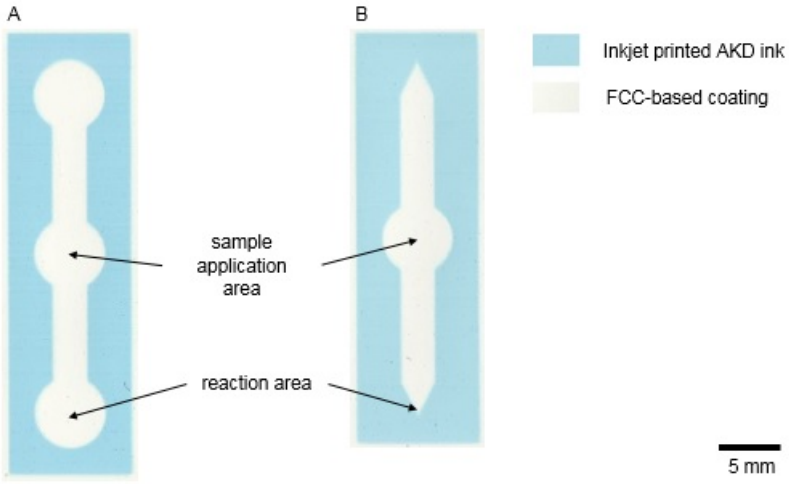

Figure 1: Preliminary glucose assay designs: A ring-detection, and B arrowhead-detection design in which the surrounding barrier is inkjet printed using AKD hydrophobising ink, leaving the inner area as original coating

2.5 Glucose tests

The following glucose tests were performed by pipetting 1 µl of 0.6 M potassium iodide to the reaction area of design A. In the first series of tests, after the potassium iodide had dried for 5 min, 1 µl of GOx/HRP (15 units of protein per ml of solution) was applied to the same spot, after which 15 µl of the respective test glucose solution (glucose concentration range spanning 0, 2.5, 5, 10, 50 and 500 mM) was pipetted into the sample application area. The second test series was performed by adding GOx/HRP either immediately after the potassium iodide or as a 1:1 mixture with the iodide. In the third test series, the sample was stored in a fridge overnight before the respective glucose solutions were added to the samples.

The fourth series of tests were performed by pipetting 0.5 µl of a 1:1 mixture of 0.6 M potassium iodide and GOx/HRP (15 units of protein per ml of solution) to the tip of the arrowhead, design B. The sample was allowed to dry for a couple of minutes before 10 µl of the respective glucose solution (once again spanning the concentration range 0, 2.5, 5, 10, 50 and 500 mM) was pipetted into the sample application area.

The colour change was observed qualitatively in both pattern designs.

3. Results and discussion

The findings from the experimental procedures are reported here, beginning with discussion regarding the important features of the pattern design and the preliminary and future potential optimisation options of the glucose tests.

3.1 Pattern design

The current pattern designs are suitable for experiments in which the reagents are pipetted by hand, though we aim to fabricate smaller assays in the future. The main factors influencing the fabrication include the coating formulation and properties such as the thickness and evenness of the coating layer. Currently, channels with a width of approximately 500 μm can be printed using inkjet and AKD ink (Koivunen, et al., 2016).

Two primary aspects of the designs must be considered, firstly the ease of reagent application and secondly the ease of assay in respect to colour generation.

The experiments showed that design A might be better than design B in regard to reagent application. When the reagents are applied to the ring-reaction area (design A) they spread evenly without wicking into the channel. A lower volume of the reagents had to be applied to the arrowhead-reaction area to avoid spreading which could not be completely avoided, as can be seen in Figure 4. Furthermore, the surface tension of the reagent solution complicated the reagent application. In future tests, microcapillary tubes could be used to apply the reagents more precisely.

The shape of the reaction area affects the concentration of the colour front. In design A the brown colour forms a coffee ring appearance, since the enzyme solution migrates and concentrates to the "outer ring" limits as the water evaporates (Deegan, et al., 1997; Jutila, Koivunen and Gane, 2015; Wang, et al., 2012). In design B, the colour concentrates toward the tip of the arrowhead. The arrowhead design might, therefore, be better suited for the assay, despite its more challenging aspects for reagent application, because it ensures that all the reagents are concentrated in the same spot.

More testing is needed to determine the optimal design.

3.2 Glucose assays

The first tests, in which potassium iodide and GOx/HRP were allowed to dry in between each component application on the filter papers, showed that the colour change did not occur even after 30 min following glucose addition. Thus, it became questionable as to whether the enzyme remained active using this inter-drying construction. For the two tests, however, in which the reagents and glucose were applied on top of each other without drying periods, when performed on the two different filter papers using 500 mM glucose solution, it was clearly observed that the enzymes were indeed active, suggesting that the reagents might need to be added right after each other or together as a mixture. Both of these approaches were then tested on the coated design A with success, showing that the inter-drying construction was not detrimental when used with the coating. However, no colour change was observed after the samples had been stored in the fridge overnight before glucose addition. The same storage test procedure was repeated for the agent treated filter papers by storing the samples in the fridge over the weekend, and this time colour change was observed, suggesting that perhaps some component in the coating formulation is hindering the reaction after extended exposure. A similar test conducted using a binderless coating showed that the colour change occurred reliably when glucose was added to the samples the next day, indicating that aging in combination with the microfibrillated cellulose (MFC A) might not be suitable for the assay.

Figure 2 shows the colour formation in the fourth series of glucose tests, i.e. those made using the arrow-head design B. As discussed earlier, applying the reagents to the tip of the design proved to be challenging. This is most evident in the 5 mM glucose solution sample. Quantitative analysis of the colour intensity was not performed at this stage of the research.

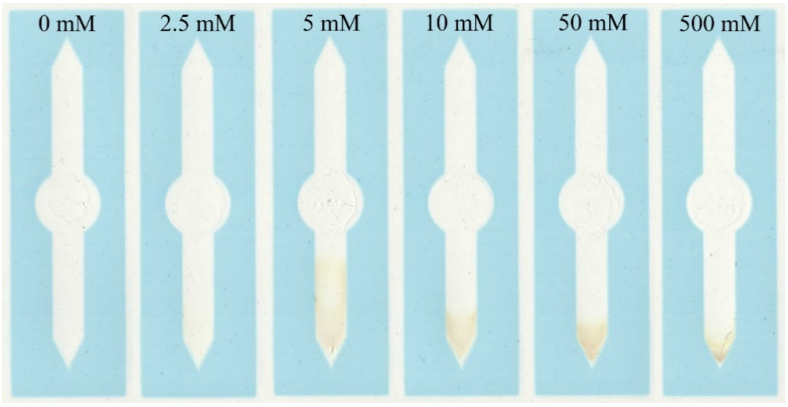

Figure 2: Colour change from colourless to brown in the fourth test series with the arrowhead-design when various glucose concentrations ranging from 0 to 500 mM were tested

3.3 Colorimetric detection

The colour change was not as evident on the coated substrate as on the filter papers (Martinez, et al., 2007). The high light scattering of the coating substrate reduces the intensity of the colour signal due to the background "white noise". The use of a suitable colour filter during the colorimetric analysis will likely solve this challenge.

4. Conclusions

FCC-based coatings in combination with inkjet-printed hydrophobic patterns could be used as reaction platforms for glucose assays. The preliminary results show that glucose test agent oxidation takes place successfully on freshly agent primed coated substrates, but that the reactivity is lost over time in the presence of microfibrillated cellulose (MFC A) binder, and so the coating formulation requires further optimisation. It might be the case that the high surface area and partial film formation of the microfibrillated cellulose binder followed by hornification leads to this undesirable isolation of the reagents.

5. Future work

In future work the coating formulation, assay design, reagent application process and detection will be explored further. This includes possible modification of the reagent area, use of enzyme activity enhancing substances and determining the detection sensitivity of the assay. The glucose assay can be used to verify the performance of a coated reaction platform, after which the platform could be adapted for detection of other analytes.

Potential for inkjet printing the biomolecules poses a challenge of its own, which includes optimising the ink formulation and the printing process to maintain enzyme activity. Various FCC coating formulations will be tested to find the optimal coating formulation. The addition of MFC and PVOH, which block the pores of the coating in the reaction spot making the coating more transparent and thus potentially enhancing the detection, will also be explored.

The test protocol will be optimised also and the enzyme activity and colour stability over longer periods on multiple coating formulations and different inkjet-printed patterns will be explored. The possibility of printing the reagents or spotting using an instrument adopting microlitre, nanolitre and picolitre dispensers, will be explored to enable fabrication of even smaller assays.

The samples were scanned with an Epson Expression 1680 scanner (Seiko Epson Corporation). The quantitative analysis, i.e. analysis of greyscale intensities from the samples, can be performed using a software analysis package, such as ImageJ software (National Institute of Health).

The results of the future work will be reported later in the form of a peer reviewed journal article.

List of abbreviations

AKD	Alkyl ketene dimer
CMC	Carboxymethyl cellulose
FCC	Functionalised calcium carbonate
GOx	Glucose oxidase
HRP	Horseradish peroxide
MFC	Microfibrillated cellulose
POC	Point-of-care
PVOH	Polyvinyl alcohol
µPAD	Microfluidic paper-based analytical device

Acknowledgement

Funding for the project was wholly supported by Omya International AG (Jutila and Koivunen, Aalto University).

References

Cai, L., Wang, Y., Wu, Y., Xu, C., Zhong, M., Lai, H. and Huang, J., 2014. Fabrication of a microfluidic paper-based analytical device by silanization of filter cellulose using a paper mask for glucose assay. *Analyst*, 139(18), pp. 4593–4598.

Cate, D.M., Adkins, J.A., Mettakoonpitak, J. and Henry, C.S., 2015. Recent Developments in Paper-Based Microfluidic Devices. *Analytical Chemistry*, 87(1), pp. 19–41.

Cook, C.C., Wang, T. and Derby, B., 2010. Inkjet Delivery of Glucose Oxidase. *Chemical Communications*, 46(30), pp. 5452–5454.

Deegan, R.D., Bakajin, O., Dupont, T.F., Huber, G., Nagel, S.R. and Witten, T.A., 1997. Capillary flow as the cause of ring stains from dried liquid drops. *Nature*, 389, pp. 827–829.

Di Risio, S. and Yan, N., 2007. Piezoelectric ink-jet printing of horseradish peroxidase: effect of ink viscosity modifiers on activity. *Macromolecular Rapid Communications,* 28(18-19), pp. 1934–1940.

Hakola, L. and Lehtinen, K., 2014. Printed paper based glucose sensor manufactured in pilot scale. In: *NIP & Digital Fabrication Conference, 30th International Conference on Digital Printing Technologies*. Philadelphia, PA, 7–11 September 2014, IS&T, pp. 254–257(4).

Jenkins, G., Wang, Y., Xie, Y.L., Wu, Q., Huang, W., Wang, L. and Yang, X., 2015. Printed electronics integrated with paper-based microfluidics: new methodologies for next-generation health care. *Microfluidics and Nanofluidics*, 19(2), pp. 251–261.

Jeong, S.G., Lee, S.H., Choi, C.H., Kim, J. and Lee, C.S., 2015. Toward instrument-free digital measurements: a three-dimensional microfluidic device fabricated in a single sheet of paper by double-sided printing and lamination. *Lab on Chip*, 15(4), pp. 1188–1194.

Jutila, E., Koivunen, R. and Gane, P.A.C., 2015. Effect of coating pigment, binder type and binder amount on planar liquid wicking on coated substrates. *Journal of Print and Media Technology Research*, 4(3), pp. 173–186.

Jutila, E., Koivunen, R., Bollström, R., Sikanen, T. and Gane, P., 2016. Reaction platforms for enzymatic testing. In: P. Gane, ed. *Advances in Printing and Media Technology: Proceedings of the 43rd International Research Conference of iarigai*. Toronto, Canada, August 2016. Darmstadt: iarigai, pp. 39–48.

Koivunen, R., Jutila, E., and Gane, P.A.C., 2015. Inkjet printed hydrophobic microfluidic channelling on porous substrates. *Journal of Print and Media Technology Research*, 4(1), pp. 7–17.

Koivunen, R., Jutila, E., Bollström, R. and Gane, P.A.C., 2015. Inkjet-printed reaction arrays on pigment coated substrates. In: P. Gane, ed. *Advances in Printing and Media Technology: Proceedings of the 42nd International Research Conference of iarigai*. Helsinki, September 2015. Darmstadt: iarigai, pp. 107–114.

Koivunen, R., Jutila, E., Bollström, R. and Gane, P., 2016. Hydrophobic patterning of functional porous pigment coatings by inkjet printing. *Microfluidics and Nanofluidics*, 20(6):83.

Li, X., Tian, J., Nguyen, T. and Shen, W., 2008. Paper-based microfluidic devices by plasma treatment. *Analytical Chemistry*, 80(23), pp. 9131–9134.

Li, X., Tian, J., Garnier, G. and Shen, W., 2010. Fabrication of paper-based microfluidic sensors by printing. *Colloids and Surfaces B: Biointerfaces*, 76(2), pp. 564–570.

Martinez, A.W., Phillips, S.T., Butte, M.J. and Whitesides, G.M., 2007. Patterned paper as a platform for inexpensive, low-volume, portable bioassays. *Angewandte Chemie International Edition*, 46(8), pp. 1318–1320.

Martinez, A.W., Phillips, S.T., Carrilho, E., Thomas III, S.W., Sindi, H. and Whitesides, G.M., 2008. Simple telemedicine for developing regions: camera phones and paper-based microfluidic devices for real-time, off-site diagnosis. *Analytical Chemistry*, 80(10), pp. 3699–3707.

Martinez, A.W., Phillips, S.T., Whitesides, G.M. and Carrilho, E., 2010. Diagnostics for the developing world: microfluidic paper-based analytical devices. *Analytical Chemistry*, 82(1), pp. 3–10.

Määttänen, A., Fors, D., Wang, S., Valtakari, D., Ihalainen, P. and Peltonen, J., 2011. Paper-based planar reaction arrays for printed diagnostics. *Sensors and Actuators B: Chemical*, 160(1), pp. 1404–1412.

Nishioka, G.M., Markey, A.A. and Holloway, C.K., 2004. Protein damage in drop-on-demand printers. *Journal of the American Chemical Society*, 126(50), pp. 16320–16321.

Olkkonen, J., Lehtinen, K. and Erho, T., 2010. Flexographically printed fluidic structures in paper. *Analytical Chemistry*, 82(24), pp. 10246–10250.

Peele Jr, J.D., Gadsden, R.H. and Crews, R., 1977. Semi-automated vs. visual reading of urinalysis dipsticks. *Clinical Chemistry*, 23(12), pp. 2242–2246.

Sameenoi, Y., Nongkai, P.N., Nouanthavong, S., Henry, C.S. and Nacapricha, D., 2014. One-step polymer screen-printing for microfluidic paper-based analytical device (μPAD) fabrication. *Analyst*, 139(24), pp. 6580–6588.

Sechi, D., Greer, B., Johnson, J. and Hashemi, N., 2013. Three-dimensional paper-based microfluidic device for assays of protein and glucose in urine. *Analytical Chemistry*, 85(22), pp. 17033–10737.

Wang, T., Cook, C. and Derby, B., 2008. Inkjet printing glucose oxidase for biosensor applications. *ECS Transactions*, 16(11), pp. 15–20.

Wang, T., Cook, C. and Derby, B., 2009. Fabrication of a glucose biosensor by piezoelectric inkjet printing. In: *Third International Conference on Sensor technologies and Applications: SENSORCOM '09*. Athens, 18–23 June 2009. IEEE Computer Society.

Wang, T., Cook, C.C., Serban, S., Ali, T., Drago, G. and Derby, B., 2012. Fabrication of a glucose biosensor by piezoelectric inkjet printing. *ArXiv*:1207.1190.

WHO, 2016. *Global Report on Diabetes*. [pdf] World Health Organization. Available at: <http://apps.who.int/iris/bitstream/10665/204871/1/9789241565257_eng.pdf> [Accessed February 2017].

Yang, Y., Noviana, E., Nguyen, M.P., Geiss, B.J., Dandy, D.S. and Henry, C.S., 2017. Paper-based microfluidic devices: emerging themes and applications. *Analytical Chemistry*, 89(1), pp. 71-91.

Yoo, E.-H. and Lee, S.-Y., 2010. Glucose biosensors: an overview of use in clinical practice. *Sensors,* 10(5), pp. 4558-4576.

Yun, Y.H., Lee, B.K., Choi, J.S., Kim, S., Yoo, B., Kim, Y.S., Park, K. and Cho, Y.W., 2011. A glucose sensor fabricated by piezoelectric inkjet printing of conducting polymers and bienzymes. *Analytical Sciences*, 27(4), pp. 375–379.

Zhong, Z.W., Wang, Z.P. and Huang, G.X.D., 2012. Investigation of wax and paper materials for the fabrication of paper-based microfluidic devices. *Microsystem Technologies*, 18(5), pp. 649–659.

Investigating Opportunities for 3D Digital Package Prototypes in the Proofing Workflow

Amanda Whyte, Natalia Lumby and Reem El Asaleh

Ryerson University, Toronto Canada

E-mail: amanda.whyte@ryerson.ca; nlumby@ryerson.ca; reem.elasaleh@ryerson.ca

Abstract

Today's brands are challenged to stand out on shelf, more than ever before. Complexity of product packaging is increasing, while more products are being developed at growing speeds. Virtual proofing can offer unique advantages in a packaging workflow. This study investigates the use of 3D digital mock-ups to learn how this new technology can be used. Methods include product testing, preliminary interviews with an experienced group of users, and in-depth interviews with a variety of stakeholders in the packaging workflow, representing a dozen brands. Study participants describe their proofing workflow then, using the free Esko Studio app on iPad, they are filmed interacting with sample products to understand the opportunities and limitations of 3D digital mock-ups. Results suggest that hard copy proofs are preferred for approval, especially for colour accuracy. Interviewees did however see a valuable role for 3D mock-ups as part of the marketing and sales function—identifying the need for new digital assets earlier during product development as the industry pushes towards omni-channel retailing.

Keywords: packaging, workflow, proofing, 3D, mock-up

1. Introduction and background

The packaging industry is a thriving and competitive market. Designs are more advanced than ever—all one needs to do to experience this phenomenon is walk down the toothpaste aisle of any drugstore today. SKU proliferation (many "flavours" of one brand), along with increasingly complex combinations of substrates and specialty finishes, are used to attract the consumer's attention on shelf. Studies confirm that atypical food packaging can trigger the consumer to notice and analyze other claims, such as nutritional values, and to distinguish high quality information from low-quality information (van Ooijen, et al., 2016).

This study interrogates the current packaging workflow, with a focus on proofing. In particular, the research is focused on using specialized 3D mock-up software on a tablet device (iPad). We propose that added packaging complexities require a more robust proofing workflow. This is relevant because it is often cost prohibitive to provide prototypes for specialty packaging. Paradoxically, it is these complex design combinations that require prototypes. In order to fill this gap, new 3D visualization technology has the potential for brand owners to experience these packages digitally.

In addition to understanding the current proofing demands in a packaging workflow, the study explores the possibility of assessing special brand colours as well as complex finishes in a digital environment using 3D visualization. Complex designs in the packaging industry ensure that the product is noticed (Heiniö, 2010; Rundh, 2009). Strategic branding can place the product's packaging as a direct advertisement at point of sale, and can provide quick recognition of loyal brands since an estimated 73 % of product decisions are made at point of purchase (Silayoi and Speece, 2007). The package should contain informational,

emotional and functional value as well as display effective designs for visibility, shopability, sustainability, and differentiation, thus driving consumption (Heiniö, 2010).

As seen in the results of this research, the cooperation and effective communication between the numerous stakeholders in the production process is essential for a successful package. The complexity in the amount of stakeholders make the process either difficult to identify or difficult to adhere to. With stakeholders often dispersed geographically, we explore the possibility of 3D digital mock-ups for proofing as a potential alternative to physical mock-ups, decreasing time to market and addressing SKU proliferation in a highly competitive environment.

2. Materials and methods

This study includes product testing, preliminary interviews with an experienced group of users, and finally in-depth interviews with a variety of stakeholders in the packaging workflow. The breadth of information sources is a holistic approach to documenting current package workflows and allows us to visualize the said workflow and explore how 3D proofing fits in.

2.1 Software/hardware selection and file preparation

The focus of the study is to explore how a company can include 3D digital proofing in a packaging workflow. A variety of software and hardware tools were used. The digital assets, which were created as demonstrations of 3D mock-ups, were created using Adobe Illustrator, Esko Deskpack plug-ins as well as Esko Studio Visualizer. During the interviews they were shared using the free Esko Studio app on an Apple iPad. Tablets were selected for this research study because they offer a new area of opportunity. In addition to their low cost, tablets are also portable, allowing for the engagement of new stakeholders. The iPad specifically was selected because it has excellent colour capabilities compared to Android devices and other tablet computers (El Asaleh, 2016). Both software brands (Adobe and Esko) were selected on the basis of their market leadership in the packaging sector, and availability to the researchers.

Firstly, a series of 3D packages was digitally constructed with a variety of specialty finishes (ex. silver foil). Designs included a foil pouch, a toothpaste box, and a wine label (Figures 1–3). All of the mock virtual packages were inspired by leading brand designs, so that the interviewees would feel familiar with the product, eliminating the possibility of novelty skewing the results.

Figure 1: Toothpaste box with a metallic substrate and embossed lettering

Figure 2: Chocolate pouch with gold foil stamping

Figure 3: Wine label with gold foil stamping and logo embossing

2.2 Preliminary interviews

The preliminary interviews and product testing began at a vendor specific roadshow. Fifteen packaging experts were asked to answer questions related to their proofing needs and preferences prior to viewing the digital mock-ups. Following this set of questions, subjects were asked to interact with the 3D virtual proof on an iPad. Researchers then observed and took note of how the subjects interacted with the technology.

2.3 Interviews

In-depth interviews were conducted following the preliminary testing. Twenty-four industry professionals from a dozen companies were interviewed. This group consisted of printers, brand owners and prepress production specialists. The companies represented in the study are all established in their fields, with the individuals interviewed having 2+ year of experience. While the age of the sample was not collected the experience of interviewees breaks down to: 47 % having 2 to 5 years, 20 % having 5 to 10 years, 7 % having 11 to 15 years, and 26 % having 16+ years of experience in their field. All interviews were conducted on site at company locations, allowing for the research to look at the package in the same environment that would normally exist for that specific stakeholder. In addition to analyzing responses, the interviewees' hand motions were video recorded to catalogue how the application was used and limitations were identified.

3. Results and discussion

Overall the sentiment towards 3D digital mock-ups was overwhelmingly positive. The following section will identify the advantages and disadvantages as noted by study participants, along with a discussion of the potential workflow opportunities. The interviewees' assessment of the technology itself will also be examined.

3.1 Opportunities for 3D digital mock-ups

The response to being able to see a package mock-up on screen was received well by a majority of stakeholders interviewed. All of the subjects used digital proofs such as PDFs at some stage of their workflow. According to our study, 46 % of stakeholders were making use of 3D digital mock-ups as part of their process. The advantages for 3D mock-ups commonly identified in the interviews included: faster communication and shorter proofing cycles, the ability to use the digital assets in new ways, such as sales presentations and online, as well as allowing stakeholders to see a representation of the final product prior to any manufacturing costs had been incurred. Respondents also liked the idea of being able to display the 3D proof on a tablet device, thus making this brand asset highly portable.

Concerns did exist over colour accuracy, especially given that the proofs could be accessed in an uncontrolled lighting environment. Respondents commented that the quality of 3D mock-ups is currently highly variable, with the quality attained often driving how the asset can be used. Some respondents did indicate that they would rather sign off on a physical proof that will remain unchanged, suggesting that 3D mock-ups are a valuable asset, but not a proofing tool. One respondent noted "things look different when they are in your hands. It is an emotional connection." Having virtual 3D mockups would reduce travel and printing costs, especially beneficial since increasingly not all workflows can accommodate the timelines associated with physical mock-up proofs. In one interview, a brand owner at a craft beer brewery noted that in the case of a can or bottle a mock-up would be highly valuable. This market is dominated by large brands (Pepsi and Coca-Cola) that take up the resources of the supplier—with no time for mock-ups left for smaller players.

While there is no industry standard in package proofing, general themes did inform our analysis. Figure 4 identifies a proofing workflow most commonly used by the study participants (with some participants omitting some portions of the workflow). Here we have indicated where stakeholders have seen potential for 3D mock-ups. Interviewees identified that the product's life cycle stage was an important determinant of whether or not mock-ups are needed. New product launches were cited as needing more digital assets.

Brand owners in particular were enthusiastic about the potential to use 3D mock-ups as sales collateral in retail pitch presentations.

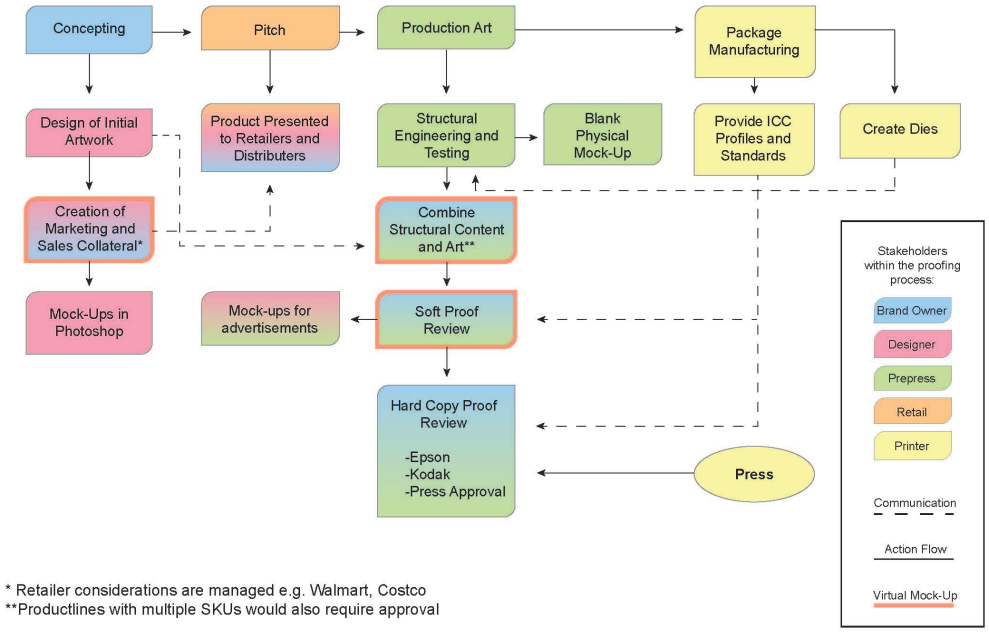

Figure 4: Current packaging workflow as interpreted through in-depth, in-person interviews from various company stakeholder representatives

The nature of the product category itself impacted the need for a mock-up. For example, one stakeholder identified that it was difficult for brand owners to see how their designs will look when applied around a bottle or can. Seeing the artwork applied to these specific shapes could clarify artwork placement. The use of virtual prototypes to model 3D renderings of point-of-purchase (POP) displays and structural designs was a notable discussion. It is possible to reduce the cost of POP displays by processing designs virtually and digitally communicating changes before sending the files to a structural department for testing. Timelines and cost were both important factors to interviewees.

The potential to use 3D mock-ups was attractive in situations where the product timeline was aggressive. Further, some stakeholders identified that digital files can often be provided at a lower cost than a hard-copy proof, especially if handwork would be required to provide a sample (like in the case of a unique plastic container such as a yogurt tub).

The technologies used for current proofing methods varied greatly between participants, ranging from an emailed PDF to working with integrated prepress solutions that allow for real time collaboration and colour accurate soft proofs. Interestingly, while participants were working within different environments, there was a common gap that they saw as fitting 3D digital mock-ups. Overwhelmingly, interviewees identified such proofs as fitting the sales and marketing function of their workflow. There was a lack of confidence towards them being used as a print production tool—but they were enthusiastically embraced as a value add.

This study has confirmed the lack of industry standard practices in package proofing. As part of the interview we asked participants to rate the importance of the accuracy of colour, substrate and specialty finish on the proof. Not all stakeholders interviewed had experience dealing with all three items. For example some did not use specialty finishes and therefore were unable to provide an assessment. Summarized in Table 1, participants rated colour accuracy as 8, proofing substrate being representative of the final sub-

strate used as an 8, and the ability to see specialty finishes on the proof as 6.5. There were no significant differences in these results when separated by level of experience, though several participants did comment that assessing proofs has a learning curve. Given the exploratory nature of the study, the sample is not representative enough to assess how experience level or stakeholder type impacted the sentiment towards virtual proofing. A future study may combine diffusion of innovation theory to identify whether an individual's own approach to technology (for example being an early adopter) has an impact on the company's adoption of virtual proofing technology.

Table 1: Identifying what is important to participants on a proof

How important is...	
colour accuracy?	8.0
seeing the proof on the final substrate?	8.0
seeing the specialty finishes on the proof?	6.5

Using 3D digital prototyping is new in the industry, replacing the previous digital proofing method of still product images. Measuring its effectiveness as perceived by brand owners will be an important contribution to the industry, especially since tactile finishes are very popular today. Studies have shown that tactile finishes do have an impact on the quality as perceived by consumers (Abdalkrim, and AL-Hrezat, 2013; Keif, Twomey and Stoneman, 2015; Saastamoinen, 2013).

3.2 Analysis of 3D mock-up technology used: Esko Studio Viewer

The current state of package proofing, according to this study and the discussions and interviews with stakeholders, suggests that although there is value with soft proofs, hard copy proofs are still highly valued for colour accuracy and tactile finishes. Digital proofs are mainly considered when checking content and during initial design concepting. In this study, participants identified 3D visuals as supplementary to the marketing function. Respondents who are already working in 3D identified that there are varying levels of quality in 3D rendering, ranging from being appropriate for internal concepting, all the way to photorealistic renderings that can be used as brand assets aimed as consumers. A total of 33 % of interviewees noted they have seen or used a type of Esko software in the past. Further, 40 % said they have used 3D renderings whether themselves or their respective creative agencies for their customers.

Each of the study participants had an opportunity to interact with a 3D mock-up using Esko Studio on an iPad. Table 2 identifies the features participants commonly noted as being attractive when using the technology. Immediately, there was a divide between those familiar with tablets for other applications and those less familiar, with an impact on how they moved around the environment. Esko chose to use industry standard gestures to move around the environment, but they were still confusing for those unfamiliar with Apple products. Notably, users often zoomed in and could not move the package, not knowing how to pan around the zoomed in object. Those that had difficulties interacting with the app were more likely to have a negative response to virtual prototypes in general and argued the importance of a physical prototype.

Table 2: Advantages of the Esko Studio iPad app

→	Easy to use
→	Uncluttered interface
→	Interaction with the product
→	Ability to view "on-the-go"
→	Ability to see some substrate & finishing features

Participants were also asked to share any suggestions they had for improving the technology. The functional features suggested, were ones common to production PDF proofs. Suggestions included: the ability to comment and have real-time viewing, the ability to see spot colour breakdown and to see separations, and having the ability to change the background and lighting conditions. Those less familiar with iPads felt it was important to add a beginner's tutorial for gestures, and navigation arrows for rotation.

One advantage of the application that was linked to proofing workflow was the ability to view the 3D mock-ups on a mobile device or a tablet. Participants were quick to identify that individuals who worked with clients, and were on the road a lot could benefit from this technology. Having an app as a production person on the other hand would be less critical as their environment was more likely to include a computer than an iPad. Upon seeing the technology, one production stakeholder immediately said, "My sales people would love this". Both brand owners and production personnel indicated that 3D mock-ups would be a great marketing tool.

4. Conclusions

The complexity of current packages is on the rise as products struggle to differentiate themselves amongst other brands on store shelves. Consumers are experiencing a broad array of specialty finishes and substrates. From a proofing perspective, creating physical prototypes for these types of packages can be expensive and time consuming. Nonetheless, study participants still prefer to see physical proofs, especially for colour approval. Participants indicated that they are comfortable approving substrates and some specialty finishes from a sample, without seeing a proof using those specific items. This is likely the result of training and good supplier relationships.

Nonetheless, participants were very positive toward 3D mock-ups as a value added component of their existing proofing workflow. In particular, the marketing and sales functions were identified as being the key stakeholders benefiting from 3D images. This is an important finding as the nature of software capabilities will depend on the type of user that developers target. Another implication of this finding is that 3D mock-up files may be used for a broader variety of functions than just proofing. Several participants identified the need for digital assets with the continued push for online retailing. Many online retail experiences are limited to static product shots that do not allow the buyer to interact with the package.

With 3D mock-ups becoming available as early as the product ideation stage it is possible for retailers and brand owners to experiment with presales of products that deliver just in time. This study is a springboard to gather insights from the ecommerce perspective, knowing that omni-channel retailing is projected for growth averaging 15–20 % internationally across multiple categories (Rigby, et al., 2012). The way people are shopping is changing. Another study found that, 70 % of shoppers today start by looking at retail items online (Blake, and Morier, 2014). Given the potential of purchasing in digital stores, the digital 3D mock-up shows growth, especially when compared to the current industry standard – a static product shot.

In addition to identifying the stakeholder group that is most likely to benefit from 3D mock-ups the study revealed that specific product development scenarios could impact how valuable a digital mock-up is to the process. In particular, new products were identified as needing more brand assets than products, which are already on the market. Products with structural complexity, such as point of purchase displays were as favourable towards using 3D visualization. Now that we understand these functions better there may be an opportunity to separate the functions of proofing for production and mock-ups for marketing in a future study.

The next phase of this research will move to evaluate a broader variety of 3D visualization software, targeting the packaging industry. Understanding the features of a range of products will allow for further analysis of this growing area in digital assets.

Acknowledgments

This research is made possible with the support of the Faculty of Communication & Design at Ryerson University. We would like to also thank Esko for their support throughout the project.

References

Abdalkrim, G.M. and AL-Hrezat, R.S., 2013. The role of packaging in consumer's perception of product quality at the point of purchase. *European Journal of Business and Management*, 5(4), pp. 69–82.

Blake, A. and Morier, R., 2014. *Ecommerce Packaging Optimization Guidelines*. PAC Next. [pfd] Available at: <http://www.pac.ca/assets/ecommerce-document-online-version.pdf> [Accessed June 2017].

Heiniö, S., 2010. Package design and strategic branding. In: *Proceedings of the 17th IAPRI World Conference on Packaging*. Scientific Research, pp. 237–241.

Keif, G.M., Twomey, C. and Stoneman, A., 2015. Consumer perception of tactile packaging: a research study on preferences of so touch and hi rise coatings in cosmetic packaging. *Journal of Applied Packaging Research*, 7(1).

van Ooijen, I., Fransen, M.L., Verlegh, P.W.J. and Smit, E.G., 2016. A typical food packaging affects the persuasive impact of product claims. *Food Quality and Preference*, 48, pp. 33–40.

Rigby, D., Miller, K., Chernoff, J. and Tager, S., 2012. Omnichannel retailing: digital disruption and retailer opportunities. *Bain Retail Holiday Newsletter*, 2. [online] Available at: <http://www.bain.com/Images/BAIN_BRIEF_Retail_holiday_newsletter_%232_2012-2013NEW.pdf> [Accessed June 2017].

Rundh, B., 2009. Packaging design: creating competitive advantage with product packaging. *British Food Journal*, 111(9), pp. 988–1002.

Saastamoinen, I., 2013. Touch and Feel – The Role of Tactile Qualities on Board Packages. Master Thesis. Helsinki University, Faculty of Agriculture and Forestry.

Silayoi, P. and Speece, M., 2007. The importance of packaging attributes: a conjoint analysis approach. *European Journal of Marketing*, 41(11/12), pp. 1495–1517.

Formulation of a Bio-based and Water-based Ink for Flexography

Fanny Bardot[1], *Charles Bouchard*[2], *Olivier Tonnoir*[2], *Anne Blayo*[1], *Gérard Mortha*[1]

[1] Univ. Grenoble Alpes, CNRS, Grenoble INP*, LGP2, F-38000 Grenoble, France
[2] Siegwerk France SAS, P.O. Box 506, 74105 Annemasse Cedex, France

E-mail: fanny.bardot@lgp2.grenoble-inp.fr; anne.blayo@pagora.grenoble-inp.fr

Abstract

Lignin is the second most abundant organic substance after cellulose. It is also the most abundant renewable source of aromatic compounds. Lignin is already known as a potential binder for printing ink application. However, to the best of our knowledge, no ink company is using lignin in present-day production. Over the past few years, environmental concerns has grown to such an extent that it became a potential marketing advantage for many products. Water-based flexographic inks are no exception. Incorporate lignin into water-based flexographic ink is hence of great interest and will be the aim of this study. Two main difficulties must be overcome: the dark colour of the unmodified lignins and the relative hydrophilic character thus low wet resistance of the chemically bleached lignins. After finding a proper balance between these two characteristics, water-based flexographic inks were formulated and successfully tested at a lab scale.

Keywords: bio-based polymer, water-based flexographic ink, lignin

1. Introduction and background

Over the past few years, environmental concerns has grown to such an extent that it became a potential marketing advantage for many products. Water-based flexographic inks are no exception. Among the different types of flexographic inks, the latter have lower overall environmental impacts (Piluso, et al., 2009). Nevertheless, they can be enhanced and especially in terms of renewable raw materials. Indeed, consumers are more and more sensitive to the packages that deliver and protect their products and even more regarding food-contact packaging. The use of lignin as bio-sourced compounds is hence an opportunity to replace petroleum-sourced products.

Lignin is the second most abundant organic substance after cellulose. It is also the most abundant renewable source of aromatic compounds. Indeed, in 2010, 70 million tons of lignin were extracted from wood by the pulp and paper industry (Laurichesse and Avérous, 2014). At present, the main use of lignin, 95 % of the world's lignin supply, is as a fuel. However, lignin is known to have a high potential in replacing petroleum-based products (Laurichesse and Avérous, 2014). It is indeed an interesting candidate to produce some resins or polymers, such as polyols (Borges Cateto, 2009), some thermosets and thermoplastic polymers (Llevot, et al., 2015) or to be used as a compound or a filler in diverse applications.

Incorporate lignin into water-based flexographic ink is hence of great interest and will be the aim of the study.

Lignin is already known as a potential binder for printing ink application. Several patents were found dealing with either raw or modified lignin in black or coloured inks. However, to the best of our knowledge, no ink company is using lignin in present-day production. Lignin is mainly used without prior chemical modification. This is the case in US2449230 (Irion, 1948). This patent deals with kraft lignin and lignosulfonates

as a binder in black, yellow and blue inks for different applications such as newspaper printing. Similarly, in US2525433 (Voet, 1950), a binder is created by dissolving lignin into organic water-miscible solvents, e.g. glycols, ethers of the glycols, ester of the glycols, methyl ethyl ketone, … and subsequent mixing with carbon black to give a non-tacky film.

US4891070 (Dilling and Dimitri, 1990) described a method where lignin amine salts are used as a binder for aqueous ink. However, binder and so forth the inks prepared with this type of lignin are not storage stable. In US5188665 (Schilling, 1993), Westvaco Corporation declares that combination of lignin amine salt resin and organic amine, such as styrene-acrylic acid or rosin resin can be used in a black aqueous printing ink to improve storage stability.

Lignin can also be modified for subsequent application. Lignin is hence even used in more recent ink formulation such as in inkjet ink composition. Black inkjet ink of US6045606 (Matzinger, 2000) is composed of water-based solvent and carboxylated lignin in proportion between 0.1 % and 20 %. This ink is said to present excellent water resistance properties while achieving excellent print quality, jetting properties, storage stability, reliability, and drying times. WO 2015062910A1 (Caes, Rivas and Noirot, 2015) from Siegwerk highlights the use of nitrated lignin ester as a binder in printing ink in replacement of nitrocellulose.

The mentioned patents do not resolve the problem of lignin colour. Even if some of them deal with other inks than black ones, they do not mention any colouristic deviation due to brown colour of lignin. US4612051 (Miller and Dilling, 1986) copes with this problem and describes the utilization of lignin acetate binder in water based flexographic ink formulations. Water-insoluble non-sulfonated reductive acetylated lignin leads to less colouristic deviation than non-modified one when incorporated into an ink. Furthermore, this invention is said to reduce surface tack and the colour. In the same way, US4454066 (Dilling and Sarjeant, 1984) demonstrates that a reduction of lignin colour is possible for subsequent use in diverse ink formulations and exhibits very low staining, low azo dye reduction, good heat stability, pigment grinding efficiency, and dispersion stability.

The manufacturing of printing inks has several impacts on environment throughout the process. It can affect the resources (increasing scarcity of fossil and mineral resources…), the human health (carcinogen substances, breathing issues, climate imbalance…) and the ecosystems (eco-toxicity, acidification, eutrophication…). According to EuPIA (2013), improvement of environmental impact of printing ink is already a question under investigation. Some renewable raw materials are already used, such as cellulose derivatives, bio-ethanol, vegetal oils, but the proportion is still limited and has to be increased.

Current regulations require more environmental friendly inks and a decrease in Volatile Organic Compounds (VOC). Indeed, even inks appearing to be “greener” such as water-based inks are not completely environmental-friendly, notably in terms of recyclability or renewable raw material (EuPIA, 2013). Nevertheless, a trend is growing with more environmental care. Actually, according to a study by Pira International (Spear, 2010), the global environmental friendly inks market was valued at € 5.8 billion in 2009 and it is projected to reach almost € 7.2 billion by 2014, with a CAGR (Compound Annual Growth Rate) of 4.5 % in the 2009–2014 timeframe. In accordance with this study, the development of new eco-friendly inks is expected, such as improved sustainable raw materials. Obviously, water-based inks are already “greener” than petroleum-based inks. Piluso, et al. (2009) realized an Eco-efficiency analysis of solvent-based, water-based and UV-cured inks for flexographic printing inks in film application and compared their economic and environmental impacts. Water-based flexographic system was found to have the lowest impacts in terms of costs, energy consumption, emissions, resource consumption, risk potential and land use. In other words, in addition to the lowest life cycle costs, it demonstrates the lowest impacts in five of the six environmental impacts categories with the exception of toxicity potential. Regarding this category, it shows an impact slightly higher than the one of UV-cured system. However, even with a reasonable environmental finger-

print, the water-based flexographic inks still contain a large amount of damaging and petroleum-based chemicals. Over the last years, more and more inks entirely or partially based on renewables resources were introduced to the market (Robert, 2015). To go further, manufacturing of an ink should be nontoxic, environmentally friendly, using renewable and biodegradable components but also combining waste management and energy saving.

This study will focus on water-based flexographic inks. As such, the target ink should comply with the specific requirements of the printing process, e.g. rheological properties, colour, no migration and wet and rub resistance… As demonstrated above, water-based inks for flexography are more eco-friendly than the other inks. However, it still contains lots of petroleum-based products. More particularly, one of the main components of these inks, the vehicle, is based on petroleum-based styrene-acrylic resins. To resolve this problem, the resin will be hence based on renewable compound, e.g. lignin macromolecule. Consequently, the impact on ink properties of the presence of lignin, either bleached or not, will be studied.

2. Materials and methods

Preliminary studies proved that obtaining bleached lignin solutions with correct wet resistance was possible. In this part, a Protobind 3000 (PB3000) bleached lignin with hydrogen peroxide in sodium hydroxide solution during 40 minutes in nitrogen atmosphere, isolated with HCl, was tested into a yellow and a cyan ink in partial replacement of a styrene-acrylic resin. PB 3000 is a lignin purchased from GreenValue Enterprises LLC, commercializing lignin products from ALM India. It is extracted after the soda cooking of annual plants (wheat, corn and rice).

In order to get a reference, PB3000 was also introduced into ink. Both lignin-containing inks, called "*Lignink*", were compared to one standard ink. After formulation, rheological properties and surface tension of lignin resins and corresponding inks were measured. Inks were then printed and characterized in terms of CIE $L^*a^*b^*$ values, colouristic deviation, gloss, rub resistance and water resistance.

2.1 Formulation of inks

The formulations of the inks with lignin and the reference ink are presented in Table 1. Basically, an ink is formulated with a pigment base containing pigments in acrylic solution and an extender. This extender is composed of a colloidal acrylic resin mixed with a styrene-acrylic co-resin and additives such as wax, alcohol and antifoam. Regarding *Lignink* formulation, lignin solution replaces partially the colloidal acrylic resin. Without lignin, this emulsion resin accounts for 10.9 % in the total weight of the ink whereas it accounts for 5 % in *Lignink*. Therefore, this particular extender is realized with a lignin solution at a mass fraction of 20 % either bleached or not, and a let down varnish, containing the same styrene-acrylic co-resin and additives. The extenders are then mixed with a pigment base to produce the ink. Yellow inks, shown in Figure 1, demonstrate that presence of lignin has a significant impact on colour even if the effect of bleaching (sample on the left) is noticeable. However, standard yellow ink remains purer than the other inks.

Table 1: Formulation of water-based flexographic inks

Compounds (mass fraction %)	*Lignink*	Standard ink
Lignin solution (a mass fraction of 20% lignin)	66.5	-
Let down varnish	33.5	-
Standard extender	-	100
Extender	60	60
Pigment base	40	40

2.2 Application tests: printing of lignin solutions and inks

Every lignin solution and inks were printed using K hand coater #2. It consists in wired bar, i.e. a stainless steel wired was winded onto a stainless steel rod, which allows a control of the wet film thickness. With a K bar #2, wet film deposit is equal to 12 µm. Lignin solution is dropped off on the coated paper using a Pasteur pipette. A K bar #2 is then placed on the substrate and fastly pulled toward the user. Inks were also printed with Handproofer, an anilox hand roller. It consists in an engraved roller (200 lines-10 cm^3) and a rubber cylinder. Some ink is placed in the nip of the rollers and the whole system is rolled onto the coated paper. Finally, inks were also tested on IGT-F1 machine with a print run of 0.3 m/s and an anilox of 10 cm^3. Ink is dropped off on the anilox. Excess of ink is scraped with a blade and ink from the anilox is then transferred to the form cylinder and the cliché and finally transferred to the coated paper.

Figure 1: Aspect of yellow inks: with modified Protobind (left), without lignin (middle) and with unmodified Protobind

3. Results and discussion

3.1 Characterization of the lignin solutions and the corresponding inks

3.1.1 Rheological properties

During flexographic process, the ink is under shear and the associated shear rate depends on the speed of the machine. For easy application, ink should be shear-thinning. Rheological properties were first evaluated on lignin solutions and then on inks with a cone and plate rheometer (MCR02, Anton Paar).

Figure 2 presents the viscosity variations as a function of shear rate for unbleached and bleached lignin solutions. Both solutions have a shear-thinning behaviour. This behaviour is confirmed in Table 2, which presents n-exponent values from the Ostwald-de Waele model, for both lignin solutions. With $n < 1$, both bleached and unbleached lignin alkaline aqueous solutions demonstrate a shear-thinning behaviour. For a given shear rate, and more particularly for low values, viscosity of bleached lignin solution is lower than that of unmodified lignin solution whereas, for higher shear rate, difference between the two solutions is small.

Indeed, bleaching increases the amount of carboxyl groups leading to a change in lignin interactions when dissolved in an aqueous alkali solution. Solvation of lignin molecules is hence more important and each molecule can slip past one another more easily with addition of hydrophilic ionisable groups. At higher rate, effect of chemical modification is reduced and viscosity of both unmodified and bleached lignin solution is similar.

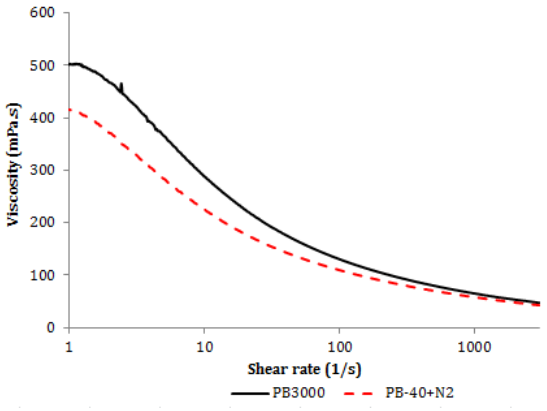

Figure 2: Dynamic viscosity as a function of shear rate for PB3000 (black straight line) and bleached PB3000 (red dotted line) in alkaline solution at a mass fraction of 20 %

Table 2: The parameters (k and n) of the Ostwald-de-Waele model, with the R^2 fitting calculated from the flow-curve of lignin solutions

Lignin solution	k (Pa · s^n)	n	R^2
PB3000	0.42	0.74	0.993
Bleached PB3000	0.32	0.77	0.992

The shear stress and the dynamic viscosity versus shear rate (Figure 3) flow curves for the different inks were also measured. The n-exponent values from the power-law model of each ink are written in Table 3. As expected, colour does not change the behaviour of the solution. According to Figure 3 and Table 3, unmodified *Ligninks* have a shear-thinning behaviour whereas bleached *Ligninks*, and standard inks to a lesser extent, are close to a Newtonian behaviour with n values almost equal to 1.

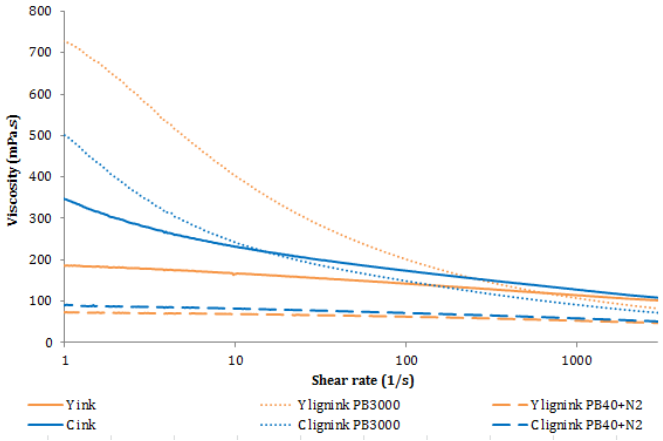

Figure 3: Dynamic viscosity as a function of shear rate for the different inks (cyan and yellow)

Considering the rheological behaviour of bleached lignin solution shown in Figure 2, for a given shear rate, Figure 3 highlights that bleached *Ligninks* have a lower viscosity than the other inks. In bleached *Ligninks*, as shear rate increases, ink compounds are more readily oriented and/or break compared to unmodified *Ligninks* or standard inks.

Industrially, an estimation of viscosity, and more particularly kinematic viscosity, is routinely measured with an Afnor Cup #4 to compare with commercial water-based flexographic inks. According to literature (Havlinova, et al., 1999), flexographic inks require flow times of 18–35 s (outlet diameter of 4 mm). Evaluation is reported in Table 4. Kinematic viscosity of bleached *Lignink* is much lower than other inks

and comply with flexographic inks specifications. This value is in accordance with the previous assertions. Unmodified *Lignink* and standard inks need hence further adjustment to fit with viscosity requirements.

Table 3: The parameters (k and n) of the Ostwald-de-Waele model, with the R^2 fitting calculated from the flow-curve of the inks

Ink	k (Pa · s^n)	n	R^2
Yellow standard ink	0.19	0.94	0.999
Yellow *Lignink* PB3000	0.62	0.76	0.996
Yellow *Lignink* Bleached PB3000	0.07	0.95	0.999
Cyan standard ink	0.36	0.85	0.999
Cyan *Lignink* PB3000	0.43	0.78	0.998
Cyan *Lignink* Bleached PB3000	0.10	0.93	0.999

Table 4: Kinematic viscosity, expressed in flow time, of inks measured with AFNOR Cup #4

Ink	**Viscosity (flow time) AFNOR Cup #4 (s)**	**Equivalent (mPa · s)**
Yellow standard ink	38	≈ 90
Yellow *Lignink* PB3000	38	≈ 90
Yellow *Lignink* Bleached PB3000	20	≈ 40
Cyan standard ink	36	≈ 85
Cyan *Lignink* PB3000	33	≈ 75
Cyan *Lignink* Bleached PB3000	18	≈ 35

3.1.2 Surface tension

Surface tension of lignin solutions and corresponding inks were measured on a Soigma 70 Tensiometer (KSV Instrument) and compared in Table 5. This property gives an idea of the wetting ability of a solution on a substrate. In literature, surface tension is expected to be lowered by chemical modification, such as hydrogen peroxide oxidation, done on lignin (Ren and Li, 2001). However, after oxidation, surface tension of bleached lignin solution is barely decreased. Similarly, addition of bleached lignin into an ink tends to have a limited impact on lowering of surface tension. The situation of unmodified Yellow and Cyan *Lignink* is different. Mixing unmodified lignin solution with other components to formulate an ink leads to creation of higher amount of foam compared to addition of bleached lignin solution instead. After few hours, foam disappeared in case of bleached *Lignink* but remained stable in case of unmodified *Lignink*. Therefore, antifoam was necessary added in unmodified *Lignink* to collapse the foam and print the ink. Consequently, unmodified *Lignink* surface tension decreased and the measurement is misrepresented. Once again, this is an argument in favour of using bleached lignin rather than unmodified one.

Table 5: Surface tension of lignin solutions and inks

Solution or ink	**Surface tension (mN/m)**
Lignin solution PB3000	35.4
Lignin solution bleached PB3000	34.4
Yellow standard ink	41.0
Yellow *Lignink* PB3000 (+antifoam)	34.2
Yellow *Lignink* Bleached PB3000	39.1
Cyan standard ink	39.7
Cyan *Lignink* PB3000 (+antifoam)	24.5
Cyan *Lignink* Bleached PB3000	39.5

2.3 Characterization of the printed samples

Each ink was printed with a Hand Proofer, a K handcoater #2 and an IGT-F1 laboratory flexographic press to simulate the flexographic process on coated paper (WTTJ or Rieger).

2.3.1 Optical properties: colour and gloss

For K Handcoater #2 and Handproofer, CIE $L^*a^*b^*$ values were measured with a spectrophotometer SpectroEye X-Rite in reflectance mode (45°/0° geometry – D50 illuminant, 2° standard observer) and compared with the standard corresponding inks in Figure 4 and Figure 5, respectively. The colour differences ΔE^*_{ab} were then calculated (Table 6 and Table 7).

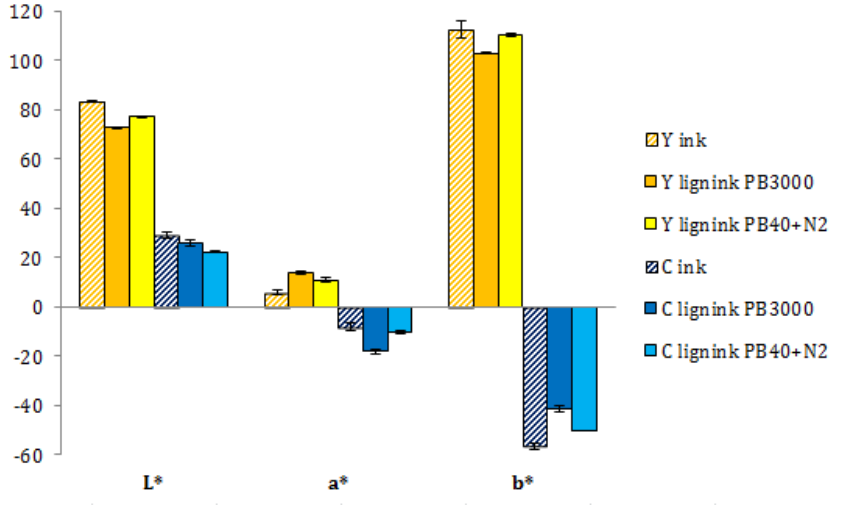

*Figure 4: CIE L*a*b* values of Yellow and Cyan inks printed with Handcoater*

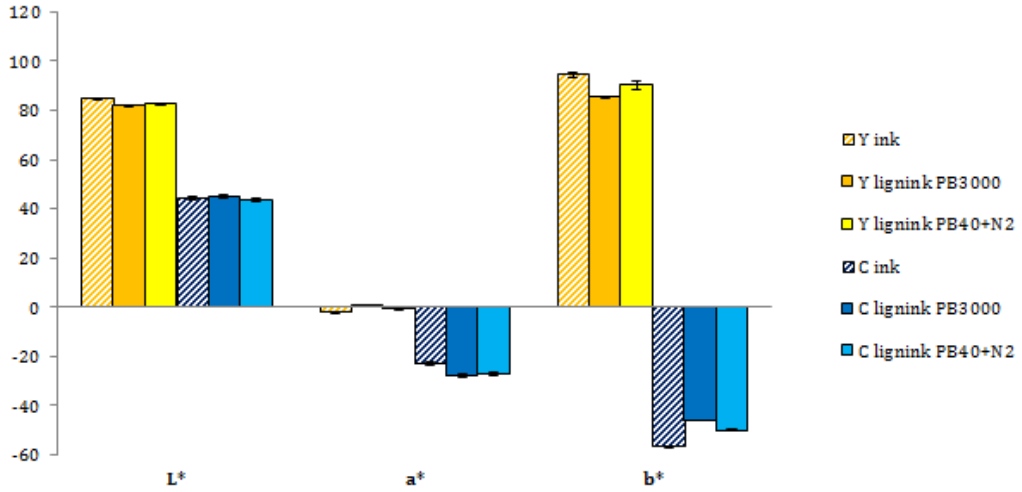

*Figure 5: CIE L*a*b* values of Yellow and Cyan inks printed with Handproofer*

As expected, whatever the colour and the printing process, colour differences are more pronounced for the inks made from unmodified PB3000 compared to bleached lignin. After bleaching, ΔE^*_{ab} is significantly reduced for yellow and cyan ink from 16.8 to 8.5 and 18.4 and 9.6, respectively, in case of printing with a Handcoater and from 9.6 to 4.7 and 11.9 to 8.3, respectively, in case of printing with a Handproofer. Nevertheless, these ΔE^*_{ab} are still too high to be unperceived by human eyes. Unmodified or bleached PB3000, incorporated into ink, leads to printable inks on a lab scale flexographic press. Once printed, colour difference is less noticeable even if unmodified Ligninks tend to be more “greenish” and less “fresh” than others.

Regarding the ability of the ink to be transferred from the cylinder to the substrate, bleached *Lignink*, and unmodified *Lignink* to a lesser extent, lead to a slightly lower but reasonable transfer compared to standard inks.

Table 6: Colour differences between standard ink and Ligninks (Handcoater printed)

Ink	**ΔE^*_{ab}**
Yellow *Lignink* ink PB3000	16.8
Yellow *Lignink* Bleached PB3000	8.5
Cyan *Lignink* PB3000	18.4
Cyan *Lignink* Bleached PB3000	9.6

Table 7: Colour differences between standard ink and Ligninks (Handproofer printed)

Ink	**ΔE^*_{ab}**
Yellow *Lignink* PB3000	9.6
Yellow *Lignink* Bleached PB3000	4.7
Cyan *Lignink* PB3000	11.9
Cyan *Lignink* Bleached PB3000	8.3

Gloss measurements for the printed samples, measured at a reflexion angle of 60° (geometric condition) showed that gloss tends to slightly decrease after replacement of the resin by lignin solution during ink formulation. However, such a decrease is limited when bleached lignin solution is used instead of unmodified lignin. This is an argument in favour of the bleached lignin solution.

2.3.2 Mechanical properties: rub and wet resistance

Hot rub and rub resistance of cyan samples printed with Handproofer on coated paper (Rieger) were evaluated. According to these results, rub and hot rub resistances of standard inks seem to be lower than for both *Ligninks*.

Hot rub resistance seems even to be enhanced for bleached *Lignink*. Each printed sample is more damaged after hot test compare to the one realized at room temperature. Nevertheless, rub resistance comply with the requirements for both *Ligninks*.

Wet resistance tests after one week were also conducted. Contrary to hot rub and rub resistance test, wet resistance of cyan printed samples is better for standard inks compared to unmodified and bleached *Ligninks*. Pekarovicova and Husovska (2015) assert that emulsion resins are needed for film-forming properties and water resistance. This emulsion resin, present in the standard inks, is partially replaced by lignin solution either bleached or not in case of *Ligninks*. Results of wet resistance test are hence in accordance with literature.

Furthermore, regarding wet resistance of printed lignin solutions, bleached *Lignink* has a lower wet resistance than unmodified *Lignink*. Indeed, presence of higher amount of hydrophilic groups combined with the presence of residual sodium salt can have an impact on wet resistance of formulated inks.

2.3.3 Drying speed

Drying speed was quantified by using a glass bar. Immediately after printing with a Handcoater #1 (6 µm wet film thickness) and every 5 seconds, the glass bar was pressed against the printing sample until drying.

Presence of lignin tends to decrease slightly the drying speed but all the *Ligninks* are still complying with the requirements.

4. Conclusions

PB3000 and Bleached PB3000 lignin solutions were used in replacement of styrene-acrylic emulsion resin to formulate some bio-sourced inks, called *Ligninks*. Rheological properties of both *Ligninks* were found close to those of water-based flexographic standard inks. Bleached *Lignink* was even found better since it does not need further viscosity adjustment to comply with requirements. Similarly, bleached *Lignink* tends to have a slightly lower surface tension than unmodified *Lignink*. Presence of bleached lignin limits the foaming ability and reduces the foam stability in the ink and therefore the printing issues. Both *Ligninks* are printable either with a lab scale machine, simulating flexographic process, or with a Handproofer and a Handcoater.

However, presence of lignin even bleached leads to a significant colour deviation.

Notwithstanding, contrary to unmodified *Ligninks* for which colour deviation is too important, bleached *Lignink* could be easily used in some non-constraining fields. Actually, presence of bleached lignin will limit the gamut, which is the area of the reproducible colours by inks combination. In the same way, addition of unmodified lignin reduces the gloss of the printed sample whereas incorporation of bleached lignin limits this decrease. Presence of bleached lignin, and unmodified one to a lesser extent, enhances rub and hot rub resistance of the printed samples. The latter will hence comply with one of the main functions of the printed substrates, which is to resist handling of operators and customers. Drying time conforms to the constraints as well. Nevertheless, wet resistance of bleached *Lignink* is reduced compared to unmodified *Lignink* and even more to standard ink. Some improvements are hence still needed in terms of wet resistance to obtain an ink that fulfil with every requirements. Once again, without further enhancements, bleached *Lignink* could even so be used in some nonconstraining fields. Further works could be first investigated in ink formulation. Only ready-to-use extenders with fixed amount were used during these first trials of formulation. Results presented in this paper give then only an insight of the bleached lignin potential in water-based flexographic ink formulation.

Acknowledgments

LGP2 is part of the LabEx Tec 21 (Investissements d'Avenir – grant agreement n°ANR-11-LABX-0030) and of the Energies du Futur and PolyNat Carnot Institutes. This research was made possible thanks to the facilities of the TecLiCell platform funded by the Région Rhône-Alpes (ERDF: European regional development fund). The authors are grateful to ANRT for the financial support.

References

Borges Cateto, C.A., 2009. *Lignin Based Polyurethanes* : *Characterisation, Synthesis and Application*. Doctoral Dissertation. Faculdade de Engenharia da Universidade do Porto and Institut Polytechnique de Grenoble.

Caes, B., Rivas, M. and Noirot, P.-A., Siegwerk Druckfarben AG & Co., 2015. *Printing ink with nitrated lignin ester as binder component*. Pat. WO 2015062910.

Dilling, P. and Sarjeant, P.T., Westvaco Corporation, 1984. *Reduction of lignin color*. U.S. Pat. 4,454,066.

Dilling. P. and Dimitri, M.S., 1990. *Lignin amine salt as binder for aqueous printing ink composition*. U.S. Pat. 4,891,070.

EuPIA, 2013. *Environmental Impact of Printing Inks: Information note*. [pdf] European Printing Ink Assocoation. Available at: <http://www.eupia.org/uploads/tx_edm/2013-03-05_EuPIA_Environmental_Impact_of_Printing_Inks.pdf> [Accesed February 2017].

Irion, C.E., Margot Corporation, 1948. *Liquid printing ink containing a lignin compound*. U.S. Pat. 2,449,230.

Laurichesse, S. and Avérous, L., 2014. Chemical modification of lignins: towards biobased polymers. *Progress in Polymer Science*, 39, pp. 1266–1290.

Llevot, A., Grau, E., Carlotti S, Grelier, S. and Cramail, H., 2015. From lignin-derived aromatic compounds to novel biobased polymers. *Macromolecular Rapid Communications,* 37(1), pp. 9–28.

Matzinger, M., Westvaco Corporation, 2000. Water-based ink jet ink compositions containing carboxylated lignin. U.S. Pat. 6,045,606.

Miller, J.E. and Dilling, P., Westvaco Corporation, 1986. Water-based printing ink compositions containing a lignin acetate binder. U.S. Pat. 4,612,051.

Pekarovicova, A. and Husovska, V., 2015. Printing ink formulations. In: J. Izdebska and S. Thomas, eds. 2016. *Printing on Polymers: Fundamentals and Applications*. Oxford: William Andrew, pp 41–55.

Piluso, C., Serafano, J., Kloock, L.M., Grandke, R. and Bradlee, C.A., 2009. *Eco-Efficiency Analysis Demonstrates the Environmental and Economic Benefits of Flexographic Printing Inks in Film Applications*. [pdf] BASF USA. Available at: <http://www2.basf.us/naftaresins/documents/Eco-Efficiency-Analysis-Paper.pdf> [Accessed February 2017].

Ren, C. and Li, Z., 2001. Oxidative degradation characteristics of the products of wheat straw alkaline lignin. *Linchan Huaxue Yu Gongye,* 21, pp. 49–54.

Robert, T., 2015. Green ink in all colors - printing ink from renewable resources. *Progress in Organic Coatings,* 78, pp. 287–292.

Schilling, P., Westvaco Corporation, 1993. *Lignin amine salt-based binders for water-based black ink formulations*. U.S. Pat. 5,188,665.

Voet, A., Huber Corporation, 1950. Sept 23. *Inks*. U.S. Pat. 2,525,433.

Smart Packages by Means of Intelligent Codes

Mustafa Bilgin and Johannes Backhaus

Bergische Universität Wuppertal, Rainer-Gruenter-Straße 21, 42119 Wuppertal, Germany

E-mail: bilgin@uni-wuppertal.de; jbackhaus@uni-wuppertal.de

Abstract

Via Internet of Things a package reports the history of its exposition to critical environmental influences. In this paper, a concept of how to print sensitive dyes as codes on packages is introduced. The codes are supposed to be checked for information about critical exposure of a package. They are comprised of sensitive dots which can be translated into information about changes in terms of water/moisture, temperature, UV-light, pressure, acids etc. There are different types of stimuli responsive sensitive dyes that are modified by different additives. One type is reversible, while the other is irreversible and remains in a switched colour state after exposition. These irreversible "sensors" operate independently from an external energy supply. This concept follows a certain procedure: at first, a code is generated and printed on a package by using sensitive dyes. Later, the code can be scanned and analysed so that data about the packages' history is transferred and displayed on a suitable hardware, e.g. a smartphone. Older states of the packages' history and other convenient information are shown. In addition, the code printed of sensitive dyes serves as a significant anti-counterfeit feature. In this paper, the concept and first research results will be represented. At first, observations about the printability of codes are presented. Printability will be examined with regards to printing parameters such as layer thickness, halftone dots and other technical parameters. Furthermore, the behaviour of different sensitive dyes will be looked at. Afterwards, a proposal for the design of an intelligent, readable code – such as the QR-code, which is able to communicate with the Internet – will be made.

Keywords: stimuli responsive dyes, sensitive dyes, intelligent packaging, smart packaging, intelligent code

1. Introduction and concept

Both product identification and information about originality and condition of goods are highly relevant in a globalised world. Counterfeit on the one hand and adverse environmental influences (destruction due to environmental effects) on the other hand, are factors that need to be identified and prevented. While counterfeit protection applies to all goods, environmental conditions during storage and transport only damage certain products such as food, pharmaceuticals, cosmetics, chemicals, seeds etc.

The aim of this research work is to develop a system for packages that enables to find out to what extent the package has been exposed to harmful influences. The concept (Figure 1) is based on a 2D/3D code whose printed dots are composed of different sensitive dyes (2D) and of different layer thicknesses (3D). These kinds of sensitive dyes switch their colours irreversibly due to relevant external influences. Code analysis and comparison provide information about the code's state and intensity of influences on the package. Analysis instruments include customary smart devices (e.g. smartphones) as well as a web server that stores information on the original code. Both the smart devices and the web server communicates via Internet of Things (IoT) supplied by web interface and middleware. The Internet of Things is the connection of anything (e.g. packaging) equipped with sensors, software and wireless technologies (NFC, Bluetooth, 2D/3D code etc.) to an autonomous network (Ashton, 2009).

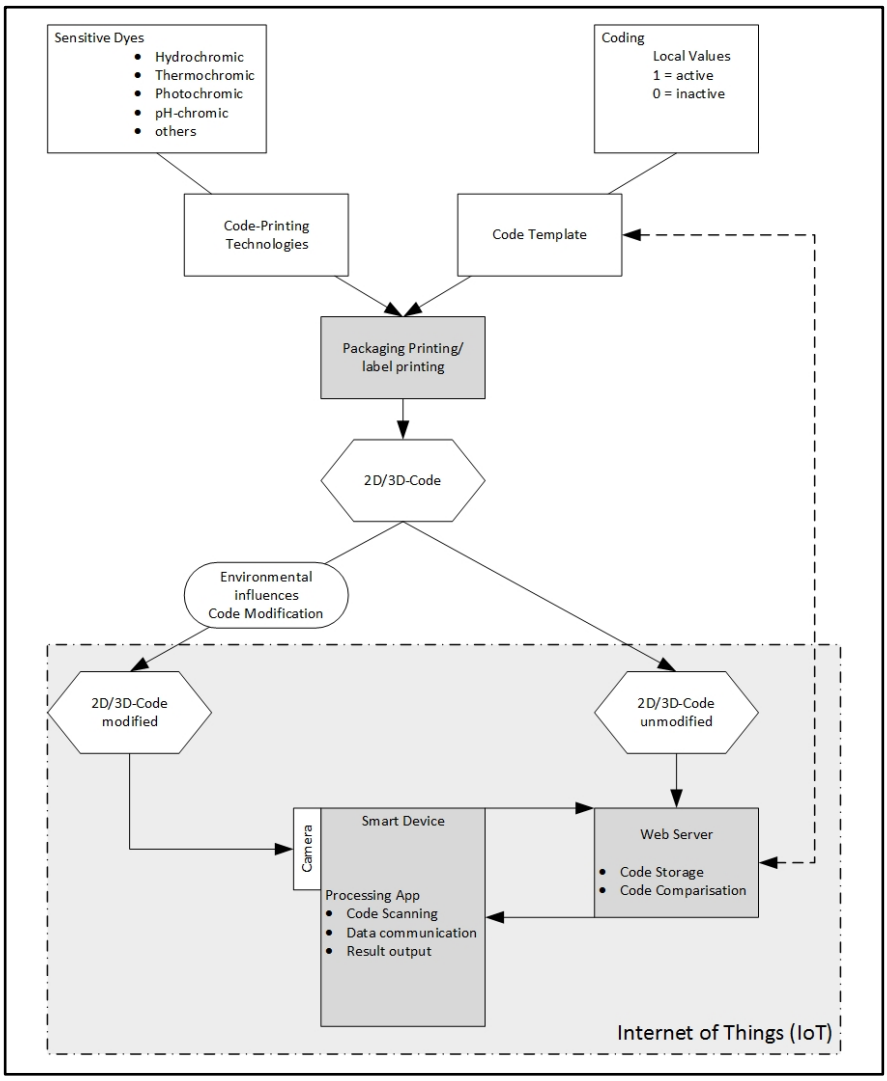

Figure 1: General concept of IoT based history tracing for packages

2. Methods and materials

2.1 Types and properties of sensitive dyes

Sensitive dyes are made of colour-bearing groups of molecules in the form of chromophore structure, often in organic solutions. Chromophore structures have covalently unsaturated groups of conjugated π-bond systems that are responsible for absorption in UV or visible range (Latscha, Kazmaier and Klein, 2016). They can be affected by molecular structure variations, induced by delocalised electrons (resonance) in reaction to external physical or chemical stimulations. The molecules of the chromophoric substances change their absorption properties (λ-Shift) of their inherent chromophoric structures. Beyond visible wavelengths, chromophores are subjectively considered colourless just like benzene, C_6H_6 (λ max = 255 nm) (Latscha, Kazmaier and Klein, 2016).

Sensitive dye molecules can switch between two states and change their chemical structures if they are affected by physical influences like water/moisture (hydrochromism), temperature (thermochromism), intensity of light/UV-light (photochromism), pressure (piezochromism), acids (pH-chromic) etc. (Hunger, 2003). There are different chromophoric behaviours. One type of molecule resets after exposure (reversible), while the other type remains irreversibly in the switched colour status (Dobrinski, Krakau and Vogel,

2010). Here, the irreversible type of chromophores is of interest because they document former physical and chemical load.

2.2 Printability, adequate printing technologies

The future aim is to print sensitive dyes by using inkjet printing. This printing principle seems to be ideal for printing the required codes. For one thing, a printing form is not necessary; for another thing, defined multi-layer printing is enabled in order to generate dots of one sensitive dye in different thicknesses.

However, today irreversible sensitive dyes are not yet available for inkjet; they are only available for screen-printing and flexo. Thus, the first experiments shown here base on screen-printing. In addition, the appropriate inkjet technique of sensitive irreversible dyes has yet to be developed in further experiments. For instance, thermal inkjet is not suitable for thermochromic dyes. For the application of the thermochromic dye, the direction of the stream must be controlled electronically by piezoelectric inkjet (Lent and Elue, 1988). Regarding these aspects, sensitive dyes will be modified for inkjet use afterwards. The results of the pre-investigation in screen-printing will be used to carry out further investigations by piezoelectric inkjet.

Printing experiments have been based on test screens, which show dots, QR codes and dot distances of different sizes as well as continuous areas (Figure 2). All specimens were printed on a semiautomatic screen printer (SPS-Uniprint), UV-exposure unit (AKTICOP 5000), using different polyester screens (thread count *F*n = 140/cm; 100/cm; 71/cm; 54/cm, with mesh angle = 45°); squeegee angle: 13.5°; printing speed: 116 mm/s; snap-off (distance between screen and substrate): 1.5 mm.

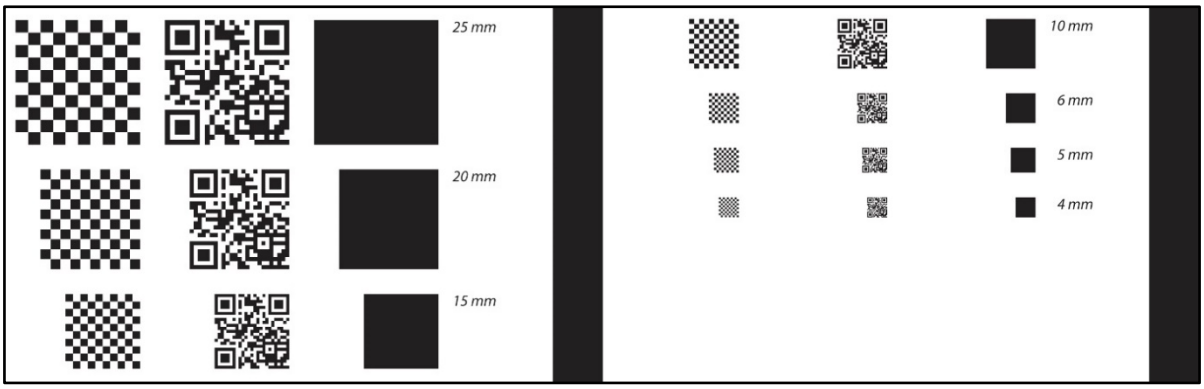

Figure 2: test screen with dots, codes distances and coherent areas

In the first experiment, the test screen was printed on a uniform substrate (Table 1), to check the functionality of the irreversible sensitive dyes, as an active and inactive colour change. Due to contamination, the respective dots of the code irreversibly changed, as to be seen below:

Hydrochromic dye: black → transparent
Thermochromic dye: white → black
Photochromic dye: transparent → dark blue
pH-chromic dye: pink → grey-blue

In the second experiment, different layer thicknesses of sensitive dyes were applied by Mayer rod also to a uniform substrate to make statements about the sensitivity of reaction.

2.2.1 Standardization

In order to ensure the reproducibility of this experiment, a standardization was prepared during the application, measurement and storage of the printings. Possible influences were recorded. Variables such

as temperature and humidity were controlled by air-conditioning in the laboratory. The temperature was continuously 20 °C (+/– 1 °C); the relative humidity was 55 % (+/– 1 %).

2.2 Materials

Table 1: Material overview

Substrate:	Multicolor Mirabell™ Chromo-duplex-carton with white and double-faced front and a grey pigmented back (Papyrus Deutschland GmbH & Co. KG). Thickness: 0,340mm Grammage: 250 g/m^2
Dyes:	Hydrochromic dye (LCR Hallcrest) Thermochromic dye (Smarol) Photochromic dye (skyrad) Thinner: Ce-Jet® 090 (7101M000002) Retarder: VZ 2 (7102M000002)
Screen Photo emulsion:	FOTECOAT 1833 Stencil thickness below mesh: 6-7 µm

The materials used in the experiment are shown in Table 1.

3. Results

Further investigations show that sensitive dyes will react in different modes. This fact has to be considered when printing the codes. In fact, the consequences cannot be fully predicted yet. Figure 3 shows first results. Based on microscope video recordings, the change of colours was observed until no more change could be seen.

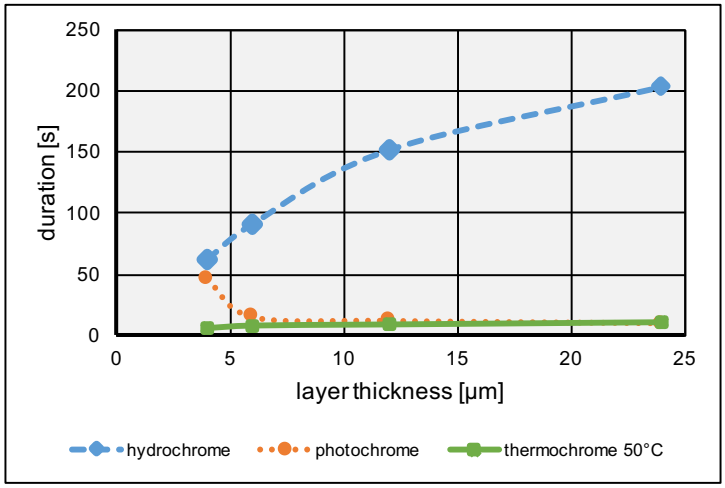

Figure 3: Duration of colour changeover (visually estimated saturation)

Thermochromic dye changes very fast and a dependence of layer thickness only is to be realised for thin layers. Heat conduction of thermochromic dye appears to be high and the colour change of upper layers may cover the dot's lower layers quickly.

Photochromic dyes: After daylight contamination, the colour of photochromic dyes changes completely within a few seconds. A spectral photometric analysis of colour change must follow (tested dye was config-

ured UV sensitive). The light seems to pervade the dye-layer immediately and initiates the colour change. In addition, colour-changing time seems to decrease with layer thickness (Figure 3). This could be because the photochromic dye dot is bombed by light with a spill over of photons (Herbst and Hunger, 1995). Only when a sufficient layer thickness is reached, there are enough reactants to show an entire colour changes.

Hydrochromic dyes: In order to cause a change of colour water molecules have to diffuse into the layer. The following observations and measurements are based on microscope video recordings immediately after water loading the printed hydrochromic dye. (Microscope: Keyence 3D Laser Scanning Confocal Microscope).

Then four phenomena occur:

First: Colour transition starts at the dot's' edges as well as at the rough surface peaks.

Second: Duration of colour transition depends on the thickness of the layer (Figure 3).

Third: The surface of the hydrochromic dye proves water-repellent. When coated with water two effects can be observed: water on the hydrochromic dye film contracts to single drops (surface tension effect: one substance, in this case water, is of high surface tension and the other substance is of low surface tension). Water next to the hydrochromic dye is absorbed by the board (Figure 4).

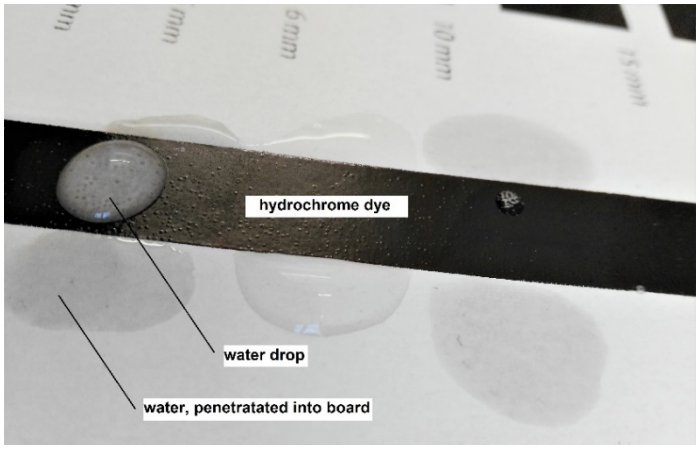

Figure 4: Hydrochromic dye, water repellent

Primary contamination: The hydrochromic dye is directly top down contaminated by the water drops upon it. Contamination areas are circular, according to the drop's contact areas.

Secondary contamination: The absorbed water partially imbues the board and contaminates the hydrochromic dye from the bottom gradually. After several hours, an additional small increase in colour change can be observed (Figure 5).

Fourth: A contaminated dot of hydrochromic dye not only shows colour change but also its volume decreases significantly. First calculations shows that the volume decreases about 45 %. This phenomenon very clearly can be observed at the roughness peaks on the surface of a dot: many of them are levelled.

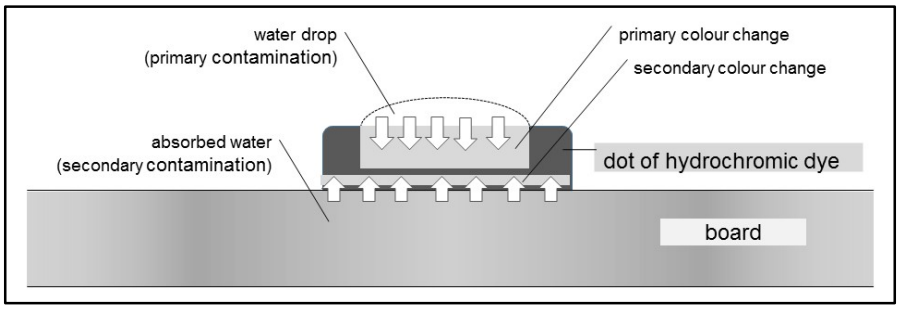

Figure 5: Primary and secondary contamination of hydrochromic dye

Figure 6 shows a topographic profile of a dot, generated with a laser microscope (low areas: blue; high areas: magenta-dashed). Left photo: dot before water contamination, about 60 % of the dot area shows peaks. Right photo: dot after contamination, peak areas are reduced to about 30 %.

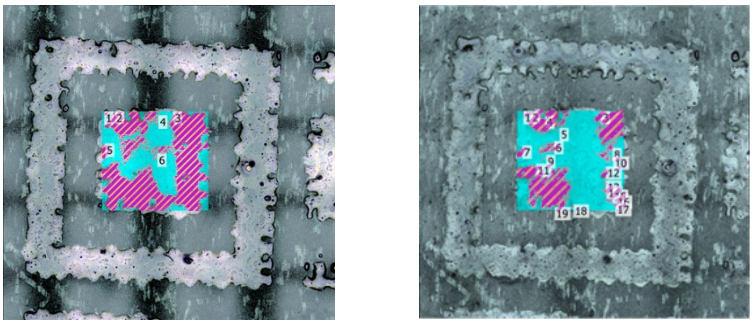

Figure 6: Roughness peaks on surface of a dot of hydrochromic dye (magenta: areas of peaks)

Hydrochromic dye shows longer duration for changing colour. Water molecules must penetrate inside the dye before the colour changes (Figure 3). This mass transport takes more time than the transport of heat or photons (thermochromic and photochromic dyes). These facts have to be considered when a code is designed as well as the insight into the behaviour of colours which change in dependency to layer thickness and to duration of the contamination.

3.1 2D/3D code

Coding: Every dot of dot matrix code, like an invented system of a QR code (Denso Wave, 1994; International Organization for Standardization, 2015) can appear in two modes: either active → value = 1 or inactive → value = 0. Irreversible sensitive dyes switch modes while changing colour trough external contamination (2D coding). Dots of different layer thicknesses can give information about intensity/ duration of contamination (3D coding). In order to receive reliable information from dot analysis, it is recommended to place several equal (dye and layer thickness) dots per code. A randomized allocation of the dots (Figure 7) will prohibit clusters of equal dots, which are at risk of partial contamination of one single cluster. Furthermore, randomisation is also an effective anti-counterfeit feature.

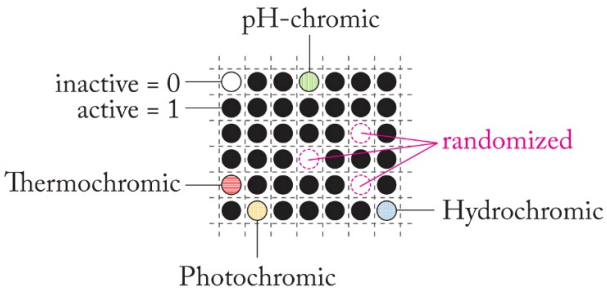

Figure 7: Randomized positions in a matrix

This way of coding enables different information to be included in one single code: the kind of contamination by environmental influences (temperature, water, UV-light, etc.); intensity as well as duration of influences (by means of layer thickness); limits of influences (e.g. one dye for change colour at −18 °C, another dye for change colour at 25 °C); and other conventional information, independent of sensitive dyes.

3.2 Hardware and software

Smart devices, smartphones, tablets, smart glasses etc. are very popular. They are all equipped with lots several sensors. Here, the image sensor inside the camera is of importance on the hardware side, while, web- applications (e.g. browser) and TCP/IP communication are important on the software-side for internet communication. Smart devices can read the information of the 2D/3D code and send data via browser to a secure website or bi-directionally to a secure web-server. The server represents the other important hardware component of the system.

Particular applications for smart devices are not necessary because the browser can directly access the web-server via web interface. A responsive design allows a uniform presentation of the content of a web page on different end devices, independently of brands and operating systems (Figure 8). The server includes data of the web mask (website) to be accessed by the browser via TCP/IP. Encrypted data exchange operates via web-server to a MySQL-database. The web interface is based on HTML, CSS and contains a PHP form.

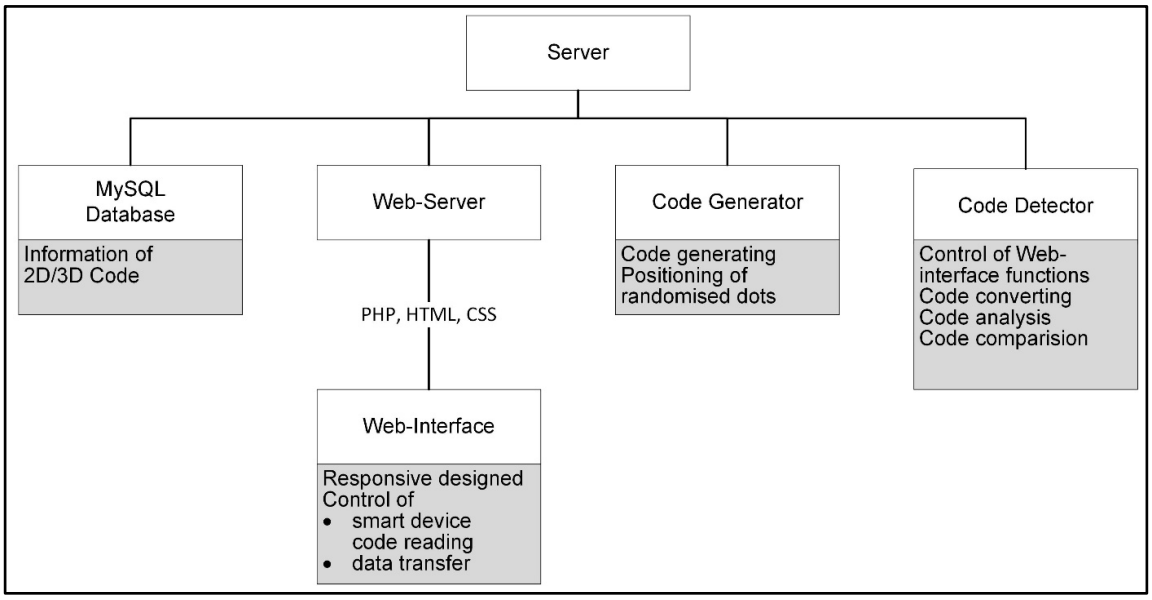

Figure 8: Software Concept

3.2.1 Qualitative limits of smart devices (cameras)

The quality of smart device cameras (e.g. autofocus, colour fidelity, etc.) has to be examined as it can generate the recording of deviant code information. This is required in order to develop tough data transfer software for the data.

In order to transfer the content of the 2D/3D code colour image information of the camera, the content at first has to be transformed into grey scale information by means of a server side monochrome filter. This is an interim step of binarisation of the entire code. During this process, the colour shift of the device can falsify grey scale conversion and binarisation.

4. Conclusions, further research work

Dynamic codes on packages can provide information about the packages' contamination history by environmental influences. This can be of interest for many kinds of packages such as fresh and frozen food, pharmaceuticals, medical and technical-products, cosmetics, hardware etc. Therefore, a general concept was developed based on 2D/3D codes made of sensitive dyes and data communication via Internet of Things. One additional aspect is the device-independent front-end (user interface). The design of the dot matrix enables flexible coding and multifunctional storage of information (Lenk, 2007; 2014).

Fundamental knowledge of different sensitive dyes is known, but experiments in printing and contamination show that a general handling of sensitive dyes is unappropriated. Each dye needs particular handling and shows specific reactions which have to be considered when coding and analysing data. In fact, the choice options of irreversible sensitive dyes are few but it is known how to modify the sensitivity of dyes for different areas of purpose. The functionality of sensitive dyes as an irreversible active and inactive switch can be realized. Through contamination, the respective dots of the code irreversibly change. Furthermore, it has to be examined, how other technical parameters, e.g. halftone dots, can influence the functionality and sensitivity of the printed dyes.

The particular chemical structures of sensory dyes are important regarding their printability. For example, thermochromic materials can differ in their structures, which can base on light reflection, light absorption, light scattering and burst of microencapsulation. There are two kinds of thermochromic classes: cholesteric liquid crystals and thermochromic composites based on leuco dyes (Seeboth and Lötzsch, 2013), which have to be considered in future research. There is also a concept and design for data generation, handling, transfer, analysis and storage. This has to be programmed, implemented and tested.

References

Ashton, K., 2009. *That 'Internet of Things' thing: in the real world, things matter more than ideas*. RFID Journal. [online] Available at: <www.rfidjournal.com/articles/view?4986> [Retrieved 02 May 2017].

Denso Wave, 1994. *QRcode 20th anniversary*. [video online] Available at: <http://www.denso-wave.com/en/adcd/qrcode_20th_anniversary/> [Retrieved 15 February 2017].

Dobrinski, P., Krakau, G. and Vogel, A., 2010. *Physik für Ingenieure*. 12. Auflage. Wiesbaden: Viewg+Teubner | GWV Fachverlage GmbH, p. 220.

Herbst, W. and Hunger, K., 1995. *Industrielle Organische Pigmente: Herstellung, Eigenschaft, Anwendung*. Zweite, vollständig überarbeitete Auflage. Weinheim: VCH Verlagsgesellschaft mbH, pp. 98–99.

Hunger, K. ed., 2003. *Industrial Dyes, Chemistry, Properties, Applications*. Weinheim: WILEY-VCH Verlag GmbH and Co. KGaA, p. 569.

International Organization for Standardization, 2015. *ISO/IEC-18004:2015 Information technology -- Automatic identification and data capture techniques -- QR Code bar code symbology specification*. Geneva: ISO.

Latscha, H.P., Kazmaier, U. and Klein, H.A., 2016. *Organische Chemie: Chemie-Basiswissen II*. 7. Auflage., Berlin, Heidelberg: Springer Verlag, p. 540.

Lenk, B., 2007. *Handbuch der automatischen Identifikation - Band 1*. 2. Auflage. Kirchheim: Monika Lenk Fachbuchverlag.

Lenk, B., 2014. *Handbuch der automatischen Identifikation - Band 2*. 2. verbesserte Auflage. Kirchheim: Monika Lenk Fachbuchverlag.

Lent, B.A. and Elue, P.N., Videojet Systems International, Inc., 1988. Thermochromic jet ink, United States Patent 4,756,758.

Seeboth, A. and Lötzsch, D., 2013. Thermochromic and Thermotropic Materials. Singapore: Pan Stanford Publishing Pte. Ltd., p. 139.

Canadian Magazine Publishers – State of the 'App'

Christopher Smyth and Carman Fan

Ryerson University, School of Graphic Communications Management, Toronto, Canada

E-mail: csmyth@ryerson.ca

Abstract

This paper is an analysis of print based Canadian consumer magazines, studying a selection of titles, their equivalent digital issues, and overall website architecture. It investigates how publishers are currently integrating a variety of digital platforms, and interactive approaches. Overall, the use of interactive elements in digital editorial content is relatively low, appearing in less than half of the issues. Video is leveraged in just over a third of these interactive examples. The use of interactivity in advertisements is significantly lower. In addition, the magazines' websites are not configured to provide a high level of usability and support for interactivity on mobile devices. The sites generally rate as both slow and not mobile 'friendly'. As well, the sites do not appear to be taking steps to address the possible use of ad blocking technologies. This study forms a useful benchmark for how Canadian publishers are currently leveraging digital infrastructure. It highlights how publishers today may be focusing their efforts on less popular devices and platforms, 'native apps' for tablets and the iOS, while their readers are migrating to the use of Internet browsers on smartphones.

Keywords: digital editions, interactive, magazines, mobile, native app, tablet, smartphone

1. Introduction and background

This paper is an analysis undertaken on a selection of print based Canadian magazines, and how they are currently integrating a variety of different digital edition formats. It also includes the different platforms used, as well as the use of interactivity in editorial and advertising content. In addition, it reviews each magazine's website architecture, including support for mobile (smartphones) as well as ad blocking technologies.

1.1 Background

Apple introduced the iPad almost 7 years ago (Ritchie, 2017), and the resulting market for tablets shifted the way readers consume content. This presented a fresh opportunity for publishers to re-engage with their audiences, which had been moving online for some time, by leveraging a familiar magazine format within a new digital framework.

However recent industry reports have indicated that, as an overall industry, publishers may not have capitalized on this opportunity. Today's rise in the use of smartphone devices ('mobile') may present a renewed opportunity for consumer magazines to engage their readers, and monetize their content.

For the purposes of this research, a magazine, either print or digital, is being defined as something that has a clear beginning, middle and an end. It is a structure that contains curated content, which has been through an editorial review, and has an enhanced 'aesthetic treatment' applied. They are 'date stamped', and are issued on a weekly, monthly, or quarterly basis (Santos Silva, 2011).

The focus of this research project is on consumer publications, because of their wider audience, and their relative importance to media and culture. The initial goal is to identify which different platforms consumer publishers in Canada currently use for distribution – are Canadian publishers focusing on devices and approaches that have the greatest potential to reach audiences?

One concern is that the wide variety of technologies available, with different operating systems, device sizes and screen aspect ratios, creates a barrier for publishers "seeking a broader distribution footprint". As well, there has been discussion in the publishing industries about specific digital formats, and whether to invest in downloadable 'native apps' or offer web-based versions.

This analysis investigates a selection of Canadian magazine titles, first for the availability of digital editions, their specific formats, and which devices and platforms are supported. Next, the digital editions found were analysed with regards to interactive editorial and advertising content. The frequency and type of interactive features were catalogued; these affordances include 'clickability' of text/images, as well as video and audio content (Miric, 2015).

In addition, the magazines' websites have been checked for their ability to adjust to different screen sizes, their relative speeds, as well as overall support for mobile devices. Related to this, as Canadian consumer magazines are heavily supported by advertising revenue, each site's response to the use of 'ad blocking' technologies was tested.

This analysis of the current state of magazine platforms is useful to help identify and benchmark trends, which could provide valuable insights for publishers considering a shift in platform strategy.

2. Materials and methods

There are approximately 975 English language consumer magazine titles published in Canada (Magazines Canada, 2015), covering a wide range of themes and of varying circulation levels. An in-depth analysis of each title was impractical due to shear volume.

Selection criteria; the 17 leading editorial categories were identified, using published circulation data from Canadian Advertising Rates and Data – cardonline.ca, Magazines Canada, as well as the International Federation of the Periodical Press (FIPP, 2014).

In each category, sample titles were selected with lower, moderate, and higher circulation rates in an effort to capture information from a variety of different 'size' magazines (not every editorial category had titles in each circulation 'band').

- Lower circulation is defined as 1 to 99 999
- Moderate circulation is defined as 100 000 to 499 999
- Higher circulation is defined as 500 000 to 1 million plus (Magazines Canada, 2015)

When more than one title was available, the criterion was to have as many different publishers included (many publishers offer titles in multiple categories and/or have multiple titles). This was done in an effort to analyse a wider range of digital strategies. A total of 35 titles were selected, representing 26 different publishers. Please see 'Appendix A' for a list of categories, publishers, titles, and circulation numbers.

From this sample set, the availability of different formats of digital editions, platforms and device support was documented. Print and digital versions (iPad tablet) of the same title and issue were obtained for anal-

ysis. The relative number and type of interactive elements leveraged in the digital editions were identified, and catalogued.

In addition, website usability, speed, and responsiveness, both mobile and desktop, were explored through tools, including Google's 'PageSpeed' tests – testmysite.thinkwithgoogle.com, and 'BrowserStack' – www.browserstack.com.

Finally, the websites for each title were tested for their response to the use of ad blocking technologies using an Internet browser. This was accomplished using two identical Apple iPads, both running iOS 9 and the 'Safari' browser; one configured with 'Crystal', a leading ad blocking software, the other without.

3. Results and discussion

3.1 Digital edition formats

A total of 86 % of the magazines studied offers and publish some format of digital editions that correspond to their print issues (Figure 1). The format of these digital editions can be a 'digital replica', an 'extended PDF', or a 'native app'.

A 'digital replica' is an electronic version of the print edition, usually derived from the Adobe Portable Document Format files (PDF) that were created to transfer content for the production of the print issue. There are no additional interactive features built into this digital edition type.

'Extended PDF' editions are also 'replicas', but have some basic interactive elements incorporated for enhanced usability, such as a link to another relevant article.

A 'native app' refers to a magazine that is designed and created specifically for a digital device. It is generally considered as providing a superior user experience, compared to other options. Native apps typically have added features; multimedia content, connectivity through social media channels, as well as including additional content from the print issue. They are generally more expensive to produce (Nordicity, 2009).

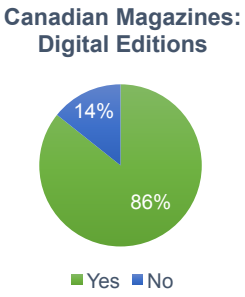

Figure 1: Of the 35 titles reviewed, 86 % offer digital editions

Of the titles offering digital editions, Figure 2, almost 75 % offer a 'native app' version, with 67 % offering a 'replica' edition. The 'extended PDF' edition is less popular at just under 50 %. Many publishers opt to offer digital editions in more than one format, offering a native app version, but also a replica (often delivered through a digital newsstand platform such as Magzter, Zinio or Texture).

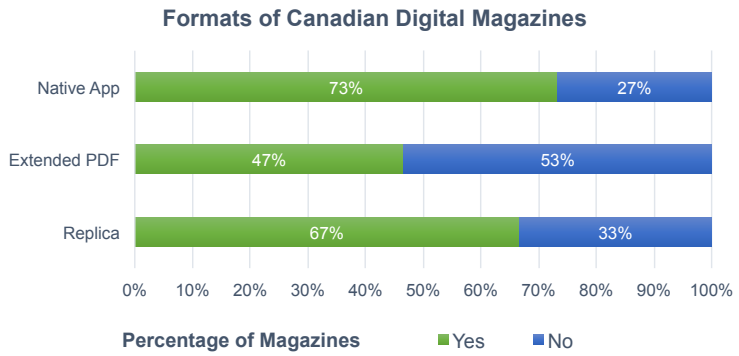

Figure 2: Different formats of digital editions of the 30 titles offering digital editions; note that 63 % of the magazines offering digital formats utilize multiple formats

In our sample, 19 titles offer more than one digital format, 10 only offer a replica edition, and 1 provides just an extended PDF. No title provides only a 'native app' digital edition.

3.2 Native App platforms

As shown in Figure 3 below, the majority of titles offering a 'native app' supports both tablets and smartphones, however 9 % (two titles) publish for tablets only.

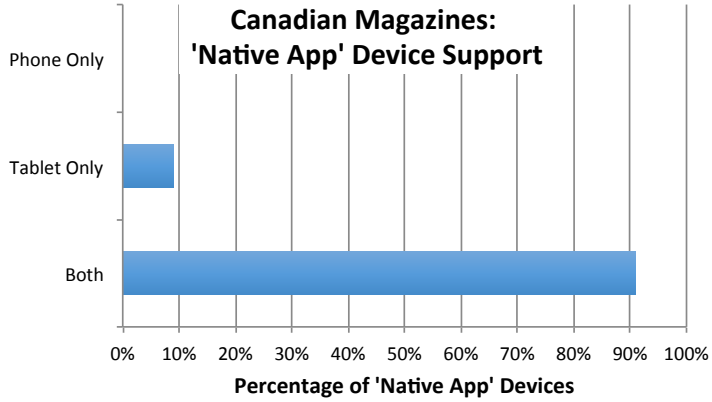

Figure 3: 'native app' device support

3.2.1 Tablets

Android and iOS are the two primary operating systems for tablets. Apple's iOS is used primarily in their devices (iPad and iPhone), while Google's Android operating system is used in a variety of tablets and smartphones (e.g. Samsung, LG, HTC, Nexus). In the North American market, Apple has the majority share of the tablet market, with over 70 % of tablets running iOS (Statista, 2016a).

Publishers appear to understand this, with 100 % of titles offering native apps for tablets supporting the iOS, while almost 75 % support both iOS and Android. No titles publish exclusively for Android based tablets.

3.2.2 Smartphones

In Canada, the leading operating system (late 2015) for Smartphones is Google's Android, with just over 50 % of the market. Apple follows with slightly more than 38 %, with the balance being some other brand of operating system (OS) (Hardy, 2015).

As with tablets, 100 % of titles with smartphone 'native apps' support the iOS, with 75 % supporting both iOS as well as Android. As with tablets, no titles publish exclusively for Android devices. Understanding the larger market share for Android, publishers may wish to consider a shift in platform focus for smartphones.

3.3 Interactivity

From the set of magazines offering both print and 'native app' editions, a specific print issue was compared with its digital counterpart, to examine the interactive features available in editorial and advertising content.

3.3.1 Editorial content

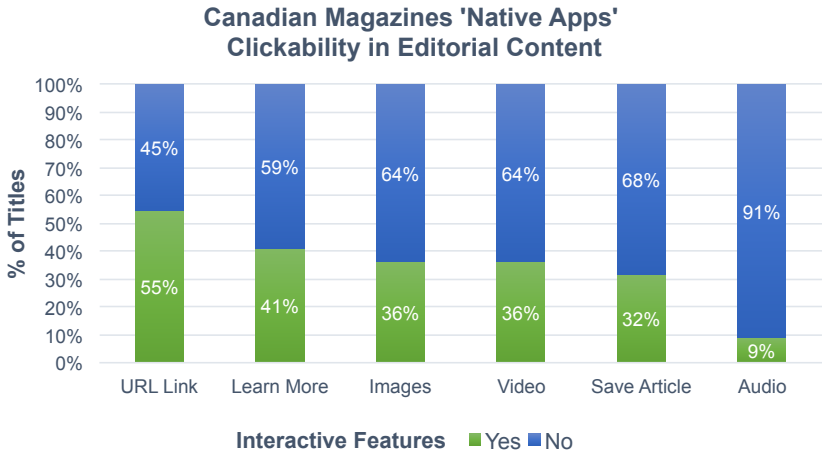

Figure 4: 'native app' editorial content interactivity

Additional links to other stories and content were the most common interactive element, used in 55 % of 'native app' issues Figure 4. Options for readers to interact with the content, to 'learn more' or to save the article for future reference, were also popular, respectively used approx. 40 % and 30 % of the time. For enhanced multimedia content, several options were available, with just over one third of issues offering editorial related video, or additional images (for example, a 'slideshow'). Audio was least popular, with 9 % offering recordings of interviews or similar content.

3.3.2 Advertising content

Advertisements were identified using accepted industry standard classifications (Idealliance, 2013): Straight from Print (SFP) ads are repurposed directly from the referenced print version, and can include a single link to an external website, Figure 5. Designed for Tablet (DFT) ads have been designed to fit devices – users do not need to 'tap and zoom' to read content. They can also include multiple external links. Enhanced for Tablet (EFT) ads are also designed for tablets, but also include multimedia such as animations, slideshows, video, or audio, as well as multiple external links.

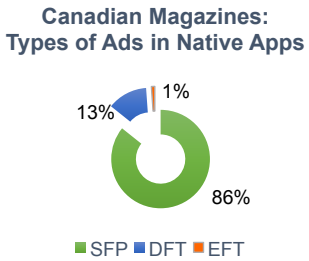

Figure 5: Ad types in digital editions

A total of 540 full page and half page ads were analyzed, with 1 % being identified as EFT, meaning they included interactive features beyond links to additional content. Examples of the interactive features found included video tutorials for applying beauty products, as well as multiple links to external social media sites. In some cases the ads took a measurable amount of time to load (more than four seconds), or caused the application to 'freeze'.

Of the total number of interactive ads identified, 10 % were 'house ads', advertising the magazine itself, its services, or other titles from the publisher. These ads could be serving a dual purpose, first to advertise the listed service, but also as 'interactive examples' for potential advertisers.

3.4 Magazine website architecture

3.4.1 Responsiveness

Each title's website was tested for support for adaptive/responsive design. These web design approaches are designed to reformat content for ease of use on different devices, screen sizes (aspect ratios) and resolutions, and configurations. This was tested by using Google's Chrome browser (v52 – released August 2016), BrowserStack, and by manually 'sizing' an Internet browser window.

In general, responsive designs change size 'fluidly' as they are scaled, Figure 6. Adaptive sites change in 'steps' or 'hitch' as the pageview size is changed (Alters and Hollis, 2017). Non-responsive sites do not adjust, and as a result the content is not easily accessible to the reader on tablets or smartphones.

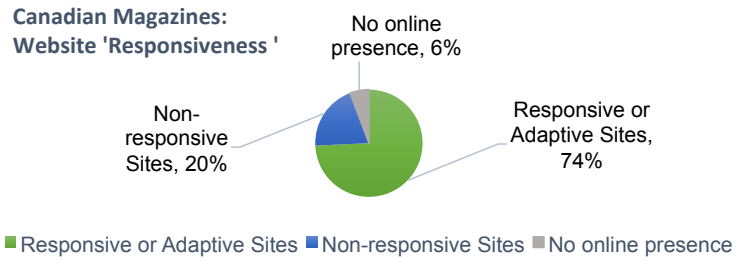

Figure 6: Magazine website responsiveness

Almost 75 % of the magazines evaluated had websites that adapted to the screen resolution of the device readers were using. However, 20 % had a site that did not accommodate different devices. Note that 6 % (2 of the 35 titles researched) did not have a website presence, Figure 6.

3.4.2 Desktop and mobile website speeds

The growth of the tablet market in Canada has slowed relative to the growth of a few years ago. In 2016, 40 % of Canadians reported using a tablet (Statista, 2016b), while approximately 75 % of adults had smartphones (Catalyst, 2015).

Regardless of the device, speed is important to online readers (Jacob, 2011), with some studies demonstrating that a page will be abandoned if it does not load within 3 seconds, a benchmark supported by John Mueller, a leading Webmaster Trends Analyst with Google (Schwartz, 2016).

The sample set of Canadian Magazine websites was analyzed to determine their overall speed. These tests were undertaken using a set of tools from Google, called PageSpeed (n.d.). The tools work to check a variety of server settings and page (code) configurations. They are not related to a user's bandwidth.

The results show, Figure 7, that the majority, almost 75 % of titles, have desktop sites that are relatively fast, rating 85 % or higher. A smaller number, 12 % of titles, have relatively slower speeds of 60 % or lower.

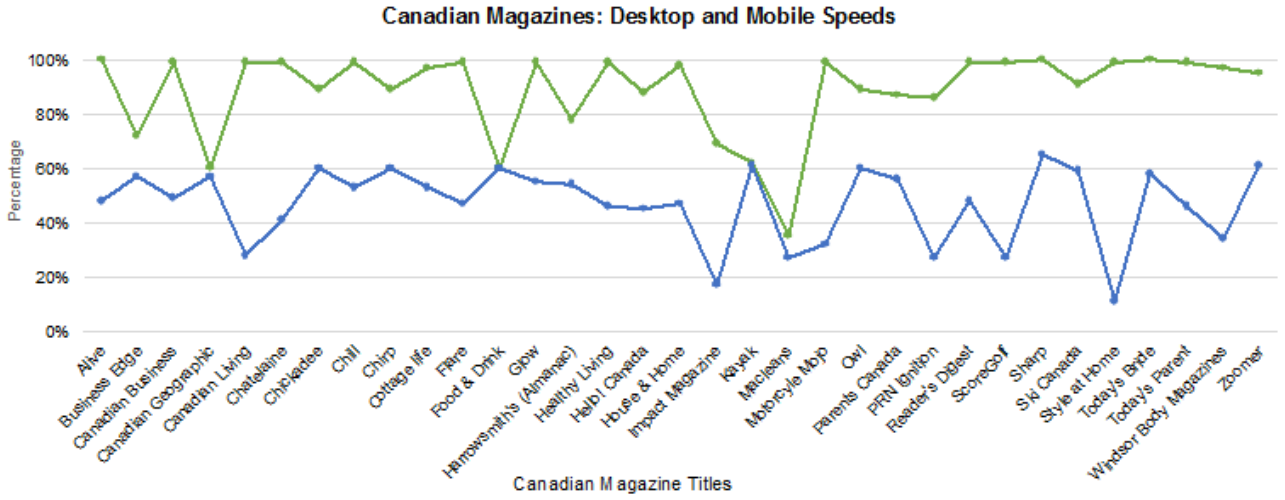

Figure 7: Magazine desktop and mobile sites relative speeds.

Mobile speed, however, is measurably lower than desktop, with 25 % of titles rating 40 % or lower speeds, and the highest speed being 65 %. Speed improvement suggestions, from PageTools, include enabling compression, as well as image optimization, for faster file transfer speeds (Sexton, 2016). It is also important to eliminate unnecessary page loading scripts, such as JavaScript and cascading style sheets (CSS), in the important 'above-the-fold' content (what the reader sees when they first land on a page) (Tarcomnicu, 2016). As well, landing page redirects should be avoided; they duplicate requests to the server, which increases the latency time to deliver the content to the reader (KempRugeLawGroup, 2015).

3.4.3 Mobile friendliness

In addition to load speed, a site being accessed from a mobile device benefits from being designed from a mobile user's perspective. Mobile 'friendliness' is the term used to describe this, the overall experience, different resolutions, font choices, and navigation tools (Ghazarian, 2014).

Of the 33 sites checked, 18 % rated 70 % or higher, with only one title above 80 %, Figure 8. Almost 20 % of the sites rated fairly low, below 40 %. The results demonstrate that magazine sites are generally not configured to be mobile friendly.

Reviewing the results by category there are no clear trends. However, titles that could be considered a leisure time activity, for example 'Automotive', 'Beauty', 'Fashion', 'Lifestyle' and 'Woman's' have moderate ratings, while 'Business' and 'Food & Drink' have higher scores. Perhaps this is because the latter groups might be accessed outside of the home more frequently (work, shopping), and benefit from a more 'mobile' focus. In some cases, magazines have built sites that are optimized for the mobile experience, but are not fast (e.g. 'Macleans'), with potential negative impact for their mobile audience.

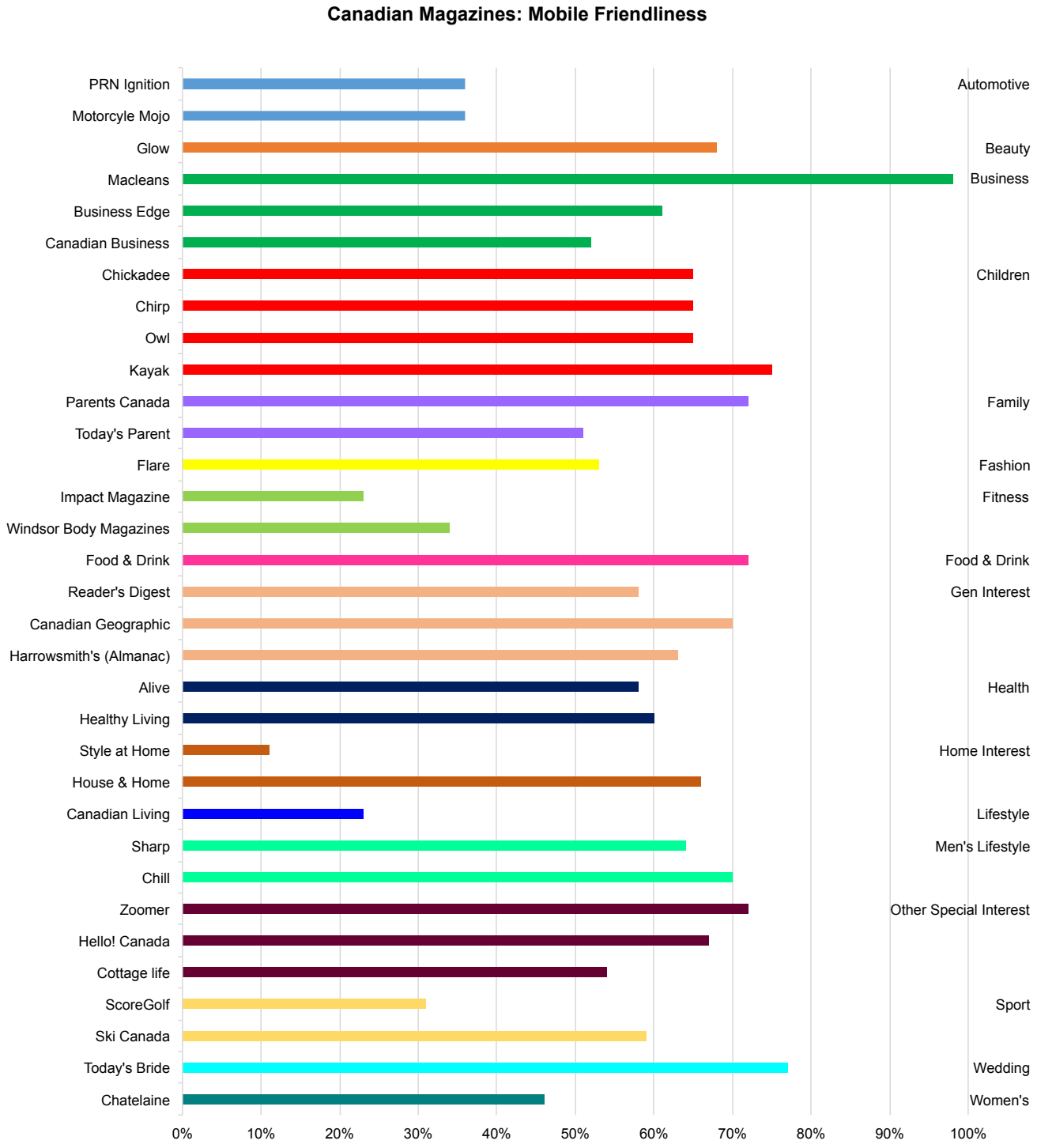

Figure 8: Canadian magazine sites 'mobile friendliness'

3.4.4 Ad blocking

Magazine readers install 'ad blocking' technology for a variety of reasons, which include faster delivery of content (An, 2016). 'Blockers' work by preventing 'requests' for the ad content from originally leaving the browser when the viewer navigates to a page. If an ad is 'blocked' it is not 'seen', and cannot contribute revenue for the publisher. Blockers accomplish this by checking the destination request of browsers, and "turning away those destined for specific no-go ad servers" (Blanchfield, 2016). An Ad Server is a web-based tool, delivering the actual ad content for publishers (Adobe, 2016). The ad content files are generally not available on the Publishers' websites. Ad blockers appear to be growing in popularity, posing a poten-

tial challenge for publishers who rely on advertising revenue to support content. A 2015 Pagefair study of ad blocking in Canada estimated the use of ad blocking software at 20 %. A different 2015 study, from Sourcepoint/comScore, placed it at 17 % (Lindzon, 2016).

It is possible for websites to determine if a visitor is using ad blocking technology, and deliver an alternative message (Kulp, 2015). Magazine publishers can use this in an effort to appeal to readers to turn off their blockers to help support the content. The magazine sites in this project were also evaluated for ad blocking responses. Two identical iPads were used, both running the same version of Apple's iOS 9 and Apple's Safari browser. One iPad also had 'Crystal', the most popular ad blocking technology for iOS 9 (Welch, 2015), enabled.

Just over 90 % of the magazine websites evaluated contained advertising content. Of the ones delivering ads, 90 % of these could be successfully blocked using 'Crystal', Figure 9. Note that other versions of ad blocking software might return different results depending on how the magazine's website and the blocking software were configured.

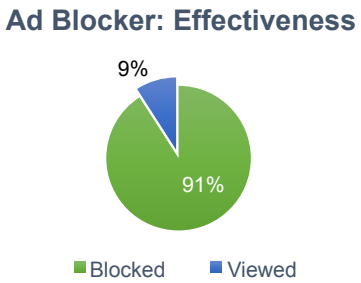

Figure 9: Percentage of sites tested where ads could be successfully blocked

In this analysis, none of the sites tested returned a message requesting the reader to 'alter their browsing behaviour', meaning disable their 'blocker'. Canadian magazine publishers may be taking the approach of not wishing to be perceived as potentially 'antagonizing' their readers with message requesting that they turn off blockers (Cunningham, 2015). Alternatively, perhaps their approach to blocking is still evolving – with 87 % of ads being SFP, publishers are not necessarily working with advertisers to create ad content specifically for mobile – it could be that publishers are not understanding the potential impact of ad blockers.

4. Conclusions

The analysis determined that the majority of leading Canadian consumer magazines offers digital editions of their issues. These editions are available in a variety of formats, with 73 % publishing a 'native app' version, that can fully support multimedia and interactivity. All of the 'native app' publishers also offer either a digital replica (41 %), or extended PDF (41 %) version as well, with 18 % offering all three versions. Publishers appear to be exploring multiple platforms for extended reach; it is relatively economical to create a replica version for distribution through a newsstand platform.

Publishers appear to favour tablets slightly over smartphones, with full support for the iOS platform, and partial support for Android. However, smartphones have a larger market share in Canada, and the most popular operating system for them is Android. This mismatch between publishers' digital focus and potential audience could be a source for concern for publishers in the future.

These 'native app' versions, however, contain relatively moderate amounts of interactivity or multimedia editorial content. The most commonly found interactive elements relate to navigation ('learn more' 41 %,

'links' 55 %), while the commonly found multimedia types were images and video, both at 36 %. The relatively lower levels of editorial interactive and multimedia content is presumably related to the higher cost of resources to produce this material, as well as to support it for multiple devices. Overall, the use of interactivity in advertising content is minimal, again presumably related to resources.

With regards to website architecture, while the majority (74 %) of the sites checked are built to be viewed on a variety of screen sizes and resolutions, they are not generally designed to offer the best support for mobile devices, with regards to speed, or to configuration. Publishers may be missing an opportunity to engage with a growing potential audience by offering more interactive content on mobile.

There is also potential for impact on advertising revenue streams if the current use of ad blocking technology increases in the Canadian market. Publishers do not appear to be taking steps to attempt to change the behaviour of readers using blockers. It may be that the revenue from mobile currently is not significant enough for magazines to address the issue. However, publishers, if they have not already done so, may wish to consider tactics to address blocking.

In a 2013, at the Interactive Advertising Bureau conference Eric Schmidt, former CEO and executive chair of Google, encouraged publishers and advertisers to adopt a ''mobile first'' strategy, citing that mobile will be a key driver for the digital display advertising market. The research presented here demonstrates that Canadian publishers who wish to grow their digital audience should further consider a shift in strategy from 'native app' editions targeted towards tablets, to website digital editions designed for smartphones.

One area of future study could include evaluating the use of social networks by magazines to allow readers easily to share a magazine's content. Providing content to smartphones via a website may provide greater potential readership network effects than on a tablet. This work could also include the technologies that support these 'deep' links.

In addition, a similar analysis of competitive titles and categories in the United States publishing market could serve as an additional useful benchmark, to evaluate strategies in a similar market.

Acknowledgments

The Authors would like to acknowledge the financial support of Ryerson University through their Fall/Winter 2016/2017 Work Study Research Assistant Program, as well as Ryerson University's Faculty of Communication and Design through a 2016 Undergraduate Research Opportunity (URO) research assistantship Grant.
As well, thanks go to Amanda Whyte, Undergraduate Research Assistant, Ryerson University, School of Graphic Communications Management, for her excellent work in organizing and cataloguing the periodicals.

References

Adobe, 2016. *TubeMogul Joins Adobe*. [online] Available at: <https://www.tubemogul.com/> [Accessed 10 February 2017].

Alters, M. and Hollis, M., 2017. The preferred use of responsive web design versus adaptive web design in various industries. In: *2017 Technical Association of the Graphic Arts (TAGA) Conference Proceedings*.

An, M., 2016. *Why People Block Ads (And What It Means for Marketers and Advertisers.).* [online] Hubspot research. Available at: <https://research.hubspot.com/reports/why-people-block-ads-and-what-it-means-for-marketers-and-advertisers> [Accessed 8 August 2016].

Blanchfield, S., 2016. *The Dangers of Playing Cat and Mouse with Adblock*. [online] PageFair. Available at: <https://pagefair.com/blog/2016/the-dangers-of-playing-cat-and-mouse-with-adblock/> [Accessed 9 August 2016].

Catalyst, 2015. *With Growth comes Change: The Evolving Mobile Landscape in 2015*. [online] Catalyst. Available at: <http://catalyst.ca/2015-canadian-smartphone-market/> [Accessed 11 January 2017].

Cunningham, S., 2015. *Getting LEAN with Digital Ad UX*. [online] Interactive Advertising Bureau. Available at: <https://www.iab.com/news/lean/> [Accessed 4 February 2017].

FIPP, 2014. *FIPP World Magazine Trends 2014/2015.* London: Fédération Internationale de la Presse Périodique (International Federation of the Periodical Press).

Ghazarian, A., 2014. *The Pros and Cons of Responsive Web Design vs. Mobile Website vs. Native App*. [online] Designmodo. Available at: <https://designmodo.com/responsive-design-vs-mobile-website-vs-app/> [Accessed 18 January 2017].

Hardy, I., 2015. *Apple tops Samsung in Canadian smartphone market share*: comScore. [online] Mobilesyrup. Available at: <http://mobilesyrup.com/2015/03/27/comscore-canada-smartphone-android-apple-os-market-share/> [Accessed 4 January 2017].

Idealliance, 2013. *OpenEFT (Enhanced for Tablet) Designed for Tablet Magazine Guide: DRAFT 3 for Public Comment.* [online] Idealliance. Available at: <http://www.prismstandard.org/openeft/draft3/guides/OpenEFT_DFT_Guide_Draft3.htm> [Accessed 4 December 2016].

Jacob, S., 2011. *Speed Is a Killer - Why Decreasing Page Load Time Can Drastically Increase Conversions*. [online] Kissmetrics. Available at: <https://blog.kissmetrics.com/speed-is-a-killer/> [Accessed 6 February 2017].

KempRugeLawGroup, 2015. *Fixing Render Blocking Javascript and CSS in the Above-the-fold content.* [online] Moz. Available at: <https://moz.com/community/q/fixing-render-blocking-javascript-and-css-in-the-above-the-fold-content> [Accessed 18 January 2017].

Kulp, P., 2015. *Websites know you're using ad-blockers, and they're coming for you*. [online] Mashable. Available at: <http://mashable.com/2015/09/12/passive-agressive-ad-blockers/#pMIP7ZGtJ8qn> [Accessed 22 July 2016].

Lindzon, J., 2016. *PageFair Reports Ad Blockers Actually on the Rise in Canada*. [online] Marketing. Available at: <http://www.marketingmag.ca/tech/pagefair-reports-ad-blockers-actually-on-the-rise-in-canada-184184> [Accessed 11 February 2017].

Magazines Canada, 2015*. Consumer Magazine Media: Fact Book 2015*. [online] Magazines Canada. Available at: <https://magazinescanada.ca/wp-content/uploads/2016/11/consumer_fact_book_2015_english_final.pdf> [Accessed 20 June 2016].

Miric, M., 2015. *Exploration of Affordances in Subscription-based Digital Magazines.* [PDF] Toronto: Ryerson University. Available at: <http://www.ryerson.ca/content/dam/graduate/digitalmedia/Abstracts-2014-2015/Marijana_Miric_MRP.pdf> [Accessed 20 December 2016].

Nordicity, 2009. *Study of Digital Magazine and Newspaper Publishing in Canada.* [PDF] Nordicity. Available at: <http://www.nordicity.com/media/20121112ghttxgyq.pdf> [Accessed 18 August 2016].

PageSpeed, n.d. *About PageSpeed Insights*. [online] Available at: <https://developers.google.com/speed/pagespeed> [Accessed February 2017].

Ritchie, R., 2017. *Happy 7th anniversary iPad!*. [online] iMore. Available at: <http://www.imore.com/history-ipad-2010> [Accessed 3 February 2017].

Santos Silva, D., 2011. The future of digital magazine publishing. *Information Services and Use*, 31(3–4), pp. 301–310.

Schwartz, B., 2016. *Google: Keep Site Speed Below 2-3 seconds*. [online] Search Engine. Available at: <https://www.seroundtable.com/google-site-speed-recommendation-23057.html> [Accessed 6 February 2017].

Sexton, P., 2016. *Enable gzip Compression*. [online] Available at: <https://varvy.com/pagespeed/enable-compression.html> [Accessed 18 January 2017].

Statista, 2016a. *Market share of tablets in North America by device from 2Q'15 to 2Q'16.* [online] Statista. Available at: <https://www.statista.com/statistics/629385/tablet-market-share-by-device-in-north-america/> [Accessed 3 February 2017].

Statista, 2016a. *Share of people that used consumer electronic devices in Canada in 2016.* [online] Statista. Available at: <https://www.statista.com/statistics/698418/tech-device-usage-canada/> [Accessed 2 May 2017].

Tarcomnicu, F., 2016. *How to Achieve 100/100 with the Google Page Speed Test Tool*. [online] MOZ. Available at: <https://moz.com/blog/how-to-achieve-100100-with-the-google-page-speed-test-tool> [Accessed 18 January 2017].

Welch, C., 2015, Sept 24. *Best-selling iOS ad blocker Crystal will let companies pay to show you ads*. [online] The Verge. Available at: <http://www.theverge.com/2015/9/24/9393941> [Accessed 22 July 2016].

Appendix

The list of Magazine Categories, Publishers, Titles, and their Circulation numbers. Audited circulation numbers as reported to Canadian Advertising Rates and Data (cardonline), *Accept as noted. Not all titles report digital circulation numbers.

Category	Publisher	Magazine Titles	Print Circulation	Digital Circulation
Architecture / Design	Canada Wide Media	Award	10,000*	-
Automotive	Performance Publications Media Group	PRN Ignition	250,430	-
	Riptide Resources Inc.	Motorcyle Mojo	11,705	-
Beauty	St. Joseph Media	Glow	370,000	-
Business	Rogers	Macleans	195,053	39,249
	Business Edge News Media	Business Edge	157,200	-
	Rogers	Canadian Business	89,165	42,000
Children	Bayard	Chickadee	58,643	-
	Bayard	Chirp	55,277	-
	Bayard	Owl	47,427	-
	Canada's History Society	Kayak	6,088	-
Family	Family Communications	Parents Canada	100,000	-
	Rogers	Today's Parent	82,699	26,303
Fashion	Rogers	Flare	125,111	8,852
Fitness	Impact Productions	Impact Magazine	90,000	-
	Myndlogic Publishing	Windsor Body Magazines	80,000	40,000
Food & Drink	Liquor Control Board of Ontario	Food & Drink	531,333	-
General Interest	Reader's Digest	Reader's Digest	342,908	13,330
	Canadian Geographic	Canadian Geographic	12,723	1,012
	Moongate Publishing Inc.	Harrowsmith's (Almanac)	91,000	-
Health	Alive Publishing Group	Alive	172,661	-
	The Town Crier of Markham Inc.	Healthy Living	100,000	-
Home Interest	TVA Group	Style at Home	201,445	10,778
	House & Home Media	House & Home	168,220	46,705
Lifestyle	TVA publications (Transcontinental)	Canadian Living	418,278	6,875
Men's Lifestyle	Contempo Media	Sharp	140,000	-
	Chill Media Inc.	Chill	202,783	-
Other Special interest	Zoomer Media Limited	Zoomer	191,737	3,677
	Rogers	Hello! Canada	101,381	33,706
	Cottage Life Media	Cottage life	66,616	1,594
Sport	ScoreGolf Canada	ScoreGolf	120,381	-
	Solstice Publishing	Ski Canada	28,835	-
Travel	Canada Wide Media	Westworld	1,327,818	-
Wedding	Family Communications	Today's Bride	92,666	-
Women's	Rogers	Chatelaine	404,211	58,462

* Circulation as reported by magazine; not audited by third party

Predictive Modelling of Demixing and Evaporation from a Roller Nip-distributed Water-in-Ink Thin Film Emulsion using Tack Measurement

Patrick A.C. Gane[1, 2], *Carl-Mikael Tåg*[3] *and Cathy J. Ridgway*[2]

[1] School of Chemical Technology, Department of Bioproducts and Biosystems, Aalto University, FI-00076 Aalto, Helsinki, Finland
[2] Omya International AG, CH-4665 Oftringen, Switzerland
[3] Stora Enso Support Centre Mönchengladbach, DE-41600, Mönchengladbach, Germany

Email: patrick.gane@omya.com, carl-mikael.tag@storaenso.com, cathy.ridgway@omya.com

Abstract

Ink-water balance in offset printing is something of an old "chestnut" topic when it comes to defining print properties, and press and paper runnability. Despite its importance in controlling the print quality, little to no analysis has been devoted to predicting quantitatively the mixing and evaporation dynamics of a fount solution in the thin film ink-fount emulsion. The ink rheology testing technique (TackOscope), incorporating the possibility to apply an aqueous liquid (print fountain solution) to mix in an oil-based ink, thus creating an emulsion in a twin roll nip, was used to provide information relating to the tackiness property during emulsification. Internal cohesion of the ink-fountain solution emulsion is recorded as film split force between the two rollers during fountain solution titration and evaporation, and defines the intrinsic tack. The ink used showed a continuous tack increase over time, superposed on the response measured during fountain solution addition. Addition of intermediate amounts of fountain solution was shown to decrease the tack of the emulsion monotonically. After evaporation of the fountain solution the tack finally returns back to its expected undisturbed level, following the original fountain solution-free ink tack development, the result being a sigmoidal evolution to this point. A mathematical model to derive the retained fountain solution amount during evaporation is developed and demonstrated in respect to the experimental data. The evolving evaporation is seen to follow two simultaneous exponential defined functions, that of demixing, a delay function, and that of evaporation, a driving function. The results suggest that such a model for evaporation could be applied to describe the relationships between fountain solution dosage time, amount and practical behaviour in the laboratory and on press, leading, in principle, to a prediction of print quality-related issues.

Keywords: emulsification, phase demixing, evaporation from emulsion, printing, ink transfer, ink tack

1. Introduction

Water evaporation from a water-in-oil emulsion is a feature of many industrial and laboratory processes. One such application of emulsion chemistry is the commonly practised offset printing technology, in which the inked image area is differentiated from the non-image (non-printed) area in respect to surface energy by the use of water-based fountain solution, which prevents the transfer of oil-based ink onto the wetted non-image area of the printing plate in the press. This provides an excellent study platform for phase demixing and evaporation, and practitioners have long sought an understanding of how the aqueous fountain solution phase behaves during thin film print transfer. The visual appearance of a printed product plays an important communicational and aesthetic role, and expresses the value proposition of the printed product. In the case of printed surfaces, the target end-users vary in respect to aesthetic demand with many brows-

ing observers selecting a preference for a glossy image, but readers on the other hand prefer high optical density contrast and an overall matt surface (MacGregor, et al., 1994).

Tack as measured on a twin-roll device such as a TackOscope (IGT testing systems, The Netherlands) is a rheological parameter indicative of internal cohesion of the fluid as it is split at the exit of the twin-roll nip (ASTM standard for tack measurement: D 4361-97). It has a unit which is application specific, e.g. energy expended in the separation, force required to complete the split, torque needed to maintain the rotation of the rollers hindered by the film splitting, pressure in respect to force per unit area of film split, length over which the split occurs, dimensionless ratio of these etc. (Voltaire, 2006). The tack of a printing ink controls its high speed transfer properties both within the offset printing press during image forming, i.e. throughout the ink roller train and printing plate, and at the transfer point of the image from ink blanket to substrate. Tack, however, is also in practice an interface property, and together with surface energy also defines the adhesion of the ink on the printing surface of the plate or blanket as well as the substrate, thus, when properly controlled, providing a sharper and cleaner printed image. A higher tack value increases stress transfer to the substrate, and, if too high, may induce picking of fibres, fillers or coating particles from the paper surface, transferring onto, and retaining them at, the printing plates and other parts of the printing press (Aspler, et al., 1997). Oil and solvents added to the ink tend to lower the effective tack, by the effect of dilution. Higher levels of binder in the ink will raise the tack values. Naturally, also on press, the tack is decreased depending on the level of fountain solution in the emulsion per unit total film thickness. Tack can also be a key parameter in predicting wet trapping in multicolour printing (Oittinen and Saarelma, 2009). The correct or optimal water "uptake" of an offset ink is one of the vital properties needing to be designed, known and controlled to achieve satisfactory lithographic print quality and performance.

Under normal operating conditions the ink will, by means of shear action during application to the printing plate, partly emulsify the fountain solution water in the non-image area to form a water-in-oil emulsion, which reaches an equilibrium over time in the ink recirculation circuit, with any remaining water left as a surface film (Bullof, 1974). From the printing plate cylinder the image is carried over, i.e. "offset", to the paper via the blanket cylinder, thus transferring both ink and water to the paper. The lithographic printing performance depends on successful adhesive transfer of the ink-water emulsion to the substrate, and so is sensitive to the content of surface water, which ideally should be eliminated by emulsification and evaporation (Lie and Kihl, 1992). For this reason, ink-water emulsion stability, with focus on both rheological (Chou and Fadner, 1986) and thermodynamic properties (Bassemir and Krishnan, 1987), has been studied extensively using a range of laboratory techniques. One such commercial instrument, the Hydroscope (Testprint BV, The Netherlands), was developed to characterise emulsification behaviour on inked rollers in order to assess ink-fountain solution compatibility in press applications. However, all these methods measure either the tack development in a nip without fountain solution or then the rheological properties of a fount emulsified in ink.

The evaporation mechanism of water from emulsions has been extensively studied. Under conditions when the evaporation rate is controlled by mass transfer across a vapour phase, the evaporation can be slowed by repulsive inter-droplet interactions (Aranberri, et al., 2004). As well, water evaporation may be limited by diffusion in the network of water films within the emulsion. The same authors also state that a compression of the drops, as under in dynamic conditions, may lead to coalescence of the emulsion drops and the formation of a macroscopic oil film at the emulsion surface, which serves to prevent further water evaporation, resulting in a phase separation.

The stability of thin films have been studied by Bibette showing that the stability of such films in concentrated emulsions is governed by the microscopic pressure acting on the oil-water interface. As an example, large droplets are more stable than small droplets (Bibette, 1992). Bouchama, et al. (2002) claim that the initial phase of evaporation of an oil-in-water emulsion is fast evaporation of free water. The same authors

define five different regimes of evaporation based on changes in conductivity of the emulsion. The drying of the film evolves in steps where water first evaporates until an oily skin is formed on top of the film, under which the emulsion experiences a phase inversion to water-in-oil constituting the final film. Clint, et al. (1999) used a gravimetric technique to measure the rate of evaporation of water from micro-emulsions. The evaporation rates showed that water drop diffusion within the bulk micro-emulsion is rate limiting while the subsequent processes of water transfer across the liquid/vapour surface are not. We may expect, therefore, that a water-in-ink emulsion will also show an initial diffusion determined demixing phase prior to more rapid evaporation enhanced by the action of repeated film splitting until a final slow evaporation phase as the remaining micro-emulsion becomes more and more stable, changing only by a combination of diffusion and the continued creation of fresh surface for evaporation by the action of film splitting.

The aim of this study is to model the evaporation dynamic as a function of fount solution content in the ink, so that the apparent fount amount in the ink, related to the running/spraying time applied on the device, can be monitored from the ink tack simultaneously with progressive evaporation. If successful, such a model could be used to provide a measure of the amount of fountain solution actually present in an ink, and thus finally be able to interpret print properties as a function of emulsification satisfactorily both in the laboratory environment and, in principle, on press. This would finally enable the limitations in correlating tack directly with the end print properties to be accommodated within the range of application of tack, itself enabling the definition of actual fount content, and so providing the ability to understand the role of emulsification and emulsion stability in defining the print outcome.

2. Materials and methods

The heatset ink used was a low tack variant (Premoking 6000 supplied by Flint Group). The water-based fountain solution contained 5 % of isopropyl alcohol and 4 % of a non-ionic surfactant as surface tension modifying agents.

The TackOscope device (IGT Testing Systems, The Netherlands) is based on a set of contacting rotating rollers. This method comprises a system similar to that of an ink distribution chain on a printing press, with an additional feature for applying fountain solution in a controlled manner by using a precise ultrasonic spray dampening. The transfer roller is made of brass and the impression cylinder made from rubber. The device is built on the platform of a standard tack meter. The ink distribution device was run so that an increasing amount of fountain solution could be added to the ink. The monitoring of tack at different fount addition levels showed changes in ink-fount behaviour. The test result is presented as a tack against "fount consumption curve" for a given ink/fount combination. Due to evaporation from the thin film distribution, the quantitative amount of fountain solution is normally not known, but the tack is recordable and therefore could in principle be back-related to a pre-scaled relative fountain solution amount. This is the task undertaken in this study using the following running parameters:

A quantity of 4 cm^3 printing ink was placed on the distribution rollers. The rotation speed was set at 50 $m \cdot min^{-1}$ and held at 30 °C during ink distribution. During the first 30 s, the ink becomes evenly distributed on the roller surfaces, after which the actual measurement is started and the speed increased to 200 $m \cdot min^{-1}$. Depending on the desired amount of fount to be added, the machine was run for a corresponding time to apply the chosen volume from the spraying unit, which delivered fount at the rate of 10 $\mu l s^{-1}$. A schematic picture of the procedure is shown in Figure 1.

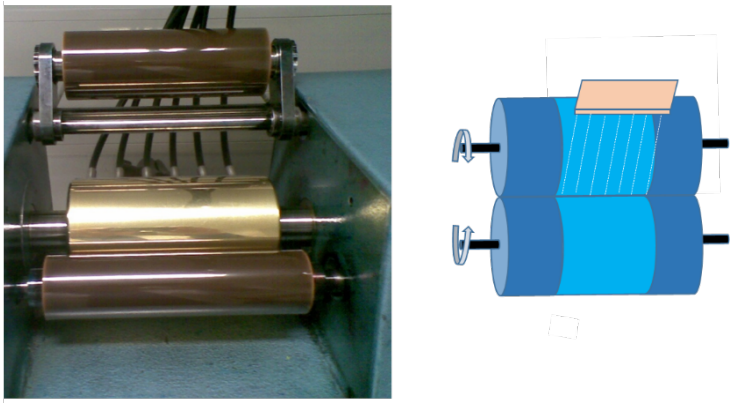

Figure 1: Procedure of ink-fount emulsification and tack recording

3. Results and discussion

In this section we follow the experimental observation of tack behaviour as a function of time and fount addition, and then use these data to develop a model for the progressive loss of fountain solution through the action of film splitting and evaporation.

3.1 Tack development as function of fountain solution addition

Figure 2 presents the development of tack with time with a constant dosage rate of fountain solution. It can be seen that the tack first of all increases under shear in the nip with the ink viscosity dominating the mix. However, at the point where the fount content within the ink destroys its cohesive structure, a collapse is seen where the tack is clearly reduced. For this test series, at 45 s of fount spraying, the tack is levelling out, and the critical point, referring to tack drop is seen after 85 s of fount spraying (as shown by the dotted lines in Figure 2). 85 s corresponds to a fount delivery of 0.85 cm^3 in the ink (mass fraction of 21 % of the original ink amount). This fount delivery, however, is not the absolute amount as the evaporation is not yet taken into account.

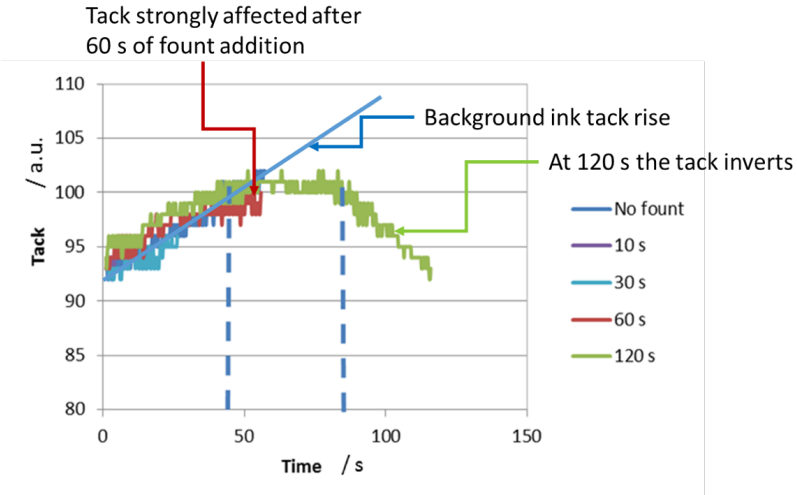

Figure 2: Ink tack as a function of fountain solution dosage time at constant rate: evaporation effects as yet not known

3.2 Model for evaporation from emulsion

It is clear that the tack measure in Figure 2 gives similar-shaped curves for all fount addition conditions over a given time range, in the sense that tack $T(t)$ first rises due to the intrinsic aging of the ink under shear

and then decreases to a minimum during fountain solution addition due to emulsified droplets lowering ink film cohesion, and any non-emulsified surface water that might be present creating a weak boundary layer. The initial linear tack aging gradient can be expressed by $k_{\text{shear aging}}$ as

$$T_{\text{ink}}(t) = k_{\text{shear aging}} t + T_{\text{ink}(t=0)} \quad [1]$$

where $T_{\text{ink}}(t)$ is the tack of the ink alone at time t as a function of the aging property under shear, and $T_{\text{ink}(t=0)}$ is the intrinsic tack of the ink at the time when shear begins. The linear constant in Eq. 1 is thus seen to apply as a component of the ink-fountain solution mix over time relating to the ink alone.

We can determine a time constant for the evaporation rate by studying what happens after fount addition is stopped. This is shown in Figure 3, where we see that the intrinsic ink tack continues to increase but the fount solution in excess first reduces tack and then is allowed to evaporate. A correction can be made for the intrinsic tack increase of the ink using the following approach.

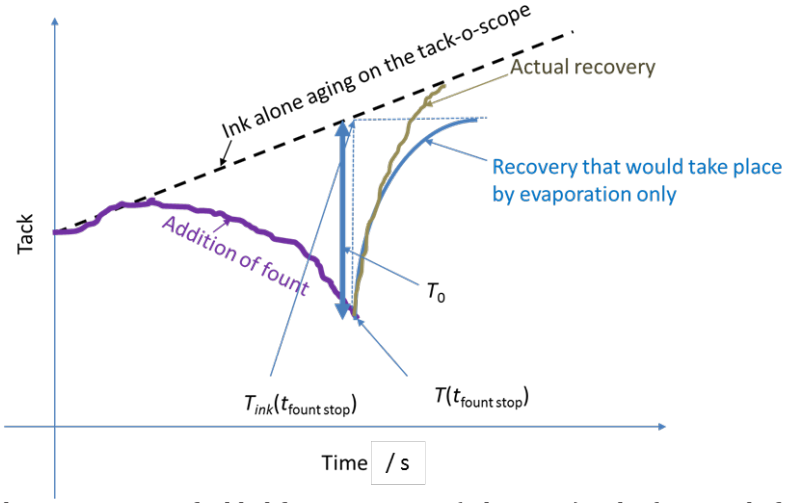

Figure 3: Following the evaporation of added fount over time (schematic) – the first single function approximation

From the dashed line in Figure 3, we see the aging of the ink under shear showing a steady background increase in tack. Superposed on this is the addition of fount solution and its subsequent evaporation. We can now compensate for the intrinsic ink tack increase by subtracting the increased amount from the start of evaporation. This gives an evaporation curve, which is defined here as a first approximation by a single function. By fitting this curve with an exponential function of time, the tack increase in the ink-fountain solution mix by evaporation only, $T_{\text{evaporation}}$, is given by

$$T_{\text{evaporation}}(t - t_{\text{fount stop}}) = T_0(1 - e^{-\{t - t_{\text{fount stop}}\}/\tau}) \quad [2]$$

where T_0 is given by

$$T_0 = T_{\text{ink}}(t_{\text{fount stop}}) - T(t_{\text{fount stop}}) = k_{\text{shear aging}} t_{\text{fount stop}} + T_{\text{ink}(t=0)} - T(t_{\text{fount stop}}) \quad [3]$$

and so the evaporation time constant τ in Eq. 3, can be determined from [4]

$$
\begin{aligned}
&T(t > t_{\text{fount stop}}) \\
&= T(t_{\text{fount stop}}) + \{k_{\text{shear aging}} t_{\text{fount stop}} + T_{\text{ink}(t=0)} - T(t_{\text{fount stop}})\}(1 - e^{-(t - t_{\text{fount stop}})/\tau}) + T_{\text{ink}}(t) - T_{\text{ink}}(t_{\text{fount stop}}) \\
&= T(t_{\text{fount stop}}) + \{k_{\text{shear aging}} t_{\text{fount stop}} + T_{\text{ink}(t=0)} - T(t_{\text{fount stop}})\}(1 - e^{-(t - t_{\text{fount stop}})/\tau}) + k_{\text{shear aging}}(t - t_{\text{fount stop}})
\end{aligned}
$$

$$
\Rightarrow \tau = \frac{t - t_{\text{fount stop}}}{\ln\left\{\dfrac{1}{1 - \left[\dfrac{T(t > t_{\text{fount stop}}) - T(t_{\text{fount stop}}) + k_{\text{shear aging}}(t - t_{\text{fount stop}})}{k_{\text{shear aging}} t_{\text{fount stop}} + T_{\text{ink}(t=0)} - T(t_{\text{fount stop}})}\right]}\right\}}
$$

Thus, we can now determine how much fountain solution remains, F, after evaporation in a given time t' after a fixed single addition level of F_0 on the TackOscope as

$$F(t') = F_0 e^{-t'/\tau} \qquad [5]$$

Consequently, if a total number, N, of timed fountain solution additions, n, are made, each at a respective time t'_{n-1}, the collective remaining amount of fountain solution in the ink-fountain solution mix, F, after starting at the first addition and summing to the last addition, each with an elapsed time $t'_n - t'_{n-1}$, recalling the state after evaporation of the sum of the previous additions must be added to the new fresh addition, is given by

[6]

$$
\begin{aligned}
&F\left(\sum_{n=1}^{N} t'_n - t'_0\right) = F_{0N} + (\ldots(F_{03} + (F_{02} + F_{01} e^{-(t'_1 - t'_0)/\tau_1}) e^{-(t'_2 - t'_1)/\tau_2}) e^{-(t'_3 - t'_2)/\tau_3})\ldots) e^{-(t'_N - t'_{N-1})/\tau_N} \ldots \\
&= F_{01} e^{-(t'_1 - t'_0)/\tau_1} e^{-(t'_2 - t'_1)/\tau_2} e^{-(t'_3 - t'_2)/\tau_3} \ldots e^{-(t'_N - t'_{N-1})/\tau_N} + F_{02} e^{-(t'_2 - t'_1)/\tau_2} e^{-(t'_3 - t'_2)/\tau_3} \ldots e^{-(t'_N - t'_{N-1})/\tau_N} + F_{03} e^{-(t'_3 - t'_2)/\tau_3} \ldots \\
&\ldots e^{-(t'_N - t'_{N-1})/\tau_N} + \ldots + F_{0N} e^{-(t'_N - t'_{N-1})/\tau_N} \ldots \\
&= \sum_{n=1}^{N} F_{0n} \prod_{i=n}^{N} e^{-(t'_i - t'_{i-1})/\tau_i}
\end{aligned}
$$

where t'_0 is the time at which the first fountain solution addition is made, t'_{n-1} is thus the time at which the fountain solution addition n is made, and $\sum_{n=1}^{N} t'_n - t'_0$ is the time between the first addition and the time at which the remaining fountain solution quantity, after N discrete additions, is desired to be known.

Clearly, Eq. 6 describes the condition where discrete additions of fountain solution are made. For an ink, such as the one used here, the value of $k_{\text{ink aging}}$ remains the same, however the start tack value for each addition is affected by the degree of evaporation that has occurred from the previous addition. This is accounted for by the exponential decay function for each addition, which is corrected by the stop time of the previous addition and the decay constant for each addition i is thus depending on the decay constant of the addition i-1, i-2 and so on. This means that for a given total fountain solution addition over fixed time, the number of single additions N made to reach the total over the same time period relates to the amount added per addition i. The same applies if the period of addition increases due to smaller addition amounts for each addition i, but now of course the evolution of evaporation for each stage is longer and so the total amount needed to be added summed over N becomes larger. The dependence on time is, therefore, the key to the state of fountain solution content volume, and if a fixed end point added volume is needed at equilib-

rium, more would have to be added in total the greater the number of small additions prior to reaching this volume versus a smaller number of larger additions. However, to prevent swings in volume content over time once the target volume is reached, then a large number of frequent small additions is naturally the better option. Using Eq. 6 in this manner would allow a further exponential addition volume and frequency to be calculated to provide optimum fountain solution consumption whilst starting and subsequently running the press under consistent conditions.

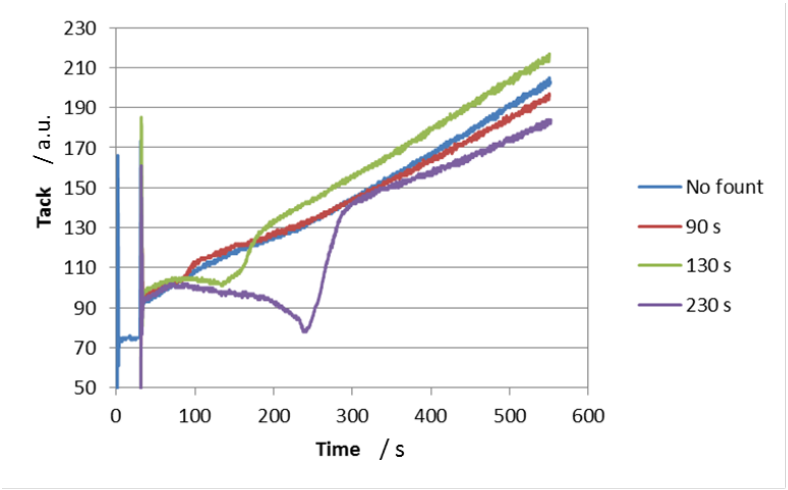

Figure 4: Tack behaviour at different fountain solution dosage levels, where the running time of the device is plotted on the x-axis and the fount dosage time is presented in the legend; the first 30 s refer to the levelling of ink on the rollers, i.e. the time before the actual measurement has started (hence some inevitable noise)

Measurements were made for longer times for the different fount solution dosage levels in order to be able to follow the evaporation and the recovery rate more closely, as shown in Figure 4. We see the background linear tack change in the ink is present for all fountain solution addition amounts. It is interesting to note that the gradient of the background tack rise does show a variation.

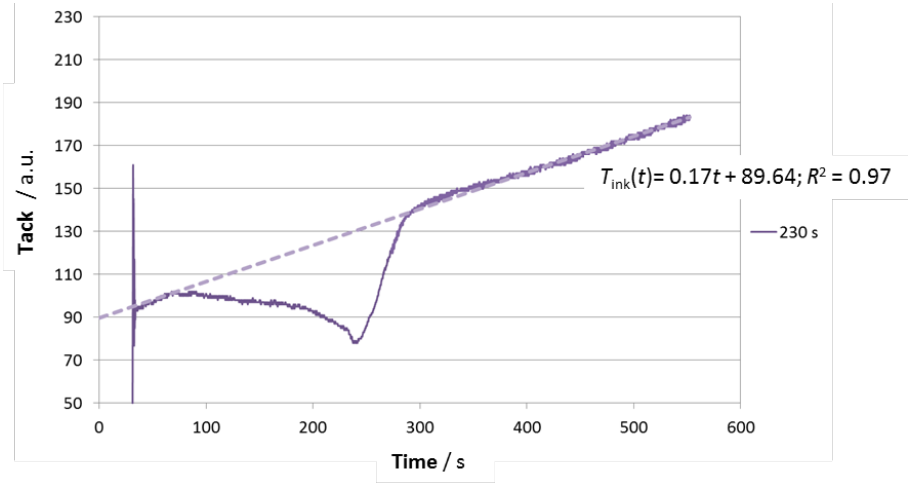

Figure 5: Initial linear tack aging gradient shown, $T_{ink}(t)$=0.17t + 89.64 with R^2 = 0.97; $T(t_{fount\ stop})$ and $t_{fount\ stop}$ are 78 (a.u.) and 230 s, respectively, where the running time of the device is plotted on the x-axis and the fount dosage time is presented in the legend; again, the first 30 s refer to the ink distribution on the rollers

However, since the variation does not follow a direct trend of fountain solution addition time, but rather moves above and below the gradient of ink alone (without fountain solution addition), we must assume that this is a variation of the process conditions and most likely related to either environmental conditions of humidity and temperature on the Tackoscope or a small difference in ink amount, which becomes mag-

nified through the action of aging as the gradient acts to differentiate between small differences in loading, rather than any material effect of the fountain solution formulation. The measurement curve for 230 s addition time is taken as an example to illustrate the application of the first approximation time constant for the free evaporation rate by studying what happens after fount addition is stopped, Figure 5.

The initial linear tack aging gradient, $k_{\text{shear aging}}$, is found by fitting a linear trend line to the linear region of the ink tack curve. $T_{\text{ink}(t=0)}$, the intrinsic tack of the ink at the time when shear begins. These values are in this case 0.17 s^{-1} and 89.6 (a.u.), respectively. The values for $t_{\text{fount stop}}$ and $T(t_{\text{fount stop}})$ are also extracted from this graph, 230 s and 78 (a.u.), respectively. Using this information $\tau(t)$ can then be calculated for times greater than $t_{\text{fount stop}}$, as shown in Figure 6.

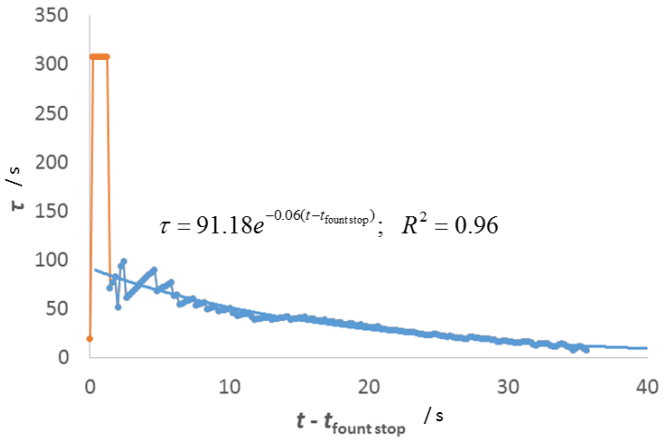

Figure 6: τ over the time range 240–275 s (0–35 s after stopping the addition of fountain solution), R^2= 0.96

The behaviour of τ is shown graphically in Figure 6. The value of τ is not constant but gradually decreases. Values of τ at times less than 250 s are erratic since evaporation data are necessarily limited and not fully established. The main region of interest for correction is from after $t_{\text{fount stop}}$ until the point where the tack curve returns to the level predicted by ink aging alone, in this case at ~ 300 s. The dependence of τ over time suggests that the fount is not free to evaporate as a separate phase. It is frequently postulated that fount solution forms an inverted emulsion in the ink. This is supported by the time dependence of evaporation rate, i.e. demixing. To account for this, Eq. 2 should be modified to reflect the time dependence of τ, as follows

$$T_{\text{evaporation}}(t - t_{\text{fount stop}}) = T_0(1 - e^{-\{t-t_{\text{fount stop}}\}/\tau(t-t_{\text{fount stop}})}) \quad [7]$$

where now,

$$\tau(t - t_{\text{fount stop}}) = \tau(t_{\text{fount stop}})e^{-\{t-t_{\text{fount stop}}\}/\tau_{\text{demix}}} \quad [8]$$

From Figure 6 we see that τ_{demix} is a constant having the value 16.67 s, and $\tau(t_{\text{fount stop}})$ = 91.18 s.

Using a suitably modified Eq. 5,, where $t' = t - t_{\text{fount stop}}$ in this case, we can now determine how much fountain solution remains after evaporation at a given time t' after a fixed single addition level of F_0. Over an addition time of 180 s, ~ 2 cm^3 of fountain solution are added. A cumulative value can be given such that the amount of fountain solution remaining after a specific time interval could be known, Figure 7.

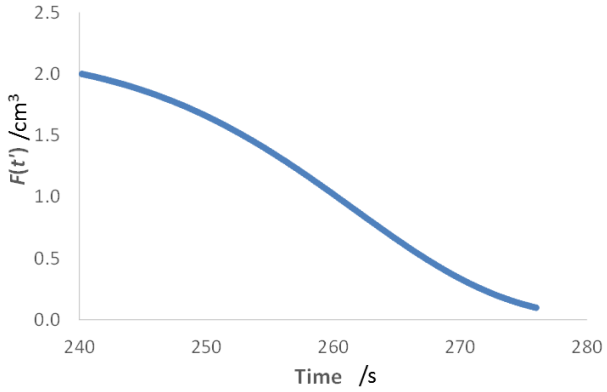

Figure 7: F(t´) over the time range 240–275 s; the function is seen to be sigmoidal reflecting the two stages of demixing and subsequent evaporation

A summary of the conditions and modelling parameters for the 230 s experimental period (180 s of fountain solution addition) is shown in Table 1.

Table 1: Fountain solution addition conditions and fitting parameters for the case of 230 s addition period

Period of fountain solution addition	**Background ink tack rise gradient**	**Tack at fount addition stop**	**Time constant for demixing**	**Time constant for evaporation after demixing decay**
$t_{\text{fount stop}}$ / s	$k_{\text{shear aging}}$ / a.u (tack units) · s^{-1}	$T(t_{\text{fount stop}})$ / a.u.	τ_{demix} / s	$\tau(t_{\text{fount stop}})$ / s
180	0.17	78	16.67	91.18

Future work could be devised to apply the model under printing press conditions.

4. Conclusions

We may conclude that:

I. The measurement of tack as a function of fountain solution addition and time could provide a relatively easy way to follow the dynamics at different printing press stations, which could be used as a monitoring tool to predict and control the offset ink-fountain solution process properties.

II. A model methodology to derive the retained fountain solution amount after evaporation, for a series of additions over time, has been developed and demonstrated. This descriptor could be used for any evaporative system occurring during a separable host component change, i.e. in this case the tack growth of the ink alone during shear superposed on the effect of fountain solution addition and subsequent progressive evaporation.

References

Aranberri, I., Binks, B.P., Clint, J.H., and Fletcher, P.D.I., 2004. Evaporation rates of water from concentrated oil-in-water emulsions. *Langmuir*, 20, pp. 2069–2074.

Aspler, J.S., Perron, L., Zang, Y.-H. and Larrondo, L., 1997. Printing tack development and coated paper structure. In: *Proceedings of the Technical Association of the Graphic Arts*, Rochester, NY, pp. 162–178.

Bassemir, R.W. and Krishnan, R., 1987. Optimizing lithographic performance-a physical-chemical approach. In: *TAGA Proc*., p. 560.

Bibette, J., 1992.Stability of thin films in concentrated emulsions. *Langmuir*, 8, pp. 3178–3182.

Bouchama, F., Estramil, G., Autin, A.J.E., Koper, G.J.M., 2002. Film formation from concentrated emulsions studied by simultaneous conductometry and gravimetry, *Colloids and Surfaces A: Physicochem. Eng. Aspects*, 210, pp. 129–135.

Bullof, J.J., 1974. Emulsions in printing and the graphic arts. In: K.J. Lissant, ed., *Emulsions and emulsion technology, part II, vol. 6, Surfactant Science series*, p. 573.

Chou, S.M. and Fadner, T.A., 1986. Shear stability of fountain solution emulsified in lithographic inks. In: *TAGA Proc*., p. 37.

Clint, J.H., Fletcher, P.D.I. and Todorov, I.T. 1999. Evaporation rates of water from water-in-oil microemulsions. *Phys. Chem. Chem. Phys.*, 1, pp. 5005–5009.

Lie, C. and Kihl, L., 1992. Control of ink/water balance with help of an on-line densitometer. In: *TAGA Proc*., p. 443.

MacGregor M.A., Johansson, P.-Å. and Beland, M.-C., 1994. Measurement of small-scale variation in printed paper – Topography explains much of the variation for one paper. In: *Proceedings of the 1994 International Printing and Graphic Arts Conference*, pp. 33–43.

Oittinen, P. and Saarelma, H. eds., 2009. *Print media – principles, processes and quality, papermaking science and technology*. Fapet Oy.

Tåg, C.-M., Toiviainen, M., Juuti, M. and Gane, P.A.C., 2012. Online detection of moisture in heatset printing: liquid transfer to printed and non-image areas. *Nordic Pulp and Paper Research Journal,* 27(1), pp. 112–121.

Voltaire, J., 2006. *Ink film splitting acoustics in offset printing*. Doctoral thesis. Royal Institute of Technology. Stockholm.

The Yin and Yang of Colors – how to calculate the exact Complementary Color to a specific chromatic Brand Color

Michael Abildgaard Pedersen

The Danish School of Media and Journalism (former Graphic Arts Institute of Denmark),
Department of Media Production and Management, Copenhagen

E-mail: map@dmjx.dk

Abstract

This paper will test a research question about whether or not it is possible to calculate the exact Complementary Color to a specific Brand Color in different color systems. A method is proposed and tested in five different color systems: CIELAB, RGB, CMYK, Spectrum and HSB including device independent, device dependent, additive and subtractive color systems. In each color system, it is attempted to calculate the Complementary Color to an orange Brand Color (Pantone 151 C). The results are compared to the results from an online Adobe Creative Cloud Service, *Adobe Kuler* which was chosen because it seems to be widespread among design professionals when finding Complementary Colors. It is concluded that it is possible to calculate a Brand Color's exact Complementary Color by using the technical specifications of the Brand Color as a starting point for this paper's method. *Adobe Kuler's* suggestions for Complementary Colors are far from this paper's calculated Complementary Colors and it is proven that Adobe Kuler's Complementary Colors are not technically correct according to this paper's methods. The color difference between this paper's calculated Complementary Color and Adobe Kuler's Complementary Color is ΔE^*_{ab} 62.5, ΔE_{00} 43.5 and ΔH^*_{ab} 12.6.

Keywords: complementary color, brand colors, graphic design, Adobe Kuler

1. Introduction and background

When Graphic Designers, Art Directors and other design professionals create new visual identities to Brand Owners they enter a process in which they have to decide which colors they should choose to represent the company in logos, design line and the other elements of the company's visual identity.

When the primary Brand Color has been chosen it will often be accompanied with other supporting colors or secondary colors, which also will be specified in the corporate Brand Manual. In principle, these supporting colors can be divided into four main categories:

A. *Achromatic Colors:* This can be a supporting Black, White and/or Grey. This is the neutral choice that will keep the focus on the Brand Color. (e.g. LG, AP, Canon, Fujitsu, Huawei)
B. *Monochromatic Colors:* This can be a supporting color, which has another shade/chroma of the Brand Color. E.g. a blue Brand Color which is accompanied by a darker or lighter blue. This is a choice that amplifies the signal value of the Brand Color. (e.g. BlackBerry, NATO, PayPal,)
C. *Analogous Colors:* This can be a supporting color, which have another hue close to the Brand Color. E.g. an orange Brand Color can be accompanied by a yellow or red supporting color. This choice will create a harmonic, rich and almost monochromatic look but also bears the risk of having a lack of contrast. (e.g. KODAK, McDonald's)

D. *Complementary Colors:* This is a supporting color which is the "opposite" color of the Brand Color. E.g. an orange or yellow Brand Color can be accompanied with a blue color. This choice ensures the largest possible contrast between the Brand Color and the supporting Color. (e.g. AT&T, GÈANT, Walmart).

While the first three possibilities (A to C) largely are a matter of subjective personal preferences, including corporate values, then the latter possibility (D) is mostly an objective technical matter.

Some designers argue that if you need two colors in your pallet it should be complementary colors (Schmidt, 2013). Other designers evaporate;

> *Complementary colors balance each other as they are opposites [...] In their brightest intensities, they literally command attention, so they are especially effective when used in packaging, advertising, at point of purchase, banners, sports uniforms or other usage where exuberant and instant attention is important.* (Eiseman, 2000)

However, when a Designer wishes to use a Complementary Color, it can prove difficult to find the exact Complementary Color, the exact technical opposite color. While it would be relatively simple to find the complementary color to a basic color like Black, Red, Blue etc. then it may prove to be a greater challenge to find the exact Complementary Color to e.g. an aborigine purple or an olive green.

The Designer might turn to some sort of color wheel or color circle where it is possible to get an indication on which hue area the Complementary Color is placed. However, even though these color wheels are built to also showing the Complementary Colors then they are far too limited to provide the exact answer. Newton's color wheel from 1704 contains seven colors, Goethe's color circle from 1793 contains six colors, Munsell's color circle from 1915 contains ten colors/hues or fourteen color tones RAL's has thirty-six colors and NCS' has forty colors. Thus, it is not possible to find the Complementary Color for more than a few Brand Colors – those who are already placed in the color wheels.

Today's online universe has provided services like *Adobe Kuler* in which it apparently is possible to find a Complementary Color to any color (https://color.adobe.com). However, when you look at the color values it doesn't seem to be the exact technical Complementary Color, as proven later.

Therefore, it would be much more reliable if the Complementary Color could be found by calculation.

2. Research questions and methods

Since all Brand Colors can be described and specified in various color models with specific color code values (Pedersen, 2016) that means that every color has a unique technical specification. Thus, it should be possible to use this technical specification to calculate the unique technical specification of the Complementary Color.

By first defining the relationship between a color and its Complementary Color, a formula for calculating this is proposed. This formula will be tested in both device independent, additive and subtractive color systems: CIELAB, RGB, CMYK, HSB and Spectrum.

Throughout this paper Pantone 151 C (PMS151C) is used as an example of a Brand Color to which the Complementary Color shall be calculated. This color where chosen because it is a typical Brand Color and because it is out of CMYK gamut like more than half of all Brand Colors (Pedersen, 2016).

By interviewing five different professional designers from different companies on how they find their Complementary Colors today I found that they all used the online service *Adobe Kuler* (color.adobe.com). Therefore, this online service has been used to check whether or not this paper's suggestions correspond to Adobe Kuler's complementary color proposals.

All CMYK and CIELAB-values presented in this paper were found by using PANTONE COLOR MANAGER Software (version 2.1.0.249 for Windows) from which the official Pantone CMYK (CP) and CIELAB values where read out.

All calculated ΔH^*_{ab}, ΔE^*_{ab} and ΔE_{00} values were found by using these official Pantone CIELAB values and the CIELAB values from *Adobe Kuler* as basis for the calculations.

All HSB and RGB values were found by first adjusting Adobe Photoshop, Color Settings, Color Space to Absolute Colorimetric Rendering Intent and relevant ICC-profiles and later entering the official Pantone CIELAB values into the Photoshop's Color Picker after witch HSB and RGB values was read out.

3. Results and discussions

The word COMPLEMENTARY derives from the Latin COMPLEMENTUM which means, *"That which fills up or completes"*. We know this symbolic principle represented in Yin and Yang. Together Yin and Yang completes the whole and make a balance. Even though Yin and Yang seems opposite or contrary, they are in fact complementary, interconnected, and interdependent. Together they create the complete and make a balance. Yin is complementary to Yang and vice versa. Thus, in the world of colors, a Complementary Color is the specific color, which together with the primary color completes the whole and creates a balance – The Yin and Yang of Colors (Figure 1).

Figure 1: Two complementary colors in Yin and Yang

In the light of the above, the first task must be to define *the complete* and *the balance*. *The complete* can be considered as the entire color space and the neutral axis as the balance point. Depending on the color space chosen, *the complete* is either black or white and therefore the assumption is that a Color + a Complementary color = black or white or vice versa; if we subtract a color from the color space (from *the complete*), what restores the balance must be the Complementary Color. Therefore, it should be possible to calculate the complementary color to any Brand Color by using the technical specification of the Brand Color as basis for the calculation. Thus, a Complementary Color to a Brand Color can be defined as:

$$A^c = \{B\} - \{A\} \quad [1]$$

where

$B = \{Color\ Space\}$

$A = \{Brand\ Color\}$

and where A is a proper subset of B

$A \subset B$

3.1 Finding the Complementary Color in the device independent CIELAB color space

Since the device independent color space CIELAB contains all visible colors including all Pantone, RGB, CMYK, RAL, NCS, Munsell colors etc. it would be possible and obvious to use CIELAB as a basis for calculating all Complementary Colors. However, this involves the risk of not noticing whether a device dependent color is placed within the gamut or not. Therefore, it is important first to investigate whether or not the current Brand Color can be reproduced in a device dependent color space. There is a probability that if the Brand Color is out of gamut for e.g. CMYK then the Complementary Color might also be out of gamut, as illustrated in the Figure 2.

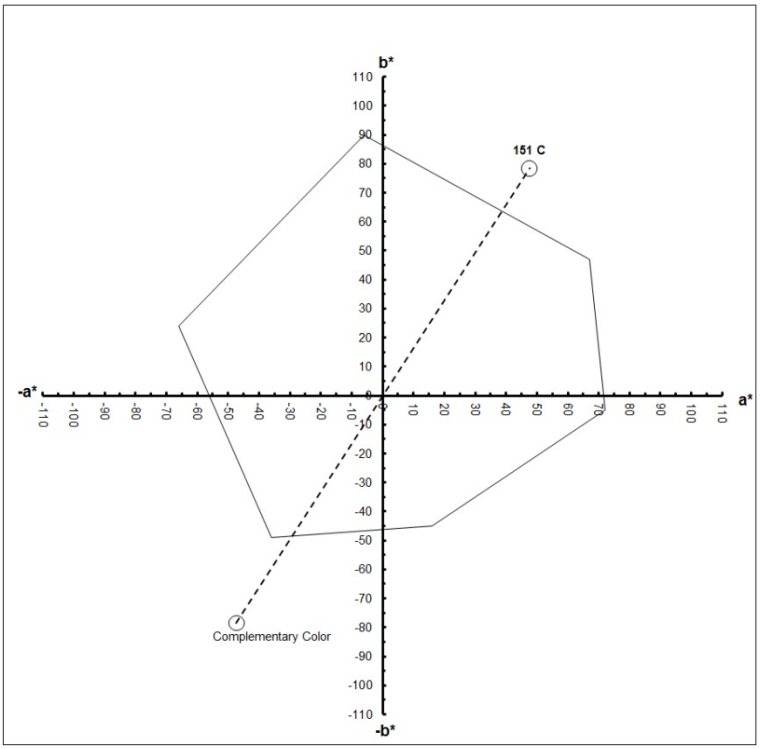

Figure 2: CIELAB ab diagram showing the Brand Color Pantone 151 C and the calculated Complementary Color both being out of CMYK gamut (FOGRA 39)

According to the Pantone Color Manager software Pantone 151 C has the following CIELAB values: L^* 69.68, a^* 47.27, b^* 78.51.

Therefore, the Complementary Color can be determined as:

$$A^C = \begin{Bmatrix} L^* & 100 \\ a^* & 0 \\ b^* & 0 \end{Bmatrix} - \begin{Bmatrix} L^* & 69.68 \\ a^* & 47.27 \\ b^* & 78.51 \end{Bmatrix} \quad [2]$$

$$The\ Complementary\ Color\ A^C = \begin{Bmatrix} L^* & 30.32 \\ a^* & -47.27 \\ b^* & -78.51 \end{Bmatrix}$$

Table 1: A practical example of finding the complementary color in CIELAB

COLOR SPACE {CIELAB}	–	BRAND COLOR {PMS 151C}	=	{COMPLEMENTARY COLOR}
L^* 100	–	L^* 69.68	=	L^* 30.32
a^* 0	–	a^* 47.27	=	a^* -47.27
b^* 0	–	b^* 78.51	=	b^* -78.51

In the device independent CIELAB color space the coordinates of the two colors shows that they have the same distance to the center of the neutral axis, as illustrated in Figure 2.

The distance between the Brand Color and the Complementary Color is 187.5 ΔE^*_{ab}

3.2 Finding the Complementary Color in the device dependent RGB

In the classic illustration showing the additive color system we see that cyan is the Complementary Color to red. This can be evidenced by:

Figure 3: The additive color system

$$A^C = \begin{Bmatrix} R & 255 \\ G & 255 \\ B & 255 \end{Bmatrix} - \begin{Bmatrix} R & 255 \\ G & 0 \\ B & 0 \end{Bmatrix} \quad [3]$$

$$The\ Complementary\ Color\ A^C = \begin{Bmatrix} R & 0 \\ G & 255 \\ B & 255 \end{Bmatrix} = CYAN$$

According to Adobe Photoshop Pantone 151C has the following AdobeRGB values: R:236, G:131, B:23. Thus we have the following equation:

$$A^C = \begin{Bmatrix} R & 255 \\ G & 255 \\ B & 255 \end{Bmatrix} - \begin{Bmatrix} R & 236 \\ G & 131 \\ B & 23 \end{Bmatrix} \quad [4]$$

$$The\ Complementary\ Color\ A^C = \begin{Bmatrix} R & 19 \\ G & 124 \\ B & 232 \end{Bmatrix}$$

Table 2: A practical example of finding the complementary color in AdobeRGB

COLOR SPACE {AdobeRGB}	–	BRAND COLOR {PMS 151C}	=	{COMPLEMENTARY COLOR}
R: 255	–	R: 236	=	R: 019
G: 255	–	G: 131	=	G: 124
B: 255	–	B: 023	=	B: 232

In the device dependent RGB color space the center of the neutral axis is R:128, G:128 and B:128. The distance of each RGB value to this axis is the same; the Brand Color's R:236 is 108 away from the neutral axis' R:128 like the Complementary Color's R:19 is 108 away from the neutral axis' R:128. And the same goes for the G-values and the B-values.

3.3 Finding the Complementary Color in the device dependent CMYK

In the classic illustration showing the subtractive color system we see that red is the Complementary Color to cyan. This can be evidenced by:

Figure 4: The subtractive color system

$$A^C = \begin{Bmatrix} C & 100 \\ M & 100 \\ Y & 100 \end{Bmatrix} - \begin{Bmatrix} C & 100 \\ M & 0 \\ Y & 0 \end{Bmatrix} \qquad [5]$$

$$The\ Complementary\ Color\ A^C = \begin{Bmatrix} C & 0 \\ M & 100 \\ Y & 100 \end{Bmatrix} = RED$$

In practical use it can be discussed whether or not the fourth process color Black should be a part of the equation since the subtractive color system only have three primaries; CMY. It is proposed that when black is not a part of the Brand Color then it shouldn't be part of the Complementary Color. Otherwise the Complementary Color would contain 100 % black. However, if the Brand Color have a significant black component (e.g. a dark green C:90 M:30 Y:90 K:30) then the Complementary Color should contain black as well (A^C: an aborigine purple C:10 M:70 Y:10 K:70).

According to Pantone Color Manager Software, Pantone 151 CP (Coated Paper) has the following CMYK values: C:0 M:60 Y:100 K:0. Thus we have the following equation:

$$A^C = \begin{Bmatrix} C & 100 \\ M & 100 \\ Y & 100 \\ (K & 100) \end{Bmatrix} - \begin{Bmatrix} C & 0 \\ M & 60 \\ Y & 100 \\ (K & 0) \end{Bmatrix} \quad [6]$$

$$The\ Complementary\ Color A^C = \begin{Bmatrix} C & 100 \\ M & 40 \\ Y & 0 \\ (K & 100) \end{Bmatrix}$$

Table 3: A practical example of finding the complementary color in CMYK

COLOR SPACE {FOGRA51}	–	BRAND COLOR {PMS 151 CP}	=	{COMPLEMENTARY CMYK}
C: 100	–	C: 000	=	C: 100
M: 100	–	M: 060	=	M: 040
Y: 100	–	Y: 100	=	Y: 000
K: 100	–	K: 000	=	((K: 100 (0))*

* in this case Black is not a part of the Brand Color and therefore not a part of the Complementary Color

In the device dependent CMY(K) color space the center of the neutral axis is C:50, M:50, Y:50, (K:50). It is seen that the Brand Color's M:60 and the Complementary Color's M:40 have the same distance to this center's M:50. They are both 10 away from the center.

3.4 Examination of the calculated Complementary Colors versus Adobe Kuler's suggested Complementary Colors

To examine how the previous calculated Complementary Colors corresponds with the Complementary Colors that designers find through *Adobe Kuler*, Pantone's reference values where entered into *Adobe Kuler* and *Adobe Kuler's* results was compared with the calculated results.

When entering Pantone 151C's corresponding AdobeRGB values (R:236, G:131, B:23) into *Adobe Kuler* it will propose a Complementary Color with the RGB values: R:23, G:183, B:236.

This shows that Adobe Kuler doesn't use this paper's proposed method since the two sets of RGB values don't add up to 255. According to Adobe Kuler *the complete* is: R:259, G:314, B:259 (R:236+23=259), (G:131+183=314), (B: 23+236=259) which in all three cases exceeds her maximum of 255 in the RGB color space. Thus, Adobe Kuler's proposed Complementary Color is not the exact technical Complementary Color to this Brand Color.

When entering Pantone 151C's CIELAB values into Adobe Kuler we find that there is a huge difference between the calculated Complementary Color and Adobe Kuler's proposed CIELAB values for the Complementary Color.

Table 4: Comparison

Pantone's reference CIELAB values for PMS 151C			→	Calculated Complementary Color		
	L^*	a^*	b^*	L^*	a^*	b^*
	69.68	47.27	78.51	30.32	-47.27	-78.51
Pantone's reference CIELAB rounded values entered into Adobe Kuler			→	Adobe Kuler's Proposed Complementary Color for PMS151C		
	L^*	a^*	b^*	L^*	a^*	b^*
	70.00	47.00	79.00	72.00	-16.00	-44.00
Numerical differences between the two Complementary Colors				ΔL^* 41.68	Δa^* 31.27	Δb^* 34.51
Color Differences				ΔH^*_{ab} 12.6	ΔE^*_{ab} 62.5	ΔE_{00} 43.5

3.5 Finding the Complementary Color in the visual spectrum

In the visual spectrum the spectral reflectance of the Complementary Color will be the inverse of the spectral reflectance of the Brand Color.

$$A^C = \{\text{Equal Energy (1)}\} - \{R_\lambda \text{ (the spectral reflectance of the Brand Color)}\} \qquad [7]$$

In the example below, this formula have been implemented in Microsoft Excel and subsequently measurement of the Brand Color (PMS 151C) has been conducted with a spectrophotometer (X-Rite SpectroEye) calibrated and set in accordance to ISO 12647-1:2013

nm	Brand Color Spectrum	Compl. Color 1 - Brand Color
380	0,0305	0,9695
390	0,0267	0,9733
400	0,0276	0,9724
410	0,0323	0,9677
420	0,0351	0,9649
430	0,0336	0,9664
440	0,0320	0,9680
450	0,0316	0,9684
460	0,0321	0,9679
470	0,0324	0,9676
480	0,0364	0,9636
490	0,0516	0,9484
500	0,0867	0,9133
510	0,1259	0,8741
520	0,1477	0,8523
530	0,1565	0,8435
540	0,1655	0,8345
550	0,1939	0,8061
560	0,2740	0,7260
570	0,4287	0,5713
580	0,6049	0,3951
590	0,7207	0,2793
600	0,7704	0,2296
610	0,7911	0,2089
620	0,8033	0,1967
630	0,8123	0,1877
640	0,8214	0,1786
650	0,8285	0,1715
660	0,8339	0,1661
670	0,8347	0,1653
680	0,8347	0,1653
690	0,8334	0,1666
700	0,8332	0,1668
710	0,8342	0,1658
720	0,8325	0,1675
730	0,8311	0,1689
740	0,8311	0,1689
750	0,8311	0,1689
760	0,8311	0,1689
770	0,8311	0,1689
780	0,8311	0,1689

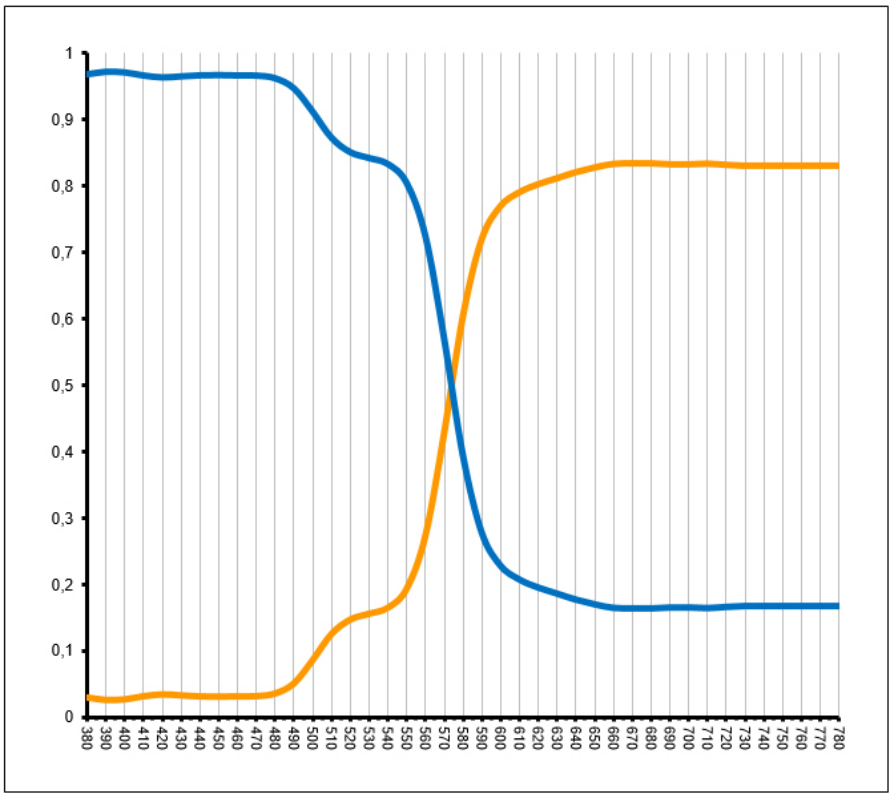

Figure 5: Orange curve: Spectral distribution of the orange Brand Color (Pantone 151 C)
Blue curve: the Complementary Color to the orange Brand Color (1 minus the spectral distribution of the Brand Color)

3.6 Finding the Complementary Color in Color Systems with Hue Angles

In color systems where colors are defined as metric hue angle degrees the previous presented model is not direct applicable.

In the HSB color space (Hue, Saturation, Brightness) the color is placed on a 360° circle while the Brightness and Saturation are defined as percent. Thus, if we use the previous presented model we will get an invalid result:

$$A^C = \begin{Bmatrix} H & 360° \\ S & 100\% \\ B & 100\% \end{Bmatrix} - \begin{Bmatrix} H & 31° \\ S & 100\% \\ B & 100\% \end{Bmatrix} \quad [8]$$

$$The\ Complementary\ Color\ A^C = \begin{Bmatrix} H & 329° \\ S & 0\% \\ B & 0\% \end{Bmatrix} = Black$$

In this case the complementary color to an orange would be calculated to be a black, which makes no sense. We have to leave the Saturation and Brightness as they are and concentrate on the Hue angle. Here, it is important to recognize that the Complementary Color always will be positioned on the exact opposite half of that of the Brand Color.

Therefore, the distance between the Brand Color and the Complementary Color will always be 180° and therefore 180° must be added or subtracted to the value of the Brand Color depending on the numerical value of the Brand Color.

When the Brand Color's hue angle is ≥ 180° then 180° must be subtracted from hue angle.
When the Brand Color's hue angle is ≤ 180° then 180° must be added to hue angle.

$$A^C = \{Brand\ Color° \pm 180°\} \quad [9]$$

EX.1: $A^C = \{31° + 180°\} = 211°$
EX.2: $A^C = \{211° - 180°\} = 31°$
EX.3: $A^C = \{92° + 180°\} = 272°$

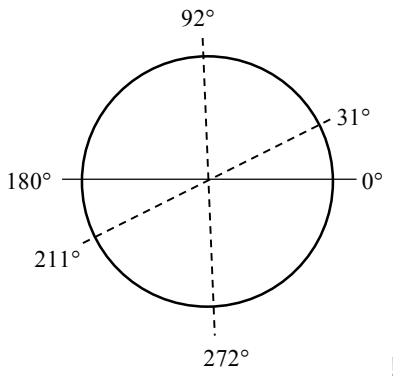

Figure 6: A 360° hue circle with two Color's hue angles and their matching Complementary Colors

4. Conclusions

It can be concluded that it is possible to calculate a Brand Color's exact Complementary Color by using the technical specifications of the Brand Color as a starting point for this paper's proposed method.

Adobe Kuler makes suggestions for Complementary Colors that are not technically correct according to this paper's methods and they are far from this paper's technical calculated Complementary Colors although they are in the same hue area.

References

Eiseman, L., 2000. *PANTONE Guide to Communicating with Color.* Cincinnati, Ohio: HOW Books.

Pedersen, M.A., 2016. Why most brand manuals fail when it comes to defining brand colors and how to determine acceptable color deviations for specific brand colors. In: P. Gane, ed. *Advances in Printing and Media Technology: Proceedings of the 43rd International Research Conference of iarigai*. Toronto, Canada, August 2016. Darmstadt: iarigai.

Schmidt, K. W., 2013. *CMYK Guide: Composing Colors*. Copenhagen: Grafisk Kommunikation ApS.

Microscale Halftone Analysis: measurement Framework and Convolution Strategy to differentiate Physical and Optical Dot Gain

Louis Vallat-Evrard, Lionel Chagas, Raphaël Passas and Nadège Reverdy-Bruas

Univ. Grenoble Alpes, LGP2, F-38000 Grenoble, France
CNRS, LGP2, F-38000 Grenoble, France
Agefpi, LGP2, F-38000 Grenoble, France

E-mail: louis.vallat-evrard@lgp2-grenoble-inp.fr, nadege.reverdy@pagora.grenoble-inp.fr

Abstract

Separating optical dot gain and physical dot gain is essential to predict with good accuracy spectral reflectances of halftone prints. In this work, we present a measurement framework associated with two new strategies to separate the optical dot gain from microscope captured halftone dots. These two strategies are developed, based on the model associating the ink transmittance, convolved with the paper point spread function, to obtain the optical dot gain participation in the total reflectance. Line spread functions for the papers used in our experiments are measured. It is shown that the papers considered behaved similarly as measurements of papers found in the literature with a global light scattering around 0.1 mm. Two optical dot gain separation strategies are presented and investigated. These two methods show an effective separation and images treated reveal un-inked surfaces previously masked by optical dot gain. For the first strategy, the two ink surface coverage measurements methods, the Murray-Davies based on micro optical densities and image processing threshold methods, showed maximum optical dot gain impacts of respectively 1.7 % and 8.4 % for offset, 4.9 % and 1.0 % for ink-jet and 4.2 % and 5.0 % for electrophotography. For the second strategy, these global optical dot gain impacts were raised to respectively 23.6 % and 18.7 % for offset, 20.0 % and 1.0 % for ink-jet and 14.3 % and 6.9 % for electrophotography. Results of optical dot gain were compared to literature for the offset processes where optical dot gain was classically measured between 5 % to 15 %. Analyses of the impact of the two optical separation strategies were conducted by comparing the gray values along the same halftone dots and showed the positive effect of the two strategies on the optical dot gain removal.

Keywords: print, point spread function, optical dot gain, Yule-Nielsen effect, ink spreading

1. Introduction and background

By observing an halftone print or by measuring an halftone area with optical devices (i.e. densitometry, spectrophotometry or microscopy) a phenomenon called optical dot gain (ODG) or Yule-Nielsen effect occurs. Depending on the paper properties, this phenomenon tends to reduce the perceived or measured reflectance of prints (Yule and Nielsen, 1951). The ODG effect is caused by the lateral light transport in paper (light diffusion). In fact, an incident photon arriving on the paper will not necessarily be reflected at the exact same location of its entering location. Dictated by the point spread function (PSF) of the paper, the photon arriving at will have a probability to exit the paper at a location () given by the probability density described by the PSF. This light diffusion is not problematic on blank paper, however, the ink having the property of absorbing part of the light, photons arriving at a location of blank paper, diffuse and can exit the paper under an inked surface. These photons are then absorbed by the ink, resulting in a decrease of the spectral reflectance. The ODG effect has been carefully studied and modeled (Kriss, 2015), in order to improve models predicting the output reflectance of a print. However, fewer studies have investigated the

impact of the ODG on the microscopic measurement of halftone dots. To obtain the actual surface of an ink deposition at the microscale, performing a microscopic measurement of halftone dots, it is then required to separate the local reflectance generated from ODG effect and the local reflectance from the ink absorption. To perform this separation authors have investigated different methods. Yang, et al. (2001) and Hersch and Yang (2008) proposed a method based on physical models describing the spectral reflectance or transmittance. Fleming, et al. (2002), Namedanian (2013) and Rahaman, et al. (2014) proposed a method based on the analysis of histograms of the captured images. Nyström (2008) and Ukishima (2010) proposed a method combining optical transmission and reflection microscopy to isolate ODG. Finally, Kristiansson, et al. (1997) proposed to measure directly the ODG with the Lund microscopy method. These methods are promising however they are either difficult or impossible to use for large number of measurements, or depend on image acquisition characteristics or perform only a partial separation. Moreover, it is interesting to note that obtaining a reference to compare separation methods is extremely difficult, as it requires a reliable non-optical measurement method to image the halftone dots at microscopic scale over a large area.

In this work we propose a new framework for optical microscopy halftone dots acquisition and image processing allowing to separate ODG and ink spreading on the surface of the paper. This framework establishes a precise protocol to obtain extended information from optical reflection microscopy measurements of halftone dots, through high dynamic range principle. Separation of ODG from captured images is then performed following two strategies developed according to Arney, et al. (2003) and Modrić, et al. (2014) model. Results of the two separation strategies are then analyzed and compared with reference of classical ODG found in literature.

2. Materials and methods

2.1 Paper, printing and test form

The microscope acquisition and ODG separation methods were tested on three different processes: offset, ink jet and electrophotography. The specifications for these three processes are detailed in Table 1. The printing form consists in a series of patches of different gray levels, ranging from 0 % to 100 % of grayscale. In order to print these continuous tones, halftoning was performed with Photoshop CS6 bitmap function, setting the output resolution to the resolution of the printer, the line per inch to 150 lpi and the shape of halftone dots to circular.

Table 1: Paper, printing and test form specification

Printing process	Printing resolution [dpi]	Halftone cell size [pixel]	Singular pixel size [µm]	Paper	Ink
Offset: Heidelberg Speedmaster 52	2 540	17 × 17	10.0 × 10.0	Glossy coated paper 135 g/m^2	Black Novavit 918 supreme bio
Ink jet: Epson Stylus Pro 4900	1 440	10 × 10	17.6 × 17.6	Epson standard proofing 205 g/m^2	Epson PK T6531 Black
Electrophotography: Ricoh Aficio MP C2800	1 200	8 × 8	21.2 × 21.2	Glossy coated paper 135 g/m^2	Ricoh MP C3000 Black

Differences in the native resolution of the printers resulted in different numbers of ink dot surfaces accessible to reproduce the grayscale wedge. According to Table 1, the offset process having a resolution of 2 540 dpi, has 290 gray levels accessible. On the contrary, the electrophotography process having a resolution of 1 200 dpi, only has 65 gray levels accessible. Thus, we can observe in Table 2 that the halftone theoretical ink surface coverages for each gray values differ depending on the approximation due to the number of

accessible gray levels. A maximum difference of 0.2 % is measured from theoretical continuous grayscale percentages to nominal halftone ink coverages. Effective ink coverage (EIC) are measured, around 20 % higher than nominal ink coverage (NIC) (Figure 5). Therefore, the variation caused by the print resolution represents only 1 % of ink coverage increase and can be neglected.

Table 2: Relations between grayscale value and halftone theoretical ink surface coverage

	Continuous tone gray values		**Halftone printing form ink surface coverage**		
Patch #	Gray value	Gray value percentage	Offset	Ink jet	Electrophotography
000	255/255	0.0 %	0.0 %	0.0 %	0.0 %
005	242/255	5.1 %	5.2 %	5.0 %	5.1 %
015	217/255	14.9 %	14.9 %	15.0 %	14.8 %
030	179/255	29.8 %	29.8 %	29.8 %	29.7 %
060	102/255	60.0 %	59.9 %	60.0 %	60.2 %
100	0/255	100.0 %	100.0 %	100.0 %	100.0 %

A Zeiss Axio Imager M1m optical microscope mounted with a Canon 1200D reflex camera (RGGB sensor, modified to monochromatic, 18.8 megapixels, CMOS camera) is used with an EC Epiplan Neofluar 20X/0.5 HD DIC objective. Total magnification on sensor is 32× with a physical pixel size of 4.3 µm/pixel × 4.3 µm/pixel. Thus, the calibrated system captures images of 0.133 µm/pixel × 0.133 µm/pixel, giving an observation field of 585 µm × 391 µm (reduction of sensor surface due to the modification into monochromatic sensor). The Canon 1200D camera is set to save images in CR2 raw format, allowing us to retrieve the measured value of reflectance for each photodetector. Using this raw format, no white balance compensation or interpolation is performed by the camera. The only controls for the sensor is the level of photon (in fine electron) amplification: ISO level and the time for the integration of the photons on the surface of the photodetectors: exposure time. The ISO parameter is set to 800 and exposure time is independently fixed for each image captured, ranging from 3.125 ms to 10 s. The 90° polarized reflected light microscopy configuration is chosen to capture halftone dots, thus excluding specular reflections and taking into account ODG (Nyström, 2008). A halogen lamp Zeiss Hal 100 is used as light source for the microscope and the lamp voltage is set to 10.7 V. The source used is not a standard illuminant however a blue filter is applied to have a spectrum closer to D65 standard illuminant. 42 200 lux is measured with a luxmeter and this luminance is set for all measurements.

2.2 Line spread function measurement

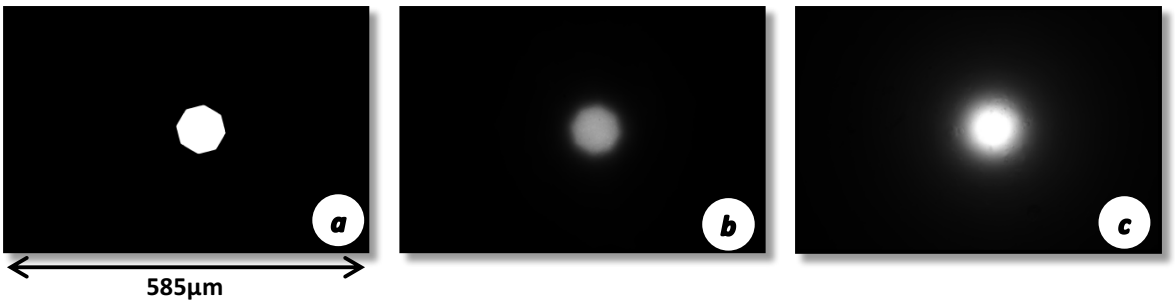

Figure 1: Knife edge illumination measurements: (a) perfect specular mirror, (b) glossy coated paper, (c) Epson standard proofing paper

From the captured image of a projected knife edge realized by closing the focal aperture of the incident illuminant on the microscope, an image showing light diffusion is obtained (Figure 1 (b) and (c)). By subtracting this image to the image of the reference containing the representation of the focal aperture

(Figure 1 (a)), we can calculate the half edge spread function (ESF) of the paper in all directions. This subtraction method allows to reduce the amount of noise generated in the second half on the ESF that is due to paper reflectance heterogeneities. From the half ESF, the complete ESF can be recovered thanks to the ESF assumed symmetry, represented in Figure 2. It is then possible to calculate the line spread function (LSF) by derivation of the edge spread function. We take the hypothesis that the light scattering on paper is isotropic. By averaging the LSF and applying a 2π rotational symmetry, we obtain an approximation of the point spread function (PSF).

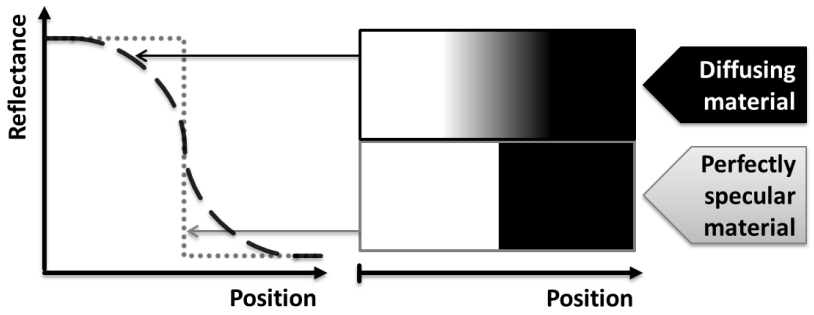

Figure 2: Edge spread function for a diffusing material (long dashes line) and for a perfectly specular material (round dots line) and 2D representation

2.4 Image processing to separate optical dot gain on captured images

The theory to separate the ODG is based on the model (Equation 1) proposed by Arney, et al. (2003) and discussed by Modrić, et al. (2014). This model establishes the relation between the reflectance at each point of a surface $R(x,y)$, as a function of the paper reflectance $R_p(x,y)$, the ink transmittance $T(x,y)$ and the convolution of $T(x,y)$ and PSF(x,y). The aim of the separation method is to obtain a reflectance image without ODG: $R_{NDG}(x,y)$. As shown in Equation 2, $R(x,y)_{NDG}$ is equivalent to $R(x,y)$ of Equation 1, except that the PSF(x,y) is set to 1. $T(x,y)$ can then be written as the square root of the fraction of $R_{NDG}(x,y)$ and $Rp(x,y)$. By knowing $T(x,y)$, $R_{NDG}(x,y)$ can be computed. Two strategies are developed to compute $T(x,y)$ from $R(x,y)$. The first strategy is developed from the following hypothesis: the convolution of $T(x,y)$ and $PSF(x,y)$ can be approximated by the convolution of the $PSF(x,y)$ and of the square root of the fraction of reflectance $R(x,y)$ divided by the paper reflectance $R_p(x,y)$. This hypothesis theoretically overestimates the ODG effect: the ink surface coverage is larger on the transmittance calculated from the reflectance than on the true transmittance. Once the convolution term is calculated, it is possible to obtain $R_p(x,y)$x$T(x,y)$ by division with $R(x,y)$, (Equation 1). It is then straightforward to compute $R_{NDG}(x,y)$, (Equation 2). This first strategy is summarized in Equation 3.

$$R(x,y) = R_p(x,y) * T(x,y) * [T(x,y) \circledast PSF(x,y)] \quad [1]$$
With $\circledast$ the convolution operator

$$R_{NDG}(x,y) = R_p(x,y) * T(x,y)^2, \quad \text{with PSF(x,y)=1}$$
$$T(x,y) = \sqrt{\frac{R_{NDG}(x,y)}{R_p(x,y)}} \quad [2]$$

$$\text{Hypothesis: } [\sqrt{\frac{R_{NDG}(x,y)}{R_p(x,y)}} \circledast PSF(x,y)] \text{ approxiamted by } [\sqrt{\frac{R(x,y)}{R_p(x,y)}} \circledast PSF(x,y)]$$
$$T(x,y) = \frac{R(x,y)}{R_p(x,y) * [\sqrt{\frac{R(x,y)}{R_p(x,y)}} \circledast PSF(x,y)]}$$
$$R_{NDG} = R_p(x,y) * T(x,y)^2 = (\frac{R(x,y)}{R_p(x,y) * [\sqrt{\frac{R(x,y)}{R_p(x,y)}} \circledast PSF(x,y)]})^2 * R_p(x,y) \quad [3]$$

The second strategy also focuses in obtaining $T(x,y)$ but uses a different hypothesis stating that the function $T(x,y)$ can be obtained by the thresholding of the reflectance $R(x,y)$ at a threshold value t. The term t, expressing the threshold value is then added to the function of the transmittance $T_t(x,y,t)$ to highlight that $T_t(x,y,t)$ is obtained by thresholdings of $R(x,y)$ for all threshold values t in the range [0 - 65 535]. Simulated $R_s(x,y,t)$ are obtained, computing Equation 1 for all threshold t, substituting $T(x,y)$ for $T_t(x,y,t=t)$. To find the threshold value t describing best $T(x,y,t)$, the measured $R(x,y)$ is compared with all simulated $Rs(x,y,t)$. By minimizing the root mean square of $R(x,y)$ and $R_s(x,y,t)$, the argument t_r is determined. $T(x,y,t=t_r)$ that best describes $R(x,y)$ is then determined. Obtaining the reflectance without ODG $R_{NDG}(x,y)$ becomes straightforward using Equation 2 substituting $T(x,y)$ with $T(x,y,t=t_r)$. This strategy is synthetized in Equation 4.

$$\begin{aligned}&\text{Hypothesis: } T_t(x,y,t) \text{ obtained by thresholding of } R(x,y) \text{ at threshold value t}\\&R_s(x,y,t) = R_p(x,y) * T_t(x,y,t) * [T_t(x,y,t) \circledast PSF(x,y)]\\&t_r = argmin(\sqrt{(R(x,y) - R_s(x,y,t))^2}) \text{ for all threshold values t in [0-65536]}\\&R_{NDG}(x,y) = R_p(x,y) * T_t(x,y,t=t_r)^2\end{aligned} \quad [4]$$

The two strategies are computed for the three different printing processes: offset, ink jet and electrophotography, for patches ranging from 0 % to 100 % surface coverage. Resulting separations are analyzed by two different approaches:

- EIC calculated with the Murray-Davies formula based on optical densities obtained with microscope captured images.
- EIC measured through image processing, counting the number of pixel remaining after an automatic thresholding using Otsu method. Let's note that the definition given by the Murray-Davies model is that a solid ink patch represents 100 % of surface coverage. To respect this definition, EIC are multiplied by a constant to obtain 100 % for the solid ink patch.

3. Results and discussions

3.1 Line spread function measurement of paper

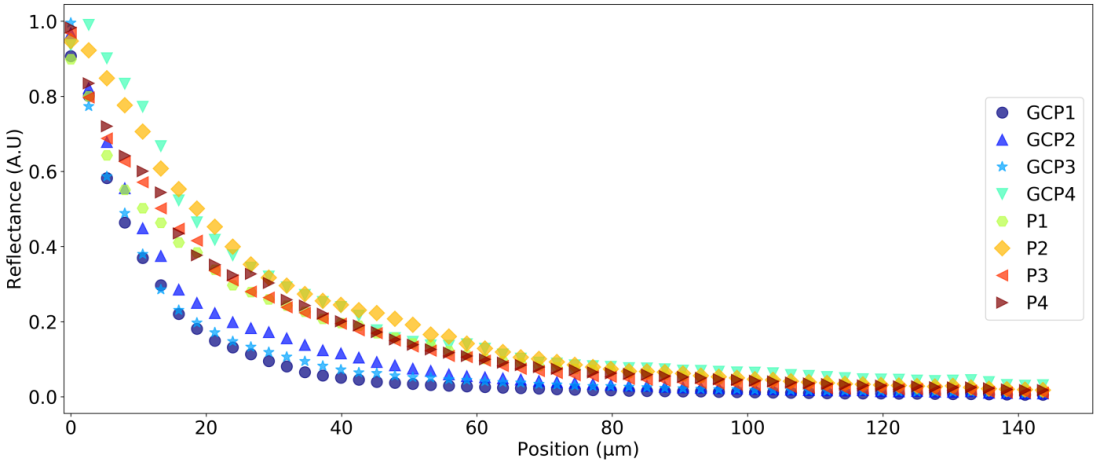

Figure 3: Line spread function of: GCP1=Glossy coated paper used in this study, GCP2=Silver blade coated paper, GCP3=Mondy "the glossy paper", GCP4=Epson standard proofing paper, P1=Condat offset paper, P2=Clairefontaine clairalfa paper, P3=Vertaris recycled, P4= Inapa laser classic paper

The line spread functions of various papers including the papers presented in this work are shown in Figure 3. Globally, a difference between coated and uncoated papers is pointed out. It is interesting to note that the Glossy coated paper used in the present study behaves as a coated paper with a shallower line

spread function. On the contrary, the Epson standard proofing paper, although coated, behaves more like an uncoated paper having a larger line spread function. These results are consistent with literature, with a global light scattering of about 0.1 mm (Linder, et al., 2013; Petric Maretić, et al., 2013).

3.3 Separation of optical dot gain from total dot gain analysis

In Figure 4, the results of the separation of ODG from TDG of offset printing patches are depicted. Comparing row 2 and 3 from row 1, the areas where the ODG was impacting the print are observed. Small unprinted areas on the inked dots appear dark on images presenting TDG. Images without ODG showed unprinted areas more clearly. Separation of ODG seems to be more pronounced for strategy 2. Indeed, due to the thresholding used for strategy 2, only a single ink thickness is kept, neglecting areas of light inking. ODG separation results, for ink-jet and electrophotography, are presented in Appendix 1. For these two processes presenting less small blocked areas, the effect of ODG removal, is observed particularly around the dots. It is interesting to note that for inkjet an over separation area appears for strategy 1. This behavior may be induced by a different light scattering effect due to penetration of the ink into the first layers of the substrate.

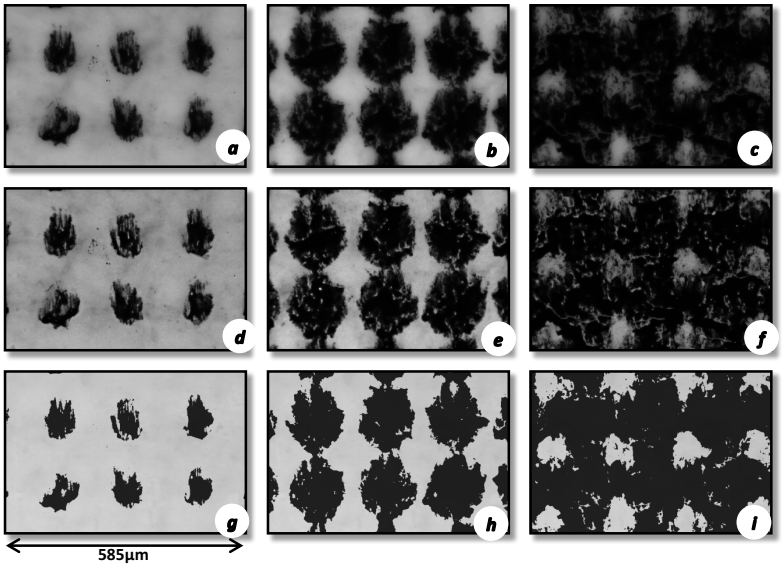

Figure 4: (a, d, g) 10 % of NIC, (b, e, h) 40 % and (c, f, i) 60 %. (a, b, c) images of TDG, (d, e, f) images obtained with strategy 1 and (g, h, i) images obtained with strategy 2

The separation of ODG was analyzed comparing EIC calculated with the microscopic optical density and thresholding image processing methods (Figure 5 and Appendix 2). For the offset process, considering the measurement based on the micro optical densities (Figure 5 (a)), the removal of the ODG reduces, for the first strategy, the tonal value increase of a maximum of 1.7 % at 30 % NIC. High and low NIC are less impacted by the ODG, since there is less paper surface to diffuse the light or ink surface to absorb the diffused light. For strategy 2, results show a higher ODG, with a maximum of 23.6 % at 20 % NIC. The ODG calculated with the second strategy reduces with the increase of ink coverage. Interestingly low NIC are mostly impacted by ODG, suggesting that there would be no ink spreading below 20 % NIC. Looking at strategy 1 measured with the thresholding technique, (Figure 5 (b)), a higher ODG is observed with a maximum of ODG of 8.4 % at 50 % NIC. Comparing the histogram of the gray values distribution, it can be noticed that the image with the TDG has a larger distribution than the one having no ODG obtained through strategy 1. This difference in distribution occurs mostly when the un-inked paper surface becomes small. Since the threshold algorithm is based on the analysis of the gray values distribution, ink surface coverage calculated could become biased. However, this is not the case as both measurement methods give similar results for ODG above 80 % NIC. For strategy 2, the result of EIC measurement based on threshold gives similar result than the method based on micro optical densities. The maximum ODG is about 18.7 % at a NIC of 40 % and

decreases for high and low NIC. Similar trends are observed for the electrophotography and inkjet processes, as illustrated in Appendix 2. For the electrophotography, the maximum ODG is respectively of 4.2 % and 14.3 % at 50 % NIC for strategy 1 and strategy 2 for the measure based on micro optical densities. For the measure based on thresholding, maxima are measured at 5.0 % and 6.9 % at 50 % NIC for strategy 1 and strategy 2. For inkjet, the maximum ODG is respectively of 4.9 % and 20.0 % at 30 % NIC for strategy 1 and strategy 2 for the measure based on micro optical densities. For the measure based on thresholding, maxima are measured at 1.0 % at 30 % NIC for both strategies. Classical values for ODG for the offset process (printer at 1 200 dpi, halftone at 150 lpi) with coated paper, are found in literature between 5 % to 15 %, (Namedanian and Gooran, 2011; Nyström, 2008). The values found for ODG for the offset process are then in the same range or slightly higher than classical ODG found in literature.

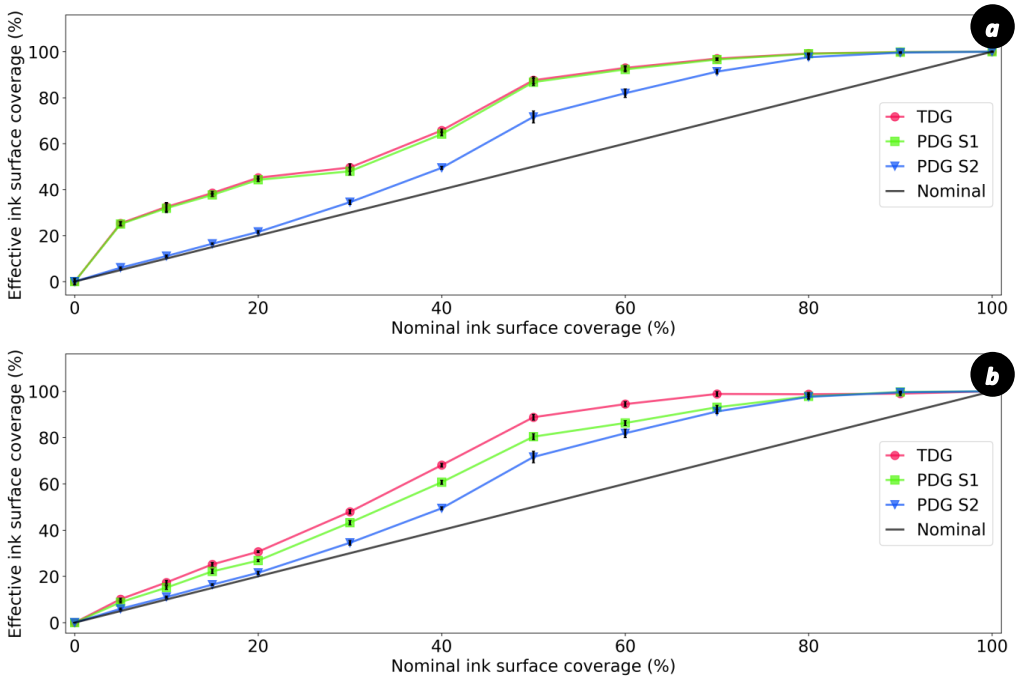

Figure 5: EIC as a function of the NIC for TDG patches and for patches with ODG removed with strategy 1 (PDG S1) and strategy 2 (PDG S2): (a) Murray-Davies micro optical density method, (b) thresholding method

3.4 Optical dot gain separation local analysis

With the difficulty to obtain reliable references, performance evaluation of the two ODG separation methods is difficult to conduct. However, analyzing the performance of the method by qualitative observation of the printed dot evolution (with ODG and without) is possible (Figure 6 and Appendix 3). It can be noticed, on this graph, that there are 3 main gray values families. The first one located in the low gray values represents the ink. The second located in the high gray values represents the paper. The in-between gray values family with levels around 20 000/65 535 represents the area most impacted by ODG. This third gray values family is mostly present for the printed dot with TDG. Effects of the ODG separation strategies can be observed as pics highlighted by the arrows are moved from low gray values to high gray values. Globally, ink gray values level and paper gray values level remain the same after the separation of ODG for the two strategies compared to the TDG. Small offset is found for the paper gray values level of the strategy 2 separation, where its value is found closer to the value of blank paper. Decrease effect of the paper reflectance due to ODG is observed for the TDG printed dots. The ODG separation strategy 1 should theoretically remove this effect and gray values for paper should be similar to the one on blank paper. It is not completely the case for the first strategy, and shows that the ODG removal was not complete. Overall, the two strategies show a satisfying removal of ODG on the inked surfaces. Similar observations are made from Appendix 3. It can be outline that for the inkjet process the difference between paper gray value levels is even more marked.

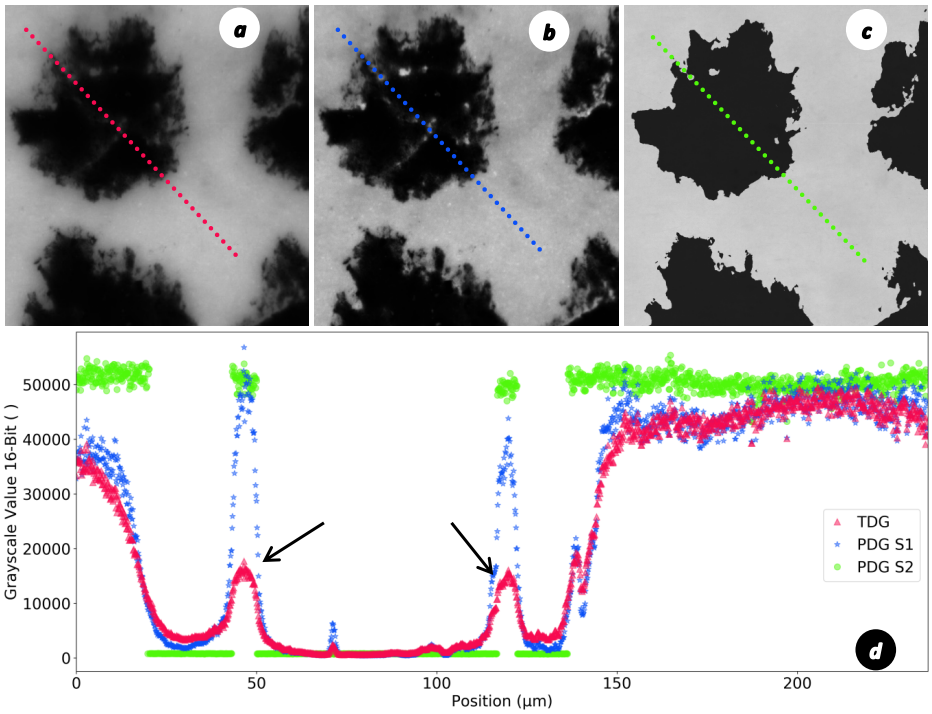

Figure 6: Offset printed dot of 30 % NIC on paper for (a) capture with TDG, (b) ODG removed capture with strategy 1 and (c) ODG removed capture with strategy 2; (d) gray values as a function of the position along the lines represented on images (a, b, c).

4. Conclusions

The measurement framework presented in this work as well as the convolution strategy allowed to separate ODG from TDG. PSF for the papers used in the present experiments were measured and compared with other papers PSF. It was shown that the papers considered in this study behaved similarly to papers referenced in the literature, with a global light scattering around 0.1 mm. Two ODG separation strategies were presented and investigated. The two methods showed an effective separation and images treated revealed un-inked surface previously impacted by ODG. For the first strategy, the two EIC measurements methods, the Murray-Davies based on micro optical densities and image processing threshold methods, showed a maximum ODG impact of respectively 1.7 % and 8.4 % for offset, 4.9 % and 1.0 % for ink-jet and 4.2 % and 5.0 % for electrophotography. For the second strategy, these global ODG impacts were raised to respectively 23.6 % and 18.7 % for offset, 20.0 % and 1.0 % for ink-jet and 14.3 % and 6.9 % for electrophotography. Results of ODG were compared to literature for the offset processes where ODG was measured between 5 % to 15 %. The values found for ODG for the offset process are then in the same range or slightly higher than classical ODG found in literature. Analyses of the impact of the two optical separation strategies were conducted by comparing the gray values along the same halftone dot lines. It was found that the results of the two strategies are closer to a bimodal distribution, accounting only for ink gray levels and paper gray levels. These analyses showed the positive effect of removal of ODG on the inked surfaces. However, paper gray levels for strategy 1 was not exactly matching the gray levels of blank paper, showing that the ODG removal was not total. We conclude that this new ODG separation showed great qualitative effect in removing the ODG effect. Quantitative evaluation of the two separation strategies performances remains difficult to conduct because of the difficulty in obtaining a reliable reference of the true ink distribution on paper. Continuation of this work should focus on finding a reliable reference of ink distribution without ODG for printed halftone dots on paper.

Abbreviations

ODG: Optical dot gain
PDG: Physical dot gain
TDG: Total dot gain
NIC: Nominal ink coverage
EIC: Effective ink coverage

Acknowledgments

This research was supported by grants from the Agence Nationale pour la Recherche (A.N.R., France – ANR-10-CORD-019), the LabEx Tec 21 (Investissements d'Avenir - grant agreement N° ANR-11-LABX-0030) and of the Énergies du Futur and PolyNat Carnot Institutes (Investissements d'Avenir - grant agreements N° ANR-11-CARN-007-01 and ANR-11-CARN-030-01), TekLiCell platform funded by the Région Rhône-Alpes (ERDF: European regional development fund). Acknowledgment to D. Naud, S. Collet and students at Argouges high school, 61 Rue Léon Jouhaux, 38029 Grenoble, France. Acknowledgment to GRAFI print, 15 Rue Baptiste Marcet, 38600 Fontaine, France.

References

Arney, J.S., Chauvin, J., Nauman, J. and Anderson, P.G., 2003. Kubelka-Munk theory and the MTF of paper. *Journal of Imaging Science and Technology*, 47(4), pp. 339–345.

Fleming, P.D., Cawthorne, J.E., Mehta, F., Halwawala, S. and Joyce, M.K., 2002. Interpretation of dot area and dot shape of inkjet dots based on image analysis. In: *NIP & Digital Fabrication Conference: International Conference on Digital Printing Technologies*. Society for Imaging Science and Technology, pp. 474–477.

Yang, L. and Hersch, R.D., 2008. Kubelka-Munk model for imperfectly diffuse light distribution in paper. *Journal of Imaging Science and Technology*, 52(3), pp. 30201–030201–7.

Kriss, M., ed., 2015. *Handbook of Digital Imaging.* Chichester, UK: Wiley.

Kristiansson, P., Nilsson, C.M., Busk, H., Malmqvist, L., Elfman, M., Malmqvist, K.G., Pallon, J., Sjöland, K.A., Utui, R.J. and Yang, C., 1997. Optical dot gain on newsprint determined with the Lund nuclear microprobe. *Nuclear Instrument and Methods in Physics Research Section B: Beam Interactions with Materials and Atoms*, 130(1-4), pp. 303–307.

Linder, T., Löfqvist, T., Coppel, L.G., Neuman, M. and Edström, P., 2013. Lateral light scattering in fibrous media. *Optics Express*, 21(6), pp. 7835–7840.

Modrić, D., Petric Maretić, K. and Hladnik, A., 2014. Determination of point-spread function of paper substrate based on light-scattering simulation. *Applied Optics*, 53(33), pp. 7854–7862.

Namedanian, M., 2013. *Characterization of Halftone Prints based on Microscale Image Analysis*. Ph.D. Dissertation. Linköping University.

Namedanian, M. and Gooran, S., 2011. Characterization of total dot gain by microscopic image analysis. *Journal of Imaging Science and Technology*, 55(4), pp. 40501–40501–7.

Nyström, D., 2008. *High Resolution Analysis of Halftone Prints: A Colorimetric and Multispectral Study*. Ph.D. Dissertation. Linköping University.

Petric Maretić, K., Milković, M. and Modrić, D., 2013. Akaike information criterion in the edge analysis of the screen element. *Tehnički Vjesnik*, 20(3), pp. 441–447.

Rahaman, G.M.A., Norberg, O. and Edström, P., 2014. Microscale halftone color image analysis: perspective of spectral color prediction modeling. In: Proceedings 9015, Color Imaging XIX: Displaying, Processing, Hardcopy, and Applications: IS&T/SPIE Electronic Imaging. San Francisco, CA, 2–6 February 2014. SPIE.

Ukishima, M., 2010. *Prediction and Evaluation of* Color *Halftone Print Quality Based on Microscopic Measurement*. PhD Dissertation. University of Eastern Finland and Chiba University.

Yang, L., Lenz, R. and Kruse, B., 2001. Light scattering and ink penetration effects on tone reproduction. *Journal of Optical Society of America A*, 18(2), pp. 360–366.

Yule, J.A.C. and Neilsen, W.J., 1951. The penetration of light into paper and its effect on halftone reproduction. In: *Proceedings TAGA 3*, pp. 65–76.

Appendices

Appendix 1: (a, d, g) 10 % of EIC, (b, e, h) 40 % and (c, f, i) 60 %. (a, b, c) images of TDG, (d, e, f) images obtained with strategy 1 and (g, h, i) images obtained with strategy 2.

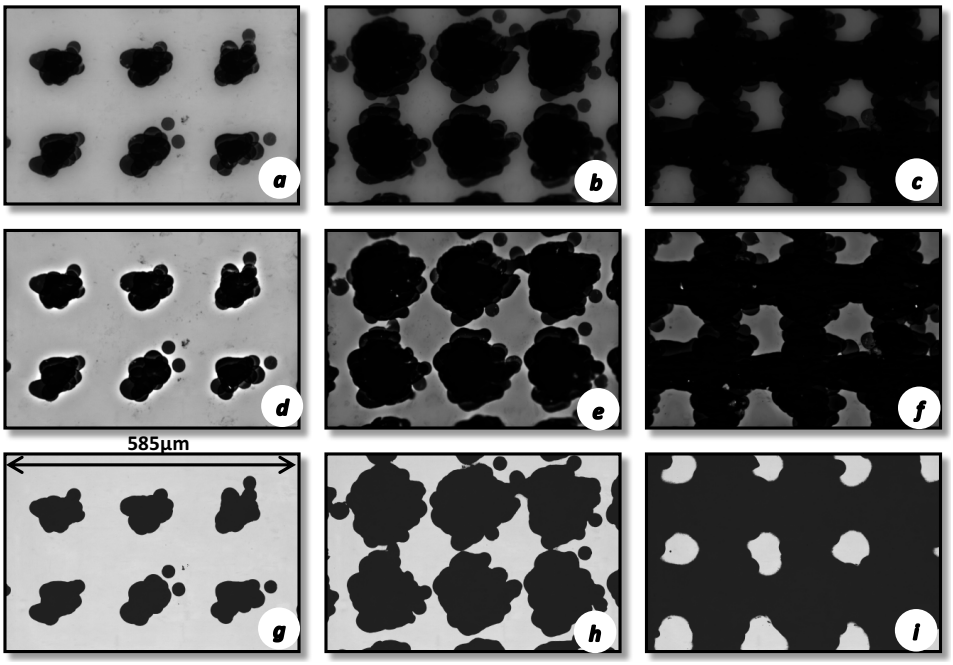

Figure 7: Results of the separation of ODG for ink-jet printing

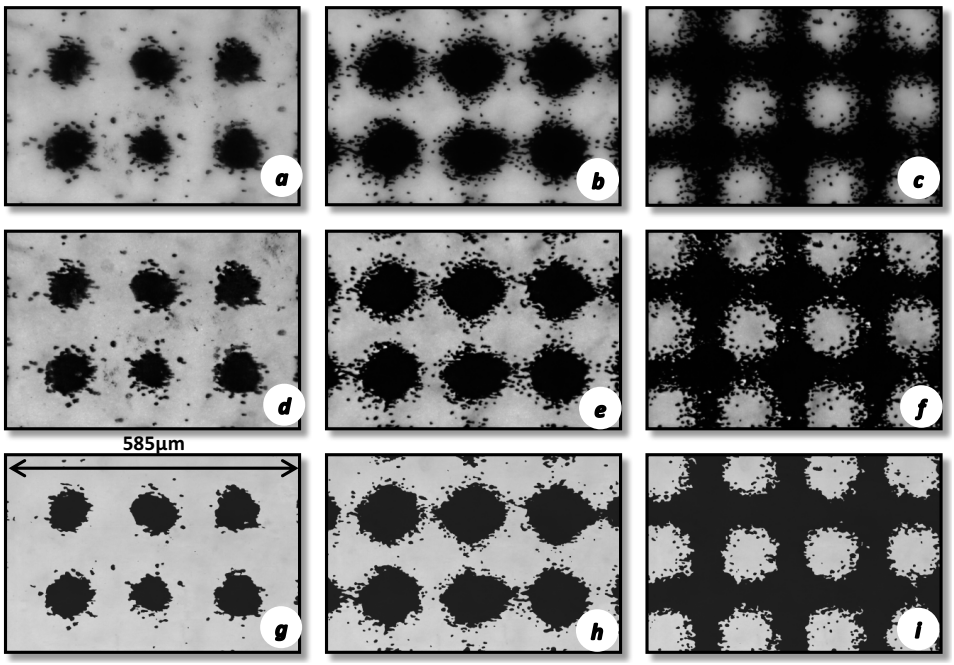

Figure 8: Results of the separation of ODG for electrophotography printing

Appendix 2

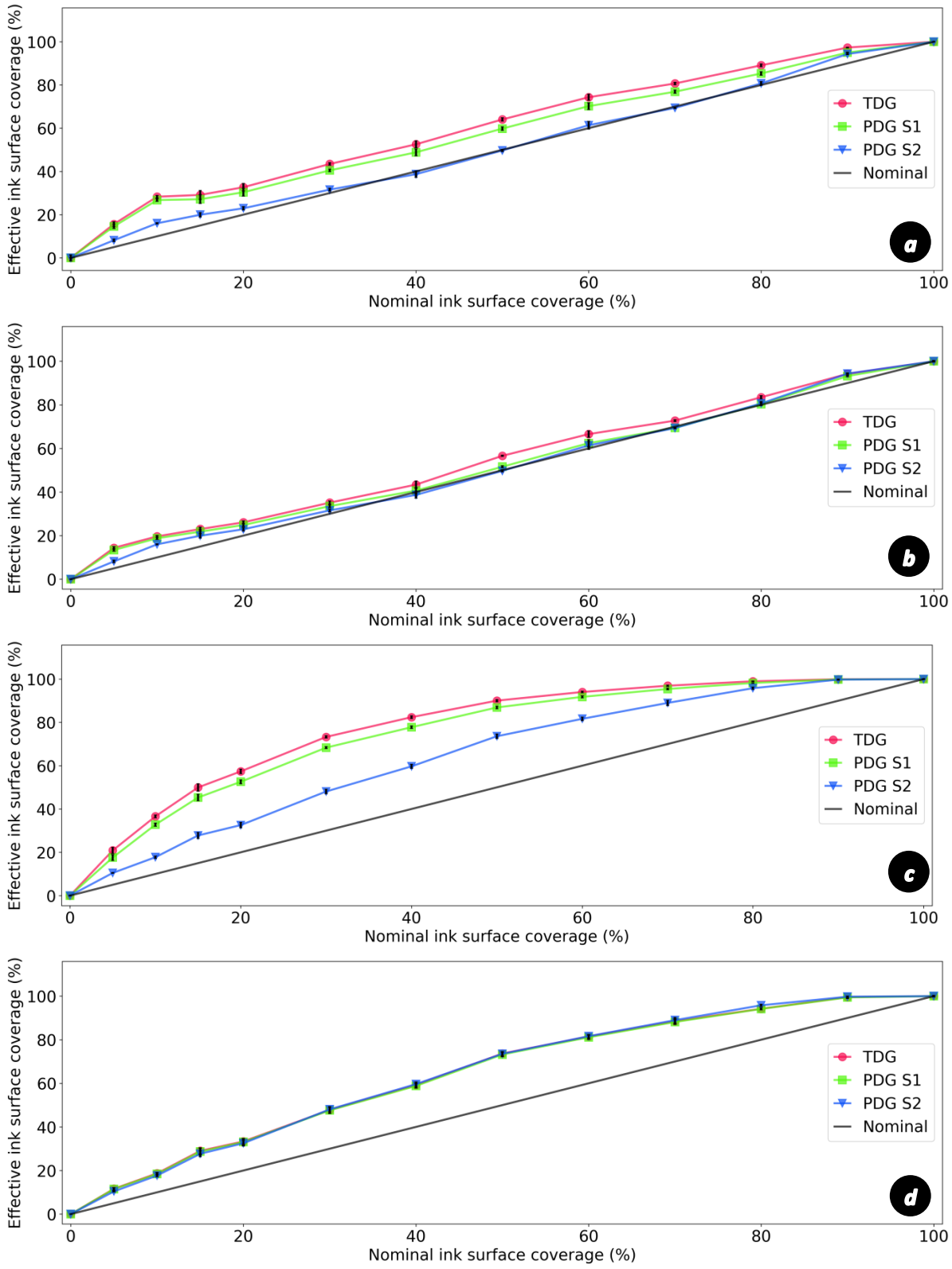

Figure 9: EIC as a function of the NIC for TDG patches and for patches with ODG removed with strategy 1 (PDG S1) and strategy 2 (PDG S2): (a) and (b) electrophotography, (c) and (d) inkjet, (a) and (c) Murray-Davies micro optical density method, (b) and (d) thresholding method

Appendix 3

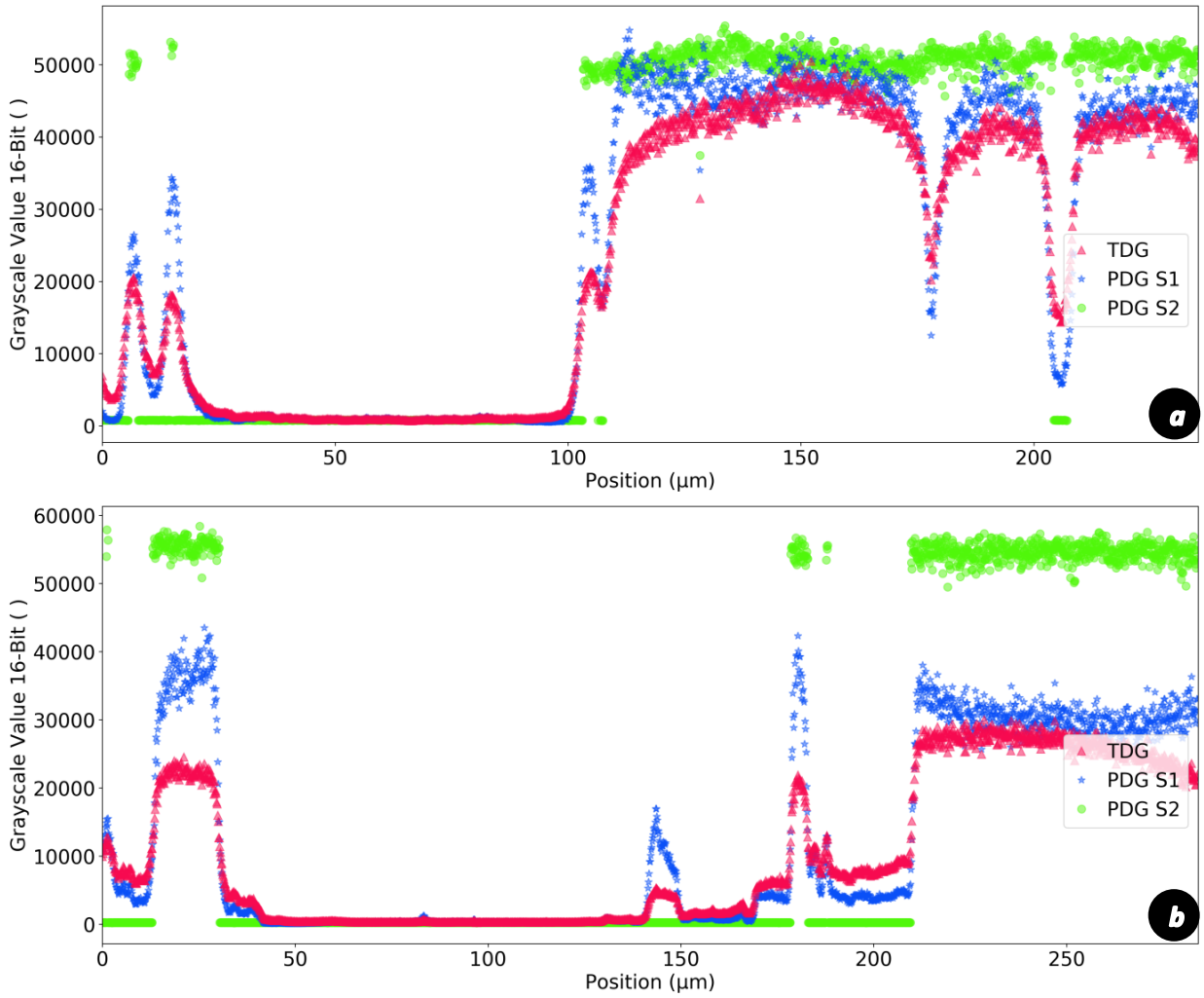

Figure 10: Gray values as a function of the position for printed dots of 30 % NIC (a) electrophotography and (b) inkjet; (PDG S1) ODG removed with strategy 1 and (PDG S2) with strategy 2

Special Examination for the Durability of Text Books

Csaba Horváth

Óbuda University, Institute of Media Technology and Light Industry Engineering, Doberdó u. 6., H-1034 Budapest, Hungary

E-mail: horvath.csaba@rkk.uni-obuda.hu

Abstract

Although nowadays the use of the devices of electronic communication as an option is more and more frequently considered, school books have still remained the fundamental learning aids. But what is a durable school book like? The article describes the test methods that the authors have determined for the description of the structural durability of school books. There were seven types of school books differing from each other in format and/or binding technology tested, and applied to model the book-using "'habits" of students; the results have been systematically arranged, and options have been determined for the improvement of durability properties. In summary of the test results, it can be claimed that with respect to durability school books are made ideal when they are designed in smaller dimensions and with the smallest possible weight. It is better to have paperback covers, because during the performed tests hardcover books reflected more serious damage.

Keywords: textbooks, durability, bookbinding, universal book tester

1. Introduction

Today, during the production of books nearly all the binding operations are performed with machines. These technologies have developed a lot in the past 5–6 decades, especially the so-called perfect binding techniques. They properly satisfy the demands relating to the general use of books (ACTS, 2012).

It is primarily libraries that have had demands for so-called durable books, while this need has become increasingly stressed in the production of school books, too. In recent years, Hungary has particularly seen this issue associated with the quality properties of the so-called durable school books coming to the focus of attention. The fact that the need for durable school books has become important has been largely fostered by the government's effort launched in 2014 for the provision and distribution of durable school books. Requirements relating to school books (especially durable school books) are stipulated in Ministerial Decree 17/2014 (March 12) of the Ministry of Human Capacities. In terms of structural considerations and book binding, from among the provisions set out in the Decree it is only the so-called technological requirements that bring about harder tasks and challenges than before:

"**§ 38.** Technological requirements pertaining to durable books:

a) assembling the sheets of the school book with the use of thread-stitching or backlash lining,
b) durable and at the same time light form of binding: reinforced paperback (cover: at least 260 grams/square meter, cellulose-containing cardboard four times grooved), or hard-covered, or flexible binding,
c) B/5 or A/4 sized book block,
d) use of light inner paper,
e) surface finishing of the cover (thermofoil)."

Based on the Decree, from a technological (binding) perspective books are evaluated with the respect to the following criteria.

"A) Criteria of evaluation for school books of general subjects
II. Technological (binding) criteria
1. Dimensions of the book block, number of pages, mass and weight with respect to the age of the student
2. Quality of the used paper and other materials, durability of the book
3. Typography, fonts types, font sizes, system of highlights and displays
4. Page-setting, ratio and harmony of texts to images, typography of highlights and displays
5. Quality and legibility of printing, application of colours.**"**

It is apparent that the above-quoted Decree does not set out specific criteria, requirements in relation to the structural, mechanical properties of school books (durable books), the concept of durability.

Although the printing industry and the various research institutions associated with the printing industry apply well-known test techniques, methods and devices that are useful for determining the mechanical properties of a given book (mostly constituents) with respect to a specific requirements or even set of criteria, at the same time the methods for the evaluation of these test methods and the obtained results are not covered in any standardized, broadly accepted system. It means that generally accepted, objective methods and standards that would determine the mechanical and technological durability of bound books, and in particular the so-called durable books (library books and school books), on the level of definitions and substances are not available.

To promote the resolution of the issues listed above, our study has had the goal to elaborate quality indicators for durable school books, as well as define and model the properties of their durability.

2. Methods of the research

On the one hand, as it has been mentioned above, currently there is no uniform, generally accepted test method or standard that would specify the requirements in association with the examination and review of the binding quality of bound books, their durability, or the evaluation of the obtained results.

On the other hand, we are able to summarize the known test methods that are currently used for the verification of the binding quality of new, completed and bound books (Rebsamen, 2002; 2003a; 2009). Nevertheless, these test methods are not suitable for shedding light to information in relation to expected lifetime, its resistance to the mechanical and other impacts that affect the book during use. There are different devices from various manufacturers to examine the binding strength of books made with perfect binding. Examples include the Smithers' Pira Book tester or the Moffett Page Pull tester-80 (Figure 1).

In the absence of appropriate standards, it is a difficult challenge to accurately adjust binding strength tests, as with the different device types the same results can be achieved with dissimilar settings. With the given equipment, such "online" (i.e. in the process of manufacturing) quality control actions may as well be carried out to help to reduce the number of defective products. Testing yields quick and prompt results, which allows machine operators to correct/adjust production lines in the course of manufacturing. If the problem with inadequate binding strength is caused by the defect of the glue, then it can be promptly detected with the help of the mechanical test.

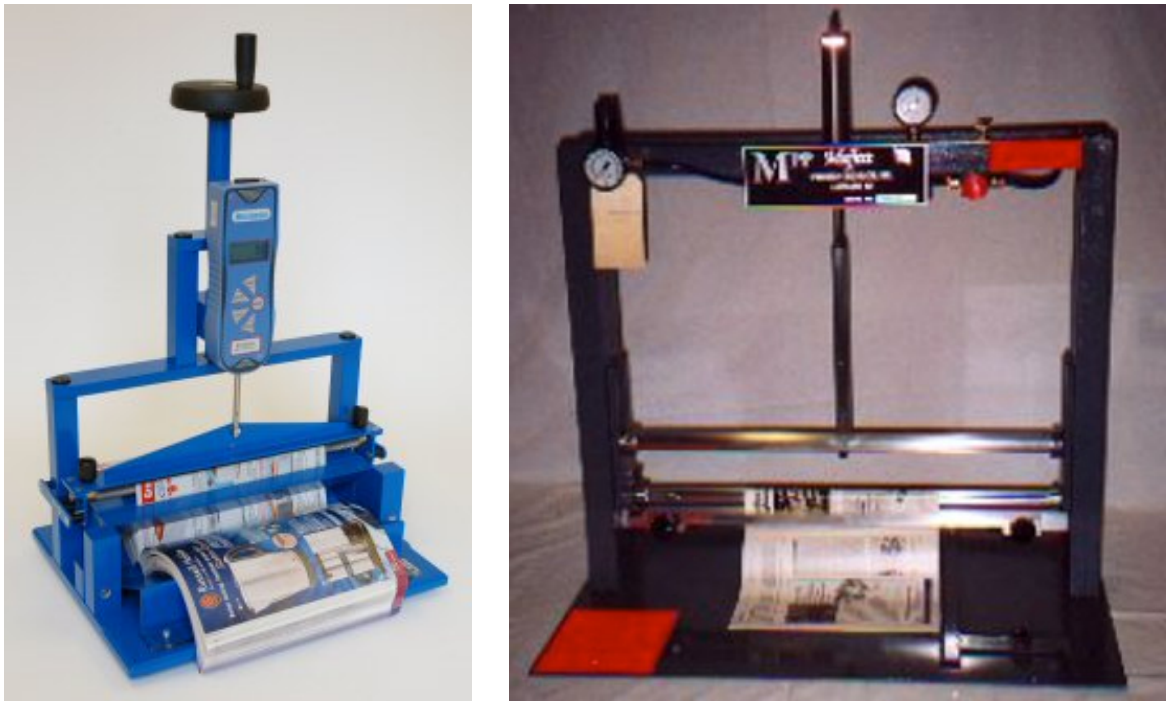

Figure 1: Smithers' Pira Book tester and Moffett Page pull tester-80

During the examination conducted with the MOFFETT Flex tester-40 equipment (Figure 2), loading is exercised on the clamped and tested book pages cyclically, in contrast with the form of loading used by the above-described binding strength testing devices (non-recurrent stress that gradually increases up to the limit of binding strength). With the equipment, the stress that imitates page turning is exercised on the tested page of the book at a 40 cycles/minute rate. Two types of loading strengths can be applied. The number of stress cycles is recorded, and the equipment automatically stops when the examined page becomes torn, or any other damage takes place. The binding strength of the given book can be described with the number of the stress cycles (and the extent of the applied loading). A main difference of this type of equipment in comparison with the previous devices is that it can be used only with perfect bound books.

Figure 2: MOFFETT Flex tester-40

Figure 3: Moffett UBT-9 Universal Book tester

The Moffett UBT-9 (Figure 3) is designed to test the durability, that is, it evaluates several aspects of a hard-cover binding; the abrasion resistance of covering materials, the integrity of the hinges, the stiffness and resistance to de-lamination of the boards, and to a limited degree, the durability of the sewn or adhesive bound book blocks (Rebsamen, 2003b; 2013; Hyatt, 1988).

The device consists essentially of a rectangular test chamber constructed of steel, lined with 50 by 50 mesh of No. 304 stainless steel wire 0.009 inch in diameter. The chamber is supported and rotated by a drive shaft attached perpendicular to the centre of its base. Viewed from the front, the drive is inclined at an angle of 20° from the horizontal, and rotates in a clockwise direction at a speed of 20 rpm. The dimensions of the test chamber vary with the size of the volume being tested (MSST, 2012).

The spine of the book is perpendicular to the squared ends of the chamber. As the chamber rotates, the book slides in a regulated manner, receiving impact stresses on the bottom, along with the abrasion of the edges and shoulder, and some flexing of the hinges. The principle actions of the UBT are pulling of the head-cap, sliding the book off the shelf, dropping the book on a book truck or a return box, and sliding the book across the table or down a chute! The capabilities of the Moffett UBT-9 are presented in Table 1.

Table 1: Capabilities of the Moffett Universal Book Tester Model-9

Actions Produce the Following Results
1. abrasion of the shoulder of the spine
2. abrasions of the edges of the cover
3. light abrasion of the cover surface
4. distortion by impact
5. abrasion of the tail-cap and edges
6. hinge flexing action
7. breaking and tearing of the internal hinge
8. failure of sewn or adhesive bindings and splitting of the spine
9. abrasion and turning up of the edge of cover*

* We have assessed the testing of this property to be important.

The tested school books are used at primary and secondary schools. All of them have been provided by the manufacturers for testing. Their properties are specified in Table 2.

Table 2: School books subjected to testing and their properties

Book No.	Cover	Binding	Size	Tested Quantity
7–9	hard-covered	thread-stitched	A4	3 pcs
13–15	hard-covered	thread-stitched	B5	3 pcs
16–18	hard-covered	thread-sealed	B5	3 pcs
19–21, 25–27, 28–30	soft-covered	thread-stitched	A4	3 pcs
4–6	soft-covered	thread-stitched	B5	3 pcs
22–24	soft-covered	perfect bound with PUR	A4	3 pcs
1–3,10–12	soft-covered	perfect bound with PUR	B5	3 pcs

3. Results

Due to the limitations of the extended abstract, only a part of the study will be presented. For paperback school books, durability tests assessing the conditions of the spine edges and corners, as well as binding conditions have been carried out. The other tests are conducted in a similar manner, and summed up in the conclusion.

3.1 Abrasion at the spine edges

From among the B/5 sized school books with perfect PUR binding, the school book with the 250 g/m^2 cardboard cover and non-gloss foil coating (Figure 4) proved to be the best concerning the abrasion of spine edges. The abrasion is hardly visible to the naked eye. The moderate damage is also due to the light, 230 gram weight of the book, as the book smashes against the sides of the machine with less power.

Figure 4: The B5 sized book showing the least abrasion on the spine edges

Similarly, from among the B5 books the largest extent of spine abrasion has been suffered by the 496 gram school book (Figure 5) with perfect PUR binding.

Figure 5: The largest extent of spine edge abrasion has been experienced for B5 sized book No. 10–12

With respect to the properties of the cover, it has a flexible cover of small square meter weight that does not compensate for the weight of the book.

Figure 6: The A4 sized, No. 28–30 thread-stitched school book with a smaller extent of spine edge abrasion

In the A/4 format, the best final result has been achieved by the 410 gram, thread-stitched school book (Figure 5). Its cover is of 260 g/m^2 weight. During the test, abrasion apparently occurred after the 50th minute, but it did not change drastically even by the end of the 60th minute.

Figure 7: The A4 format, No. 25–27 thread-stitched school book with a considerable extent of spine edge abrasion

The thread-stitched book (Figure 3.7) proved to be the book with the worst spine edge. The weight of its cover is 260 g/m^2. It was thinner and more flexible than the most durable book, and therefore the book showed no rigidity in the test machine. It smashed against the walls of the chamber more easily, and due to their flexibility it more easily leant against the rounded corners, and therefore suffered abrasion over a larger area.

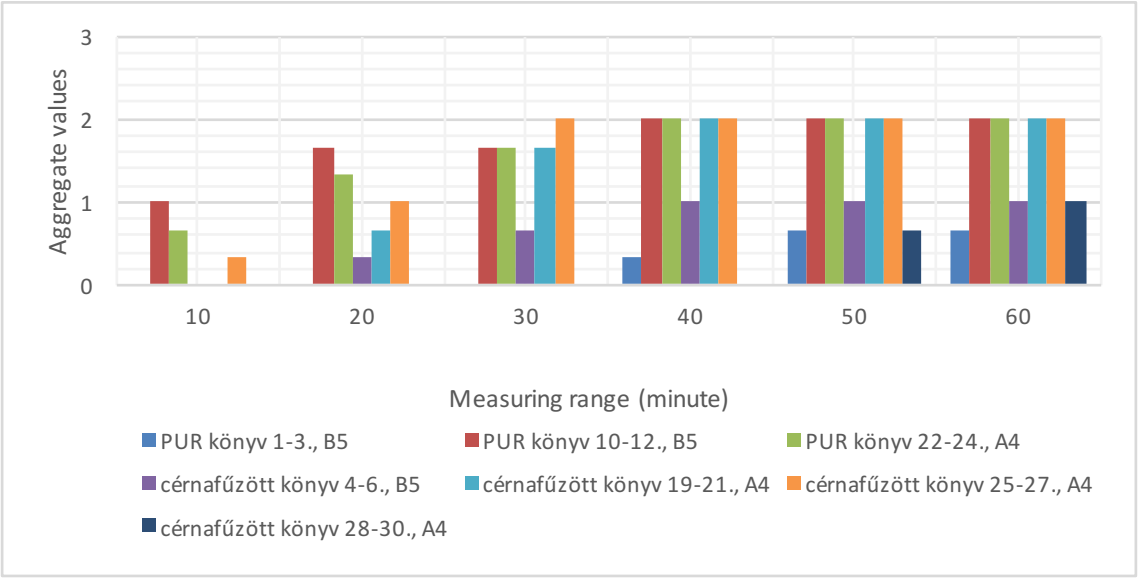

Figure 8: Spine edge abrasion for paperback books

In the light of the aggregated evaluation (Figure 8), it can be claimed that while initially the B5 school book with perfect PUR binding showed strong abrasion, the spine edge abrasion of A4 school books surpassed this extent of abrasion, and eventually even worse statistics could be obtained. It is also dependent on the type of the cover material and the weight of the book. In general, the worst type was the Aurocard paper type in the case of large-format books. With respect to spine edge abrasion, smaller format books achieved better results.

3.2 Abrasion at the spine corners

For the study of spine corners, the smallest extent of abrasion has been experienced for the same book where the least spine edge abrasion has been seen (Figure 2). No signs of impacts can be detected at the corners. The upper part of the spine edge can be regarded to belong to the corner section. This part – extending 10 mm along the spine edge towards the middle of the book block – has not become considerably worn, either (Figure 9). In the opening of the book, it can be observed that along this line the cover has not become worn so that any tear could be observed when pages are turned.

Figure 9: Slight spine corner abrasion on the No. 28-30 thread-stitched school book

By the end of the measurement, more serious corner damage has been detected in the case of three books. Two types of school books (Figure 10) that have the same type of covers and inner sheets – their corner damage has been also similar. On the other hand, in the measuring range it can be seen that over time book No. 19–21 and No. 25–27 have not suffered comparable abrasion even with similar base materials. The abrasion has been the most significant in the head section, as in both cases the covers have been worn down to the adhesive layers, and therefore they have become detached and torn down to a depth of 5 mm together with the end papers, along the spine edges.

Figure 10: Spine corner abrasion of the No. 25–27 and No. 19–21 school books

In B5 size, the 570 gram No. 10–12 school book with perfect PUR binding (Figure 11) proved to be the least durable at the edges. Because of its weight, the flexible block and thin cover made the book rub along the rounded sides of the chambers, and smash against the spines. For this book type, the cover has become worn down to the adhesive layer along the spine edge, while in the head the extent of abrasion was even more serious. It means that the cover material has become so much worn that together with the end paper the spine has torn up to 5 mm along the spine.

Figure 11: Strongly worn spine corners in the No. 10–12 school books with perfect PUR binding

According the summary shown in the graph (Figure 12), paperback school books have been given evaluation over value 2 on the aggregate. All of them have been considerably changed, damaged.

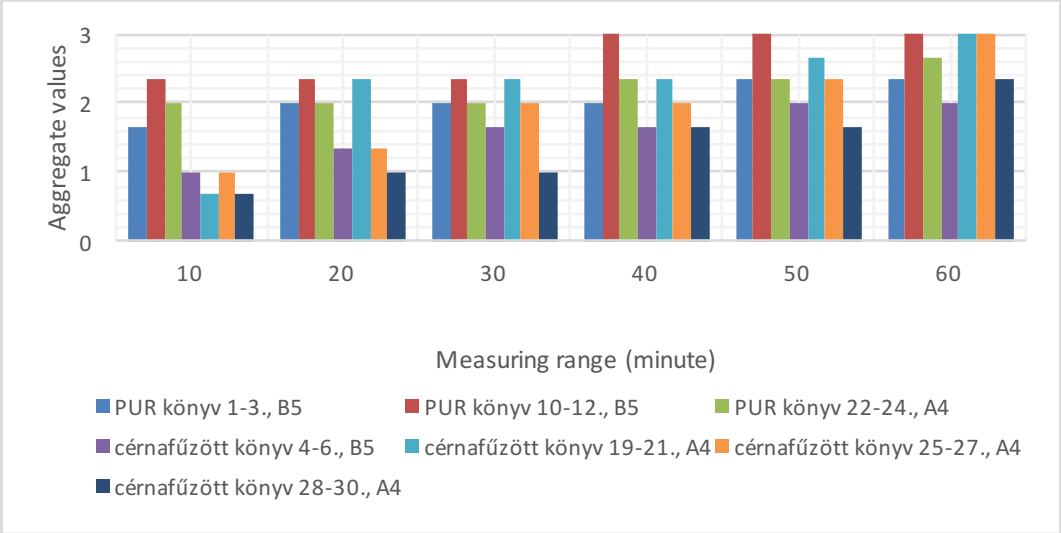

Figure 12: Spine corner abrasion for paperback books

This change has not caused damage to the spine binding. Better results in the abrasion of spine corners have been achieved for B5 format books.

3.3 Conditions of spine binding

The most durable binding has belonged to the B5 sized No. 10–12 school book with perfect PUR binding. The graph reflects that no values have been given to it. The perfect PUR binding has proved to be strong enough in for the 496 gram weight. The sheets have remained stable.

Figure 13: Conditions of binding on the A4 format, No. 25–27 thread-stitched school book

The A4 format, No. 25–27 thread-stitched school book has proved to have the weakest binding (Figure 13). It has the largest weight among paperback school books. As a result of the large format and 570 gram weight, the thread-stitched spine edge has suffered larger impacts, and therefore this binding has weakened more significantly and sooner than the others. The stability of sheets has changed only to a smaller extent. Impacts have concentrated along the spine edge, and therefore this part has demonstrated stronger abrasion, as a result of which the first sheet has become torn in the head.

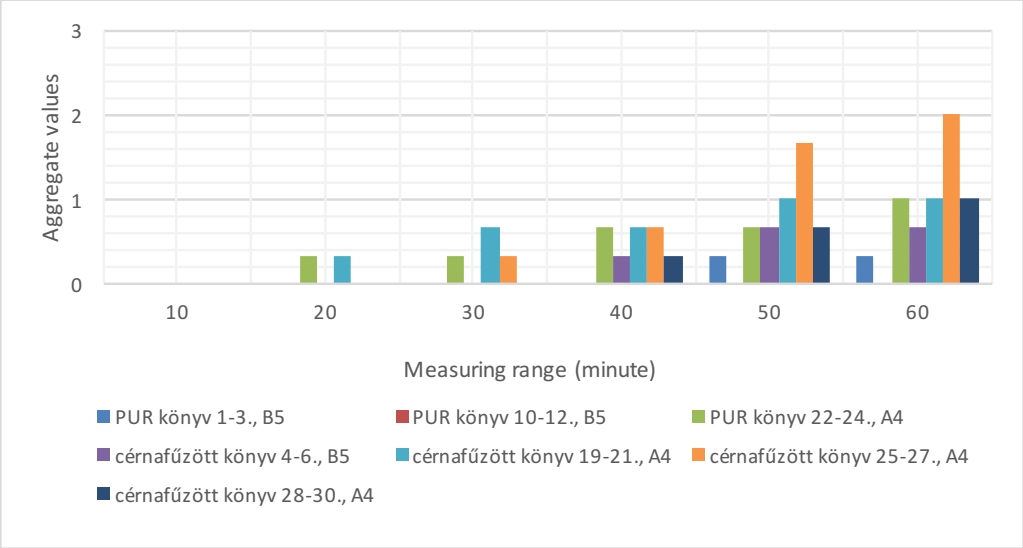

Figure 14: Conditions of spine binding for paperback books

By the end of the 60th minute, the binding has fallen into pieces in nine of the cases (Figure 14). The quality of the received school books can be regarded as appropriate. According to the summary tables, minor changes have occurred only at the end of the 50th minute.

4. Conclusion

In summary of the test results, it can be claimed that with respect to durability school books are made ideal when they are designed in smaller dimensions and with the smallest possible weight. It is better to have paperback covers, because during the performed tests hardcover books reflected more serious damage.

It has also been proved that it is reasonable to modify the test methods described in the referenced technical literature, because the recommended full testing time (60 minutes) that we have also applied is insufficient. In our experience – and it is also reflected in the results –, it is too short. Outcomes showing serious or total damage have occurred less frequently than expected.

Obviously, another conclusion that can be potentially drawn in view of the measured results, that the examined test books have had better than average quality in view of durability. Still, it can be true. Nonetheless, based on our studies this assumption cannot be scientifically confirmed.

The test method has to be refined in two respects. On the one hand, the damage time or intensity should be increased until total destruction so that clean-cut quality-related findings could be made in connection with the individual binding technologies. On the other hand, it is important to compare the accelerated destructive study with real-life use to see at what intensity the model examination can lead to the accessibility of the expected durability requirements. In this context, tests have already been conducted, and the associated results are still under processing.

References

ACTS, 2012. *Manufacturing Standards and Specifications for Textbooks, 2012 Ed*. Palm Coast, Florida: Advisory Commission on Textbook Specifications.

Hyatt, G., 1988. *Factors Affecting the Strength and Openability of Tight Backed, Adhesive Bound, Hardcover Volumes*. MSc Thesis. Rochester Institute of Technology.

Rebsamen, W., 2002. Why books fall apart? *The New Library Scene*, 21(4).

Rebsamen, W., 2003a. Perfect binding good enough for library use? *The New Library Scene*, 22(1).

Rebsamen, W., 2003b. Superior materials used in library binding make the difference! *The New Library Scene*, 22(3).

Rebsamen, W., 2009. Testing hardcover bindings with an all new UBT. *The Endpaper*, *A Newsletter from HBI and the Library Binding Institute, November 2009*.

Rebsamen, W., 2013. Warp-free cover-boards? There are none. *The Endpaper, A Newsletter from HBI and the Library Binding Institute, December 2013.*

Quality Testing of Samples from Multi-Layer-Printing Process using the Method of Visual Color Assessment

Heike Gute, Edgar Dörsam and Hans Martin Sauer

Institute of Printing Science and Technology, Technische Universität Darmstadt, Magdalenenstr. 2, 64289 Darmstadt

E-Mail: gute@idd.tu-darmstadt.de; doersam@idd.tu-darmstadt.de; sauer@idd.tu-darmstadt.de

Abstract

Components and effects are crucial part of the finishing stage of printing products. The demand for their integration into the finishing processes is continuously increasing in the sector of packaging printing. The project "Limitations of over-printing" was focused on the application process of labels and RFID tags into the printing process. The research viewpoint added to the pre-competitive individuality project Constraints of multi-layer-printing. The research project aims to determine the potential and constraints of the multilayer-printing with focus on the achievable quality of printing when different materials are applied. One part of the project was the development and the performance of a visual test which gives information about the perceived quality by test persons. The intention of this paper is to show the visual color assessment planning and realization. Special attention will be obtained to the two visual test methods of pair comparison and ranking order.

Keywords: over-printing process**,** visual color assessment, pair comparison, ranking order

1. Introduction and background

Many products in today's world require some type of packaging. Packaging protects the product and provides the costumer information about the product. However, an increasing demand can be observed to use packaging as a platform for marketing, product distribution surveillance, and for providing supplemental information for the consumer. In order to supply information to the packaging, labels or radio-frequency identification (RFID) tags can be applied. The additional product information by labels or RFID tags often requires the application the labels and RFID tags to packaging surfaces on which will subsequently be printed. However, until to date, there is no standard process fully described or developed which allows applying these labels or tags on packaging in such a way as to preserve quality standards of finishing, ideally making the labels invisible but completely functional. Actually, the preservation of finishing quality compromises the invisibility of label edges and surface textures of the label on the original material.

In this project, we aim to identify a process for over-printing of stacked labels on print products, while the finishing quality should match the original standards. In order to determine relevant parameters for an adapted printing process, we apply visual color assessment technique, using different combinations of printing substrates and labels in correlation with process parameter optimization. Furthermore, we develop an additional evaluation tool, based only on metrological analysis. The selected and prepared printing samples are evaluated with these two methods. This twofold evaluation will give us in depth knowledge about parameter settings and interactions present in the multi-layer-printing process.

Visual testing techniques are of particular interest, as they allow us to learn more about the quality of the printing products as perceived by test persons, in comparison to the metrological determination of quality features.

1.1 Method of visual assessment of printed samples

Assessment of print products is an important step towards product quality and acceptance by the consumer. The method of visual color assessment is a standard procedure used in industry. This method includes the evaluation of printing samples by test persons and includes the color perception of human beings. Color and printing quality perception are technical aspects to a minor degree, but is an essentially feature of human eye and brain interaction as it provides an individual color interpretation. Interpretation of, e.g., colors is further influenced by cultural and environmental preconditions of the individual. The analysis of printing samples by the visual color assessment method is based on the visual color interpretation by dimension and number (Haas, 2012). For measurement instrumentation in the printing industry is this physiological presentation the basis for the measurement system. Also, the analysis is based on information obtained from visual appraisal by human beings. The results of both often differ from each other. Therefore, it is highly beneficial to apply both methods.

1.2 State of the art of visual color assessment

The method of visual color assessment is used in different sectors of mechanical engineering, such as the package printing industry and the automotive industry. The method provides a first and direct estimate. In printing industry, a print control strip is provided for assessment. However, only few detailed studies have been published on this topic, e.g. Lübbe (2013). A visual color assessment with a scientific background is time-consuming. To date only a small number of comprehensive studies exist (Kehren, 2013).

Extensive scientific studies based on working hypotheses are developed in a first step, depending on the specific research objectives. In the sequel an experimental procedure is developed, and the conditions of the assessment are defined. (Helbig and Bose, 1993). The group of individuals which participate in the testing may be chosen randomly for each experiment. Depending on the underlying questions and applications of the specific experiment, the group of individuals can be formed by experts in the field of printing or the general public. However, it is crucial to ensure that all participating individuals possess a full physiologically normal perception of colors (Haas, 2012). Irregularities in the perception of color lead to a bias of the result and therefore, the results of individuals with incorrect color vision need to be excluded from the data set.

1.3 Research objectives

The objective of this visual test is to obtain information about the by individual perceived quality of over-printed labels. The group of individuals is randomly chosen from the general public, which will allow insight in possible markets. A large number of data is to be obtained in order to facilitate a comprehensive analysis.

2. Materials and methods

This study compares 33 samples which were selected from a total set of 330 printed samples. Each sample represents a unique set of the various printing parameters. Figure 1 shows the sample layout.

Each sample represents a unique set of parameters, which determines the production process of the sample. This process compromise of the printing technique used the primary printing substrate without any applied label and the label itself, which can be understood as a secondary substrate applied. Furthermore, the thickness of the imprinted layer is an important part of the printing process and facilitates the compensation of any step between the height level of the primary and secondary substrate.

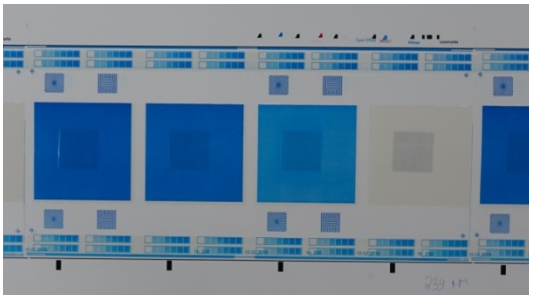

Figure 1: Printing sample: full-area squares are printed on coated paper

Each sample represents a unique set of parameters, which determines the production process of the sample. This process compromise of the printing technique used the primary printing substrate without any applied label and the label itself, which can be understood as a secondary substrate applied. Furthermore, the thickness of the imprinted layer is an important part of the printing process and facilitates the compensation of any step between the height level of the primary and secondary substrate.

2.1 Experimental setup of visual color assessment

The experimental procedure consists of two main phases: test planning and the test procedure which include the evaluation. For the test planning were used the method of Design of Experiments, whereby up to 14 variable parameters were defined to characterize a sample class. The samples were then produced in an extensive printing run. The evaluation was based on two methods: the metrological evaluation and the visual testing procedure. For the second method, specific working hypotheses had to be formulated which related the visual assessment results to the set of characteristic parameters: printing technique, printing substrate (primary substrate without an applied label), label (applied secondary substrate), thickness of the imprinted layer which compensates the level and the step between the printing substrate and the label.

2.1.1 Working hypothesis

In order to elaborate a working hypothesis which could be evaluated by the experiment, the following aspects were considered: 1. the influence of the printing technique, 2. the influence of the printing substrate on the quality, 3. visibility of difference between the samples with and without a label under the printed layer in the visual color assessment, 4. impact of printing speed, 5. influence of an optional primer that has been applied on the printing substrate and 6. influence of the printed layer thickness on the residual level differences at the label edges.

For the evaluation research questions were derived for censorship of the samples by the test persons. These research questions, applied in a questionnaire, were used to rate the hypotheses in respect that they could yield a quantitative measure for their evaluation. For experimental reasons, the research questions were organized in six sections, which were answered independently. Care was taken that the wording of the questions used a clear and accessible language, which ensured that the test persons were able to answer quickly and to the specific point. Additionally, this adaptation of the questions ensured that biasing and training effects of the test individuals by the visual color assessment results would be avoided over the assessment procedure.

2.1.2 Methods of the visual color assessment

Testing visual perception can be performed following different methods. Helbig and Bose (1993) describes a number of methods for visual color assessment. This study uses the methods of sample pair comparison and rank ordering.

The research questions from (1) to (6) are regarded by pair comparison experiment. For a first overview about the achieved quality 10 % of the samples created in total were chosen and prepared for visual color assessment. The selection of samples is adapted to the needs of the working hypothesis to be tested. This is described in the next section. Specifically, it was ensured that the samples were not distinct in other respect than that related to the research question. The samples were placed next to each other such that the test observer could appraise them simultaneously. We regarded the result of Kehren (2013) that pair comparison test can be considered significant only in case that the number of samples per test person is small. Furthermore, the method allows a direct comparison of multiple processes where samples are pairwise compared with each other. The result shows which sample has been assigned the highest quality level by the test persons. Figure 2 shows the method of paired comparison.

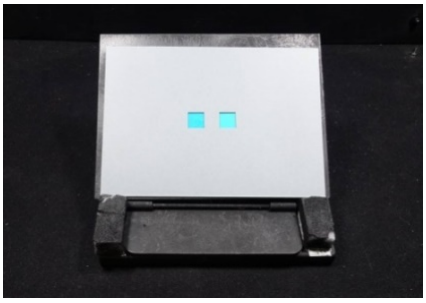

Figure 2: Visual color assessment with the method of pair comparison

The research question of part (7) is analyzed by using the method of rank ordering. In this procedure, the test persons are asked to rank the printing samples according a specific feature. Criteria are only given for the extrema of the ranking, e.g. the intensity of the edge perception. In order to avoid any bias, samples representing the highest and lowest score of the ranking scale were not specified. The samples had the format of cards for this experiment. Figure 3 shows six cards which were organized in the presented order by a test person.

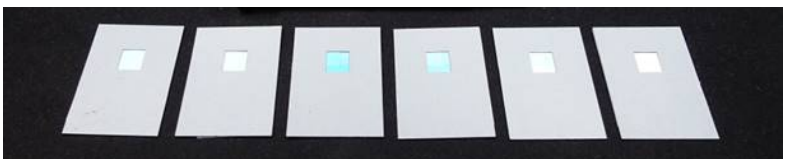

Figure 3: Samples for the method of ranking order

With the experiment of pair comparison, we used 51 sample cards. In while the ranking order experiment the set was reduced to 27 smaller cards, with only one printing sample on each card.

2.1.3 Visual color assessment conditions

All visual tests were performed under identical conditions in terms of illumination and observer perspective. The identical conditions ensure the comparability of the obtained data. The parameters which define the test conditions are the geometric setup of the samples and the type of light, the observer, and the physiological condition of the test person. The type of light is set to the standard illumination for printing of D65. The norm observer of 2°, as the physiological conditions was assumed for the experiment. These conditions determine the rest of the conditions such as the geometry of the setup like the distance of 60 cm between sample and observer and viewing geometries and light conditions of 45°/0° as incident angle. The observer distance was constrained by a chin rest. When the person was located, the room was darkened and all other distracting light sources were removed.

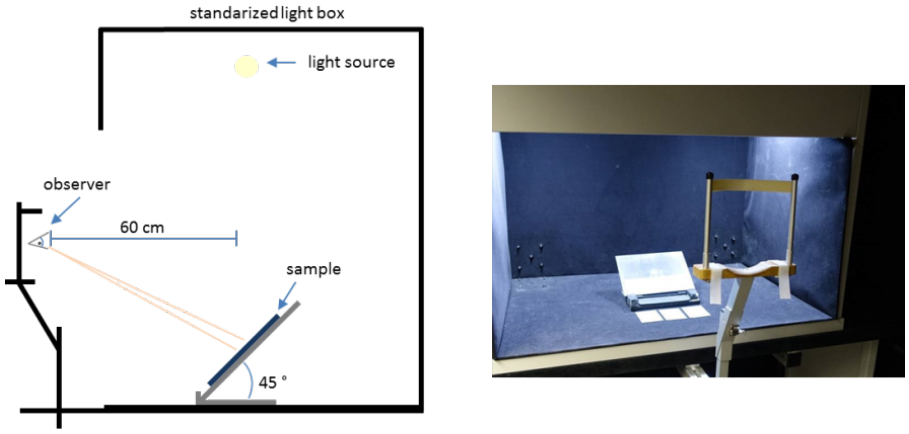

Figure 4: Test setup; left side: the geometry of the setup; right side: installation in the black room

The sample dimensions were also derived from the conditions. The samples measured 2 cm in the diagonal. The distance between the samples was 1.5 cm and was adjusted according to the sample size and the distance view. Furthermore, the sample distance accounted for the visual discrimination performance, which is ideal when the samples are in touch distance from the test person (Lübbe, 2013). The samples were placed in a neutral grey mask in order to ensure a uniform background for all samples. The selected grey color was chosen such that it would not distract the test person's attention from the sample. The setup is shown in Figure 4.

2.2 Test procedure

Two-thirds of the tests took place in the laboratory of the Institute of Printing Science and Technology. The other third took place in the laboratory of three different participating companies. For statistical analysis, information about the test persons, such as gender, age and visual aids were acquired. In a preparatory step, all test persons had to complete two color visual test, *Ishihara Color Deficiency Test* (Ishihara, 1943) and the *Farnsworth-Munsell 100 Hue Test* (Farnsworth, 1943), followed by instructions for the sample evaluation. Example cards of printing products were provided in order to familiarize the test persons with the printing products and format. Following the preparations, the test persons were asked the research questions as defined for the visual color assessment.

The visual evaluation of the samples was carried out in random order. The test persons were asked to answer all questions spontaneously. Answers and additional notes were collected by a questionnaire. All questions and parts of the sample evaluation were completed in one run without any break. The total time for completion of all questions was kept under the limit of 40 minutes. The time period of 40 minutes is described in literature as a limit after which fatigue of the eyes begins to occur (e.g. Lübbe, 2013). Staying under this time limit, we neglected the effect of fatigue.

3. Results and Discussion

In total, 51 test persons took part in the sample evaluation, 20 were female and 31 male. This group consisted of 20 experts and 31 randomly selected persons without any printing specific knowledge. The test persons were aged between 21 and 66 years. All test persons completed the color tests with positive results which qualified them for the participation in the study.

When analyzing and discussing the results we had to consider, that the answers from the test persons were a matter of subjective perception and might therefore not be reproducible in a second trial. In the

following, the results are shown with respect to the individual research question. The results shown to not distinguish between the expert and the lay group members.

3.1 Results of the paired comparison

One main question of the project was whether the different printing processes of Flexo-, Offset- and Inkjet-printing lead to different qualities in over-printing experiment. This question can be connected with the working hypothesis "Test persons do not notice a difference in quality of the sample when produced by the different printing processes". The visual testing evaluated all three processes using the sample pair comparison test. Results are shown in Figure 5.

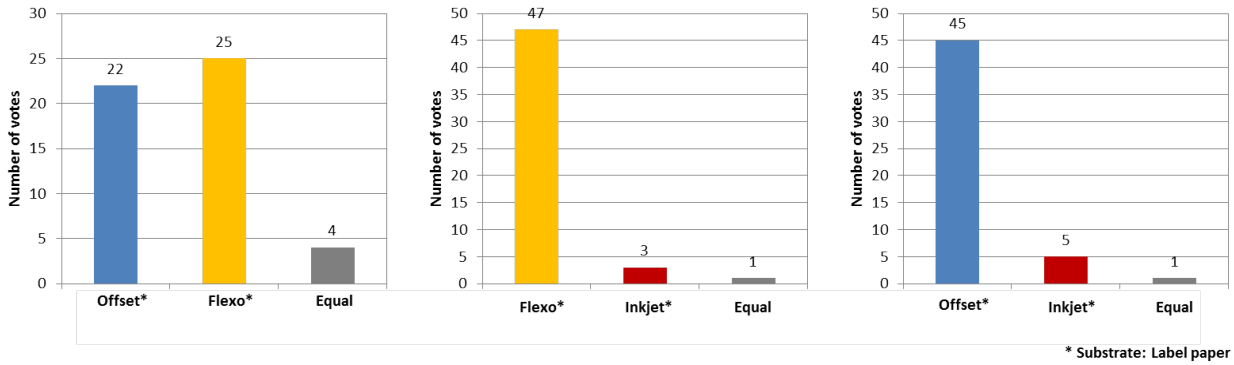

Figure 5: Number of votes by the test: color impression, printing processes, pair comparison

The samples were evaluated by the test persons considering their color impression. It could be observed that conventional printing results are preferred over the digital printing results. When comparing conventional printing only, samples were chosen equally by the test persons. Therefore, it can be assumed that the conventional printing techniques provide qualities which are accepted by the test persons.

3.2 Results of the method of ranking order

The ranking order test, focused on two aspects. Firstly, the edge which occurs between printing substrate and label was considered. Regarding the edge two assumptions were made. Firstly, it was expected that the edge would appear to intensify under over-printing by an irregular deposition of ink layers. Secondly, it was supposed on the possibility that over-printing using a grate can minimize the edge.

Furthermore, as a second aspect, the influence of the thickness of the imprinted layer, applied for level compensation, was determined. For level compensation multiple layer thicknesses were applied in order to minimize level differences at the previously described edge. In addition, it was proposed that the applied layer thickness had influence on the quality of the graphical over-print.

In order to test these assumptions, selected samples were evaluated by the test persons.

Figure 6 shows the test results of the method of ranking order regarding the visual impression of the edge. The samples in this particular ranking order test were produced in offset printing. They were presented as single cards at which one card shows a part of full surface and two cards respectively a part of printing screen.

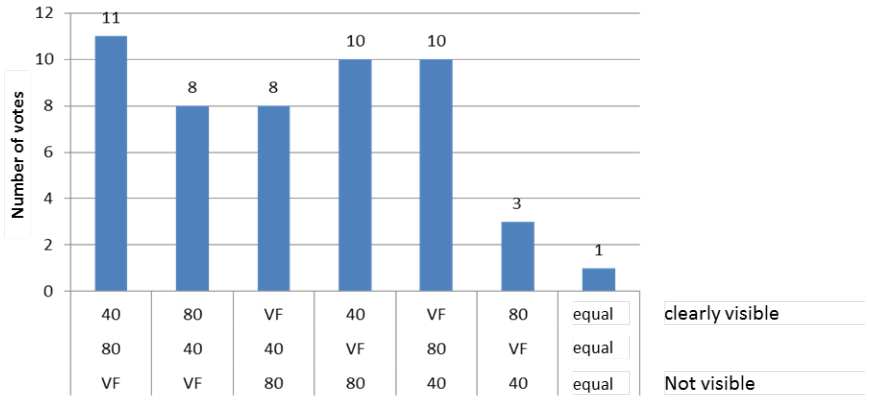

Figure 6: Results of the ranking order tests with samples which are produced in offset printing process

These particular results show that there is no priority between the full surface and the grid pattern. The results let us assume that a printing screen could not improve quality in the over-printing-process.

Further information and results can be found in the final report which is issued by Masajew, et al. (2017).

4. Conclusions

In this paper, we have presented a method for censoring the relative quality of samples from the multi-layer-printing process. For the visual test were used two methods, the pair comparison and the ranking order. The visual test conditions are adapted to the requirements and the group of test persons has been compiled from experts and those from outside the field.

The test results show that processes exist which could realize an over-printing of multiple and different materials. It was further found that the samples printed by conventional printing processes were better valued than samples of the digital process. In order to be able to make more accurate statements about the numerous parameters and find specific correlation more tests are necessary in the future. A more comprehensive consideration of the edge provides a detailed description of the influence from relevant parameters in the over-print process or from the materials.

Acknowledgments

The authors gratefully acknowledge the support from the project committee “limitations of over-printing”. Furthermore, we thank the companies whose employees have taken part in the test as experts. The project was supported by the AiF (of the German Federal Ministry of Economic Affairs and Energy) within the framework of the IGF (Industrial Community Research and Development), Grant # 18327 N.

References

Farnsworth, D., 1943. The Farnsworth-Munsell 100-Hue and Dichotomous Tests for color vision. *Journal of the Optical Society of America*, 33(10), pp. 568–578.

Haas, M., 2012. *Untersuchungen zum Verdrucken von Interferenzeffektfarben im Flexodruckverfahren*. Dr.-Ing. Dissertation. Technische Universität Darmstadt.

Helbig, T. and Bose, R., 1993. *Druckqualität: Grundlagen der Qualitätsbewertung im Offsetdruck*. Frankfurt am Main: Polygraph-Verlag.

Ishihara, S., 1943. *Tests for Colour-blindness*. 9th ed. London: Lewis.

Kehren, K., 2013. *Optical properties and visual appearance of printed special effect colors*. Dr.-Ing. Dissertation. Technische Universität Darmstadt.

Lübbe, E., 2013. *Farbempfindung, Farbbeschreibung und Farbmessung: Eine Formel für die Farbsättigung*. Wiesbaden: Springer Vieweg.

Masajew, J., Gute, H., Ahmad Al-A., Dörsam, E., 2017. *Schlussbericht 18327 N: Grenzen der Überdruckbarkeit*. Darmstadt: Technische Universität Darmstadt.

Quality Control in Job Printing: adaptable Camera Focus using Power Spectrum

Julian Schäfer, Felipe Fernandes and Edgar Dörsam

Institute of Printing Science and Technology, Darmstadt University of Technology, Magdalenenstr. 2, 64289 Darmstadt

E-mail: schaefer@idd.tu-darmstadt.de; fernandes@idd.tu-darmstadt.de; doersam@idd.tu-darmstadt.de

Abstract

Optical inspection of printed sheets becomes more and more substantial in job printing in order to reduce both errors and setup time in the cutting process. This paper provides a new method for on-sensor based focusing for cameras using an adapted two dimensional Fast Fourier Transform (FFT). Deriving from contrast based focusing and two dimensional FFT an approach is shown which uses the amplitude spectrum provided by FFT. Emphasizing high frequencies and therefore masking the power spectrum results in a method which presents sufficient accurate focusing on stacks of paper sheets. A variety of tests have been performed to verify the method provided in this paper. Four different types of paper were tested using four different test charts in order to cover a broad span of print layouts found in job printing.

Keywords: power spectrum, two dimensional FFT, focusing method, job printing, inline inspection

1. Introduction and background

1.1 Optical inspection in post processing

With the aim to increase efficiency in the printing process, post processing comes into focus as the level of automation is low compared to pre-press and press. Cutting represents a bottleneck in the printing process as succeeding processes such as hemming, gathering and binding rely on the results. As the size of printed sheets in job printing increases to include more jobs on a single printing plate and therefore reduce cost and setup time, minimizing errors during the cutting process becomes even more crucial. Even though job data is available, disruptive factors of the printing process influence the printed sheets resulting in deformation thus the job data does not match the physical data anymore. Consequently, quality inspection is a main target of manufacturers of cutting systems.

The cutting process allows stacks of sheets of various dimensions to run through the process. The maximum dimensions are given by the size of the machine table of the cutting machine, while the minimum sliceable dimensions are usually smaller than 10 cm. While the change of width and depth between jobs mean that the measuring range of an inspection system has to be adaptable, the change of the height of the paper stack means that the inspection system has to adjust its focus for every job. In this respect, the inspection task differs from most tasks seen in inline-inspection-systems where objects and distances usually stay the same as for example shown in (Pawlowski, 2010).

In this paper we provide a method for focusing with an standard 5 MP area scan camera by adjusting the distance between the surface of a stack of sheets and the camera using the power spectrum of a two dimensional Fast Fourier Transformation (FFT). The method is tested on different types of paper with different printed test patterns. To optimize the significance of the method and reduce calculation time the frequency range is adjusted.

1.2 On-sensor focusing methods

In order to focus on a subject just by using data from the imaging sensor, a difference in brightness is needed as the imaging sensor only detects brightness. Figure 1 shows the two borderlines. On the left side, a blurred digitalized edge resulting in a brightness gradient is shown resulting in uniformly distributed grey values. On the right side the same edge is digitalized with maximum sharpness. The difference in gray values at the edge and hereby the contrast is at the maximum what allows the assumption that the image is focused.

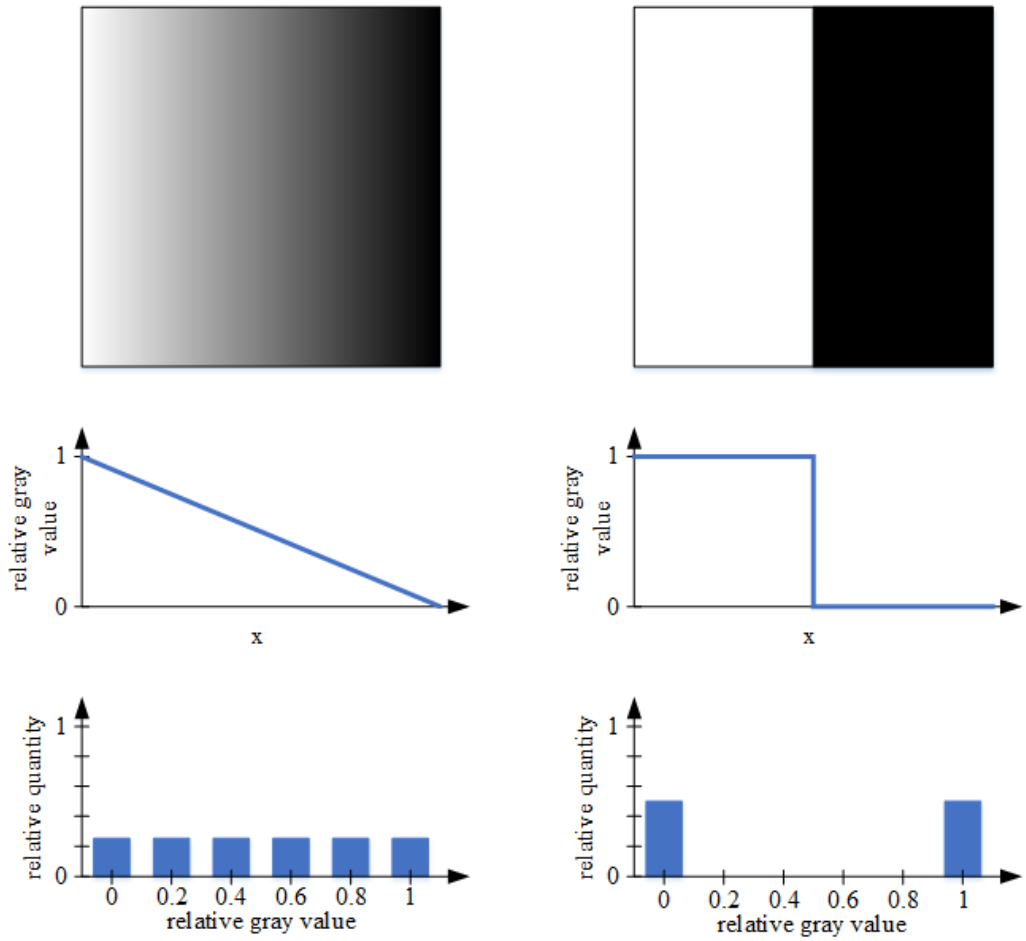

Figure 1: Blurred and sharp edges and their corresponding brightness distribution

As seen in Figure 1, the sharpest image is associated with maximum spreading of grey values. Evaluation of the spreading of an images histogram performs well for simple printing jobs, where the amount of different gray values is at a minimum. However, evaluation gets complicated for an unknown distribution of gray values where the histogram tends to be more uniform. Without a prior knowledge another method is required for focusing a camera on the large variety of printing products.

In order to improve accuracy and robustness, a focusing method based on FFT is provided. Low-pass filters reduce contrast on edges by adapting grey values of pixels according to their neighborhood. As a result, the image gets blurred (Chaudhuri and Rajagopalan, 1999; Utcke and Burkhardt, 1999; Vision & Control GmbH, 2007). By implication this means that high frequencies occur most, if the image is focused at its best.

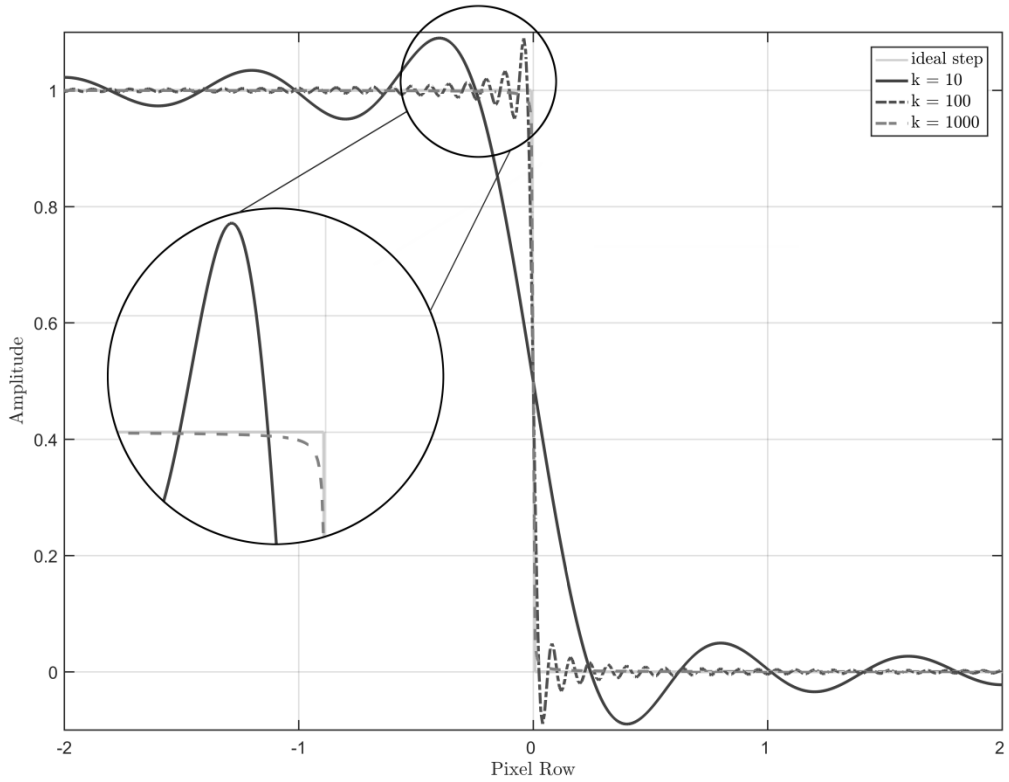

Figure 2: Fitting an ideal step at zero with Fourier series with k={10,100,1000} terms; crop not true to scale

A popular method in image processing therefore is the two dimensional FFT (Burger and Burge, 2005).

1.3 Aim of research

The aim of this research is to provide a method which allows adjusting the focus plane independent of the print layout on the sheets by varying the distance between camera and surface of the stack of sheets. First, we introduce the method in section 2.1 before the test rig and the test charts which are used are presented in section 2.2. After discussing the results of our research in section 3 we conclude and provide an outlook in section 4.

2. Materials and Methods

2.1 FFT-based focusing method

Image processing using the frequency domain offers a variety of opportunities as it allows operating with features, which are not detectable in spatial domain (Bredies and Lorenz, 2011). Furthermore, processing effort decreases due to different mathematical approaches such as a FFT (Erhardt, 2008).

After capturing an image, the data is available in the spatial domain. Each pixel is usually encoded with 8 bit resulting in 256 gray values. As a result, a gray image $\boldsymbol{G}(x,y)$ captured with an imaging sensor with m pixels in height and n pixels in width is represented by a $m \times n$ matrix. Because of further processing steps, the 256 gray values are in the interval from 0 to 1. Each pixel implies a gray value $g_{m,n}$ representing the brightness at the position specified by m and n of the image $\boldsymbol{G}(x,y)$ (see Formula 1).

$$\boldsymbol{G} = \begin{pmatrix} g_{1,1} & \cdots & g_{1,n} \\ \vdots & \ddots & \vdots \\ g_{m,1} & \cdots & g_{m,n} \end{pmatrix} \quad [1]$$

As an image in general is composed by sine and cosine waves, any image is describable as a combination of sine and cosine waves with customized coefficients (Jähne, 2005, p. 43ff.), where u and v represent the frequency of the wave. Every pixel $\boldsymbol{G}(x,y)$ with $1 \leq x \leq m$ and $1 \leq y \leq n$ of an input image is transformed into spatial domain by a discrete two dimensional FFT described by Formula 2. The resulting complex valued Fourier image $\boldsymbol{F}(u,v)$ has the same size as the image $\boldsymbol{G}(x,y)$.

$$\boldsymbol{F}(u,v) = \frac{1}{\sqrt{MN}} \sum_{x=0}^{M-1} \sum_{y=0}^{N-1} \boldsymbol{G}(x,y) \cdot \left\{ exp\left(-i2\pi \cdot \left(\frac{u \cdot x}{M} + \frac{v \cdot y}{N} \right) \right) \right\} \quad [2]$$

$\boldsymbol{G}(x,y)$ is multiplied with the exponential function elementwise and added up over rows and columns of the image matrix $\boldsymbol{G}(x,y)$ and then is scaled. Sine and cosine as initial functions for FFT are represented through the exponential function in the complex range of numbers. The Fourier image $\boldsymbol{F}(u,v)$ contains the frequency and phase information of the spatial image $\boldsymbol{G}(x,y)$. An example of a spatial image and the corresponding amplitude spectrum is shown in Figure 3. A high gray value in the amplitude spectrum originates by high amplitude of detected FFT frequency $|\boldsymbol{F}(u,v)|$ in image $\boldsymbol{G}(x,y)$ with phase $\arctan\left(\frac{\boldsymbol{F}_{Im}(u,v)}{\boldsymbol{F}_{Re}(u,v)}\right)$.

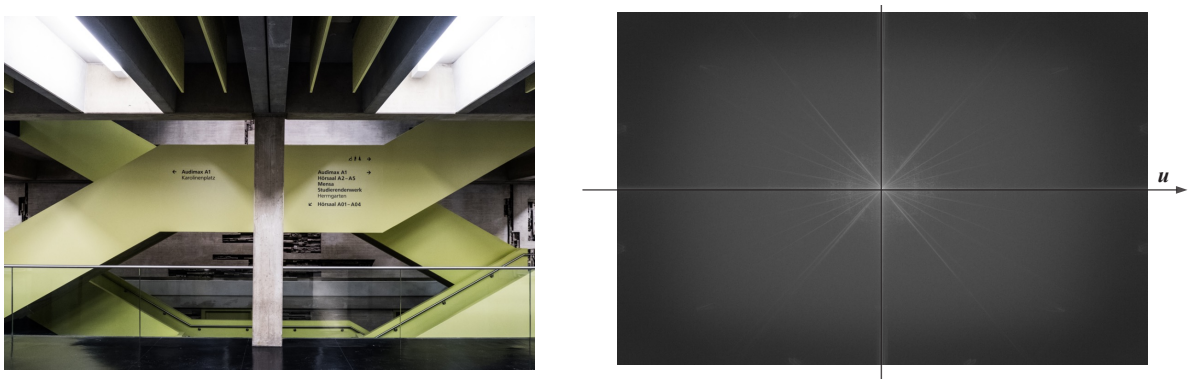

Figure 3: Input image (left) and resulting amplitude spectrum of a two dimensional FFT (right)

The square of the value of the Fourier transformation (see Formula 3) is called power spectrum according to Süße and Rodner (2014). It describes the contribution of single frequencies u and v to image $\boldsymbol{G}$.

$$\boldsymbol{P}(u,v) = |\boldsymbol{F}(u,v)|^2 \quad [3]$$

As mentioned in section 1.1, the power spectrum at high frequencies is most pronounced in a perfectly focused image. To cut down processing time herein a customized section of the power spectrum is discussed. For this purpose, only the high frequency range $\Psi(b)$ of the spectrum with bandwidth b is considered (see Figure 4) which we call the frame frequencies below.

By adjustment of Formula 3, the power spectrum of the frame – subsequently called frame power – is calculated and shown in Formula 4.

$$\widehat{\boldsymbol{P}}_{\boldsymbol{b}} = \frac{1}{n_{\Psi(b)}} \sum_{u,v \in \Psi(b)} |\mathbf{F}(u,v)|^2 \text{ with } u,v,x,y \in \mathbb{Z} \quad [4]$$

Frame power $\widehat{\boldsymbol{P}}_{\boldsymbol{b}}$ therefore can be described as a high-pass filtering with additional summation of the remaining frame with bandwidth b of the power spectrum normalized by the number of elements in $\Psi(b)$.

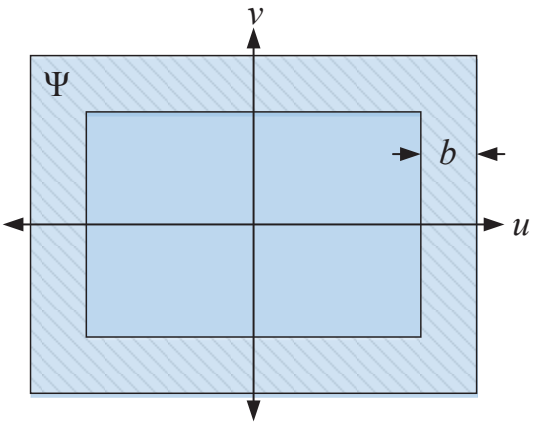

Figure 4: Frame with bandwidth b, which is used in the FFT in order to concentrate on high frequencies

2.2 Experimental setup

For the experimental setup, the 5 MP industrial monochrome area scan camera P83M-GigE-AS from PicSight (Leutron Vision, 2010) was used in combination with the Fujinon 25 mm f/1.4-22 lens HF25SA-1 (Fujifilm Corporation, 2010). As camera and lens are not equipped with an automatic focus or aperture, the focal plane of the optical system can be assumed to be in a constant distance from the imaging sensor. Figure 6 illustrates the geometry used for identifying the stack's height using the best focus.

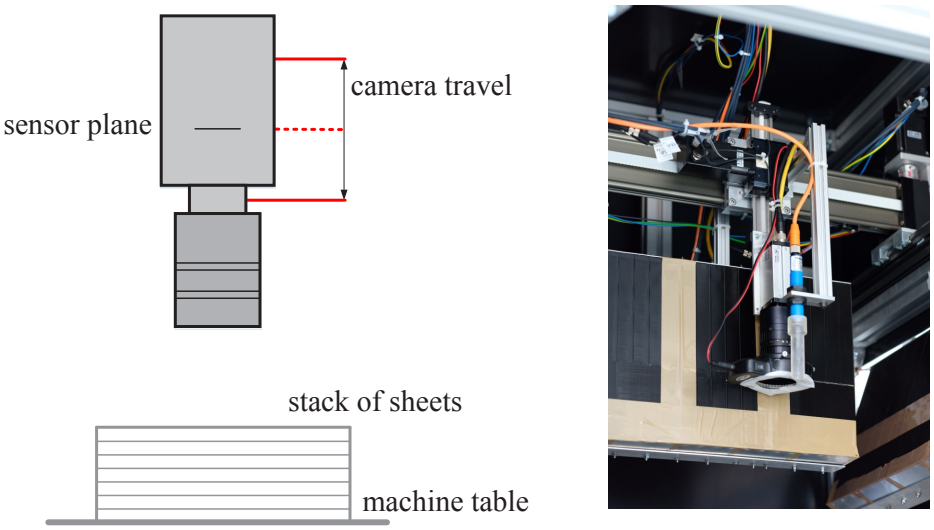

Figure 5: Geometry for identifying the height of the stack of sheets (left) and test rig (right)

In the test rig (see Figure 5 on the right) the camera is mounted to a room gantry which allows us to move and vary the height of the camera above the ground surface on which the stack of sheets will be inspected once the best focus for its height is found. For the investigation, the camera is once focused manually at a specific height on a single test-chart of which the height is assumed to be negligible. Subsequently a series of 75 images is taken of every test chart, while the camera is moved 1 mm upwards after the acquisition of each image, beginning from the lowermost camera position. By this the focal plane is moved through the pre-defined point of focus. For testing the developed method of focusing through varying the cameras height above the stack and calculating the frame power from the power spectrum, test charts were designed for two categories (see Figure 6). The first one encloses a text sample as well as a color and mono-

chrome picture. Secondly, image patterns with generic frequency distributions are used. A stroke pattern essentially contains one frequency with a clear orientation of the phase vector (u,v). In contrast, a broad spectrum extending to high frequencies, but without any preferential orientation is represented by the random binary noise pattern. In addition it is assumed that the spectral characteristics of a real printing product lie in between of those, of the generic frequency test charts. All charts are pictured in Figure 6.

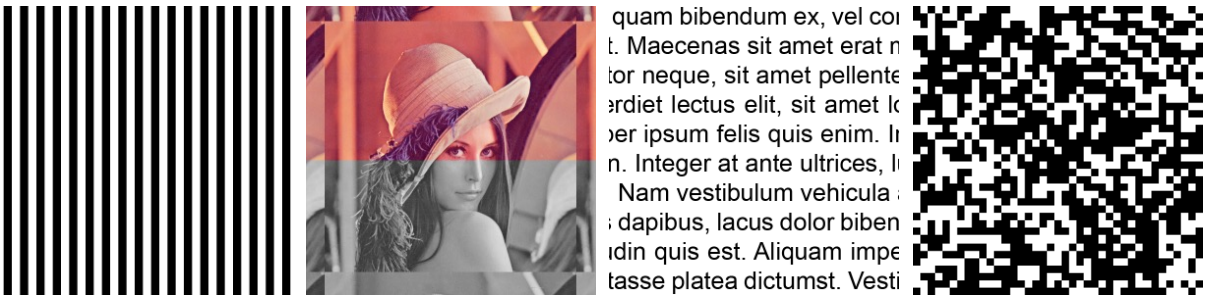

Figure 6: Test charts

The text pattern is used as a special case of a stroke pattern, and to study the effect a preferential direction (PD). Therefore, four different orientations were defined with angles (0°, 15°, 45°, 75°) to a reference direction at which the text was aligned during the experiment. For investigating the robustness of the algorithm, the test charts were printed on four different types of paper with a laser printer. This includes one glossy (Luxo Magic 150 g/m^2), one matt glossy (Zanders ikono matt 150 g/m^2), one matt (Tauro Offset 100 g/m^2 SB) and one slightly rough paper (Lorsatzpaper 100 g/m^2 SB). A constant lighting setting was established by using a circular LED camera light.

3. Results and Discussion

The frame power $\boldsymbol{P_b}$ is calculated for each image of the series with frame bandwidths $\boldsymbol{b}$ = {25, 100, 175} and scaled to the maximum frame power of the series $\widehat{\boldsymbol{P}}_{\boldsymbol{175,max}}$. By implication we assume that the test chart is focused when the maximum frame power $\widehat{\boldsymbol{P}}_{\boldsymbol{b}}$ is in between these borders. All results shown are based on the matte Tauro Offset paper, but for the comparison between matte/glossy, the glossy Luxo Magic paper is used in addition.

When comparing frame power obtained from color and monochrome pictures the results show a similar appearance before entering the focal depth, but the absolute magnitude of the frame power $\widehat{\boldsymbol{P}}_{\boldsymbol{b}}$ is larger for the colored picture (see Figure 7).

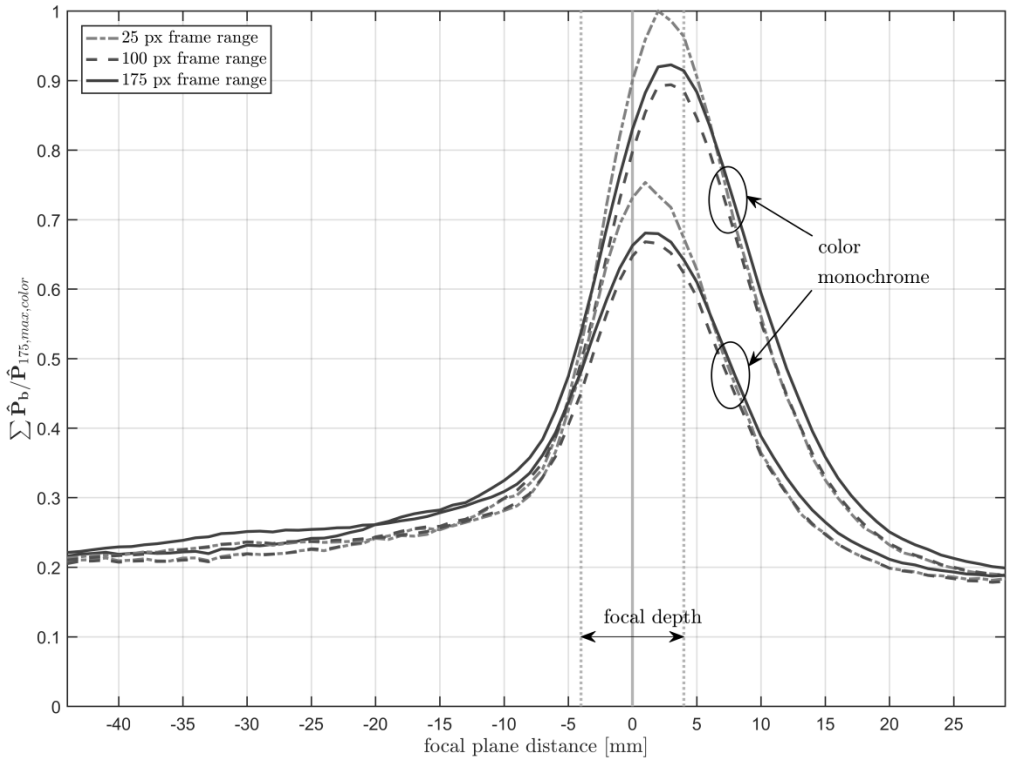

Figure 7: Power spectrum of color and monochrome picture test chart

The digitalized image of the colored picture is noisier than the monochrome picture as cutouts show in Figure 8. Also, differences in the printing screens of colored and monochrome picture printouts can be detected in visual control. For a distinct association further investigations are required.

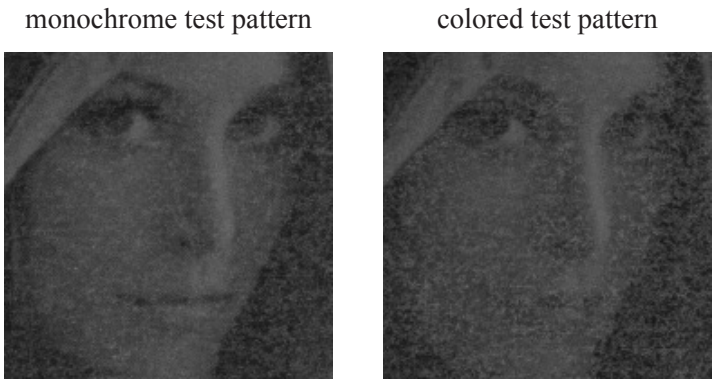

Figure 8: Digitalized monochrome and color picture test pattern using a monochrome camera

Continuing, in the experiments an influence due to different angles of text cannot be detected. Figure 9 shows the results of the text aligned at 0° (for better comparison to the stroke pattern). This result hereby matches the statement that frequency spectrums are invariant of input image rotation (Ruanaidh and Pun, 1998). Beside a global peak of the frame power , small local peaks are existent (see Figure 9), when using the sample text pattern.

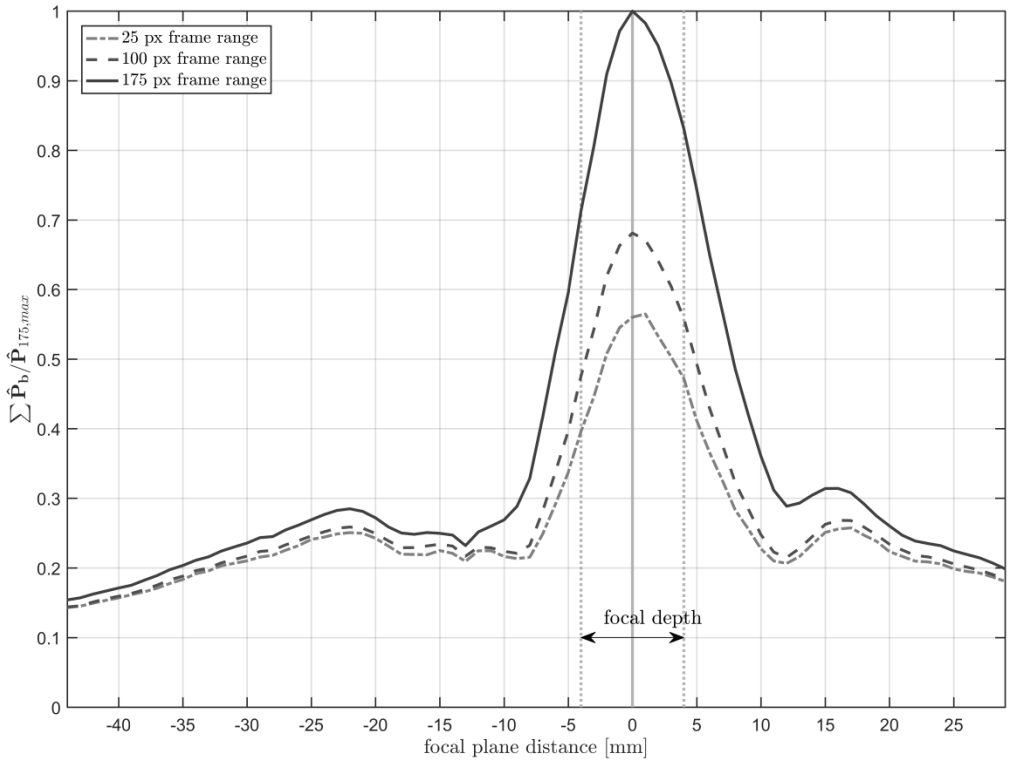

Figure 9: Power spectrum of text test chart aligned at 0°

The behavior of local peaks is even more remarkable when using the stroke pattern (see Figure 10). The derivation between the frame power $\widehat{\boldsymbol{P}}_{\boldsymbol{b}}$ and the actual point of focus goes up to $\boldsymbol{\Delta F}_{\mathbf{max}}$ = 8 mm.

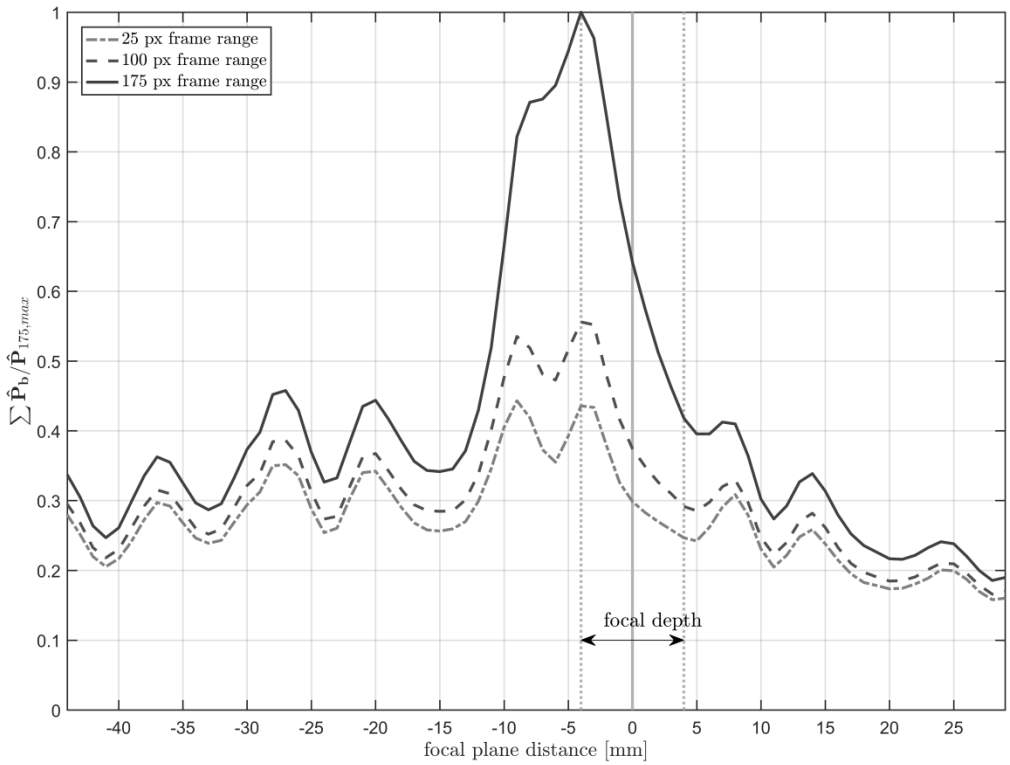

Figure 10: Power spectrum of stroke pattern showing local peaks besides global maximum

Local peaks and large deviations are invariable noticeable for all investigations with the stroke pattern. This behavior occurs because of strokes entering the image due to camera travel and resulting larger acquisition area. Reducing the printing size of the test chart so that the complete pattern is detected in the lowermost camera position prevents local peaks from occurring. However, we assume that an image sensor filling stroke pattern is not found frequently in real printing products, therefore the suitability of the introduced method is not less applicable because of these results.

Contrary to the indistinct results of the stroke pattern, outcomes of the binary noise pattern are highly convergent (see Figure 11). In visual control we detect a major influence caused by the circular light though. Because of parallelism of lighting direction and the cameras optical axis, partial reflections of the light source are captured in the images when using glossy papers. This biases the results of FFT and thus the power spectrum. For correction a light diffusor is installed which prevents sharp reflections on glossy surfaces.

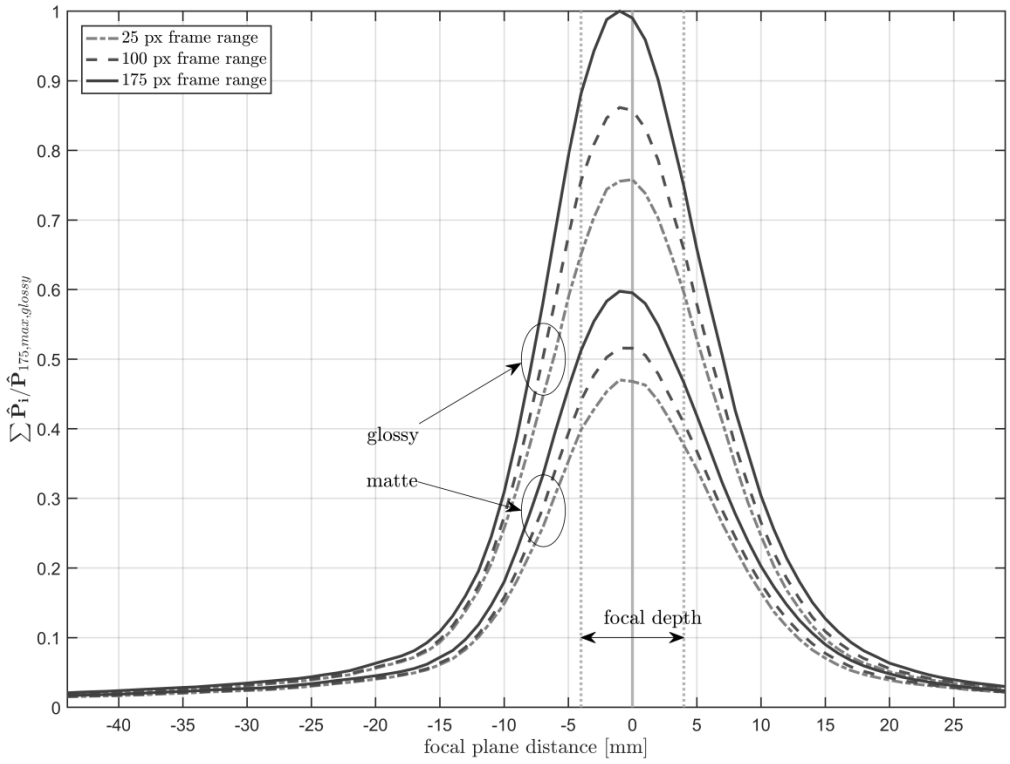

Figure 11: Power spectrum of random binary noise pattern performed with different frame ranges for glossy and matt paper

The reflectance of the paper sheet influences the absolute values of the power spectrum as well. The frame power $\widehat{\boldsymbol{P}}_{\boldsymbol{b}}$ is raised by usage of glossy papers without exception, what possibly is explained through higher contrast. Hence a resulting higher contrast of the image leads to higher amplitudes of the corresponding FFT functions, what implies larger absolute values of the FFT and thereby the power spectrum (see Figure 11). Derivations of $\boldsymbol{P}_{b,\mathbf{max}}$ to the actual point of focus, when using the binary noise test chart, lie in a span of $\boldsymbol{\Delta F}$ = ±1mm. Out of focus, small structures of the noise pattern become indistinct, hence the edge contrast is reduced drastically. Inside the focal depth structures are distinguishable and the high spatial resolution of the pattern results in a sudden detection of high frequencies. Out of all experiments the results of the noise pattern show the best results.

4. Conclusions

The method shown in this research serves as a robust alternative for focusing tasks where only data from the imaging sensor is available. No further sensor is needed within the system. The method was evaluated by using four different test charts representing a large variety of print layouts found in printing jobs. Derivations of $\boldsymbol{P}_{b,\max}$ to the actual point of focus lie in a span of $\Delta F = \pm 1$ mm for all experiments done. While an increase in frame range results in a higher frame power , even a frame range of just 25 pixels results in precise prediction of the actual focus. A variety of glossy and matt paper were tested and even though glossy paper forced difficulties with partial reflections caused by circular lighting and power spectrum performed on matt sheets showed lower maximums, the method still worked sufficiently. Finally, we show that the fiber direction does not affect the method in a relevant manner.

Acknowledgments

The authors gratefully acknowledge the financial support by the AiF (of the German Federal Ministry of Economic Affairs and Energy) within the framework of the ZIM (Zentrales Innovationsprogramm Mittelstand), grant # KF2012459PT3.

References

Bredies, K. and Lorenz, D., 2011. *Mathematische Bildverarbeitung: Einführung in Grundlagen und moderne Theorie*. Wiesbaden: Vieweg+Teubner Verlag / Springer Fachmedien Wiesbaden GmbH.

Burger, W. and Burge, M.J., 2005. *Digitale Bildverarbeitung: Eine Einführung mit Java und ImageJ*. Berlin, Heidelberg: Springer-Verlag.

Chaudhuri, S. and Rajagopalan, A.N., 1999. *Depth from Defocus: A Real Aperture Imaging Approach*. New York, NY: Springer-Verlag New York.

Erhardt, A., 2008. *Einführung in die Digitale Bildverarbeitung: Grundlagen, Systeme und Anwendungen*. Wiesbaden: Vieweg+Teubner / GWV Fachverlage GmbH.

Fujifilm Corporation, 2010. *Fujinon CCTV Lens: For FA/Machine Vision.* [online] Available at: <http://www.fujifilmusa.com/shared/bin/FUJINON-FA-MV-CCTV-LENS-Brochure.pdf> [Accessed on 15 February 2017].

Jähne, B., 2005. *Digitale Bildverarbeitung*. 6., überarbeitete und erweiterte Auflage. Berlin, Heidelberg: Springer-Verlag.

Leutron Vision, 2010. *PicSight P83M-GigE-AS: GigE Vision camera*. [online] Available at: <http://www.leutron.com/english/product/picsight/gige/P83M-GigE.pdf> [Accessed on 15 February 2017].

Pawlowski, K., 2010. *Untersuchungen zur Bestimmung der Farbdichte druckfrischer Offsetfarben mit einem Druckinspektionssystem*. Dr.-Ing. Dissertation. Technische Universität Darmstadt.

Ruanaidh, J.J.K.Ò. and Pun, T., 1998. Rotation, scale and translation invariant spread spectrum digital image watermarking. *Signal Processing*, 66(3), pp. 303–317.

Süße, H. and Rodner, E., 2014. *Bildverarbeitung und Objekterkennung: Computer Vision in Industrie und Medizin*. Wiesbaden: Springer Vieweg.

Utcke, S. and Burkhardt H., 1999. *Praktikumsversuch: Autofokus*. [online] Albert-Ludwigs-Universität Freiburg: Institut für Informatik. Available at: <http://lmb.informatik.uni-freiburg.de/lectures/praktika/BVPraktikum-I/autofokus/autofokus.ps.gz> [Accessed on 29 May 2016].

Vision & Control GmbH, 2007. Tutorial: Filter. [online] Available at: <http://www.vision-control.com/uploads/media/TU_Softwarefilter_de_2.0.0_02.pdf> [Accessed on 15 February 2017].

Analyte Separation for Microfluidic Applications by Surface Charge Modified Functional Pigment Coatings

Risto Koivunen[1], *Eveliina Jutila*[1], *Roger Bollström*[2] *and Patrick Gane*[1,2]

[1] School of Chemical Engineering, Department of Bioproducts and Biosystems, Aalto University, FI-00076 Aalto, Finland
[2] Omya International AG, Baslerstrasse 42, CH-4665 Oftringen, Switzerland

E-mail: risto.koivunen@aalto.fi; eveliina.jutila@aalto.fi; roger.bollstroem@omya.com; patrick.gane@omya.com

Abstract

Printed, self-contained sensors based on capillary transport and microfluidic principles are part of rapidly emerging research in printed functionality. Previous work into such designs has mainly focused on cellulosic papers as base substrates. In this study, the authors continue to present findings on how the use of custom-designed functional pigment coatings as alternative substrates, combined with local functionalisation by inkjet printed polyelectrolytes, allows for tailoring of surface chemistries to concentrate or separate anionic or cationic molecules. Both anionised and cationised coatings are tested and found to transport similarly charged model colourants, while separating those of opposite charge, with the extent of separation depending on colourant concentration. Furthermore, local surface chemistry reversal by new cationic (polyethyleneimine) and anionic (carboxymethyl cellulose) polyelectrolyte inks is demonstrated as a complementary method for analyte separation or concentration.

Keywords: functional coating, functional printing, inkjet printing, polyelectrolyte, separation.

1. Introduction and background

During the past decade, printed sensors based on microfluidic concepts have gained interest amongst researchers. Self-contained devices for medical or environmental monitoring applications have received particular attention. In order to avoid the need for external pumping to transport liquid, porous and permeable substrates transporting liquid by capillary action have been employed. Most common amongst these are porous cellulosic chromatography and filter papers.

In contrast to high volume fibrous substrates, pigment coatings have received limited attention for such applications, possibly since existing commercial coating formulations, typically designed for offset printing, are not suitable for such transport of aqueous solutions. The present authors have addressed this gap in research by designing custom pigment coatings (Jutila, Koivunen and Gane, 2015), investigating their hydrophobic patterning for controlled liquid transport (Koivunen, et al., 2016) and demonstrating surface charge-based concentration/separation of analytes by inkjet-deposited polyelectrolytes (Koivunen, et al., 2017). These topics in earlier phases of our research have been presented at recent IARIGAI research conferences.

The present work is a follow up study on the inkjet printed polyelectrolytes. In order to better understand the background, the reader is referred to the previous study (Koivunen, et al., 2017), where the authors successfully demonstrated separation/concentration of anionic compounds by inkjet printed cationic pol-

yelectrolyte, a method which was previously demonstrated for reducing the spreading of anionic reaction products (Hossain, et al., 2009; Hossain, et al., 2012). However, the effect of printed anionic polyelectrolytes for the concentration/separation of cationic polyelectrolytes could not be entirely demonstrated in the previous work, since the typically anionic nature of the coating itself arrested cationic test compounds. Furthermore, the tested polyelectrolyte inks suffered from unreliable jetting or from limited achievable solids content, due to limited solubility.

In the present work, a weakly cationic dispersed coating formulation will be tested, consisting of zwitterionic functionalised calcium carbonate (FCC), non-ionic polyvinyl alcohol (PVOH) as binder and cationic polyelectrolyte as dispersion additive. The cationic polyelectrolyte is expected to adsorb on the anionic sites of the FCC pigment surface, resulting in local charge reversal. In parallel, also a more anionic formulation consisting of FCC, anionic micro-fibrillated cellulose (MFC) and anionic polyelectrolyte will be tested for its interaction properties.

Functional inks based on two previously untested polyelectrolytes, anionic carboxymethylcellulose (CMC) and cationic branched polyethyleneimine (PEI), will be formulated. CMC is a water-soluble cellulose derivative, while branched PEI is liquid at room temperature and water-miscible.

2. Materials and methods

2.1 Pigment coatings

Functional coatings tested in this study were based on an FCC pigment (Omya International AG, Oftringen, Switzerland) having 110 m^2g^{-1} specific surface area, consisting of a mass fraction of 85 % hydroxylapatite and a mass fraction of 15 % calcium carbonate in an essentially shell-core structure, respectively. The high specific surface area of the coating is due to the fine porous intraparticle structure, as illustrated in Figure 1.

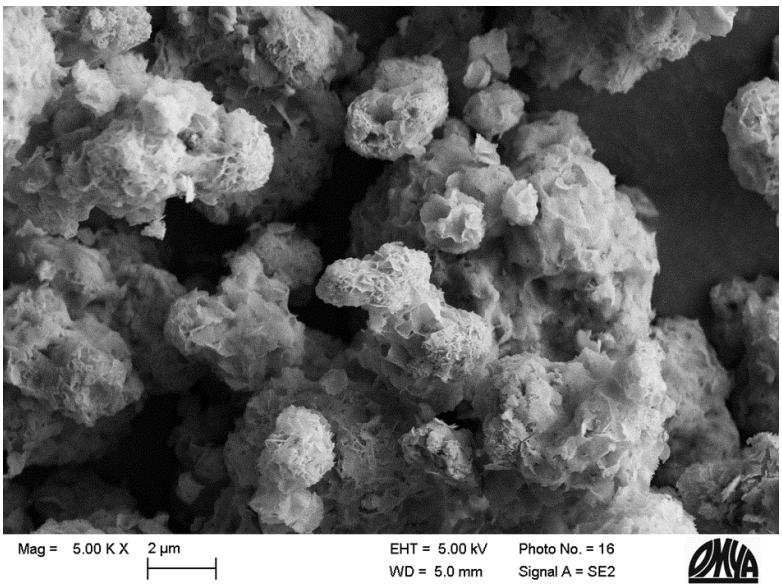

Figure 1: Close up SEM (Scanning Electron Microscopy) image of FCC pigment particle

Two aqueous coating slurries were prepared from the FCC pigment. These coatings will be referred to as anionised coating and cationised coating, and consisted of:

i. Anionised coating: 100 parts FCC, 10 parts micro-fibrillated cellulose (MFC) Arbocel MF-40-7 (J. Rettenmaier & Söhne GmbH + Co KG, Rosenberg, Germany) and 1 part sodium polyacrylate

(NaPA) of 8 kDa *Mw* (Sigma-Aldrich, St. Louis, USA, product code 416029, supplied as a mass fraction of 45 % aqueous solution), prepared to a solids content with a mass fraction of 15.15 %

ii. Cationised coating: 100 parts FCC, 10 parts polyvinyl alcohol (PVOH) BF05 (Omya International AG, Oftringen, Switzerland) and 1 part poly(diallyl dimethyl ammonium chloride) (polyDADMAC) of < 100 kDa *Mw* (Sigma-Aldrich, St. Louis, USA, product code 522376, supplied as a mass fraction of 35 % in aqueous solution), prepared to a solids content with a mass fraction of 15.99 %

where *parts* indicates dry weight content.

Slurries were applied with a mechanical drawdown K202 Control Coater (RK PrintCoat Instruments Ltd., Herts, UK) on pigmented polypropylene SuperYupo (Yupo Corporation, Tokyo, Japan) sheets of 80 μm thickness and 62 $g \cdot m^{-2}$ basis weight with a wire wound rod applying 60 μm wet slurry layer. Coated samples were dried overnight at room temperature.

2.2 Functional inks and printing

Two polyelectrolyte inks and one hydrophobising ink were prepared for this study. The polyelectrolyte inks consisted of a mass fraction of 1 % polyelectrolyte, a mass fraction of 25 % ethanol and a mass fraction of 74 % de-ionised water. Selected polyelectrolytes were:

i. anionic laboratory produced food-grade carboxymethyl cellulose (CMC) of 16.5 kDa *Mw*, prepared as an aqueous solution with a mass fraction of 32.5 % solids content, and
ii. cationic commercial branched polyethyleneimine (PEI) of 2 kDa *Mw* (Sigma-Aldrich, St. Louis, USA, product code 408700) supplied in aqueous solution with a mass fraction of 50 % nominal and 55.2 ± 2.6 % measured solid content.

The inks containing these polyelectrolytes will be referred to as CMC ink and PEI ink, respectively.

Polydispersity index data of the polyelectrolytes are not available at the time of the writing. This property can affect both jettability (longer polymer chains can contribute disproportionally to viscoelastic properties) and adsorption (in case of surface saturation, long polyelectrolyte chains adsorb preferentially over shorter ones).

For reducing surface tension of inks intended for analytical applications, on the one hand volatile organic solvent is considered likely preferable to polymer surfactants, which would remain on the substrate surfaces once the ink has dried. On re-wetting, the surfactants could then be re-dissolved and transported. If surfactant is present on a device featuring hydrophobic barriers, it can adsorb and re-hydrophilise pore surfaces, leading to permanent leaks – though such behaviour in controlled amounts can also be utilised to provide valve mechanisms (Chen, et al., 2012). However, on the other hand presence of organic solvent may affect the solubility of polyelectrolytes compared to pure aqueous solution. In order to test the solubility at higher concentrations, additional solutions with a mass fraction of 5 % polyelectrolyte, 25 % ethanol and 70 % de-ionised water were prepared.

The hydrophobising ink consisted of a mass fraction of 10 % alkyl ketene dimer (AKD) Basoplast 88 (BASF, Ludwigshafen, Germany) and a mass fraction of 0.1 % Yellow dye wood stain colourant 157 (Kremer Pigmente GmbH & Co. KG, Aichstetten, Germany, product number 94010) dissolved in p-xylene solvent. This ink will be referred to as AKD ink. Substrates printed with AKD ink were post-print heat-treated in an oven set to 105 °C for 10 min to promote AKD reaction with the coating.

The inks were printed with a DMP-2831 inkjet printer (Fujifilm Dimatix, Santa Clara, USA) with DMC-11610 cartridges of 10 pl nominal drop volume, using custom print settings. Both the printhead and mounting platen were held at a temperature of 30 °C.

Jetting reliability of inks was tested by printing a 280 mm × 200 mm chessboard pattern consisting of 5 mm × 5 mm squares. After 30 min of printing the printhead was inspected and the number of non-jetting nozzles recorded. This test was repeated 10 times per ink, with the non-jetting nozzles recovered into a freely jetting state once again before the next test round whenever possible.

The initial test pattern for hydrophobising ink consisted of rings printed at various drop spacing settings, as described in earlier work (Koivunen, et al., 2016). Test patterns for polyelectrolyte inks, intended to measure their visibility and spreading, consisted of 4 mm × 180 mm rectangles printed with 1, 2 or 3 ink layers. Once the hydrophobising efficiency was determined by the test described above, a further test pattern was printed to generate a chromatographic sample separation (separation test pattern), combining hydrophobising and polyelectrolyte inks. This pattern, shown in Figure 2, consisted of 10 hydrophilic channels, measuring nominally 3.9 mm × 50.0 mm, separated by hydrophobic barriers of 1.0 mm nominal width. Of the 10 channels, 4 were unprinted control channels, 3 channels contained printed PEI regions (of 1, 2 and 3 ink layers coverage) and another 3 channels contained CMC regions (of 1, 2 and 3 ink layers coverage), respectively. The printed polyelectrolyte regions measured nominally 3.9 mm × 4.0 mm and were located starting 10 mm from the beginning of the channel. The overall pattern, also featuring a hydrophobic barrier at the end of channels, measured 50 mm × 52 mm.

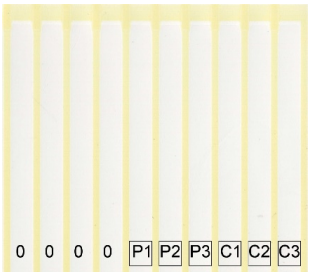

Figure 2: Scanned image of a printed separation test pattern: native coating is white and hydrophobic barriers yellow; black rectangles mark printed polyelectrolyte zones, labelled P1–P3 and C1–C3 to indicate 1, 2 or 3 layers of PEI or CMC ink, respectively; control channels labelled with 0; printing direction from top down and from left to right

2.3 Wicking and separation tests

Wicking of de-ionised water on the coatings was evaluated by cutting 5 mm × 50 mm strips from coated sheets, attaching these with double-sided tape to 25 mm × 75 mm glass microscopy slides, and placing the slides vertically in a plastic jar with a closed sealing cap. Approximately 4 mm depth of water had been previously added into the bottom of the jar, and this was allowed to wick for 5 min along the coating, after which the sample was removed from the jar and the distance travelled by the water front measured. Tests were conducted in a laboratory room held at 21 °C. Three parallel samples were tested per coating.

For the ease of detection, analytes were simulated in this study by two colourants, anionic tartrazine $C_{16}H_9N_4Na_3O_9S_2$ (Kremer Pigmente GmbH & Co. KG, Aichstetten, Germany, product number 94175) and cationic safranin O ($C_{20}H_{19}ClN_4$) (Alfa Aesar GmbH & Co KG, Karlsruhe, Germany, product code B21674). Separation of colourant from water was measured in a set-up similar to the wicking distance test, except that in this case the water at the bottom of the jar included from a mass fraction of 0.01 to 0.5 % of colourant, and the test was conducted until the water front reached the end of the strip. After this, the sample was removed from the jar and the distance travelled by the colourant front measured.

The effect of printed polyelectrolytes was tested by placing a separation test pattern vertically in a plastic jar containing approximately 4 mm depth of a mass fraction of 0.1 % colourant solution, after which the jar was closed. After the carrier liquid had travelled the full length of all 10 channels, the sample was removed from the jar, allowed to dry and, finally, scanned.

3. Results and Discussion

3.1 Coating properties

Properties of the coatings are shown in Table 1. As seen, water wicks significantly farther in the anionised coating than in cationised coating. This difference is due to the different binders in these coatings, and could be expected based on earlier work (Koivunen, et al., 2016).

Table 1: Properties of the native coatings with 95 % confidence interval.

Coating	**Anionised coating**	**Cationised coating**
Dry thickness / μm	34 ± 4	38 ± 5
Basis weight / $g \cdot m^{-2}$	9.5 ± 1.0	10.3 ± 2.0
Wicking distance (5 min) / mm	42 ± 1	19 ± 1

Table 2: Retardation factor RF between colourants and water on coatings, with 95 % confidence intervals; NA indicates that the colourant front was too faint to be detected reliably

Concentration / mass fraction %	**Tartrazine**		**Safranin O**	
	Anionised coating	Cationised coating	Anionised coating	Cationised coating
0.01	NA	0.14 ± 0.03	0.21 ± 0.03	1.00 ± 0.00
0.02	NA	0.17 ± 0.05	0.20 ± 0.03	1.00 ± 0.00
0.05	0.89 ± 0.00	0.24 ± 0.05	0.24 ± 0.05	1.00 ± 0.00
0.10	0.91 ± 0.03	0.39 ± 0.05	0.31 ± 0.03	1.00 ± 0.00
0.20	0.90 ± 0.03	0.53 ± 0.03	0.40 ± 0.03	1.00 ± 0.00
0.50	0.92 ± 0.03	0.67 ± 0.05	0.57 ± 0.03	1.00 ± 0.00

Separation of colourants from water, expressed in terms of retardation factor R_F (the ratio between distances travelled by the colourant and water fronts), as a function of colourant concentration, is displayed in Table 2. Cationic safranin O shows no separation on the cationic coating, while anionic tartrazine dye correspondingly shows little separation on anionised coating. However, both colourants show significant levels of separation when applied on oppositely surface charged coatings, with the level of separation heavily depending on the colourant concentration in the supersource, being greatest for the lowest concentrations. This suggests charge capture of some of the colourant on the pore walls, in turn partially neutralising the separating effect.

These results demonstrate that pigment coatings can be specifically formulated for transporting or separating anionic or cationic molecules. Furthermore, the variable level of separation for oppositely charged molecules could in principle be applied as a quantitative analytical method to measure concentration.

3.2 Functional inks and printing

All three inks were discovered to be initially jettable with the printer. The various designed waveforms for the inks are listed in Table 3, described by level, indicating relative displacement of the piezoelectric element within printhead, slew, indicating rate of change in level at the start of segment, and duration time length. Other jetting properties are shown in Table 4.

Table 3: Jetting waveforms for the inks

Ink	Segment	Level /%	Slew	Duration / µs
AKD ink	Jetting 1	100	0.30	12.096
	Jetting 2	0	0.05	24.192
	Non-jetting 1	13	0.30	12.096
	Non-jetting 2	0	0.05	24.192
CMC ink	Jetting 1	100	0.35	7.680
	Jetting 2	0	0.10	9.856
	Non-jetting 1	20	0.50	9.024
	Non-jetting 2	0	0.50	8.512
PEI ink	Jetting 1	100	0.30	7.040
	Jetting 2	0	0.50	4.800
	Non-jetting 1	20	0.30	7.040
	Non-jetting 2	0	0.50	4.800

Table 4: Ink jetting settings

Ink	AKD ink	CMC ink	PEI ink
Jetting frequency / kHz	3	6	3
Jetting voltage / V	17	18	20
Jetting speed (measured) / $m \cdot s^{-1}$	4–5	5	6
Nozzle jetting failure (30 min, measured) / %	0	2.5	4.0

Nozzle jetting failure in Table 4 indicates the average fraction of nozzles that were observed to be non-jetting at the end of a 30 min test period. In case of CMC ink, all such nozzles could be easily recovered with the in-built cleaning operations. However, in case of PEI ink nozzles that had become non-jetting could not always be recovered, even though the PEI is liquid at room temperature.

Regarding polyelectrolyte solubility, CMC was found to be initially soluble in the water-ethanol mixture at a mass fraction of 1 %, but not at a mass fraction of 5 %, developing clear flocs or agglomerates of precipitate. Branched PEI was found to be fully miscible with the water-ethanol mixture at a mass fraction of both 1 % and 5 %.

The amount of AKD required to print reliable hydrophobic barriers differed between the two coatings, with the anionised coating requiring a printed layer at 15 µm drop spacing, while for the cationised coating a layer printed at 25 µm drop spacing was sufficient. These settings, respectively, were applied for printing the separation test patterns. Polyelectrolyte inks were printed at 10 µm drop spacing, resulting in patterns that could be detected on the coating when observed against a background light. At this drop spacing, a single printed polyelectrolyte layer corresponds roughly to $1\ g \cdot m^{-2}$ of deposited polyelectrolyte on the substrate. The separation test patterns were printed with 16 nozzles for AKD and CMC inks, but with only 6 nozzles for PEI ink due to the presence of a few non-jetting nozzles in the printhead at the time.

3.3 Separation with printed polyelectrolytes

Results of a trial test for separating tartrazine or safranin O from a mass fraction of 0.1 % solution eluted past the polyelectrolyte printed zones are illustrated in Figure 3. Each sample was eluted until all of the channels were fully wetted.

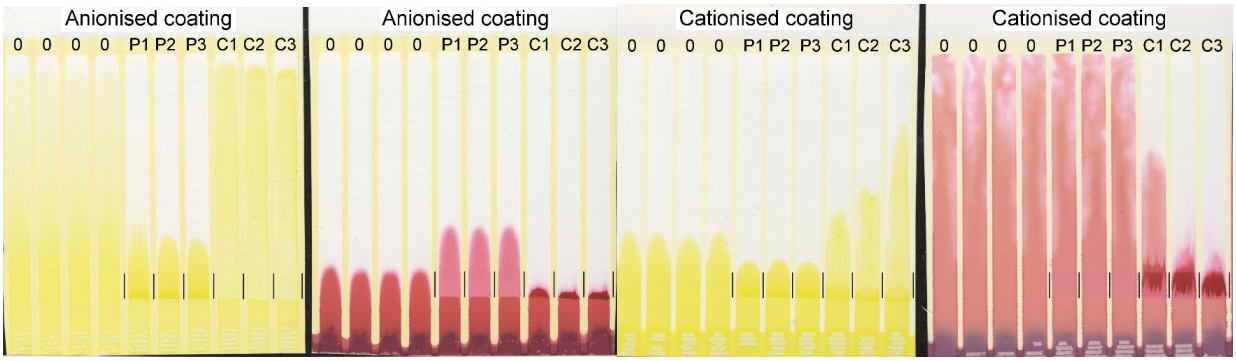

Figure 3: Scanned images of dried separation test patterns eluted with tartrazine (yellow) or safranin O solution (red): black lines next to channels mark printed polyelectrolyte zones, labelled on top P1–P3 and C1–C3 to indicate 1, 2 or 3 layers of PEI or CMC ink, respectively; control channels labelled with 0

From observing the interaction of the anionic tartrazine colourant with the printed polyelectrolyte regions, it can be seen to be arrested by the printed cationic PEI ink on both coatings, though not sufficiently to prevent it from travelling past the PEI region. A clearly visible concentration effect of the colourant can be observed at the bottom edge of the counter-charge printed region where the colourant enters, but not on the opposite edge. The anionic CMC region has no effect on tartrazine on the anionised coating, but on the cationised coating the level of separation between the colourant and water changes compared to the control channels after passing through the CMC region, with the magnitude of the effect related to the number of printed CMC layers. This effect suggests that part of the CMC desorbs from the original printed area when wetted, and subsequently becomes transported by the wicking water to the unprinted region, where the CMC re-adsorbs on the coating. Studies on CMC adsorption on hydroxylapatite surfaces have shown very flat polyelectrolyte conformation (Arêas and Galembeck, 1991).

Cationic colourant safranin O is arrested by the printed anionic CMC region on both coatings. On cationised coating it travels past the printed region, though the effect is reduced when the number of CMC printed layers increases from 1 to 2. The cationic PEI region has no effect on the cationised coating, but on the anionised coating the level of colourant separation again differs between the PEI printed channels and unprinted controls, though the magnitude of the effect in this case is not affected by the number of printed PEI layers.

4. Conclusions and future work

This study serves to demonstrate the separation of anionic and cationic model colourants on functionalised speciality pigment coatings with modified anionic or cationic surface chemistries. This modification was applied in two ways, either universally, by selecting a binder and modifying the bulk coating slurry by a polyelectrolyte additive, or locally, by depositing polyelectrolyte solution by inkjet printing. Both of these methods were combined on single samples, resulting in contrasts of anionic-cationic-anionic regions, or vice versa.

When the surface chemistry modification was conducted universally, coatings could be designed specifically to transport cationic components and separate anionic components, or vice versa. This is a significant difference to conventional cellulosic paper substrates, which are anionic by their intrinsic surface chemistry and thus transport cationic molecules very poorly. The modification of the coating surface chemistry is part of the bulk slurry preparation, not requiring any additional processing step. While the cationised coating featured significantly lower wicking speed than the anionised one, due to the choice of PVOH binder, a faster wicking cationised coating should be achievable by using MFC binder and a higher amount of cationic additive.

The separation of oppositely charged colourants on the coatings was observed to depend on the colourant concentration. While this may limit the applicability of the method with high concentration samples, it provides potentially a new analytical method for measuring analyte concentration based on the level of separation.

Two new polyelectrolyte inks were tested. Cationic PEI *could be expected* to be promising for inkjet applications, due to being of low molecular weight and liquid at room temperature, but issues with nozzles becoming non-jetting were clearly present with the settings used in this study. The other polyelectrolyte, anionic CMC, displays limited solubility when ethanol is present to reduce surface tension. Both of these polyelectrolytes induced the desired concentration/separation effect when printed on the coatings, but for practical applications they lack the reliability needed for scaling up.

Comparison studies will need to be conducted with further colourants to corroborate the findings and to better evaluate the effects involved. The effect of printed areas on separation needs to be evaluated also on channels printed over their full length. Also, further coating and polyelectrolyte ink formulations need to be explored.

List of abbreviations

CMC	Carboxymethyl cellulose
FCC	Functionalised calcium carbonate
MFC	Microfibrillated cellulose
NaPA	Sodium polyacrylate
PEI	Polyethyleneimine
PolyDADMAC	Poly(diallyl dimethyl ammonium chloride)
PVOH	Polyvinyl alcohol

Acknowledgements

The study was fully funded by Omya International AG. Silvan Fischer (Omya International AG) is acknowledged for the FCC pigment SEM image.

References

Arêas, E.P.G. and Galembeck, F., 1991. Adsorption of carboxymethyl cellulose onto hydroxylapatite. *Journal of Colloid and Interface Science*, 147(2), pp. 370–377.

Chen, H., Cogswell, J., Anagnostopoulos, C. and Faghri, M., 2012. A fluidic diode, valves, and a sequential-loading circuit fabricated on layered paper. *Lab on a Chip*, 12(16), pp. 2909–2913.

Hossain, S.M.Z., Luckham, R.E., Smith, A.M., Lebert, J.M., Davies, L.M., Pelton, R.H., Filipe, C.D.M. and Brennan, J.D., 2009. Development of a bioactive paper sensor for detection of neurotoxins using piezoelectric inkjet printing of sol-gel-derived bioinks. *Analytical Chemistry*, 81(13), pp. 5474–5483.

Hossain, S.M.Z, Ozimok, C., Sicard, C., Aguirre, S.D., Ali, M.M., Li, Y. and Brennan, J.D., 2012. Multiplexed paper test strip for quantitative bacterial detection. *Analytical and Bioanalytical Chemistry*, 403(6), pp. 1567–1576.

Jutila, E., Koivunen, R. and Gane, P.A.C., 2015. Effect of coating pigment, binder type and binder amount on planar wicking on coated substrates. *Journal of Print and Media Technology Research*, 4(3), pp. 173–186.

Koivunen, R., Jutila, E., Bollström, R. and Gane, P.A.C., 2016. Hydrophobic patterning of functional porous pigment coatings by inkjet printing. *Microfluidics and Nanofluidics*, 20(6), pp. 1–21.

Koivunen, R., Jutila, E., Bollström, R. and Gane, P.A.C., 2017. Inkjet printed polyelectrolyte patterns for analyte separation on inherently porous microfluidic analytical designs. *Colloids and Surfaces A: Physicochemical and Engineering Aspects*, 522(1), pp. 218–232.

A Method to Assess the Cross-Sectional Profile of Fused Deposition Modeling Lines

Heng Li, Bruce Myers and Shu Chang

School of Media Sciences, College of Imaging Arts and Sciences, Rochester Institute of Technology,
69 Lomb Memorial Drive, Rochester, NY 14623

Email: hl1696@mail.rit.edu, blmppr@rit.edu, shu.chang@rit.edu

Abstract

Fused deposition modeling (FDM) 3D printing construct parts by delivering thermoplastic materials first line-by-line and then layer-by-layer. As the extruded filament contacts the layer below to form a line, the cross-sectional area of the thread changes its circular shape to a more trapezoid appearance due to plastic flow. These trapezoid-shaped threads are the fundamental units of the FDM process. The change in the thread's cross-sectional profile means the actual size of the printed part will change correspondingly. Prediction of the dependence of a thread's stable shape as a function of the process and material parameters would enable one to control for the ultimate size of the fabricated parts. The aim of the work is to develop a methodology to identify and characterize the cross-sectional shape of FDM threads. The measurement system consists of a 3D computer-aided design (CAD) line test target design, production of the test target with an FDM printer, an optical microscope capable of height measurements, and a standard operating procedure. The study shows how thread widths and heights that characterize the cross-sectional shape are defined and measured. The study conducts a measurement system analysis to confirm the accuracy and precision of the measurement of the response variables.

Keywords: fused deposition modeling, cross-sectional profile, measurement system analysis

1. Introduction

As additive manufacturing (AM) has been increasingly adopted for rapid prototyping and part manufacturing, the need to determine the relationship between the part quality and the AM processes becomes crucial. Past research on part quality has aimed at developing testing and measurement methodologies for the dimensional accuracy of fabricated parts (Moylan, et al., 2012; 2014; Dimitrov, et al., 2006; Byun and Lee, 2003). Development on metrologies to characterize the size and shape of the fundamental voxel unit and size limitation of geometric patterns producible by AM print has been limited (Chang, et al., 2015; Li, Ostrout and Chang, 2016).

Recent studies have used systemic geometric artifacts as test targets (Moylan, et al., 2012; M.S.A. Manual, 2010) to determine the resolution of AM printers. These Geometric Element Test Targets (or GETT), includes simple geometric shapes, such as checkerboards or rays. These targets are printed at a sequence of sizes that span the resolution of the printer. The failure to produce features of the part at the smallest target sizes allows one to qualify the size limit of the printing systems. The GETT includes the capability to fabricate squares, converging lines in the XY plane, and the printer's resolution in the Z or the build direction.

This study establishes a method to quantitatively measure the cross-sectional profiles of the threads delivered from fused deposition 3D printing. The objective for the Z-direction assessment is to understand the geometric shape of the fundamental building block on the build platform and to relate the cross-sectional

shape to the manufacturing process. The methodology presented here defines the fused deposition modeling filament in regarding its profile characteristics. The analysis conducted validates the acceptability of the measurement method.

2. Materials and methods

Table 1 summarizes the components that constitute the measurement system. The components depicted in the table includes the test target that we designed with the 3D modeling software, the production method of 3D printing, the instrument used to profile the FDM printed lines, a standard operating procedure developed for measurement consistency among the operators, and the measurement system analysis (MSA). The last column provides content to the component in the measurement system.

Table 1: Components of MSA and their corresponding details

	Components of Measurement System	**Details**
2.1	Test Target	A 9 line sample, SOLIDWORKS® design
2.2	Production Method	3D printing, MakerBot® Replicator 2x
2.3	Measurement Instrument	Keyence© VHX-2000E series microscope at 200× magnification
2.4	Consistency Assurance	Standard operating procedure
2.5	Analysis	Measurement System Analysis (MSA), Quantum XL

2.1 Test target

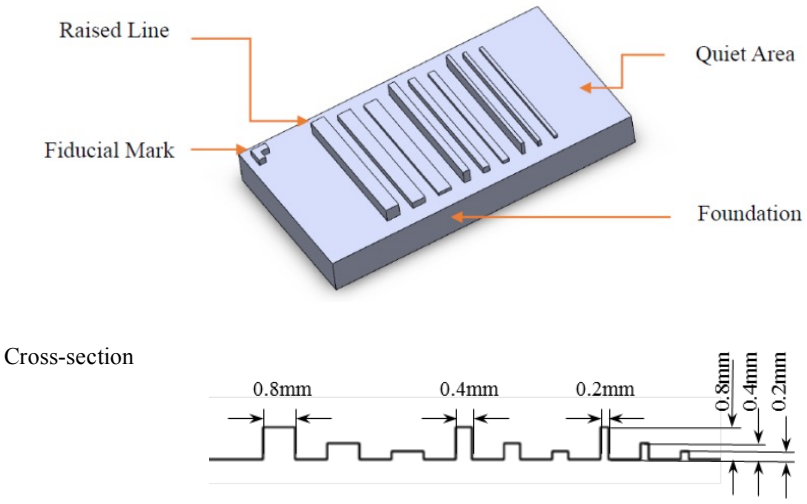

Figure 1: Test target consists of nine lines of different widths and heights; the values for the widths and heights are chosen to be of integer multiples of the print parameters

Figure 1 presents a 3D view of the line test target, designed using SOLIDWORKS® modeling software. The target has four parts: raised lines, a fiducial mark, the quiet area, and the foundation. The quiet area is the region without any features and is used to isolate the raised lines. The top plane of the foundation is defined as the reference plane and the zero for the height measurement. The fiducial mark provides a mean to locate and orient the test target with the microscope. The lines have different widths and heights. From left to right, three lines of the same widths are grouped together and in the order of 0.8 mm, 0.4 mm, and 0.2 mm respectively. Within each group, the line heights vary from 0.8 mm to 0.4 mm to 0.2 mm. The same line width and different line heights within each group are further illustrated by the sketch below to present in a cross-sectional view. The separations between lines are designed as 0.4 mm to prevent aliasing between lines.

The values for the widths and heights are chosen to be of integer multiples of the print process parameters. For example, MakerBot® Replicator 2x has a 0.4 mm opening for the orifices of the extrusion head and a standard build-direction increment of 0.2 mm. We designed the target to be multiples of the 0.2 mm for the height of the line. For the width of the line, in addition to the multiple of 0.4 mm of the nozzle opening, we added a half nozzle width of 0.2 mm to explore how the print system handles partial voxels.

2.2 Production method

The MakerBot® Replicator 2x process parameters are set to be 230 °C for the extrusion temperature, 110 °C for the platen temperature. The sample material used in this study was Acrylonitrile Butadiene Styrene.

2.3 Measurement instrument

Keyence© VHX-2000E series microscope has the capability of tracking z-direction focus and stacking sequential images; it measures the z-direction values in microns. The Keyence© microscope also can sample in areas up to 100 mm × 100 mm by taking multiple planar images and stitching them together. Both functions were used in our data collections. The line test target was imaged at 200× magnification. Figure 2 displays the stitched image of the line test target. The colors in the figure indicate the height of the features with red being high and blue low.

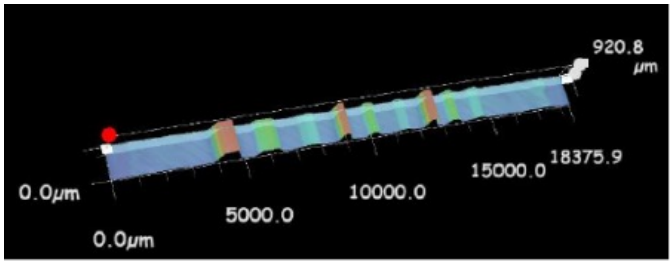

Figure 2: Stitched image of the line test target;
the colors indicate the height of the features with red being high and blue low

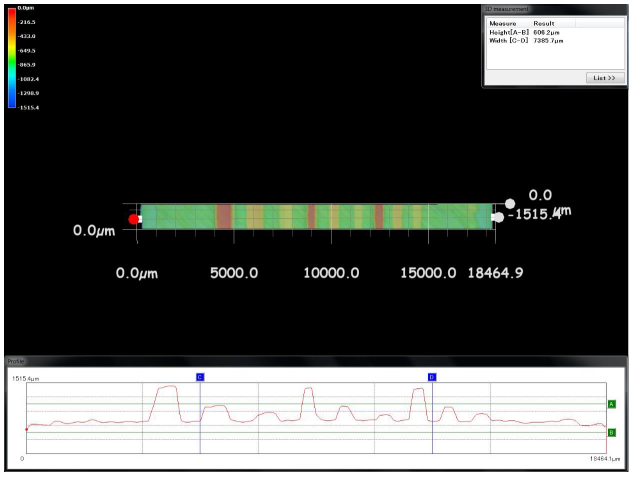

Figure 3: The widths and heights of the line GETT are mapped into a profile

The microscope software provides measurement to the height corresponding to each point on the surface. As shown in Figure 3 below, the cross-sectional profile of the line GETT is captured by a curve depicted at the bottom of the figure. The corresponding numerical values of the profile were saved as CSV files.

The Keyence© VHX-2000E microscope used in this study has an at-least 80° detection angle with respect to the horizontal surface, which implies that surfaces within 10° or less with respect vertical are interpo-

lated. All side surfaces produced here are true surfaces, as have been confirmed with angular measurements. Since the microscope has a variable observation angle of ± 60°, we have also captured images of the almost-vertical surfaces at the 15° observation angle to confirm that the measured cross-section profiles are not artifacts.

2.4 Consistency assurance

A Standard operating procedure (SOP) was written to provide instructions and standardize the measurement procedures among the operators. Standardization of procedures are an essential part of all measurement analysis to reduce the differences in measurement caused by different operators and the chances of introducing errors by the operators.

2.5 Analysis

We used Gage Repeatability and Reproducibility (R&R) Analysis of Variance (ANOVA) to conduct the measurement system analysis (MSA). The repeatability is the variation in measurements obtained with one measurement instrument when used several times by one operator while measuring the identical characteristic on the same part and the reproducibility the variation in the average of the measurements made by different operators using the same measuring instrument when measuring the identical characteristic on the same part. We designed the MSA experiment for three operators with three repeats per operator to investigate the reproducibility. The repeatability of different printed parts with the same printer came from the line target of 9 threads of different width and heights indicated in section 2.1. The MSA was to determine if the amount of variance caused by the combination of the instrument and the operators is acceptable for the intended use of the measurement system assembled.

3. Results and discussion

Figure 4 shows the cross-sectional profile (top graph) obtained from data collected for images as depicted in Figures 2 and 3. For illustration purposes, we have shown only the 0.8 mm line-width group. The bottom graph in Figure 4 displays the slope of the top graph, or the derivative of the line cross-sectional profile graph, with each line consisting of a different number of fundamental threads.

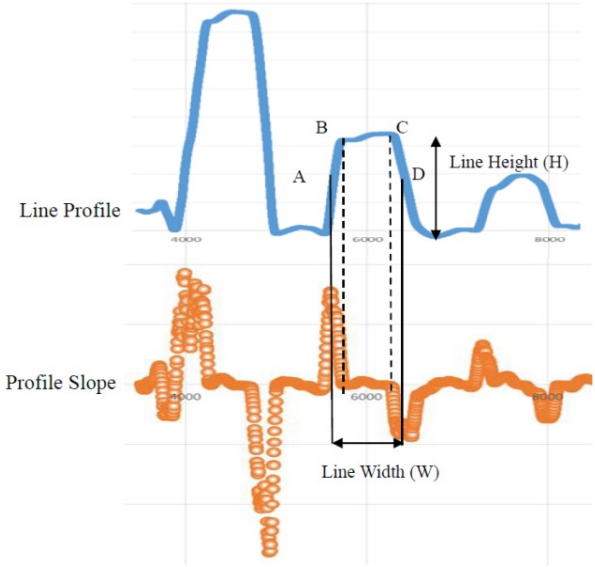

Figure 4: Cross-sectional line profile for the 0.8 mm line-width group (top graph) and its derivatives (bottom graph); the distance between the maximum and minimum values in the bottom graph defines the line width of the test target

From Figure 4, we identify the maximum and minimum values of the slope and define the separation between them as the line width. For example, the distance between point A and point D on the profile curve match the maximum and minimum points on the slope graph below and defines the line width for the middle line. Similarly, the region between locations of point B and point C has been used for the determination of line height for simplicity. Therefore, we have defined the characteristics for the line cross-sectional profile as:

- Line width = distance between A point and D point: Line Width (W) = $x_D - x_A$,
- Line height = average height values of point B and C: Line Height (H) = $(z_B + z_C)/2$.

Figure 5a shows the components of variation in line width, and the outcome from the MSA study. The vertical axis represents the percentage of the variation and the horizontal axis displays the components which contribute to the variation. There are four components contributing to the variation, as represented by the clusters of columns in Figure 4: Gage R&R, repeatability (labeled as Repeat), reproducibility (labeled as Reprod), and part-to-part (labeled as Part-to-Part). Each cluster has two columns that correspond to the percentage of component contribution (labeled as % Contribution, left column) and percentage of the component study variation (labeled as % SV), out of total study variation (labeled as % TV). The study variation for each component is the six times the standard deviation of the component and the total study variation as six times the total standard deviation.

a

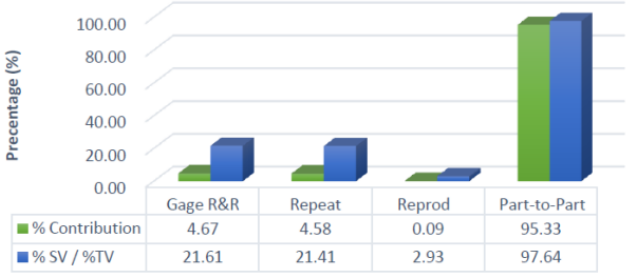

	Gage R&R	Repeat	Reprod	Part-to-Part
% Contribution	4.67	4.58	0.09	95.33
% SV / %TV	21.61	21.41	2.93	97.64

b

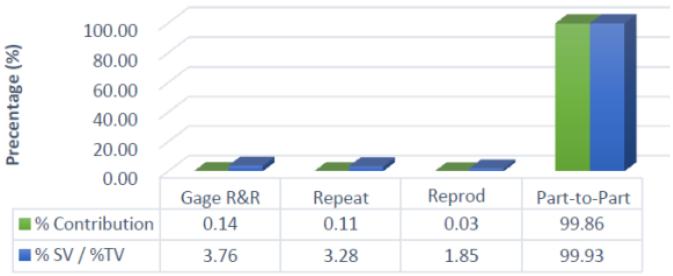

	Gage R&R	Repeat	Reprod	Part-to-Part
% Contribution	0.14	0.11	0.03	99.86
% SV / %TV	3.76	3.28	1.85	99.93

Figure 5: Comparison of component variations: (a) for line widths; (b) for heights

The largest component of the variation is the part-to-part variation. The ratio of the part-to-part study deviation (% SV) to the total study deviation (% TV) is 97.64 %, and the-part to-part contribution to the variation is 95.33 % of total variation. This is significantly larger than the respective values of 21.61 % and 4.67 % for the Gage R&R. The value of 21.61 % for the Gage R&R's % SV suggests that the measuring system established in this research is acceptable (M.S.A. Manual, 2010). In addition, comparison of % Contribution and the ratio of % SV to % TV between the repeatability and the reproducibility implies the possibility to improve the procedure of positioning the line test target on the microscope stage and underlines the consistency of the operators.

This two-way repeated ANOVA with nine replications produces a p-value of less than 0.001 for the part-to-part source, which is much less than the value of 0.05 for accepting the null hypothesis. Thus, there is a significant difference among parts populations, and the null hypothesis is rejected. In contrast, p-values for the operators (0.16 and the interaction between operators and parts (0.80 are much large than the 0.05 values; consequently, the null hypothesis is accepted as there are no significant differences among the operator behaviors and the interactions of operators with the parts.

Figure 5b shows the components of variation in the line height. The vertical axis represents the percentage of the variation and the horizontal axis the components that contribute to the variation. Similar to Figure 5a, the same four components of the variation are represented by the clusters of two columns that correspond to the percentage of component contribution (labeled as % Contribution, left columns) and the ratio of the component study variation (labeled as % SV) to the total study variation (labeled as % TV).

Similar to the line width variation, the largest contribution is from the part-to-part variation. The ratio of the part-to-part study deviation (% SV) to the total study deviation (% TV) is 99.93 %, and the-part to-part contribution to the variation is 99.86 % of total variation. The respective values for the Gage R&R are 3.76 % and 0.14 % respectively, showing excellent acceptability of the measurement system.

4. Conclusion

This research has focused on defining the characteristics of the 3D printing voxel, in this case, the lines from FDM, and developing a measurement system to assess line characteristics. The measurement system established in this study consists of the design of line test target, the target production, the measurement instrument, the development of a SOP, and the MSA.

The study has concluded that the established measurement system can detect the part-to-part differences over and above the measurement error for measuring the line widths and line heights of the lines in the target. The detected operator effect indicates that the operators are consistently measuring the samples by following the SOP. The statistically non-significant result obtained for the interaction of the operators and parts suggest that individual operators measure the same parts similarly. The MSA results indicate that the measurement system used to assess the line profile proposed in the study contributes very little to the overall variations.

Acknowledgement

This work is supported by the Melbert B. Cary Jr. Endowment.

References

Byun, H.-S. and Lee, K.H., 2003. Design of a new test part for benchmarking the accuracy and surface finish of rapid prototyping processes. In: V. Kumar, M.L. Gavrilova, C.J. Kenneth Tan and P. L'Ecuyer, eds. *ICCSA: International Conference on Computational Science and Its Application: Computational Science and Its Applications*. Montreal, Canada, 18-21 May 32003. Berlin, Heidelberg: Springer, pp. 731–740.

Chang, S., Li, H., Ostrout, N., Jhuria, M., Mottal, S.A. and Sigg, F., 2015. Geometric element test targets for visual inference of a printer's dimension limitations. In: *Proceedings of 26th Annual International Solid Freeform Fabrication Symposium*. Austin, TX, 10-12 August 2015. Austin: Laboratoty of Freeform Fabrication and University of Texas.

Dimitrov, D., Van Wijck, W., Schreve, K. and De Beer, N., 2006. Investigating the achievable accuracy of three dimensional printing. *Rapid Prototyping Journal*, 12(1), pp. 42–52.

Li, H., Ostrout, N. and Chang, S., 2016. Geometric element test targets (GETT™) for determination of 3D printers' resolution. In: *NIP & Digital Fabrication Conference, Printing for Fabrication 2016 (NIP 32)*. Manchester, UK, 12-16 September 2016. Springfield: IS&T, pp. 354–358.

M.S.A. Manual, 2010. *Measurement Systems Analysis, Reference Manual.* 4th ed. Southfield, Michigan: Chrysler Group LLC, Ford Motor Company, General Motors Corporation.

Moylan, S., Cooke, A., Jurrens, K. and Donmez, M.A., 2012. *A review of test artifacts for additive manufacturing: NISTIR 7858*. [pfd] National Institute of Standards and Technology. Available at: <http://nvlpubs.nist.gov/nistpubs/ir/2012/NIST.IR.7858.pdf> [Accessed February 2017].

Moylan, S., Slotwinski, J., Cooke, A., Jurrens, K., and Donmez, M.A., 2014. An additive manufacturing test artifact. *Journal of Research of the National Institute of Standards and Technology*, 119, pp. 429–459.

Cheap Carbon Nanodots obtained from Waste and their Use as Luminescent Material for (Water-based) Ink-jet Inks

Massimo Varisco[1], *Denis Zufferey*[1], *Fritz Bircher*[2] *and Olimpia Mamula Steiner*[1]

[1] University of Applied Sciences Western Switzerland, Haute Ecole d'Ingénierie et d'Architecture de Fribourg, Institute of Chemical Technology, Pérolles 80, CH-1700 Fribourg, Switzerland
[2] University of Applied Sciences Western Switzerland, Haute Ecole d'Ingénierie et d'Architecture de Fribourg, Institute for Printing, Route de l'Ancienne Papeterie 180, CP 146, CH-1723 Marly 1, Switzerland

E-mail: olimpia.mamulasteiner@hefr.ch

Abstract

We report here a method for the synthesis of carbon nanodots from wine industry waste. These nanoparticles were characterised and used to formulate luminescent inks. Invisible in the daylight, the inks are revealed as blue under UV irradiation (emission maximum around 430 nm).

Keywords: carbon nanodots, luminescence, security inks, ink-jet printing

1. Introduction and background

Fluorescent carbon nanoparticles or carbon nanodots (CNDs) are a new class of nanomaterials discovered accidentally in 2004 as a by-product in the synthesis of single-walled carbon nanotubes (Xu, et al., 2004). Intense research in this field has shown that the CNDs can be obtained from carbon waste sources via a simple chemical oxidation. Because of their biocompatibility, low toxicity and chemical stability (Li, et al., 2012, Lim, et al., 2015) combined with the strong and tunable fluorescence properties, these nanomaterials are believed to be able to replace: a) the semiconductor quantum dots (highly toxic) in bioimaging / biosensing, and b) conventional / UV organic dyes, because of their improved brightness and photostability (Luo, et al., 2014; Ng, et al., 2016; Dong, et al. 2015; Xu, et al., 2014; Gaddam, et al., 2014; Song, et al., 2016; Fernando, et al., 2015). Other promising applications of CNDs, but less explored, are related to their (electro)luminescent and catalytic properties. Recently it has been shown that CNDs can show phosphorescence (lifetime in the range of hundreds of milliseconds), (Deng, et al., 2013), when dispersed in a polyvinyl alcohol matrix. Their biocompatibility as well as their dispersibility in water open up very interesting perspectives for inks based on CNDs, especially in packaging for food and pharma industry. These inks, featuring anti-counterfeiting properties, can be printed on various surfaces (paper, plastic, glass) serving as a way of authentication.

We will present various low cost synthetic methods for obtaining CNDs from a bio-waste from the wine industry. The properties of the so obtained CNDs will be exposed not only as pure material, (Varisco. et al., in preparation) but also formulated in inks deposited on paper surfaces via ink-jet printing.

2. Materials and methods

We describe how experiments were made using firstly a thermal treatment of the waste followed by various extractions of the CNDs in ethanol by simple mixing, by microwave or by ultrasound exposure. This

step was followed by the acidic treatment of the CNDs and their functionalisation with various alkyl-amines in order to improve their luminescent properties. The characterisation was performed by luminescent spectroscopy, transmission electron microscopy (TEM), Fourier-transform infrared (FT-IR) spectroscopy, absorbance spectra (UV/Vis) and X-ray powder diffraction.

3. Results and discussion

The CNDs obtained after extraction and filtration have dimensions less than 10 nm, as can be seen in the transmission electron microscope (TEM) image in Figure 1. A very precise determination of particle size, however, is not possible using this technique.

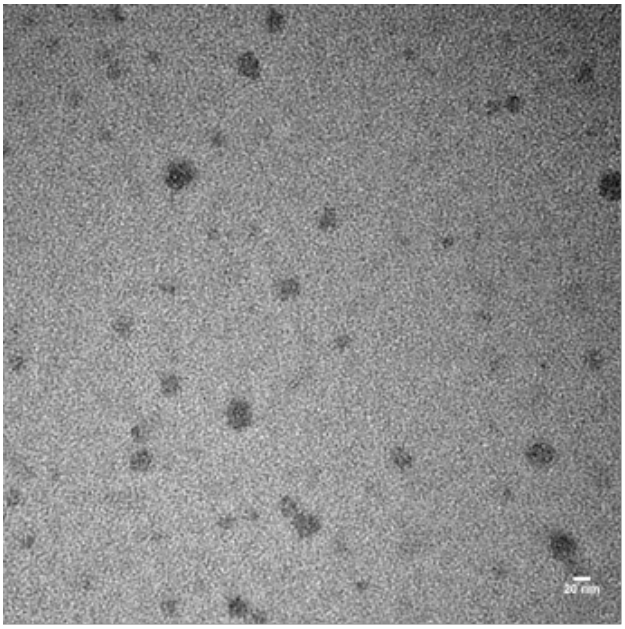

Figure 1: TEM micrographs of CNDs; scale bar 20 nm

The luminescent properties are in agreement with those reported for CNDs obtained from chemical sources (citric acid and ethylene diamine (D'Angelis, et al., 2015)) or waste sources like the brewing residue in the production of beer, (Rodrigues et al. 2015). The extraction methods applied influence greatly the luminescent output (Figure 2).

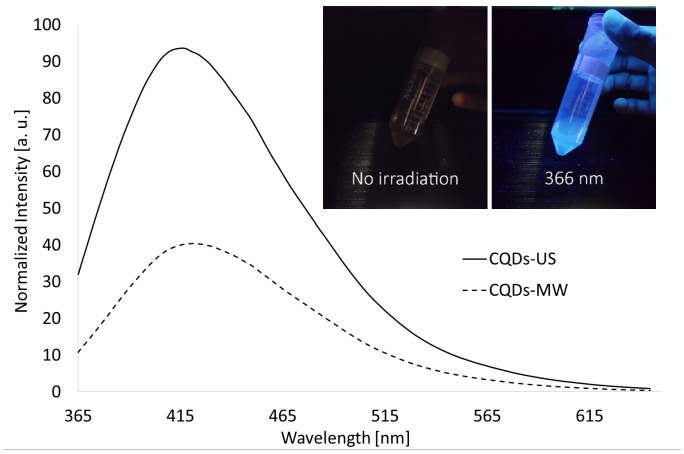

Figure 2: Emission spectra of the CNDs extracted by ultrasound (continuous line) or by microwaves (dashed line); excitation at 360 nm, maximum emission ≈ 430 nm - inset: sample without irradiation and under 366 nm irradiation

The emission intensities are increasing with the concentration of the CNDs and the shifts of the emission are small. Very high intensities were obtained with relatively low concentrations (i.e. 0.2 g/L). Moreover, the acidic treatment followed by functionalisation with dodecylamine or ethyldiamine led to even higher emission intensities. We found as well that the luminescence of CNDs is depending on the solvent used for the extraction: low for organic non polar solvents, high for water or organic polar protic solvents like the alcohols.

The wavelength of maximum emission is directly influenced by the energy of excitation, as for all other dots type. The quantum yield is not influenced by the wavelength employed, but the absorption is, thus the intensity change drastically by varying the excitation energy, as shown in Figure 3.

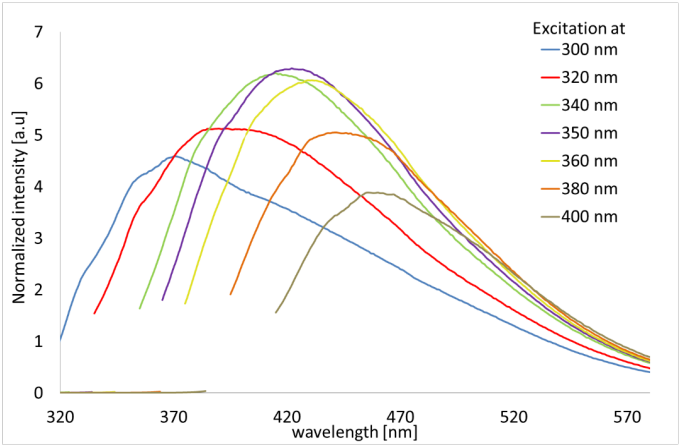

Figure 3: Emission spectra of the CNDs excited at different wavelengths

Luminescent inks based on CNDs were obtained in water or UV–curable monomers and have been ink-jetted on various paper based surfaces. Under UV-radiation these inks reveal the characteristic blue coloration.

4. Conclusions

We have shown that CNDs obtained from wine-waste are a possible new, cheap and stable carbonic material with high potential as luminescent components in security inks. The progressive shift from UV-curable to water based inks is fully supported by these nanoparticles, which are stably dispersible in water. Their electroluminescent properties are also opening up new perspectives for photonic applications such as large light emitting diode displays. We are currently exploring this issue in our laboratory.

References

D'Angelis, E.S.B.C., Correa, J.R., Medeiros, G.A., Barreto, G., Magalhães, K.G., de Oliveira, A.L., Spencer, J., Rodrigues, M.O. and Neto, B.A., 2015. Carbon dots (C-dots) from cow manure with impressive subcellular selectivity tuned by simple chemical modification. *Chemistry*, 21(13), pp. 5055–5060.

Deng Y., Zhao, D., Chen, X., Wang, F., Song, H. and Shen, D., 2013. Long lifetime pure organic phosphorescence based on water soluble carbon dots. *Chemical Communications*, 49(51), pp. 5751–5753.

Dong, Y., Cai, J., You, X. and Chi, Y., 2015. Sensing applications of luminescent carbon based dots. *Analyst*, 140, pp. 7468–7486.

Fernando, K.A., Sahu, S., Liu, Y., Lewis, W.K., Guliants, E.A., Jafariyan, A., Wang, P., Bunker, C.E. and Sun, Y.P., 2015. Carbon quantum dots and applications in photocatalytic energy conversion. *ACS Applied Materials and Interfaces*, 7(16), pp. 8363–8376.

Gaddam, R.R., Vasudevan, D., Narayan, R. and Raju, K.V.S.N., 2014. Controllable synthesis of biosourced blue-green fluorescent carbon dots from camphor for the detection of heavy metal ions in water. *RSC Adv*ances, 4(100), pp. 57137–57143.

Li, H., Kang, Z., Liu, Y. and Lee, S.-T., 2012. Carbon nanodots: synthesis, properties and applications. *Journal of Material Chemistry*, 22, pp. 24230–24253.

Lim, S.Y., Shen, W. and Gao, Z., 2015. Carbon quantum dots and their applications. *Chemical Society Review*, 44, pp. 362–381.

Luo, P.G., Yang, F., Yang, S.-T., Sonkar, S.K., Yang, L., Broglie, J.J., Liu, Y. and Sun, Y.-P., 2014. Carbon-based quantum dots for fluorescence imaging of cells and tissues. *RSC Advances*, 4, pp. 10791–10807.

Ng, S.M., Koneswaran, M. and Narayanaswamy, R., 2016. A review on fluorescent inorganic nanoparticles for optical sensing applications. RSC Advances, 6, pp. 21624–21661.

Rodrigues, C.V., Correa, J.R., Aiube, C.M., Andrade, L.P., Galvão, P.M., Costa, P.A., Campos, A.L., Pereira, A.J., Ghesti, G.F., Felix, J.F., Weber I.T., Neto, B.A. and Rodrigues, M.O., 2015. Down- and Up-Conversion Photoluminescence of Carbon-Dots from Brewing Industry Waste: Application in Live Cell-Imaging Experiments. *Journal of the Brazilian Chemical Society*, 26(12), pp. 2623–2628.

Song, L., Cui, Y., Zhang, C., Hu, Z. and Liu, X., 2016. Microwave-assisted facile synthesis of yellow fluorescent carbon dots from o-phenylenediamine for cell imaging and sensitive detection of Fe_3+ and H_2O_2. *RSC Advances*, 6, pp. 17704–17712.

Varisco M., Zufferey D., Mamula Steiner, O., Manuscript in preparation.

Xu, X., Ray, R., Gu, Y., Ploehn, H.J., Gearheart, L., Raker, K. and Scrivens, W.A., 2004. Electrophoretic analysis and purification of fluorescent single-walled carbon nanotube fragments. *Journal of the American Chemical Society*, 126(40), pp. 12736–12737.

Xu, Y., Liu, J., Gao, C. and Wang, E., 2014. Applications of carbon quantum dots in electrochemiluminescence: a mini review. *Electrochemistry Communication*, 48, pp. 151–154.

The Evaluation of Bio-Based Binders Influence on Offset Print Mottle using GLCM

Igor Karlovits[1], *Janja Juhant Grkman*[1], *David Ravnjak*[2] *and Gregor Lavrič*[1]

[1] Pulp and Paper Institute, Ljubljana, Slovenia
[2] Papirnica Vevče d.o.o., Ljubljana Dobrunje, Slovenia

E-mail: igor.karlovits@icp-lj.si

Abstract

In this paper we have researched the influence of bio-based binders on the macro print non-uniformity (print mottle) using GLCM (Gray-Level Co-Occurrence Matrix) for texture analysis. The drive for the change from synthetic (latex) binders to more green solution led to change in papermaking recipes and thus printability properties. The binders play a significant role in printing as they influence the surface properties of coatings and thus uneven surfaces lead to print non-uniformity issues like print mottle. In our research we have used one type of base paper where we have applied two types of bio-based binders with two different ratios of the SB latex replacement. After the coating on a laboratory coater we have printed the samples on a Prüfbau printability tester simulating offset printing and evaluated the print samples with GLCM algorithm. The samples were scanned and evaluated using R programming language in 4 different angles (00, 450, 900 and 1350) for several statistical texture features. The texture feature results indicate the complexity of image that smaller amount of bio-based binder results in more uniform (less complex) print while addition of higher amounts of bio-based binders increases the non-uniformity.

Keywords: bio binders, print mottle, GLCM

1. Introduction and background

The print quality is a constant topic both for printers and papermakers for decades. The printers have to be provided by papermakers with paper which have good production performances (no tearing, picking, print through, optimal ink set off) and good optical performances regarding gloss, whiteness and colour shade, as it all influences the final print product. On the other hand, there are environmental requirements and sustainability issues to make both processes (papermaking and printing) greener and environmentally acceptable. Papermakers are mainly investigating the possibilities of energy and water consumption and also great efforts are invested in finding viable environmentally friendly components which can make paper production and products more sustainable.

The printability of paper is principally determined by the surface of the coating, and its structure and topology. Pore size and pore size distribution, chemical nature and homogeneity all play an important part in influencing the interaction between paper and ink. The binder has the greatest influence on printability, but co-binders and thickeners also play a part and they have to be adapted to the printing process (Holik, 2013). Several authors investigated different aspects of the binder influence on different printability properties like Preston, Nutbeem and Chapman (2011) and Zang and Aspler (1998) which investigated the ink receptivity and ink density variation of the prints. Differences and variability of pore size/porosity, total volume of pores and coating thickness variation as well the distribution of binder within the coating and binder migration toward the coated paper surface which was indicated in researches by Al-Turaif and Bousfield (2005), Zang, et al. (2010), and Engström, et al. (1991). In her MSc thesis Madstedt (2008) was

investigated coating composition influence on print mottle in offset printing. Among other influencing factors (printing, fountain solution) on the paper side the reduction of synthetic binders component was desirable for print mottle decrease, but only to a certain amount due to problems with picking.

Bio-based binders are derived mainly from starches with the reactive extrusion process. During this process, micron size starch particles are transformed into nano-sized macromolecular units with intermolecular linkage. While styrene butadiene binders do not swell, the bio-based particles swell and thus they have a different film forming process. Findings of Bloembergen, et al. (2014) indicate that the rheological performance of bio-based binders is significantly different from that of conventionally cooked coating starches and all-synthetic binders formulations. Due to water, bio-based swollen colloid particles deform and de-swell under shear and pressure, which is a unique property of the boil binders technology. The authors conclude that the boil binders systems show unusual rheological, water retention, and wall slip properties that suggest better coater runnability with no impact on the final printed results. On the other hand a fairly recent research conducted by Lee, et al. (2015) found that a 50:50 mixture of bio-based binder have better dry pick strength but the print mottle showed similar results as all pure synthetic binder samples, with sample of 50 % of bio-based binder having slightly worse results than all 100 % synthetic binder coatings. In their paper Oberndorfer Greenall and Bloembergen (2011) conducted a trial with different bio-based binder ratios and reported a brief result that the print mottle results were comparable in spite of different ratios but with no further referencing to the investigated methods used to test print mottle.

The print mottle was extensively studied by different researchers using different approaches. One overview of the print mottle causes and solutions was done by Lee (2008) and in the master thesis work by Weingerl (2014) who also provides improved version of some mottle evaluation methods. Several more angles to the problem solving were provided by other authors (Kim-Hambermehl, et al., 1998; Chinga and Helle, 2003; Shen, et al., 2005) where they developed a correlation between absorption non-uniformity and print mottle. There are several software packages and devices for the print mottle assessment and just one standardized method in ISO/IEC 13660:2001 (International Organization for Standardization, 2001) which implies the use of a microdensitometer which in several papers has been stated as inappropriate for the graphic arts industry. Besides those methods like clusters, image statistics (histograms), image wavelength and frequency analysis (Armel, 1998; 1999; Johansson, 1999; Rosenberger, 2001; Streckel, et al., 2003) are available. Gray-Level Co-Occurrence Matrix (GLCM) was developed in the 1970's and is being extensively used for satellite images, radiology images and other image processing based texture analysis. It is a statistical method which considers the spatial distribution and variation of the pixels in a so-called gray-level spatial dependence matrix. In recent years there were studies which indicate that GLCM texture parameters have good correlation with profilometer (surface profile data) (Hladnik, Debeljak and Gregor Svetec, 2010; Hladnik and Lazar, 2011) and visual assessment of print mottle (Jurič, et al., 2016) which indicated that this was the most suitable method over 3 different ones being compared. On the basis of these findings and due to the fact, that many of the aforementioned methods used by different researchers require special equipment or proprietary software solutions, GLCM seems like an easy and affordable method for assessing print mottle as it is an established methodology for versatile use in image processing.

2. Materials and Methods

For the printability test we have used a 51 g/m^2 base paper for coating that has been coated with coating preparations containing different types of binders. We have used the bio-based binders from Ecosphere which where varied in volume ratios as can be seen in Table 1. Ratios of all other components of the coating have been kept constant in all samples. All samples were coated on a RK Lab coater in the amount of 12 g/m^2.

Table 1: Ratio of the used bio binders compared to 100 pigment particles

Binder Type	Sample 1 (%)	Sample 2 (%)	Sample 3 (%)	Sample 4 (%)	Sample 5 (%)
Styrol-butadiene	12	9	9	6	6
EcoSphere 2330	0	3	0	6	0
EcoSphere 2202	0	0	3	0	6

Differences in coatings before and after application have been noticed. Sample 1 had apparent Brookfield viscosity (100 rpm) of 1 080 mPas, and Samples 2–5 had values of 1 450, 1 440, 1 380 and 1 380, respectively. Also, differences in water retention have been found where the all styrol butadiene (SB) latex containing samples had 138 g/m^2, while Sample 2 had the value of 65, Sample 3 of 86, Sample 4 of 64 and finally Sample 5 of 77. All the samples were calendered on the laboratory calender at 105 °C and under 1 t weight/pressure. After conditioning, all the samples were printed on a Prüfbau printability tester which simulates offset lithographical printing using Prüfbau mottling ink at printing speed of 1 m/s. After printing all samples were scanned in the resolution of 300 dpi with no alterations. The scanned samples were then evaluated using the "radiomics" library of the open source language for the GLCM evaluation. For the evaluation, we have used 4 angles (0°, 45°, 90° and 135°) with an offset of 1 pixel. We measured 9 samples from each binder combination and averaged the results.

3. Results and Discussion

The results for the GLCM analysis are presented through Figures 1–3.

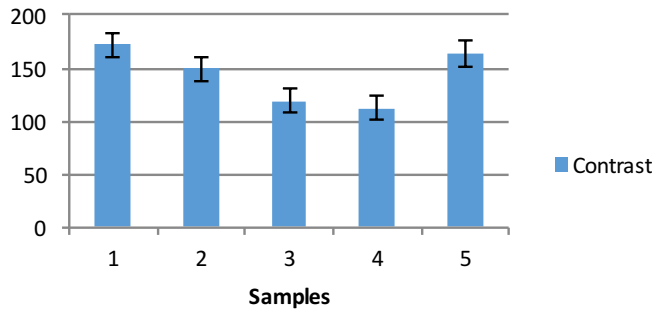

Figure 1: The GLCM contrast values

From Figure 1 it can be observed that the initial sample 1 (100 % SB binder) has the highest value of contrast with value of 171.94 while all other samples have lower contrast values with a trend of constant decrease when using the bio-based binder EcoSphere 2330, while the EcoSphere 2202 shows a decrease with 3 % addition and a result similar to SB binder (163.94) with 6 % addition.

In Figure 2 we can observe a different trend for the correlation value where the second Sample EcoSphere 2330 (3 %) has the highest correlation, then the same sample with the higher addition of the bio-based binder (both higher than latex-based binders) and Samples 3 and 5 lower values than the initial Sample 1. Correlation as a GLCM parameter measures the linear dependency of grey levels of neighbouring pixels. A value of 0 means that they are uncorrelated, while a value of 1 represents perfect correlation. These values are derived from mean and variance values of GLCM matrix elements.

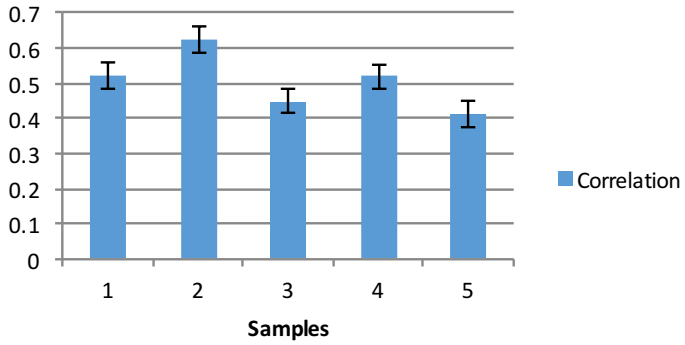

Figure 2: The GLCM correlation values

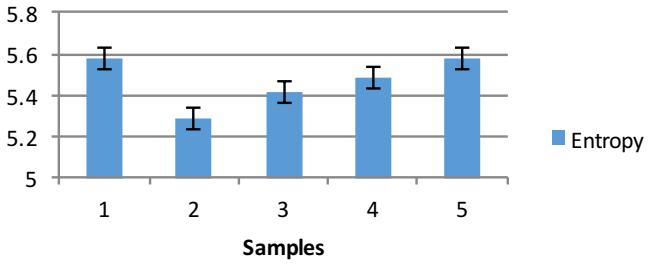

Figure 3: The GLCM entropy values

In Figure 3 Samples 2 and 3 (3 % added bio-based binder) yielded lower GLCM entropy values than the initial sample and the subsequent higher addition of bio-based latex. Entropy measures the disorder or complexity of an image. The entropy is large when the image is not texturally uniform and many GLCM elements have very small values. Complex textures tend to have high entropy and the results indicate that the Sample 2 (EcoSphere 2330 with 3 %) has the smallest value and the most homogeneous surface compared to other samples. Also, the higher content has a slightly lower value (5.48) compared to the SB binder based samples (5.57) but it can be seen that higher content of bio-based binder increases entropy and complexity thus non-uniformity of the samples. In Figure 4 the results for the energy parameter are presented. Energy quantities textural (surface) uniformity where GLCM of the image which is less homogeneous will have a large number of small entries and higher values when the grey levels of the image have a constant, more uniform form.

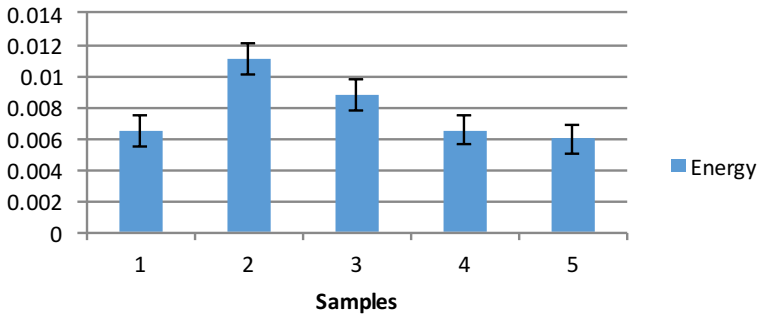

Figure 4: The GLCM energy values

Entropy is strongly, but inversely correlated with energy and in some applications, the use energy over entropy as its values belong to normalized image (Gadkari, 2004). As we can observe the energy value of sample 2 is the highest which correlates well with other GLCM parameters that this sample has the most uniform texture pattern and can be considered as the sample with the smallest print mottle values. We

have also performed the principal component analysis (PCA) to find the most influencing variable and found that contrast, correlation, and entropy are cumulatively explaining the most variations between the samples. So, we have taken those three variables as more influencing. One potential problem for contrast which has the highest variance can be the rod type of laboratory coating which produces uneven surface and can make the variation of lightness emphasized in some angles of GLCM analysis. As Sample 2 has yielded good results for correlation and entropy (two seconds most influential factors) we can assume that this sample has the lowest print mottle. We have also checked the Bekk smoothness of the paper samples before printing which is presented in Table 2.

Table 2. Bekk smoothness values of paper samples

Sample	1	2	3	4	5
(s)	77.37	118.5	92.92	83.25	80.28

4. Conclusions

Increase use of bio-based binders will increase in the future with the overall aim to greener technologies, but on the other hand, the paper and printing industry is under constant pressure for quality production. Results indicate that a smaller amount (in our case 3 %) of bio-based binder yields better results regarding print mottling in offset printing. Larger replacement of SB latex binder results in higher nonuniformity values. These results most probably are due to different viscosity values and flow properties of bio-binders which resulted in smoother papers with a better evenness of coating which leads to smaller variations in printing variation-mottling. As the coating was done on a laboratory scale with a rod, the results are limited just to these conditions, as the binders would probably behave differently in another type of coating equipment. GLCM proves to be a useful method for the analysis of mottling as it gives several statistics parameters which can give more details about differences and changes in print mottle due to mixture and paper coating recipe preparation. Some other methods like microdensitometer or linear measurement of light variations with spectrophotometers are more time consuming or not so detailed (using one averaged index) about smaller differences but with several textures parameters like presented in this paper, fine adjustment of the formulation can be carried out. Due to several parameters which can be calculated the next research step will be the optimization of the used parameters with additional samples.

Acknowledgments

The work was carried out within the RDI project Cel.Cycle: »Potential of biomass for development of advanced materials and bio-based products« (contract number: OP20.00365), co-financed by the Republic of Slovenia, Ministry of Education, Science and Sport and European Union under the European Regional Development Fund, 2016–2020. We also want to thank Vevče paper mill for providing the necessary material support.

References

Al-Turaif, H.A. and Bousfield, D.W., 2005. The influence of pigment size distribution and morphology on coating binder migration. *Nordic Pulp and Paper Research Journal,* 20, pp. 335–344.

Armel, D. and Wise, J., 1998. An Analytic method for quantifying mottle – part 1. *Flexo*, 23, pp. 70–79.

Armel, D. and Wise, J., 1999. An Analytic method for quantifying mottle – part 2. *Flexo*, 24, pp. 38–43.

Bloembergen, S., Pampolha Santos, M., Greenall, P., DeJong, R., Shin, J.Y., Jones, N., Fleming, P.D., Joyce, M.K. and Lee, I., 2014. The effects of biolatex binders on the dynamic water retention properties of paper coating formulations. *O Papel: revista mensal de tecnologia em celulose e papel*, 75(3), pp. 55–65.

Chinga, G. and Helle, T., 2003. Relationship between the coating surface structural variation and print quality. *Journal of Pulp and Paper Science*, 29(6), pp. 179–184.

Engström, G., Rigdahl, M., Kline, J. and Ahlroos, J., 1991. Binder distribution and mass distribution of the coating layer: cause and consequence. *Tappi J*., 74, pp. 171–179.

Gadkari, D., 2004. *Image Quality Analysis Using GLCM*. MSc thesis, University of Central Florida, Orlando.

Hladnik, A., Debeljak, M. and Gregor Svetec, D., 2010. Assessment of paper surface topography and print mottling by texture analysis. In*: Proceedings of ImageJ User & Developer Conference*, Luxembourg, 27–29 October 2010.

Hladnik, A. and Lazar, M., 2011. Paper and board surface roughness characterization using laser profilometry and gray level cooccurrence matrix. *Nordic Pulp and Paper Research Journal*, 26(1), pp. 99–105.

Holik, H. ed., 2013. *Handbook of Paper and Board: 2nd Revised and Enlarged Edition*. Wiley.

International Organisation for Standardization, 2001. *ISO/IEC 13660:2001 Information technology -- Office equipment -- Measurement of image quality attributes for hardcopy output -- Binary monochrome text and graphic images*. Geneva: ISO.

Johansson, P.-Å, 1999. *Homogeneity of Prints*. PhD Thesis. Kungliga Tekniska Högskolan, Stockholm.
Jurič, I., Karlović, I., Novaković, D. and Tomić, I., 2016. Comparative study of different methods for the assessment of print mottle. *Color Res. Appl*., 41(5), pp. 493–499.

Kim-Habermehl, L.H., Pollock, M., Wittbrodt, E., Roper III, J., McCoy, J., Stolarz, J., Langolf, B. and Rolf, M., 1998. Characterization of coated paper surface morphology and its correlation to print mottle. In: *Proceedings of the PanPacific and International Printing and Graphic Arts Conference*, Québec City, CA, 1998, pp. 71–76.

Lee, H.-L., 2008. Print mottle: causes and solutions from paper coating industry perspective. *Journal of Korea Technical Association of the Pulp and Paper Industry*, 40(5), pp. 60–69.

Lee, Y.K., An, G.H., Chang S. Kim, C.S. and M Won, J.M., 2015. Manufacturing of multi-layer coated paper with eco-friendly biobinder for cost saving (3) - mill trial of eco-friendly biobinder for cost saving, *Journal of Korea Technical Association of the Pulp and Paper Industry*, 47(5), pp. 127–133.

Madstedt, S., 2008. *The Impact of Coating Composition on Print Mottle and Print Gloss Variations in Sheet-Fed Offset*. Msc Thesis. Royal Institute of Technology, Stockholm, Sweden.

Oberndorfer, J, Greenall P. and Bloembergen, S., 2011. Coating and print performance of biobased latex in European graphic papers. In: *PaperCon2001 Meeting*. Covington, Kentucky, 1-4 May 2011, pp. 2180–2195.

Preston, J.S., Nutbeem, C. and Chapman, R., 2011. Impact of pigment blend and binder level on the structure and printability of coated papers. In: *PaperCon2001 Meeting*. Covington, Kentucky, 1–4 May 2011, pp 418–438.

Rosenberger, R.R., 2001. Stohastic frequency distribution analysis as applied to ink jet print mottle measuremnet, In: *IS&Ts NIP 17:2001 International Conference on Digital Printing Technologies*. IS&T, Springfield VA, pp. 808–812.

Shen, Y., Bousfield, D. W., Van Heiningen, A. and Donigian, D., 2005. Linkage between coating absorption uniformity and print mottle. *Journal of Pulp and Paper Science*, 31(3), pp. 105–108.

Streckel, B., Steuernagel, B., Falkenhagen, E. and Jung, E., 2003. Objective print quality measurement using a scanner and a digital camera. In: *DPP 2003: IS&T International Conference on Digital Production Printing and Industrial Applications*, pp. 145–147.

Weingerl, P., 2014. *Objektivne metode za določanje tiskovne neenakomernosti in njihova korelacija z vizualno percepcijo*. MSc Thesis. Univerza v Ljubljani, Naravnoslovnotehniška fakulteta, Ljubljana.

Zang, Y.-H., Du, J., Du, Y., Wu, Z., Cheng, S. and Liu, Y., 2010. The migration of styrene butadiene latex during the drying of coating suspensions: when and how does migration of colloidal particles occur? *Langmuir*, 26(23), pp. 18331–18339.

Zang, Y.H., Aspler J.S., 1998. The effect of surface binder content on print density and ink receptivity of coated paper, *Journal of Pulp and Paper Science*, 24(5), pp. 141–145.

Using ISIT as a Probe to establish Critical Roughness – film thickness relationship

Mika Anttila[1], *Martti Toivakka*[1] *and Patrick A. C. Gane*[2,3]

[1] Laboratory of Paper Coating and Converting, Faculty of Science and Engineering, Åbo Akademi University, Porthaninkatu 3, FI-20500 Turku, Finland
[2] Omya International AG, CH-4665 Oftringen, Switzerland
[3] School of Chemical Engineering, Department of Bioproducts and Biosystems, Aalto University, FI-00076 Aalto, Finland

E-mail: mika.anttila@abo.fi; martti.toivakka@abo.fi; patrick.gane@omya.com

Abstract

In the offset process, ink film splitting and release properties impact strongly on the stability of the paper surface. The determination of the pick velocity and the pick resistance is one of the most widely used surface strength tests for coated offset papers. Generally, the tack properties of a test ink or viscosity of a test oil are considered to be the control parameters for generating the separation force required to evaluate surface strength. A frequently overlooked parameter, however, is the influence of the release properties of the materials forming the print nip, i.e. print roller (blanket) and the coated paper surface. In this work, we set out to establish the relationship between paper surface roughness and the critical liquid film thickness (CFT) which determines the force level generated in respect to adhesion and surface contact area. The CFT is here defined as the film thickness distribution on the surface at which the maximum tack force (release force) value is achieved. A series of six specially designed highly latex bound ground calcium carbonate (GCC) coated papers having different roughness were tested using the Ink Surface Interaction Tester, ISIT, in respect to measured release force using the extensional tack measurement feature. Newtonian IGT pick test oil was applied at different film thickness on the application roller and the pull-off force (release force) was recorded using a range of contact nip pressure and nip dwell time. The CFT is confirmed primarily to be a function of the surface roughness for materials of defined surface chemistry. The release force maximum value, the width of the release force peak and the CFT at the maximum force can all be accurately determined. Fine GCC pigments, for example, gave low surface roughness, low CFT values and high but sharp release force peak. The high sensitivity of this test method enables new insights to be gathered into the nature of the paper surface release properties.

Keywords: release force, critical liquid film thickness (CFT), surface roughness, liquid-void space distribution, offset printing, GCC pigment coating

1. Introduction and background

Offset lithography is the most commonly used printing method in the world. The ink transfer process controls the location of ink on the surface profile of the paper (Särelä, 2004; Walker and Fetsko, 1955). Contact between blanket and paper in the printing nip is dependent on the nip dwell time and the nip pressure, and determines the degree of ink flow within the surface profile. The dwell time in an offset nip is typically 0.2 ± 0.05 ms, and since paper and blanket are viscoelastic, the deformation under nip pressure causes changes in roughness volume. The rubber surface of the offset blanket is the most compressive component of the nip and determines the pressure distribution in the nip when the contact is not complete (Oittinen and Lindqvist, 1981). Thus, the blanket surface conforms to the paper roughness, reducing the ink film thickness required to cover the paper surface (Lyne and Aspler, 1982; Bristow and Bergenblad, 1992).

Paper coatings are relatively non-deformable. Inks are incompressible and respond by flowing under the influence of pressure gradients (Bohan, et al., 2000).

The release force, the term used here to define the force required to separate a liquid film in contact with the print substrate surface during film splitting, is highly dependent on the liquid amount between the surface and the print blanket. In this work, we set out to establish the relationship between paper surface roughness and the critical film thickness (CFT), defined as the film thickness at which the maximum tack force value is achieved. The release force is measured as a function of oil amount using different nip pressure – nip dwell time combinations on an Ink Surface Interaction Tester, ISIT (SeGan Ltd., UK) applying Newtonian IGT pick test oil as the liquid film.

2. Materials and methods

2.1 Coating colours

We designed Laboratory coating formulations to provide single one side coated papers with a range of surface roughness volumes. To avoid artefacts of liquid absorption into the base sheet substrate non-absorbent impermeable synthetic paper was used (SuperYUPO® - formerly Synteape® - 115 g · m^{-2}, YUPO Corporation, Japan). A summary of coating colour formulations TP1-6 (TP0 being uncoated substrate only) is given in Table 1. The pigmented coating colours were based on 100 pph (parts per hundred parts dry pigment by weight) dispersed ground calcium carbonate (GCC) prepared with 25 pph polyvinyl acetate latex (CHP119, glass transition temperature 15 °C, supplied by CH-Polymers Oy, Raisio, Finland). High binder amount was chosen to avoid surface strength problems and excessive liquid penetration, which would have hindered interpretation of the release force and CFT results. The studied pigments, five commercial grades of GCC, ground calcium carbonate (Hydrocarb™ supplied by Omya AG, CH-4665 Oftringen, Switzerland), were chosen to have different particle size and distribution steepness, as depicted in Figure 1, determined by the Sedigraph® sedimentation technique (Micromeritics, Norcross, Atlanta USA) providing a measure of the equivalent hydrodynamic diameter distributed in respect to mass % less than *d* μm. The steepness of the particle size distribution ($d_{75\,\%}/d_{25\,\%}$) increases from the coarsest pigment to the finest: HC50 (14.6), HC60 (21.8), HC75 (34.1), HC90 (50.1) and HC98 (87.2), where HC*N* refers to Hydrocarb with *N* weight % less than 2 μm. For the coarser pigments, the pigment volume concentration in the dried coating can be seen to be under the critical point (CPVC) in respect to binder.

Table 1: Coating colour formulations and properties

		TP1	**TP2**	**TP3**	**TP4**	**TP5**	**TP6**
Pigment (GCC)	HC98	100					
	HC90		100				
	HC75			100			
	HC60				100		
	HC50					100	
Binder (PVAc latex)	CHP119	25	25	25	25	25	100
Solids content	/ %	68.6	68.6	68.5	68.3	68.2	48.7
Br. viscosity - 100 min^{-1}	/ mPa·s	620	470	210	140	40	<10
pH		8.4	8.4	8.3	8.2	8.2	7.2
Coat Weight (Avg ± σ)	/ g·m^{-2}	34.8 ± 0.2	32.4 ± 0.4	32.2 ± 0.8	30.4 ± 0.6	27.9 ±0.4	11.8 ±1.6

σ refers to the standard deviation of repeat samples about the average (Avg)

The viscosity of the coating colour formulations was measured with a Brookfield viscometer (Brookfield Digital Viscometer, Model DV-II, Brookfield Engineering Laboratories, Inc. Middleboro, USA) at rotation rate 100 min^{-1} using spindle #3. Fine GCC pigments gave higher coating colour viscosity than coarser ones, and high viscosity increased the achieved coat weight (Table 1). Blocking in rewinding was observed when pure PVAc latex (TP6) was used.

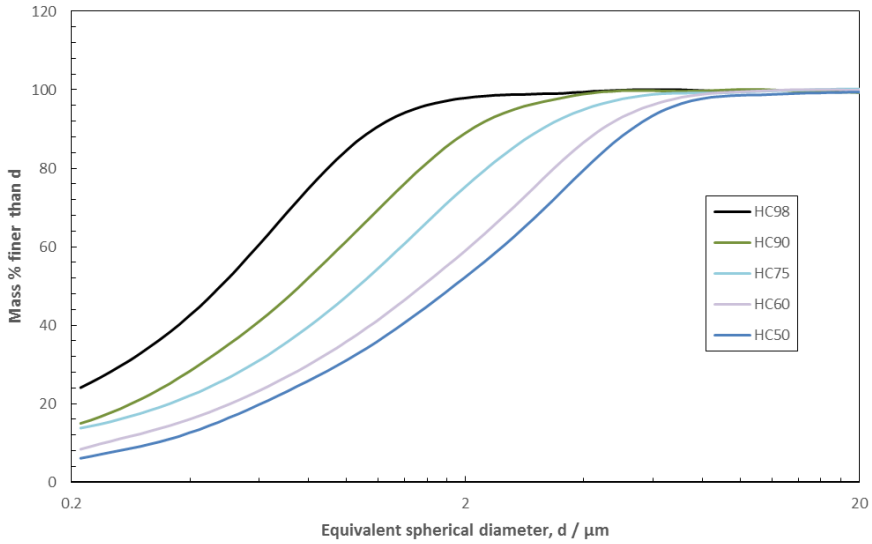

Figure 1: Particle size distribution of GCC pigments

2.2 Laboratory coating

The coatings were applied using a MiniLabo™ laboratory coater (Yasui Seiki Co., Kanagawa, Japan) by reverse gravure in the so-called kiss coating setting. The coating speed was 2 $m \cdot min^{-1}$, and the mesh resolution of the micro gravure roll was 75 lines per inch. Coated papers were dried using hot air and IR dryers. Figure 2 shows the coater and the coating method schematically.

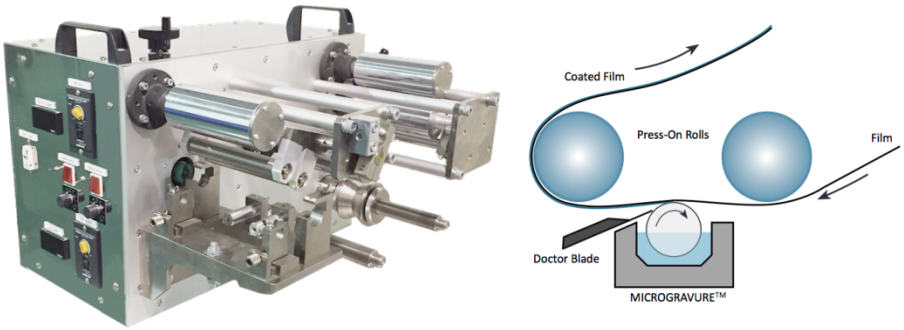

Figure 2: MiniLabo laboratory coater and principle of reverse gravure coating method

2.3 Tack force measurement (oil film release force)

The Ink Surface Interaction Tester, ISIT, (SeGan Ltd., U.K.) is normally employed for studying the ink tack-related setting rate on paper coatings (Gane and Seyler, 1994; Kamal Alm, et al., 2010; Kamal, et al., 2010, Ridgway and Gane, 2005). To establish the relationship of the critical roughness–film thickness interaction in respect to the release force, the target here is to characterise the release properties of the coating surface, and therefore avoid ink setting and damaging of the print (picking), by using an oil film and a controlled film split/pull-off mechanism.

The release force development was studied (Figure 3) by using six different infeed levels of Newtonian high viscous (110 mPa·s) IGT pick test oil (IGT Testing Systems, Almere, The Netherlands). The release force measurements were executed on conditioned substrates (at 23 °C and 50 % relative humidity). The oil was applied to the rubber covered print disc (width 20 mm, hardness 65 Shore A) with an IGT distributor (IGT inking unit AE) at 23 °C and 50 % relative humidity. The minimum oil distribution time after oil addition was 240 s and the oil application time from distribution roll to print wheel was kept constant at 90 s. The amount of oil transferred to the print disc was measured gravimetrically.

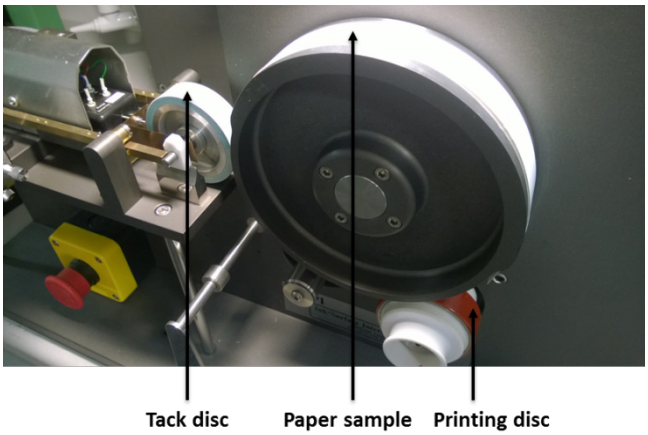

Figure 3: The Ink Surface Interaction Tester (ISIT)

Oil was transferred from the print disc to paper at the speed of 0.5 $m \cdot s^{-1}$, the number of revolutions was 10 and the printing disc was loaded against the substrate with a force of 200 N (equivalent to a line pressure of 10 $kN \cdot m^{-1}$). The test papers were coated and printed in the same orientation direction. The amount of oil transferred from print disc to the paper was also measured gravimetrically. The density of the IGT oil was determined (ρ = 0.897 $g \cdot cm^{-3}$) and the transferred oil film thickness was calculated. The thickness of oil film that was transferred from the print disc to the paper was within the range of 0–6 μm.

During the release force measurement, the smooth, offset blanket-like, covered ISIT tack disc was rolled into contact with the printed oil layer (contact pressure is defined as a relative value by the "ramp in" force, *R*, given as instrument setting level *R* = 2 or 8), held stationary (hold time, *H*, compared at *H* = 0.5 s and 12 s) and then removed under a constant acceleration (ramp down speed, set to the instrument maximum level of 1) providing a uniform extensional rate (Hencky strain condition) on the oil layer. The maximum force required to remove the tack disc was recorded as the release force. The tested area is referred to as the pull-off area. The print disc and tack disc were cleaned after each trial point using white spirit. After cleaning the white spirit was wiped off with tissue (Teholiina Universal 320 by Etera) and the surfaces dried using compressed air.

Each test strip contained 13 pull-off positions over time which could be individually evaluated – note the IGT oil is non-drying. The delay between positions was kept constant (3 s or 3.5 s). First and last data points were removed from the results and the release force average (*T*) and standard deviation (*SD*) were recorded. If any paper wrinkles were observed during testing also those data points were removed from the calculated results.

2.4 Surface topography

Parker Print-Surf roughness (clamp pressures 0.5 MPa, 1.0 MPa and 2.0 MPa) were measured according to ISO 8791-4.

Scanning electron microscopy (Jeol JSM-6335F) was used in secondary ion imaging mode for visualisation of the surface topography. Imaging was made using an acceleration voltage of 10.0 kV. Small paper samples

were attached to the microscope sample holder with conductive tape. The sample surface was coated for 15 s by platinum sputtering (Agar Sputter Coater, model 108A, Agar Scientific Ltd.) to acquire a ~10 nm thick conductive coating.

3. Results and discussion

3.1 Surface properties

The differences between particle size distributions of GCC pigments were clearly visible on the SEM images (Figure 4). The latex film coverage of the pigment seemed to be higher if coarse pigments were used, i.e. the pigment volume concentration was effectively under the critical point. The blocking tendency of the pure PVAc latex film can be seen from the SEM images (Figure 5). Latex film by itself, naturally, gave an extremely smooth surface.

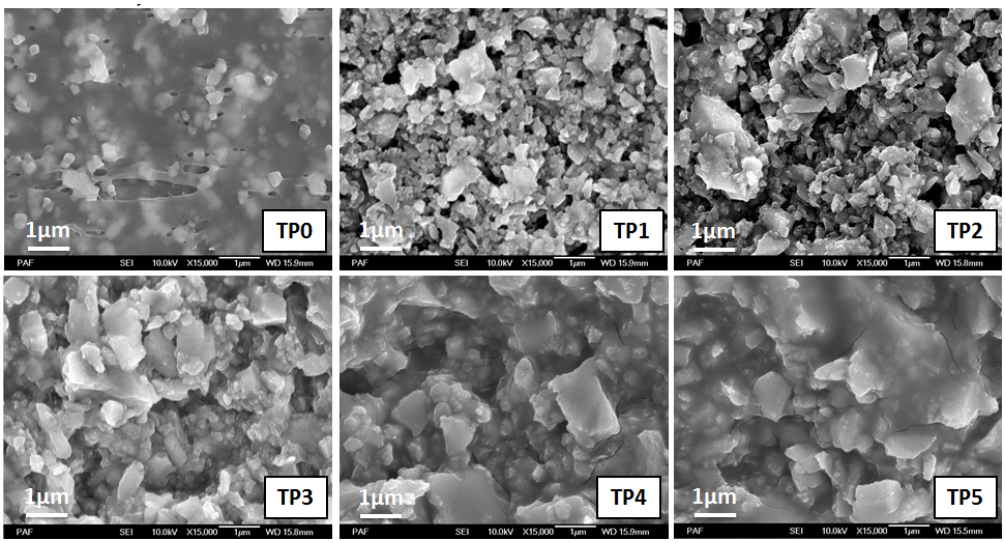

Figure 4: SEM images of the surfaces: (TP0) uncoated SuperYUPO, (TP1) Hydrocarb 98, (TP2) Hydrocarb 90, (TP3) Hydrocarb 75, (TP4) Hydrocarb 60 and (TP5) Hydrocarb 50; coating direction was from the bottom of image to the top

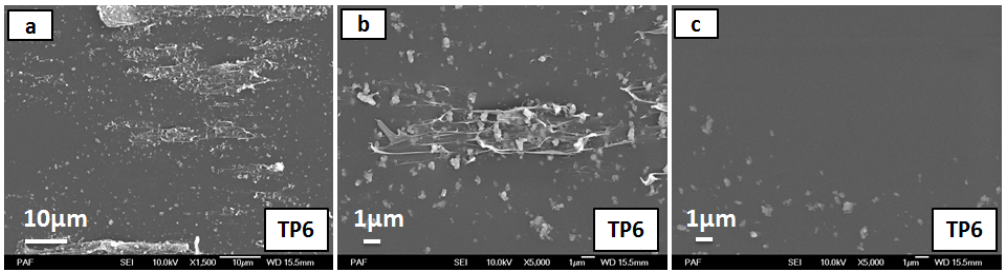

Figure 5: SEM images of the PVAc latex surface: (a) TP6, (b) blocking area and (c) TP6 blocking-free area, both at greater magnification

Surface roughness values for the studied samples are compiled in Table 2. It can be easily seen that the GCC-coated paper PPS roughness is highly dependent on the pigment particle size and distribution: the smaller the particle size, the higher the gloss and the lower the roughness of the coating. This desired relationship is to be expected and has been established in many earlier studies (Tyagi, Ray and Sood, 2010; Lu, et al., 2008). Smaller size particles enhance gloss and display lower roughness since they increase the packing density of particles by filling the void spaces (Alince and Lepoutre, 1980; Eklund, 1975; Lee, 1974). Pure latex film gave high gloss values but relatively high roughness and gloss deviation. This latter characteristic can be linked to the blocking behaviour of the pure PVAc latex film.

Table 2: Parker Print-Surf roughness results for the laboratory coated samples

	PPS20 (µm)		PPS10 (µm)		PPS5 (µm)		$PPS0_{E^*}$
	Avg	SD	Avg	SD	Avg	SD	(µm)
SuperYUPO	0.74	0.03	0.97	0.06	1.20	0.07	1.31
HC98	0.87	0.01	1.03	0.01	1.16	0.02	1.24
HC90	0.97	0.01	1.14	0.01	1.28	0.04	1.36
HC75	1.22	0.02	1.43	0.02	1.62	0.04	1.73
HC60	1.61	0.02	1.89	0.03	2.16	0.07	2.30
HC50	1.84	0.03	2.17	0.03	2.46	0.03	2.62
PVAc latex	0.68	0.06	0.86	0.08	1.02	0.11	1.11

**E refers to the extrapolated value at zero pressure*

3.2 ISIT tests

3.2.1 Oil transfer

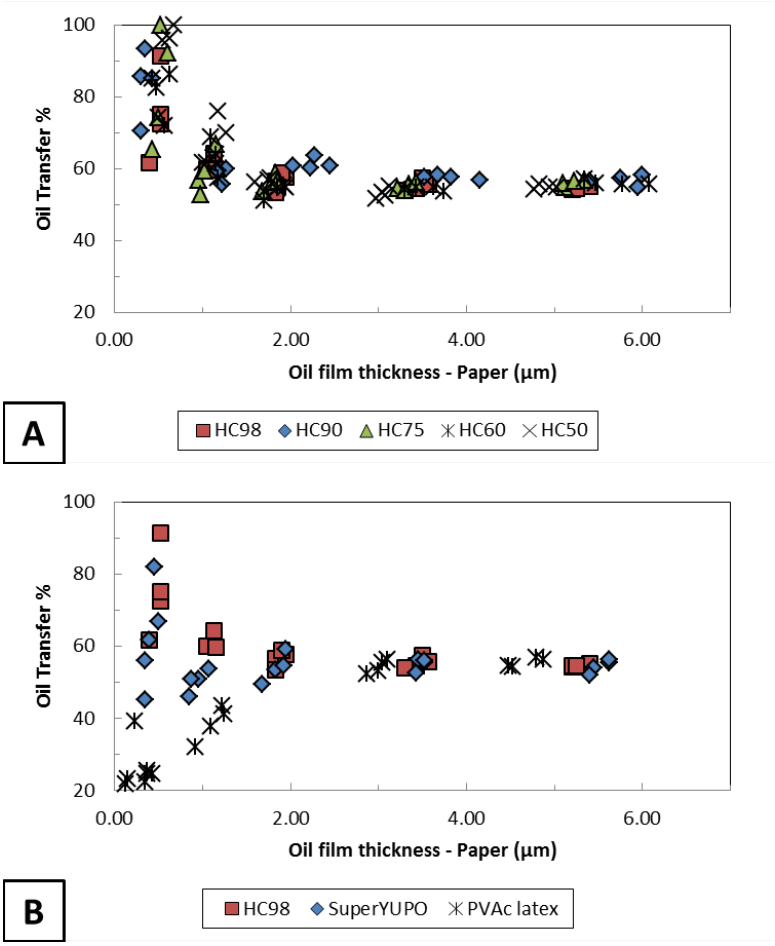

Figure 6: Oil transfer percentage curves on: (A) GCC pigment all coatings, and (B) on HC98 coating, SuperYUPO and PVAc latex, as a function of equivalent oil film thickness (µm) on the respective paper surface

Ink transfer fraction is calculated by dividing the transferred ink amount by applied ink amount. Typically, if using one printing nip system, ink transfer starts from zero, increases as a function of ink amount (increased contact area) and then levels, so that the ink transfer percentage is near 50 %, and free ink film splitting occurs. Oil transfer percentage curves of the trial points are shown in Figure 6. The number of

print disc revolutions in this study was 10, because the target was to achieve even oil coverage. After each revolution, the oil transfer to the paper surface has the ability to push the previous oil deeper into the surface roughness (Särelä, Härkönen and Paulapuro, 2002; Särelä, 2004), or more likely for coated paper enables the continued flow of the viscous oil to reach equilibrium distribution. Near 100 % oil transfer was achieved by using low applied oil amount and rough paper surface. Under this condition, almost all applied oil from the print disc was transferred into the coated paper surface structure during the 10 revolutions. If the applied oil film thickness on the coating surface was more than 3.0 µm, the oil transfer on all tested samples was almost constant. The roughness volume is, therefore, fully filled at higher oil amounts and a wet oil film splitting takes place. Pure PVAc latex surface resisted test oil transfer (de-wetting and reticulation) and the oil transfer percentage was extremely low when the print disc oil film thickness was less than 2.0 µm. Higher oil feed increased the equivalent oil film thickness on the coatings and decreased wet oil film splitting force. Oil transfer percentage onto PVAc latex was enhanced by decreasing the oil splitting force in this way.

3.2.2 Release force

The release force of each trial point was tested using six different oil amounts and four ramp in force, *R* – hold time, *H*, combinations. High nip (ramp-in) pressure (*R*8) and long nip dwell (hold) time (*H*12 s) increased the release force and decreased the variation of the measurements.

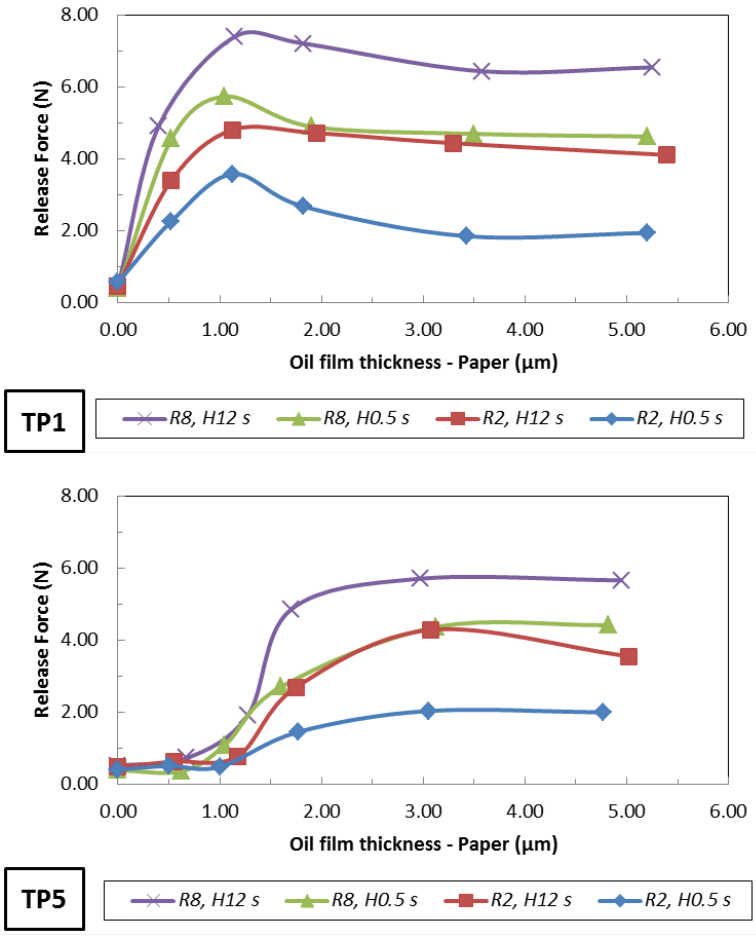

Figure 7: Effect of ramp in force (R) – hold time (H) combinations on release force: (TP1) HC98 and (TP5) HC50

The nip lengths of the ISIT measurements (defined by the pull-off area) can be controlled by nip pressure (*R*) and nip dwell time (*H*). High *R* (*R*8) and long *H* (*H*12 s) increased the pull-off area, and the release force level was increased. At high oil film thickness lateral flow, seen as oil squeeze-out from the contact area

was increased whilst the ISIT release force remained almost constant, i.e. lateral flow occurred until an equilibrium film thickness remained in the nip (Figure 7).

In Figure 8A, typical release force curves of GCC pigments are presented as a function of equivalent oil film thickness on the coating surface (*R*8, *H*0.5 s). At low oil feed levels, each additional oil increment compensated progressively for the surface roughness and thus increased the effective contact area and release force. For coarse pigments (HC50 and HC60) higher oil application level was needed before this compensation effect was observed. Initially, oil flows deep into the roughness volume under application pressure and film flow, and the release force as a result remains at first on a low constant level. The release force eventually reached a maximum value when the surface roughness under the nip was filled with oil and the maximum effective contact area was reached.

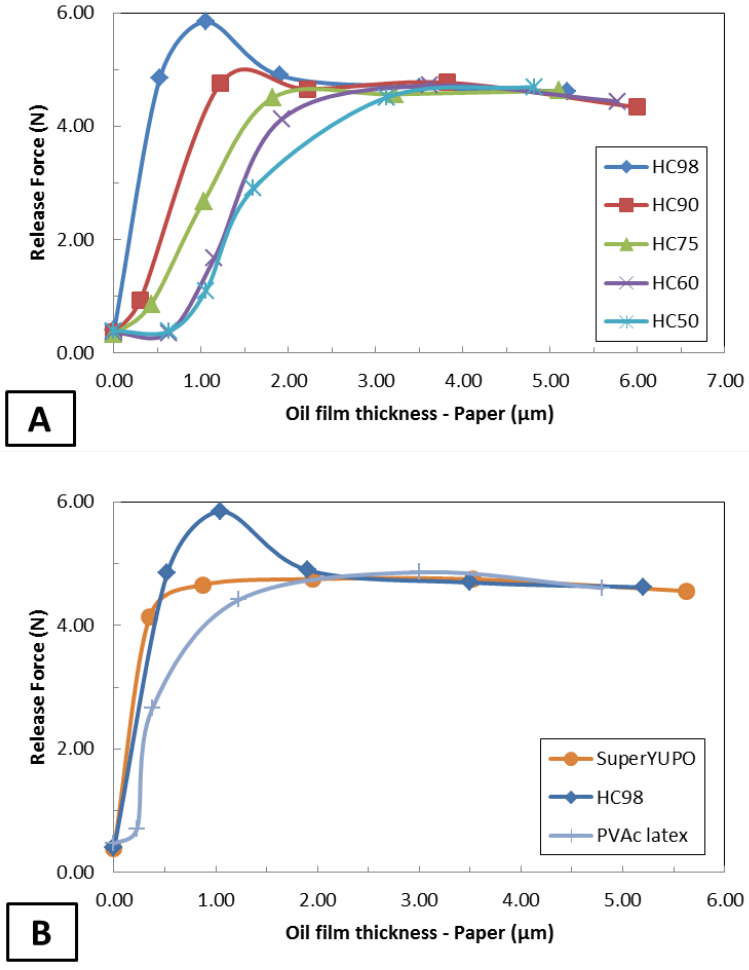

Figure 8: Release force curves of (A) GCC pigments and (B) a comparison of the smoothest GCC coating HC98, SuperYUPO and PVAc latex as a function of equivalent oil film thickness on the coating surface (R8, H0.5 s)

The release force maximum value, the width of the release force peak and the peak position in the *x*-axis (equivalent oil film thickness) were dependent on the pigment particle size. Fine GCC (TP1 HC98) gave a high and fairly narrow release force peak with low oil amount (approximately 1.0 µm equivalent oil film thickness on the coating surface). Much thicker oil film (approximately 1.5 µm equivalent film thickness) was needed to achieve the maximum release force condition when using HC90 (TP2) pigment. No clear release force peak was observed when coarse GCC pigments were used (HC60 and HC50), indicating that the contact area to oil volume ratio was insufficient to generate a thin film split mechanism.

Pure PVAc latex (TP6) gave an overall low release force at low oil film thickness because the latex surface was not wetted by the oil (Figure 8B). With all trial points the release force was almost constant if the equivalent oil film thickness was above 3.0 µm, suggesting the lateral flow (squeeze-out) led to an equilibrium film thickness in the nip, such that bulk oil film splitting was occurring and the oil viscosity dominated the resulting release force.

In Figure 9 we see a linear correlation (r^2 = 0.991) between the Parker Print-Surf ($PPS0_E$) roughness, extrapolated to at zero pressure to represent the intrinsic surface roughness without compression, and the Critical Film Thickness (CFT), corresponding to the release force maximum. This may indicate that the additional oil compensated the surface roughness and thus increased the effective contact area. At the point of CFT, surface roughness volume was totally compensated for by IGT oil volume, and the maximum thin film contact area was reached. The range (±σ) of CFT was fairly high because of the limited oil feed range that was tested.

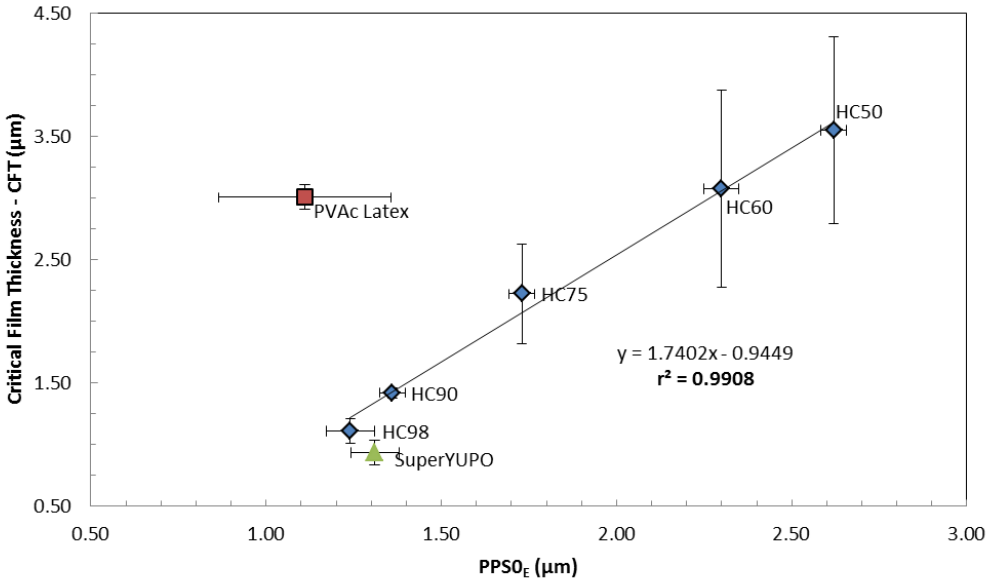

Figure 9: The Critical Film Thickness (CFT) as a function of Parker Print-Surf ($PPS0_E$) roughness; a linear fit across the roughness range generated by the GCC pigments is indicated by a solid line and the range of each data point is ±σ

4. Conclusions

Critical film thickness, defined as the equivalent oil film thickness at which the maximum release force value as measured by ISIT is reached, was shown to be a linear function of surface roughness for similar coating materials. Newtonian IGT pick test oil was used as the liquid film and the release force was measured as a function of oil amount using a range of nip pressure–nip dwell time combinations.

Incremental additional fluid compensated for the surface roughness volume and thus increased the effective contact area and resulting release force. The release force maximum value, the width of the force peak and the peak position in relation to the equivalent film thickness on the coating (CFT) revealed the surface roughness properties and their response to compression and liquid lateral flow rate (squeeze-out). This test method gives new insights into paper surface release properties and will be used further to develop a characterisation technique.

Acknowledgements

The Media Industry Research Foundation of Finland (VTS) is gratefully acknowledged for funding the research project.

References

Alince, B. and Lepoutre, P., 1980. Plastic pigments in paper coatings - the effect of particle size on porosity and optical properties. *Tappi Journal,* 63(5), pp. 49–53.

Bohan, M.F.J., Claypole, T.C., Gethin, D.T. and Megat Ahmed, M.M.H., 2000. A model for ink impression in printing contacts. *Journal of Pulp and Paper Science,* 26(11), pp. 414–419.

Bristow, J. and Bergenblad, H., 1992. Paper structure and ink-setting: factors influencing the set-off test. In: W.H. Banks, ed. *Advances in Printing Science and Technology*. London: Bentech Press, pp. 144–167.

Eklund, D., 1975. Pigment particle size - its significance in paper coating, *Cellulose Chemistry and Technology,* 9(3), pp. 299–312.

Gane, P.A.C. and Seyler, E.N., 1994. Tack development: an analysis of ink/paper interaction in offset printing. In: *1994 Tappi Coating Conference, Proceedings.* San Diego, CA, 1994. Atlanta, GA: TAPPI Press, pp. 243–260.

Kamal Alm, H., Ström, G., Karlström, K., Schoelkopf, J. and Gane, P.A.C., 2010. Effect of excess dispersant on surface properties and liquid interactions on calcium carbonate containing coatings. *Nordic Pulp and Paper Research Journal,* 25(1), pp. 82–92.

Kamal, H., Ström, G., Schoelkopf, J. and Gane, P.A.C., 2010. Characterization of ink–paper coating adhesion failure: effect of pre-dampening of carbonate containing coatings. *Journal of Adhesion Science and Technology,* 24(3), pp. 449–469.

Lee, D.I., 1974. A fundamental study on coating gloss. In: *Tappi Coating Conference Proceedings*. Atlanta, GA: TAPPI Press, pp. 97–114.

Lu, Z., Zhang, M., Wang, R. and Wu, G., 2008. Particle size distribution and packing structure of calcium carbonate pigments: effect on art paper characteristics. *Appita Journal,* 61(5), pp. 379–382.

Lyne, M.B. and Aspler, J.S., 1982. Ink-paper interactions in printing: a review. In: M. Hair and M.D. Croucher, eds. *Colloids and Surfaces in Reprographic Technology.* American Chemical Society, pp. 385–420.

Oittinen, P. and Lindqvist, U., 1981. The behaviour of printing ink in an offset printing nip. *Paperi ja Puu,* 63(6–7), pp. 432–442.

Ridgway, C.J. and Gane, P.A.C., 2005. Ink-coating adhesion: the importance of pore size and pigment surface chemistry. *Journal of Dispersion Science and Technology,* 25(4), pp. 469–480.

Särelä, S., Härkönen, E. and Paulapuro, H., 2002. Evaluation of Ink Transfer Theory. In: *Proceedings of 54th Annual Technical Conference of the Technical Association of the Graphic Arts, TAGA*. Asheville, NC, 2002. Rochester, NY: TAGA, 1998, pp. 90–108.

Särelä, S., 2004. *Uncoated Paper Surface for Coldset Web Offset Printing : Set-off Studies*. Doctoral Dissertation. Helsinki University of Technology.

Tyagi, S., Ray, A.K. and Sood, Y.V., 2010. Surface characteristics of coating layers formed by coating pigments with different particle sizes and size distribution. *Journal of Coatings Technology and Research,* 7(6), pp. 747–756.

Walker, W.C. and Fetsko, J.M., 1955. A concept of ink transfer in printing. *American ink maker,* 33(12), pp. 38–40.

The Wettability Effect of CMY Water-based Flexographic Printing Inks

Zuzanna Żołek-Tryznowska[1], *Joanna Izdebska-Podsiadły*[1] *and Mariusz Tryznowski*[2]

[1] Faculty of Production Engineering, Warsaw University of Technology
[2] Faculty of Chemistry, Warsaw University of Technology

E-mail: z.tryznowska@wip.pw.edu.pl; j.izdebska@wip.pw.edu.pl; tryznowski@ch.pw.edu.pl

Abstract

The aim of this work was to study the wettability effect of CMY water-based printing inks. The effect of addition of branched polyglycerols and the impact of primary hydroxyl groups on wettability have also been investigated. The printing with water-based printing inks was performed on various plastic films (PE, BOPP, PET). The impact of branched polyglycerol on the rheology behaviour of water-based flexographic ink with an addition of 1 % of polyglycerol is presented. The contact angles of the printing inks on the printing bases were measured. The surface tension of printing inks was determined. The study confirmed the wettability of substrates by printing ink influences the optical density of the dried ink film.

Keywords: contact angle, water-based printing inks, CMY printing inks, plastic films

1. Introduction and background

Flexographic printing technology is suitable for printing on paper materials, as well as nonporous and non-absorbent substrates used in packaging industry. Flexography requires low viscosity inks, lower than 0.05–0.5 Pa·s (Havlínová, et al., 1999). There are three types of flexographic inks used for these applications: water-based, solvent-based and UV-curable. Nowadays, due to the ecological reasons, the attention in the printing industry is focused on production of water-based printing inks in order to minimize the evaporation of organic solvents into environment. Printing with water-based inks on non-absorbent substrates, for instant plastic films, is linked up with some problems. The adhesion of the water-based ink film to the plastic film is worse than solvent-based ink because of a low proper wetting of these surfaces. Moreover, the wet rub resistance of overprinted plastic films with water-based inks is usually poor.

The print quality is closely related to the wettability of the substrate by the printing ink and adhesion of the dried ink film to the substrate. Furthermore, surface tension and viscosity are the two parameters of inks which have an important influence on ink flow in the printing unit (Kipphan, 2001) and also on print quality. The wettability is connected with the value of substrate surface free energy and the type of ink. However, a high value of surface free energy does not always guarantee the high quality of the print (Izdebska, 2016). It is well-known that the surface tension of flexographic printing ink has to be lower than the surface free energy of the plastic film to allow proper wetting and adhesion between the layers of the ink film and the plastic film. Typically, plastic printing bases exhibit quite low surface free energy, i.e. 29–30 mJ/m^2, 31–36 mJ/m^2 and 43–47 mJ/m^2 for PP, PE and PET film, respectively (Izdebska, 2016; Żołek-Tryznowska, Tryznowski and Izdebska, 2016). The corona discharge treatment may be used prior printing in order to increase surface free energy, introduce surface crosslinking, modify surface morphology by increasing or reducing its roughness and crystallinity, and remove dirt and weak boundary layers (Izdebska, 2016). The increase of surface free energy of printing base results in an increase of optical density (Izdebska, 2016). The surface tension of printing inks can be in the range 22-25 mN/m and 30-37 mN/m for solvent and wa-

ter-based printing inks, respectively (Khan, et al., 2010; Kosolia and Tsatsaroni, 2010; Żołek-Tryznowska and Izdebska, 2013). On the other hand, water exhibits a surface tension of 72 mN/m, hence in order to decrease the surface tension of water-based inks, organic co-solvents or surfactants into water-based inks are added.

In our previous works, we have shown the wettability effect of polyglycerols using two various branched polyglycerols containing predominantly primary hydroxyl groups (PG-1) or primary and secondary hydroxyl end groups (PG-1,2) and their effect on the adhesion between the dried ink film (colour black K) and various plastic films used as printing bases (Żołek-Tryznowska, Tryznowski and Izdebska-Podsiadły, 2016; Tryznowski, Żołek-Tryznowska and Izdebska-Podsiadły, in press). In this work, we use branched polyglycerols containing predominantly primary hydroxyl groups (PG-1) and its derivative (PG-0), were the hydroxyl groups are blocked. The influence of polyglycerol on several printing ink properties (surface tension, contact angle) and optical density of full tone area was estimated.

2. Materials and methods

2.1 Materials

The detail synthesis of PG-0 and PG-1 is described in Tryznowski, Żołek-Tryznowska and Izdebska-Podsiadły (in press). The modifications of inks were prepared according to the descriptions of our previous works (Żołek-Tryznowska, Tryznowski and Izdebska-Podsiadły, 2016). The addition of polyglycerols was 1 %, because in our previous works we have shown, that the best print quality was achieved with the addition of 1 % of hyperbranched polyesters (Żołek-Tryznowska and Izdebska, 2012; Żołek-Tryznowska and Izdebska, 2013). As an original printing ink the water-based printing ink (Chespa, Poland) was used, of the following colours: cyan (C), magenta (M) and yellow (Y). As printing substrates three various polymer films were used: polyethylene (PE), oriented polypropylene (BOPP) and polyethylene terephthalate (PET) films. The plastic films were transparent and had a thickness of 50 μm for PE, 20 μm for BOPP and 12 μm for PET. All films were activated by a corona treatment. The surface free energy of plastic films was assessed using dyne ink test and it was equal to 40.5, 52.3 and 49.1 mJ/m^2 for PE, BOPP and PET film, respectively. The surface tension of plastic substrates was estimated by Owens-Wendt method using two tested liquids – water as a polar liquid and diiodomethane as a dispersive liquid (Żenkiewcz, 2000).

2.2 Contact angle and surface tension measurement

Prior contact angle measurement (Żenkiewicz, 2007) and printing, the rheological characteristics of the printing inks (the original process printing ink and the ink with added hyperbranched polyglycerol) were identified by a flow time in a flow cup (volume 100 mL, outlet diameter 4 mm), according to an ISO 2431:2011 standard (International Organization for Standardization, 2011). The measurements were performed at 23 °C; the relative measurement error was less than 3 % and the kinematic viscosity, expressed in flow time, was 18 ± 0.1 s for the printing inks. Contact angle and surface tension measurements of the investigated inks were performed using a DSA 30E drop shape analysis system (Krüss, Germany). Smooth and horizontal sessile drops of the liquids were deposited on a solid surface – plastic film (BOPP, PE, PET) using needles of 0.5 mm diameter. The contact angle was measured on static drops. The drop shape analysis was done 15 s after the drop deposition with Tangent method 1. The surface tension of investigated inks was determined by a pendant drop method using needles of 2 mm diameter. Environmental conditions were stable with temperature equal to 23 ± 1°C. The reported contact angle and surface tension values are the mean of five drops.

2.3. Printing

Laboratory printing was carried out with K-hand coater (RK prints, UK) using K bar characterized by 0.15 mm wire diameter and 6 μm wet ink film deposition. Printing was performed under controlled environmental conditions (23 °C and 50% RH).

2.4. Characterization of prints

The optical densities of the full-tone area were determined using a SpectroEye spectrophotometer (GretagMacbeth, Switzerland). Measurements of the optical density of the full-tone area were performed at the following settings: with polarization filter, white standard: proofing paper, density standard: DIN. The reported results are the average of the measurements from a minimum of six areas on two different prints.

3. Results and Discussion

The printability of polymer printing bases depends on the wettability of the base by the printing ink. Because of high surface tension of water in contrast to organic solvents used for printing inks, the water-based printing ink are characterized by worse wettability of the polymer base in contrast to solvent printing inks. The adhesion between the base and the dried ink layer, the print quality and mechanical properties of prints depends on wettability of the base by the printing inks. Lower contact angle is related with better wettability and with better adhesion of the dried ink film to the base. Furthermore, the printing process requires that the surface tension of the printing ink is lower than the surface free energy of the plastic film.

The values of contact angle together with surface tension of inks without and with addition of investigated polyglycerols are summarized in Table 1. The changes of contact angle for CMY printing inks for PE printing base is presented in Figure 1. The highest contact angles are observed for PE film and the lowest contact angles for BOPP film. Investigated yellow and magenta printing inks are characterized by better wettability (lower values of contact angle) in contrast to cyan printing ink. Furthermore, the values of contact angle of printing ink with addition of PG-1 are lower than values of original printing ink.

The surface tension of the ink slightly decreases with addition of 1 % of PG-1. The highest change of surface tension was observed for the cyan printing ink.

Table 1: Contact angles and surface tension of investigated printing inks

Printing ink	**Contact angle (°)**			**Surface tension (mN/m)**
	PE	BOPP	PET	
C	60.07	37.55	42.67	31.6
C + 1% PG-0	59.32	41.24	41.53	30.3
C + 1% PG-1	55.61	37.20	40.03	30.4
M	58.57	29.94	28.95	31.4
M + 1% PG-0	53.36	30.92	30.57	31.3
M + 1% PG-1	56.60	31.74	27.87	30.9
Y	59.73	35.63	42.52	29.8
Y + 1% PG-0	58.03	39.10	43.18	30.0
Y + 1% PG-1	56.72	35.70	41.88	29.3

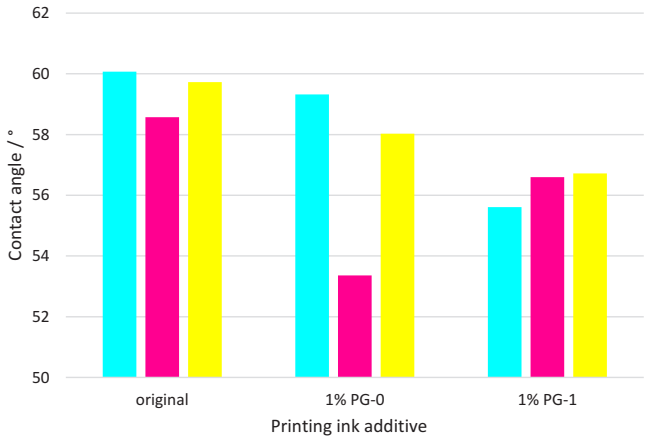

Figure 1: The changes of contact angle of CMY printing inks: original printing ink and printing inks with addition of PG-0 and PG-1 on PE printing base

Table 2: Optical densities of full-tone area of prints

Printing ink	**Optical density**		
	PE	BOPP	PET
C	2.39 ± 0.16	2.45 ± 0.03	2.46 ± 0.03
C + 1% PG-0	2.40 ± 0.13	2.50 ± 0.09	2.52 ± 0.12
C + 1% PG-1	2.12 ± 0.10	2.39 ± 0.06	2.40 ± 0.10
M	1.72 ± 0.07	1.67 ± 0.08	1.66 ± 0.06
M + 1% PG-0	1.63 ± 0.11	1.67 ± 0.09	1.57 ± 0.05
M + 1% PG-1	1.72 ± 0.05	1.66 ± 0.05	1.62 ± 0.05
Y	1.96 ± 0.02	1.93 ± 0.04	1.91 ± 0.03
Y + 1% PG-0	1.95 ± 0.01	1.96 ± 0.04	1.92 ± 0.05
Y + 1% PG-1	1.91 ± 0.02	1.92 ± 0.03	1.92 ± 0.05

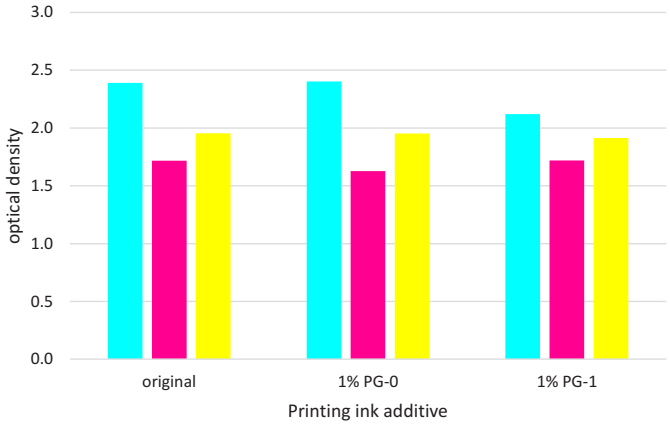

Figure 2: The changes of optical densities of CMY printing inks: original printing ink and printing inks with addition of PG-0 and PG-1 on PE printing base

The values of optical density of full tone area are listed in Table 2. The changes of optical densities of full-tone area for CMY printing inks for PE printing base is presented in Figure 2. The optical density assesses the thickness of the dried ink layer. The thickness of the dried ink layer depends on the wettability of the base by the ink during the printing process: better wettability is connected with a thinner dried ink layer and lower values of optical density. The optical density of full-tone area decreases with addition of the PG-1.

On the other hand, values of optical density of prints overprinted with the ink with addition of PG-0 are slightly higher than or equal to original printing ink or ink with addition of PG-1. The changes of contact angles of investigated CMY printing inks correspond to the changes of contact angles, as expected.

The authors plan to measure CIELAB colour parameters and gloss of prints in order to gain a broader analysis.

4. Conclusions

In this work we have demonstrated the wettability effect of CMY printing inks on selected properties. We have also investigated the effect of addition of branched polyglycerols and the impact of primary hydroxyl groups on wettability.

The impact of the polyglycerols on the wettability, surface tension, optical density of full-tone area is reported in this paper. Furthermore, the wettability of the film by the printing ink influences the print quality. We have confirmed that polyglycerols containing predominately primary hydroxyl groups in the macromolecule may improve the print quality.

Our results help to understand phenomena which occurs during printing, support the use of branched polyglycerols as performance additives for water-based printing inks and may open up new possibilities for applications of these environmentally friendly polymers.

Acknowledgments

Funding for this research was provided by National Science Centre based on decision nr DEC-2013/11/D/ST8/03371.

References

Havlínová, B., Cicák, V., Brezová, V. and Horňáková, Ľ., 1999. Water-reducible flexographic printing inks – rheological behaviour and interaction with paper substrates. *Journal of Material Science*, 34(9), pp. 2081–2088.

International Organization for Standardization, 2011. *ISO 2431:2011 Paints and varnishes -- Determination of flow time by use of flow cups*. Geneva: ISO.

Izdebska, J., 2016. Corona treatment. In: J. Izdebska and S. Thomas, eds. *Printing on Polymers: Fundamentals and Application*. Oxford: Elsevier, pp. 123–139.

Khan, M.S., Fon, D., Li, X., Tian, J., Forsythe, J., Garnier, G. and Shen, W., 2010. Biosurface engineering through ink jet printing. *Colloids Surf B: Biointerfaces*, 75(2), pp. 441–447.

Kipphan, H., ed. 2001. *Handbook of Print Media: Technologies and Production Methods*. Berlin: Springer-Verlag.

Kosolia C.T. and Tsatsaroni E.G., 2010. Synthesis and characterization of hetarylazo disperse colorants: preparation and properties of conventional and microemulsified inks for polyester ink-jet printing. *Journal of Applied Polymer Science,* 116 (3), pp. 1422–1427.

Tryznowski, M., Żołek-Tryznowska, Z. and Izdebska-Podsiadły, J., (in press). The wettability effect of branched polyglycerols used as a performance additives for water-based printing inks. *International Journal of Polymer Science.* (In review).

Żenkiewicz, M., 2007. Analysis of the most important methods of investigations of polymeric materials surface free energy, *Polimery*, 52(10), pp. 760–767.

Żołek-Tryznowska, Z. and Izdebska J., 2012. Hyperbranched polymers – their application in printing inks. *Composite Interfaces*, 19(7), pp. 441–451.

Żołek-Tryznowska, Z. and Izdebska, J., 2013. Flexographic printing ink modified with hyperbranched polymers: Boltorn™P500 and Boltorn™ P1000. *Dyes and Pigments*, 96(2), pp. 602–608.

Żołek-Tryznowska, Z., Tryznowski, M., and Izdebska-Podsiadły, J., 2016. Polyglycerols as a modern environmentally friendly additives improving the abrasion resistance of printed films. In: Ž. Pavlović, ed. *Proceedings: 8th International Symposium on Graphic Engineering and Design, GRID 2016*. Novi Sad, 2–4 November 2016, pp. 85-90.

Index of authors